Geochemical Assessment of Leaching from Coal Ash Disposal Sites

By

Xinyue Wang

Dissertation

Submitted to the Faculty of the

Graduate School of Vanderbilt University

in partial fulfillment of the requirements

for the degree of

DOCTOR OF PHILOSOPHY

in

Environmental Engineering

September 30, 2022

Nashville, Tennessee

Approved:

David S. Kosson, Ph.D., Committee Chair

Andrew C. Garrabrants, Ph.D., Committee Co-chair

John C. Ayers, Ph.D.

Craig H. Benson, Ph.D.

Kevin G. Brown, Ph.D.

George M. Hornberger, Ph.D.

Florence Sanchez, Ph.D.

Hans van der Sloot, Ph.D.

ACKNOWLEDGEMENTS

First and foremost, I would like to thank my esteemed advisor, Prof. David Kosson, for his mentorship at every stage of my Ph.D. study. Not only has he provided invaluable insights and advice on the research project, but Prof. Kosson also always has been supportive of the important decisions in my life. I have met a lot of good teachers and professors since I was a child. Now for the important five years of my Ph.D. study, the last stage of my life being a student, I feel lucky and grateful that I can have such a nice advisor. I am also deeply grateful to my co-advisor Prof. Andrew Garrabrants. I still remember the moment when I met him in the office for the first time. At that time, I did not realize that I would receive countless guidance and advice in my experimental work from him. I would also like to thank the entire committee for their technical support and insightful suggestions. Without them, I would not have been able to complete this work.

Throughout my five years at Vanderbilt University, the support of the entire research team has accompanied me along the way. First, I would like to thank Prof. Kevin Brown, Dr. Hans van der Sloot, and Dr. Johannes Meeussen for providing me so much help on the modeling tasks. I also would like to extend my sincere thanks to Rossane DeLapp, Dr. Zhiliang Chen, Dr. Chen Gruber, Dr. Peng Zhang, and other members of the research group, who spent the time to instruct me and steered me through this challenge. Every colleague in the research group would remember the freezing cold March in 2019 when we supported each other and finished the sampling work at a coal ash plant together. Thank you, Darlene, Maya, Jackie, Julie, and many other staff members in the department, for always being cheerful and willing to help me.

My gratitude also goes out to my friends, who bring joy and love into my life, making me not lonely while studying abroad. The first year was difficult for me to adapt to an entirely new environment, but a hotpot every Friday night fueled me to go through every tough week.

I would like to give my special thanks for the financial support that I received from Electric Power Research Institute (EPRI) under Program 242—CCP Land and Groundwater Management. I gratefully acknowledge the valuable comments and inputs from Mr. Bruce Hensel and Mr. Ken Ladwig (currently retired from EPRI). In addition, a portion of my geochemical speciation modeling work was supported by the U. S. Department of Energy, under

Cooperative Agreement Number DE-FC01-06EW07053, entitled ‘The Consortium for Risk Evaluation with Stakeholder Participation III’ awarded to Vanderbilt University, David S. Kosson, principal investigator.

Last but not least, my heartfelt thanks to my parents for their unwavering support and belief in me. When I was discouraged by so many ups and downs throughout the years, the encouragement and understanding from my family kept me going. Thank you, Zhiliang, my best friend, for bringing so many positive influences into my life. If I ever thought about giving up, it was you who always believed in me and gave me the confidence to continue.

I will forever cherish the memory of my Ph.D. study. Each stage of life may not be easy, but they are so meaningful and teach me to enjoy every moment in my life.

TABLE OF CONTENTS

Page

LIST OF TABLES

Table Page

LIST OF FIGURES

Figure Page

NOMENCLATURE

Abbreviation/symbol	Description
Am_{FeOOH}	Amorphous iron oxides and hydroxides
AC	Available content of a constituent
As	Arsenic
B	Boron
BGS	Below ground surface
CA	Coal ash
CCP(s)	Coal combustion products(s)
CFA	Coal fly ash
Cr	Chromium
Cry_{FeOOH}	Crystalline iron oxides and hydroxides
DDL	Diffuse double-layer
DDL-HFO	Diffuse double-layer model for hydrous ferric oxide
DO	Dissolved oxygen
DOC	Dissolved organic carbon
DIC	Dissolved inorganic carbon
DIW	Deionized water
D&M	Dzombak and Morel
EC	Electrical conductivity
Eh	Reduction-oxidation potential after correction of the potential of the reference electrode
EPA	Environmental Protection Agency
EPRI	Electric Power Research Institute
GAP(s)	Gas access point(s)
HC	Hydraulic conductivity
HFO	Hydrous ferric oxide
IC	Ion chromatograph
ICP-MS	Inductively coupled plasma – mass spectrometry
ICP-OES	Inductively coupled plasma – optical emission spectroscopy

ISO	International organization for standardization
K_{sp}	Solubility product constant
LEAF	Leaching Environmental Assessment Framework
LLOQ(s)	Lower limit(s) of quantitation
log K	Logarithm of reaction constant
LSP	Liquid-to-solid partitioning
L/S	Liquid-to-solid ratio
ΣL/S	Cumulative L/S
MDL(s)	Method detection limit(s)
Mo	Molybdenum
MS	Mass spectrometry
MSW	Municipal solid waste
NICA	Non-ideal competitive adsorption
ORP	Oxidation-reduction potential
ORCHESTRA	Modeling platform: objects representing chemical speciation and transport
pe	-log(electron concentration)
pK_{sp}	-log(solubility product constant)
QA	Quality assurance
QC	Quality control
Redox	Reduction-oxidation
Se	Selenium
SPLP	Synthetic precipitation leaching procedure
TC	Total carbon
TCLP	Toxicity characteristic leaching procedures
TOC	Total organic carbon
TIC	Total inorganic carbon
TGA	Thermogravimetric analysis
V	Vanadium
wt%	Weight percent (percent by mass)
XRF	X-ray fluorescence

XRD	X-ray diffraction
Φ	Outside diameter

CHAPTER 1

INTRODUCTION

1.1 Motivation

The combustion of coal, which is the fuel resource for approximately one-quarter of the electricity generation in the United States (U.S.), produces a large volume of residuals including fly ash, bottom ash, and flue gas desulfurization materials. In 2020, 28 million tons of coal combustion products (CCPs), representing 41 percent of CCPs produced in the U.S., were disposed of in impoundments or landfills [1]. Toxic trace constituents can accumulate in CCPs, especially in fine coal fly ashes (CFAs). The U.S. Environmental Protection Agency (U.S. EPA) has identified several constituents in CCPs that can pose risks to human health and the environment, such as arsenic (As), boron (B), barium (Ba), cadmium (Cd), chromium (Cr), molybdenum (Mo), selenium (Se), and vanadium (V) [2]. These constituents were screened according to their relatively high level of concentrations measured in CCP surface impoundments or landfills, as well as the potential hazard based on a toxicity evaluation [2].

Among the constituents of concern, several of them are oxyanions forming constituents, including As, B, Cr, Mo, Se, and V. Under environmental conditions, the relatively high mobility of these oxyanionic constituents can potentially result in leaching from CCPs deposits to the environment [2–4]. For example, as a result of a coal ash spill of 3.7 million cubic meters of CFA at the Kingston Fossil Plant, arsenic concentrations up to 2 mg/L have been detected in porewater extracted from the river sediments [5]. Such concentrations represent 200 times the corresponding national standard for drinking water. As a result, the long-term environmental safety of CCP disposal sites has received increasing concern for the 953 on-site impoundments and 432 landfills within U.S. [2]. The decision making for the management of these disposal sites requires a comprehensive assessment of contaminant leaching from the field sites. For clean-up of each site, the cost can range from millions to billions of dollars depending on the size of the site [6].

In this study, the oxyanions forming constituents including As, B, Cr, Mo, Se, and V are focused

on for the leaching assessment of CCPs. Other toxic oxyanionic constituents (e.g., antimony (Sb)) have been identified as important constituents of concern in waste materials such as in municipal solid waste incineration bottom ash [7], but herein they are not included as primary focused constituents due to the relatively low concentrations in leachates in CCP disposal sites [2].

Among different CCPs types, CFA is of most concern due to its accumulation of toxic trace contaminants; therefore, the ability to identify and understand the controlling mechanisms for leaching of oxyanionic constituents is critical for proper management and disposal of CFA. However, the large variations in the chemical composition of CFAs caused by differences in coal types, coal regions, and combustion processes [8] can result in distinct leaching behaviors of oxyanions [4,9–12]. Multiple geochemical processes (e.g., changes in pH and redox conditions, mineral precipitation/dissolution, and adsorption/desorption reactions) that might concurrently affect the leaching of a single element have been suggested to control the diverse leaching behaviors of oxyanions from CFAs in different compositions [4,9,13].

The ultimate goal of laboratory leaching characterization of CCPs is the assessment of constituent release for field disposal sites. Often these characterizations are based on batch and column leaching tests [4,10,12,14]. However, direct comparisons of concentrations in laboratory leachates and in undisturbed field porewater, as well as a fundamental understanding of how to interpret and translate the results of standard laboratory leaching tests to the context of field conditions, have been lacking. The geochemical parameters that form important controls for the liquid-solid partitioning (LSP) of constituents include pH, reduction-oxidation (redox) potential, and the ratio between the total liquid volume and the dry mass equivalent of the solid material, also known as the liquid-to-solid ratio (L/S). Leachate pH and L/S are expressly considered within the Leaching Environmental Assessment Framework (LEAF) [12,15–20] developed for the U.S. EPA. However, the LEAF tests alone are not always sufficient to understand the leaching behaviors in the field, in part, because the impacts of redox potential on LSP behaviors are not easily characterized in the laboratory. Due to the exposure to air in the laboratory, the differences in laboratory test conditions and field conditions may result in changes in geochemical speciation of redox-sensitive constituents (e.g., As, Se, and Cr) [21–23]. Therefore, the methodology to assess field release based on laboratory leaching characterization needs to account for field environmental conditions, which often has been overlooked in previously

published studies.

Additionally, the leaching characteristics of field-disposed ash are likely to differ from those of the "as-generated" ash due to handling techniques (e.g., sluicing with process water, co-mingling with other wastes) and in-field aging processes, which result from changes in major chemical composition and mineralogy of the waste material [24,25]. Understanding the changes in controlling processes for the release of constituents during disposal is necessary for long-term leaching assessment under field conditions.

Geochemical speciation modeling can be used to quantitatively and simultaneously predict the speciation of a wide range of constituents using a virtual definition of materials. Virtual materials consist of the elemental composition of the material available for leaching, the mineral assemblage of phases that control LSP, and descriptions of adsorption surface sites [26,27]. The models developed from simulating laboratory leaching data can provide a basis for improved estimation of long-term field leaching. On one hand, geochemical speciation models developed for typical materials with a variety of chemical compositions and for representative disposal scenarios would aid in the identification and comparison of the primary leaching-controlling mechanisms. However, a search of the literature indicates that a systematic application of geochemical speciation modeling on both as-generated and field-disposed ashes of various compositions has not been reported.

Geochemical speciation models also can be used to evaluate the sensitivity of leaching performance to varied geochemical parameters [26,27], hence providing insight into the relationships of constituent release under laboratory test conditions and field geochemical conditions. So far, only to a very limited extent have geochemical speciation models been interpreted and verified with field porewater data to provide insights into the effects of field pH, L/S, and redox conditions on the LSP behaviors of oxyanionic constituents.

In addition to the assessment of constituent partitioning in the field by batch leaching testing and geochemical speciation modeling, the evaluation of oxyanion release as a function of time under post closure conditions is important concerning the long-term leaching assessment for the CCP disposal site. The percolation leaching test (e.g., EPA Method 1314) has been used to simulate the dynamic leaching process of constituents from "as-generated" coal ashes [4,10,28,29]. However, the controlling mechanisms of constituent release for ashes from a wide range of

sources have not been well understood. Also, aside from the as-generated ashes, percolation testing carried out on field ashes is fundamental to estimate the release of constituents under field conditions.

Overall, this dissertation research aims to (i) provide improved geochemical speciation models for coal ashes with a wide range of solid compositions and thus identify important mechanisms and develop reaction sets for leaching predictions, (ii) characterize the mechanisms of controlling factors (environmental conditions and field handling) influencing the LSP of oxyanions in field porewater of coal ash disposal sites with different site conditions, and (iii) evaluate the long-term leaching behavior of oxyanions and identify the underlying leaching-controlling mechanisms for a range of coal ashes based on percolation leaching tests and conceptual field disposal scenarios.

1.2 Research hypothesis, objectives, and approach

1.2.1 Research hypothesis and objectives

The fundamental hypothesis of the proposed research is that the LSP of constituents will change in response to different porewater and environmental conditions (pH, redox, and L/S) in the field compared to the laboratory because of altered major constituent mineralogy and surface adsorption sites of the material.

The main objective of this research is to improve the understanding of controlling mechanisms for leaching of oxyanionic constituents (As, B, Cr, Mo, Se, and V) from coal ash in disposal sites, as well as to provide a useful approach for estimating long-term leaching in the field by leaching testing and geochemical speciation modeling. Specifically, three sub-objectives are to:

1. Develop geochemical virtual materials to simulate the leaching behavior of different types of as-generated CFAs using geochemical speciation modeling. The virtual materials were used to identify mechanisms controlling the leaching of oxyanionic constituents as a function of CFA composition. Model fidelity was evaluated by uncertainty characterization. Reaction sets identified from the geochemical speciation modeling allow for quantitative estimation of leaching under different controlling mechanisms.

2. Assess the impacts of environmental conditions and site configurations on the LSP of oxyanions under field conditions through two field studies. Specifically, one field study on a closed coal ash impoundment with strongly reducing conditions provides an opportunity to evaluate the impacts of redox conditions on the leaching of As and Se, the two primary redox-sensitive constituents. In addition, another field study on an active coal ash management unit (i.e., a dry-handled landfill on top of a historical ash impoundment) with suboxic conditions serves as a reference case to elucidate the important role of material constituent composition and site-specific conditions in influencing the field leaching behavior of oxyanions.
3. Evaluate important leaching-controlling phenomena for the dynamic leaching behavior of oxyanions under percolation conditions, including the role of different chemical processes (i.e., adsorption/desorption and mineral precipitation/dissolution reactions); the effects of field weathering; and the impacts of redox conditions on the elution of different constituents with time. The field leaching conceptual scenarios in conjunction with hydrologic conditions during post-closure periods of the coal ash disposal facility allow for the assessment of the long-term release of constituents from coal ashes.

1.2.2 General Approach and Structure of the Dissertation

The main content of the dissertation consists of six chapters, including (i) an introduction of the research background and descriptions of objectives and approach in Chapter 1; (ii) methods and results for Objective 1 in Chapter 2, for Objective 2 in Chapters 3&4 (results of two field studies are included in separate chapters), and for Objective 3 in Chapter 5; and (iii) summary of findings, conclusions, and future work in Chapter 6. Relationships between the three objectives (Chapter 2 to 5) and a summary of the approach for each objective are indicated in Figure 1.1.

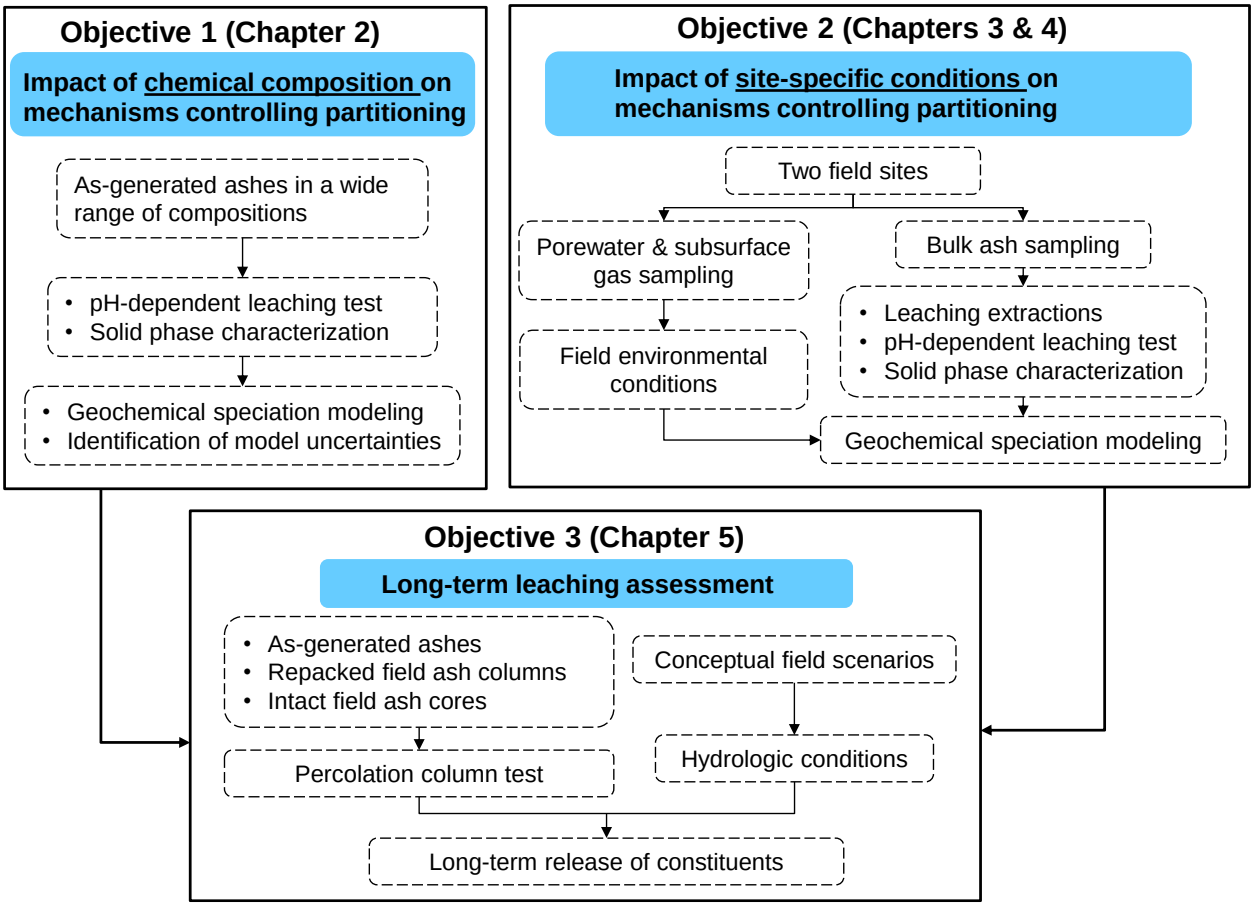

Figure 1.1 Structure and general approach of the dissertation research.

For Objective 1 (Chapter 2), pH-dependent leaching tests and solid phase characterization were carried out on six as-generated CFAs with various major chemical compositions. Virtual materials were developed by geochemical speciation modeling to simulate leaching test data, whereby different leaching-controlling mechanisms of oxyanionic constituents were systematically considered. The uncertainties were characterized for (i) the use the diffuse double-layer adsorption model and (ii) selection of mineral phases, both included in the model to simultaneously simulate multiple constituents during model development.

For the two field studies in Objective 2 (Chapters 3&4), field environmental conditions (pH, L/S, and redox potential) were characterized by in situ porewater and subsurface gas monitoring. The field ash samples were collected for a series of leaching characterizations, with the results compared to field porewater compositions. These comparisons aid in evaluating relationships

between leaching in the laboratory and in the field under the impacts of different environmental conditions. Finally, geochemical speciation modeling was carried out to simulate the field LSP of oxyanions, aiming to understand leaching-controlling mechanisms under different site conditions (i.e., material chemical composition and field environmental conditions).

For Objective 3 (Chapter 5), the L/S-dependent percolation tests were carried out on both the as-generated CFAs (from Chapter 2) and field ashes collected from the two disposal sites (from Chapter 3&4). The L/S-dependent leaching behavior of oxyanions from the percolation test was compared (i) among as-generated ashes in different chemical compositions; (ii) between as-generated ash and field-disposed ash pairs from the same facility; and (iii) between field intact ash cores and repacked ash columns in the laboratory (subject to oxidation). The comparisons aim to identify the impacts of multiple factors (i.e., chemical reactions, field weathering, and redox conditions) on the dynamic leaching of constituents. In addition, hydrological conditions of a conceptual coal ash disposal site during post-closure periods were used to relate the L/S conditions from the percolation test to leaching times in the field. The long-term release of oxyanions from coal ash in the conceptual disposal site was assessed by combining the results from the percolation tests and the estimated field environmental conditions (i.e., evolution of L/S and redox conditions).

CHAPTER 2

APPLICATION AND UNCERTAINTY OF A GEOCHEMICAL SPECIATION MODEL FOR PREDICTING OXYANION LEACHING FROM COAL FLY ASH[1]

2.1 Abstract

Three primary mechanisms (i.e., adsorption to iron oxides or analogous surfaces, Ca mineral co-precipitation, and substitution in ettringite) controlling oxyanion retention in coal fly ashes (CFAs) were identified by differentiating the leaching behavior of As, B, Cr, Mo, Se, and V from 30 CFAs. Fidelity evaluation of geochemical speciation modeling focused on six reference CFAs representing a range of CFA compositions, whereby different leaching-controlling mechanisms of oxyanions were systematically considered. For CFAs with low Ca and S content, calibration of adsorption reactions for the diffuse double-layer model for hydrous ferric oxides improved the simultaneous prediction of oxyanion leaching, which reduced uncertainties in Se and V predictions caused by nonideal adsorption surfaces and competitive adsorption effects. For CFAs with intermediate Ca content, the solubility constants for Ca-arsenates from literature and for postulated phases of B, Cr, Se, and V were used to describe co-precipitation of oxyanions with Ca-bearing minerals under alkaline conditions. For the CFA with high Ca and S content, a calibrated ettringite solid solution was used to capture the simultaneous retention of all selected oxyanions at pH > 9.5. Overall, the simultaneous leaching predictions of multiple oxyanions from a wide range of CFAs were improved by calibration of adsorption reactions and controlling solid phases.

2.2 Introduction

The high mobility of oxyanionic contaminants (As, B, Cr, Mo, Se, and V) from coal fly ash

[1] This chapter is adapted from "Application and uncertainty of a geochemical speciation model for predicting oxyanion leaching from coal fly ash under different controlling mechanisms" published in *Journal of Hazardous Materials* and has been reproduced with the permission of the publisher and my co-authors (H.A. van der Sloot, K.G. Brown, A.C. Garrabrants, Z. Chen, B. Hensel, and D.S. Kosson). *Journal of Hazardous Materials*. 438 (2022) 129518.

(CFA) under environmental conditions poses a potential risk to the environment, leading to increasing public concern about the safe disposal of CFA [2,3]. The ability to identify and understand the controlling mechanisms for leaching of oxyanions is important for proper management and disposal of CFA. Geochemical speciation modeling can play a significant role in the decision-making process through investigation of retention mechanisms that describe contaminant behavior under laboratory and field conditions. To date, geochemical speciation modeling has been applied to quantitatively and simultaneously predict the leaching of multiple constituents from a variety of waste materials, such as CFAs [28,30,31], ladle slags [32], municipal solid wastes [27], municipal solid waste incineration fly ash [33], and cementitious waste forms [26,34]. However, the application of a single geochemical speciation model to a wide range of CFA compositions has not yet been studied. Also, the systematic evaluation of model accuracy as well as the identification and quantification of uncertainties are central components of model development that are not commonly reported.

Different ash sources have resulted in distinctly different leaching behaviors of oxyanions over a broad range of conditions [10,11,35,36]; however, the widely-used Class F/Class C grouping of CFAs, based on industrial application in concrete (ASTM C618-19, 2019), is an inadequate cross-reference for leaching behavior of oxyanions. The controlling mechanisms for retention of oxyanions are strong functions of pH, material alkalinity, and major constituent composition (e.g., Ca, Fe, and S). The leaching of oxyanions from CFAs with high alkalinity has been suggested to be strongly associated with Ca-bearing minerals, which precipitate and decrease the mobility of oxyanions at high pH [4,9,10,35,38]. Most CFA geochemical assessments focus on screening precipitated phases for a single constituent, especially major constituents (e.g., Al, Ca, Fe, and Si), based on the thermodynamic saturation status of potential phases [24,25,39]. However, such geochemical assessments often failed to identify solid phases controlling the leaching of trace constituents [28,39–41]. An important reason is the limited thermodynamic data reported for trace constituents. For example, the Ca-bearing phases controlling the leaching of most oxyanions (except for As [42,43]) have not been widely identified. In addition, current geochemical modeling studies mainly focused on common contaminants (e.g., As, Se, Ba and Cd), but a systematic modeling work extending to multiple oxyanionic constituents (i.e., As, B, Cr, Mo, Se, and V) from CFA is missing. Therefore, identification of controlling phases and developing a practical reaction set to model the leaching of oxyanionic constituents are important

and necessary to fill the knowledge gap for the leaching assessment of CFA.

Leaching of several oxyanions (e.g., As, Se, and Mo) from CFAs at acidic pH has been found to be primarily controlled by adsorption onto iron (hydr)oxides or analogous surfaces [4,13,44,45]. Several simplified adsorption models have been developed exclusively for adsorption of As and Se by CFA in simple systems [44,46,47]; however, these studies have not considered the potential competitive effects for adsorption sites by other oxyanions in complex waste systems [48–51]. In other studies, the diffuse double-layer (DDL) model [52], developed for hydrous ferric oxide (HFO), has been used to describe the adsorption of constituents to iron (hydr)oxides in diverse materials such as fly ashes [28,31,53], municipal solid wastes (MSW) [27], MSW incinerator bottom ashes [7], and other solid waste [26,34]. Compared to models with more refined descriptions of adsorption surfaces and surface complex formation (e.g., triple-layer model of Davis et al., 1978 and the charge distribution multisite complexation model of Hiemstra and Van Riemsdijk, 1996), the widely-used DDL model is a relatively simple surface complexation model with a comprehensive database of adsorption reactions for a variety of adsorbates. Therefore, the DDL model for HFO (DDL-HFO model) is a practical choice for simulating adsorption of multiple constituents in a complex system such as CFA leachates. Also, the DDL model and the Dzombak and Morel (D&M) database have been implemented in several common geochemical modeling platforms [56–58].

However, the fidelity and uncertainties of the DDL-HFO model for simulating oxyanion leaching from CFAs have not been well characterized. In many cases, the recommended reaction constants (log Ks) for surface complexation reactions in the D&M database is the weighted average of values from different datasets [52], which may span several orders-of-magnitude, yielding a significant level of uncertainty in log K values. In addition, the aforementioned competitive effects between strong adsorbates can cause substantial deviations in log K from those predicted under ideal conditions (single-component systems). Thus, the reported reaction parameters developed for freshly precipitated HFO [52] need to be evaluated when applied to CFA containing different structures of iron (hydr)oxides and when multiple types of adsorption surfaces are lumped together assuming HFO as the model surface [59–61].

In this study, three mechanisms controlling the leaching of oxyanionic constituents (i.e., As, B, Cr, Mo, Se, and V) were initially identified by differentiating leaching test results of 30 CFAs as

published in an EPA database [11]. Then, geochemical speciation modeling was conducted on six reference CFAs with a wide range of solid compositions to (i) further identify phases controlling the leaching of oxyanionic constituents as a function of CFA compositions and (ii) delineate uncertainties of using the DDL-HFO adsorption model and mineral phases to describe the liquid-solid-partitioning (LSP) of constituents.

2.3 Materials and methods

2.3.1 EPA CFA database and reference fly ash samples

Leaching test results and solid sample compositions of 30 CFAs from a previous study [11] were evaluated to facilitate the identification of likely controlling mechanisms for leaching of constituents. In this EPA database, the CFAs along with 39 other coal combustion products (e.g., gypsum and blended coal ash with scrubber sludge) came from a wide range of sources such as different facilities, coal combustion and emission control technologies, and coal types.

In addition, six "as-generated" CFAs (EFA_U, FFA_U, LAB_U, CDL_AG, KSP_AG, and PPB_U) collected directly from electrostatic precipitators at different facilities were used in geochemical speciation modeling. The solid sample characterization (§2.3.2) and pH-dependent leaching tests (§2.3.3) were carried out on these reference CFAs in this study.

The pH-dependent leaching test on the six reference CFAs followed EPA Method 1313 [62], while the leaching test on the 30 CFAs from the EPA database followed Method SR002.1 [17], a precursor to EPA Method 1313 with the same liquid-to-solid ratio (L/S) and contact time.

2.3.2 Solid phase characterization

The solid samples of reference CFAs were characterized to understand the chemical composition of materials that impact the leaching behavior of oxyanions and to provide parameters for geochemical model development (§2.3.4). The collected CFAs were analyzed for (i) major elemental composition by X-ray fluorescence (XRF); (ii) crystalline structures by X-ray diffraction (XRD); (iii) total organic carbon (TOC) by a total carbon analyzer; (iv) total inorganic carbon (TIC) by both the carbon analyzer and thermogravimetric analysis combined with mass spectrometry (TGA/MS); and (v) amorphous iron (hydr)oxides (Am_{FeOOH}) and

crystalline iron (hydr)oxides (Cry_{FeOOH}) by selective extraction tests following the ISO Method 12782-1 [63] and Method 12782-2 [64]. Details of analysis methods are provided in Appendix A.I.

2.3.3 Leaching characterization

The basis used for developing the geochemical speciation model of the six reference CFAs was the pH-dependent leaching data from EPA Method 1313, conducted as specified at an L/S of 10 L/kg-dry [17,62]. The standard EPA Method 1313 test describes the near-equilibrium LSP of constituents at end-point eluate pH values between 2 and 13 that were obtained by initial additions of predetermined amounts of nitric acid (2 N HNO_3) or potassium hydroxide (1 N KOH). Another test extraction was conducted without acid or base to provide the LSP at the "natural pH" of the solid material.

In addition, a modified EPA Method 1313 test was carried out at an L/S of 1 L/kg-dry to more closely approximate field L/S and provide additional data for model verification. The final pH values of extractions focused on a pH range of ~4 standard units, consisting of one extraction at the "own pH" (i.e., without acid or base addition) and approximately four extractions (specific number of extractions for each material modified to cover the required pH range) with final pH values adjusted by the initial addition of dilute acid or base. The term "own pH" for the water extraction at L/S of 1 L/kg-dry was used to be distinguished with the pH response to water extraction at L/S of 10 L/kg-dry ("natural pH").

According to the method standards, the extraction time specified as 24 h was sufficient for the near-equilibrium of the LSP of constituents from CFAs with 93-99 wt% particles smaller than 250 μm (particle size distribution results are provided in Figure A.3, Appendix A.XI). Following the extractions, eluate pH and electrical conductivity (EC) of extracted fluids were measured prior to filtration and analysis of metal, anion, dissolved inorganic carbon (DIC), and dissolved organic carbon (DOC) concentrations. Leaching of constituents as a function of final leachate pH is reported including the acid/base titration curve of each sample (Figure A.1, Appendix A.II).

Details regarding the description and quality assurance/quality control (QA/QC) of the pH-dependent leaching test methods and eluate analytical analysis are provided in Appendix A.II and A.III. The repeatability (equivalent to the coefficient of variation) associated with Method

1313 for coal fly ash has a median value of less than 15 % of the reported concentration of constituents, which is both constituent- and pH-dependent with the typical range for oxyanions from 3 to 30 % [16].

2.3.4 Geochemical modeling approach

Geochemical speciation modeling was conducted using the Objects Representing CHEmical Speciation and TRAnsport (ORCHESTRA) modeling framework [58] embedded in the software package, LeachXS™ [65]. Simultaneous modeling was conducted for (i) major constituents with total content > 1 wt% (i.e., Al, Ca, Fe, K, Mg, Na, S, and Si); (ii) minor constituents with total content between 0.1 and 1 wt% (i.e., Ba, P, and Sr); (iii) trace oxyanion-forming constituents with total content < 0.1 wt% (i.e., As, B, Cr, Mo, Se, and V) and reported to pose risks to ecological or human receptors [2]; and (iv) other constituents needed for model parameterization (i.e., Cl^-, CO_3^{2-}, Cu, Mn, NO_3^-, and Pb).

Virtual materials (i.e., the definition of a material consisting of available contents of constituents for leaching, mineralogy, and adsorption surface descriptions) were developed for each reference CFA through geochemical modeling. Specifically, the virtual material comprised: (i) the available contents of elements (i.e., typically the maximum amount of an element present that can participate in geochemical speciation reactions); (ii) the dissolution/precipitation reactions of solubility-controlling minerals and solid solutions; (iii) the adsorption surface of iron (hydr)oxides; and (iv) a fractionation of organic matter between solid organic matter and reactive dissolved organic matter concentrations as a function of pH. In ORCHESTRA, adsorption of ions onto iron (hydr)oxides was modeled according to the generalized DDL-HFO model [52]. Ion adsorption onto organic matter was calculated with the NICA-Donnan model using generic adsorption reactions [66,67]. Each geochemical speciation simulation also specified the L/S and reduction-oxidation (redox) state as parameters to represent test or environmental conditions.

Calibration of geochemical speciation models followed steps described in Figure 2.1. In the first step, virtual materials, including a mineral set for major, minor, and other constituents necessary for the parameterization of model (i.e., Al, Ba, Ca, Cl^-, CO_3^{2-}, Fe, K, Mg, Na, P, S, Si, Sr, and NO_3^-) were developed by fitting pH-dependent simulation curves to the Method 1313 leaching

data at L/S 10 L/kg-dry. The developed virtual materials were further calibrated for trace oxyanions and metals (i.e., As, B, Cr, Cu, Mn, Mo, Pb, Se, and V) with adsorption models including HFO adsorption and organic matter complexation. Development of the virtual materials, including definition of the available content, mineral reaction set, and organic matter complexation, along with calibration of redox conditions and model parameters is described in Appendix A.IV.

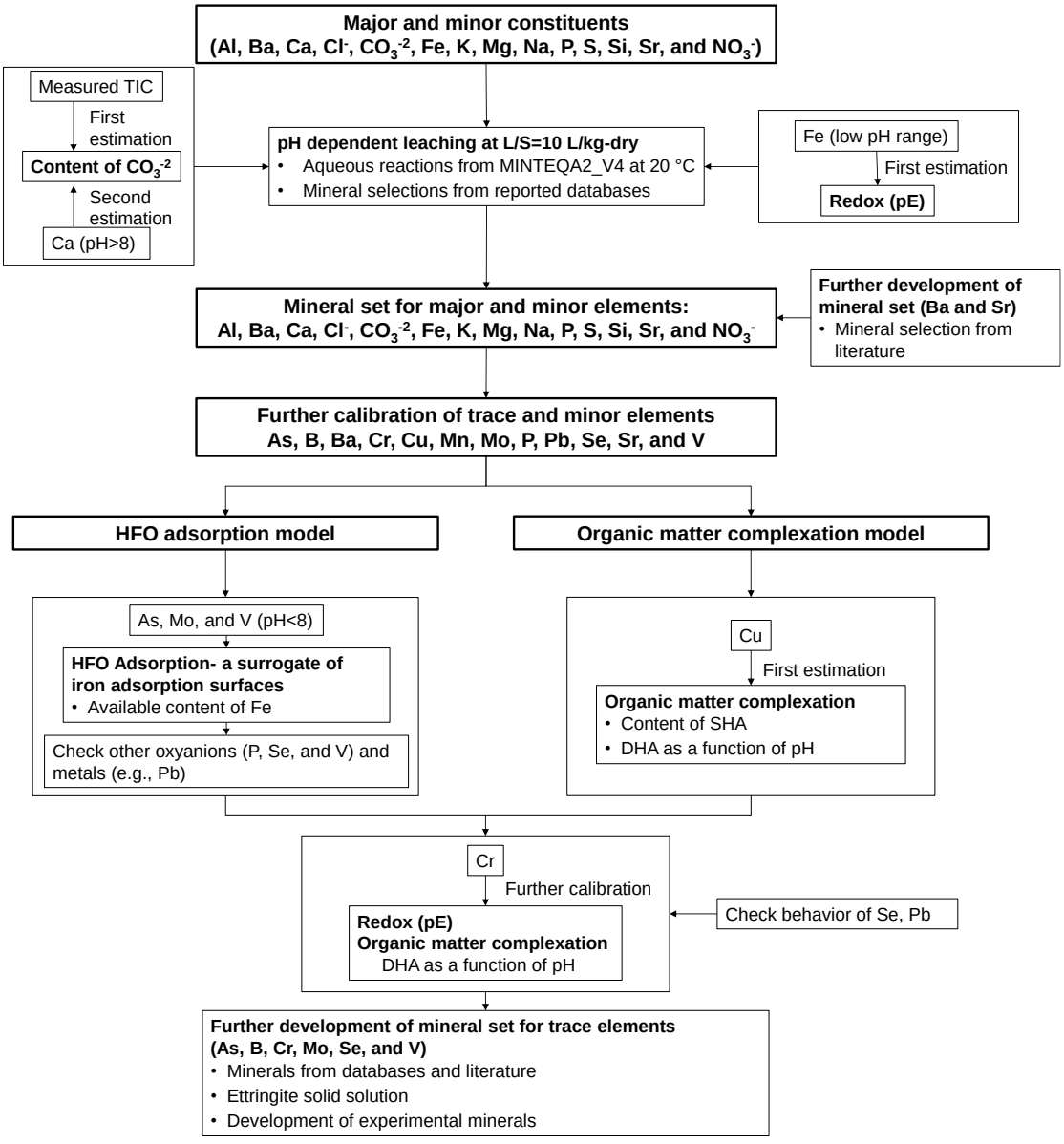

Figure 2.1. Flow diagram of geochemical speciation modeling approach.

2.3.5 Evaluation of HFO adsorption model uncertainties

The DDL-HFO model [52] includes adsorption reactions for a range of ions formed by major constituents (i.e., Ca, Mg, S, and Si) and oxyanionic constituents and trace metals (i.e., As, B, Cr, Cu, Mn, Mo, P, Pb, Se, and V). Simulations were carried out to compare the impacts of HFO adsorption of major constituents when evaluating adsorption of trace constituents (§2.4.4.1). A sensitivity study was used to adjust the reported reaction constants [52] for adsorption of trace constituents (Table A.12, Appendix A.VIII) to improve the fitting of the selected oxyanions due to the potential uncertainties of the DDL-HFO reaction set when applied to CFAs (§2.4.4.2).

In the DDL-HFO model calibration, the parameters of surface site properties (i.e., specific surface area of 600 m^2/g, two types of sorption sites including a weak site of 0.2 mol/mol-Fe and a strong site with 0.005 mol/mol-Fe site density, and acidity constants) were taken from reported values by D&M [52] to ensure the internal consistency in modeling a multi-ion system.

In the model, the number of adsorption surface sites is coupled and proportional (based on the site density: mol sites/mol-Fe) to the amount of the selected iron (hydr)oxide mineral phase accounting for the solubility of Fe in the model, allowing for the change of total HFO adsorption sites with the precipitation/dissolution of selected iron (hydr)oxides. The available content of Fe in the virtual materials was calibrated to yield the minimum residual (definition of residual is provided in Appendix A.IV) between simulation and experimental results of pH-dependent leaching of As, Mo, and V, due to their high affinity to HFO. The calibration was constrained by the measured amount of Am_{FeOOH} as a lower limit and by the Am_{FeOOH}+Cry_{FeOOH} as an upper limit (Table A.11, Appendix A.VIII).

2.4 Results and discussions

2.4.1 Mechanisms controlling the differentiated leaching behavior of oxyanionic constituents

Previous studies indicate three primary mechanisms controlling the pH-dependent leaching behavior of oxyanions in CFA including adsorption to iron oxide surfaces or analogous surfaces, co-precipitation with Ca minerals, and substitution in ettringite [4,10,13,44]. This work for the

first time identified these mechanisms by differentiating leaching behavior of oxyanions exhibited by 30 CFAs covering a wide range of solid compositions [11]. The specific mechanisms were identified in the 30 CFAs by the corresponding characteristic shape of pH-dependent leaching curve over relevant pH domains as summarized in Table A.14-Table A.15 (Appendix A.X). These tables also include the total contents of Ca, Fe, and S for each CFA.

In general, three typical types of pH-dependent leaching behavior (Type I, II, and III) for each constituent were differentiated according to the underlying controlling mechanisms (Figure 2.2 and Figure 2.3). The shaded area in each diagram is used to highlight the general shape of leaching behavior exhibited by most samples, while a few samples may not be covered in the highlighted area because of variations in chemical compositions (e.g., major elemental compositions and available content of trace constituents) [11].

Type I leaching behavior of As, Se, V, Cr, and Mo (and except for B) is characterized by a "V-shaped" pH-dependent concentration curve, typical for the leaching behavior controlled by adsorption as reported by other researchers [9,44,68,69]. For B, eluate concentrations were relatively constant with pH indicating weaker adsorption than As, Se, V, Cr, and Mo where relatively higher concentrations of As, Se, V, Cr, and Mo were obtained at the strongly acidic ($pH < 2$) and alkaline ($pH > \sim 10$) solutions. The lowest eluate concentrations were observed at acidic to near-neutral pH conditions ($4 \leq pH \leq 6$ for As, Se, V; $4 \leq pH \leq 8$ for Cr, and $2 \leq pH \leq 4$ for Mo) due to the strong adsorption of anions onto protonated surfaces. The primary adsorption surfaces include metal oxides such as iron (hydr)oxides for ion exchange with anions (e.g., AsO_4^{3-}, CrO_4^{2-}, MoO_4^{2-}, SeO_4^{2-}, and VO_4^{3-}) and solid organic matter for complexation with cation species (Cr^{3+}).

For Type II leaching behavior of the focused constituents (i.e., As, Cr, B, Se, V, and Mo), the pH-dependent leaching curve in the acidic pH range ($pH < \sim 8$) was similar to the Type I behavior; however, the major difference was in the alkaline pH range ($pH > \sim 8$) where decreasing eluate concentrations were likely caused by precipitation into Ca-bearing minerals. For example, co-precipitation of As with Ca into low-solubility calcium arsenates has been widely reported to inhibit leaching of As in alkaline solutions [4,9,10] (further discussed in §2.4.5). This conclusion is supported by the overall higher Ca total content of CFAs showing Type II leaching behavior than in CFAs with Type I behavior, consistent with findings from

Wang et al. [9] that Ca content is a primary controlling factor influencing the leaching behavior of oxyanions. Similarly, the S content in CFAs generally increased from Type I to Type II. Among the oxyanionic constituents, leaching of As and V was most sensitive to the variation of Ca content based on the number of CFAs exhibiting Type II behavior in comparison to the Type I behavior. Contrarily, only a few samples showed Type II leaching behavior of Cr and Mo, suggesting the less significant role of Ca in preventing leaching of Cr and Mo than As and V depending on the different solubilities of Ca-bearing oxyanion phases [4].

The common characteristic among all oxyanions for Type III leaching behavior was a sharp decrease in aqueous concentrations at pH > 9.5 and a minimum concentration at pH ~12. The leaching minimum of As at pH~12 was inferred from results with an improved analytical method detection limit (MDL) presented in §2.4.2; although As concentrations less than the MDL were measured for the five EPA CFAs in the Type III class (Figure 2.2). The Type III behavior can be distinguished from the Type II behavior based on the main pH range (pH > ~9.5 for Type III and pH > ~8 for Type II) where the uptake of oxyanions occurs.

Under alkaline conditions, the formation of either hydrocalumite [$Ca_4Al_2(OH)_{12}(OH)_2 \cdot 6H_2O$] or ettringite [$Ca_6Al_2(OH)_{12}(SO_4)_3 \cdot 26H_2O$] can effectively suppress the release of oxyanions by incorporating oxyanions into the crystalline structures [70,71]. However, the hydrocalumite usually precipitates at strongly alkaline pH conditions (pH > ~11.5) [70]. Also, all CFAs identified with typical Type III behavior were derived from sub-bituminous coal with significantly high amounts of Ca (> ~10 wt%) and S (> ~0.8 wt%) necessary for the formation of ettringite. Therefore, the concentration reduction of oxyanions starting from pH ~9.5 for Type III behavior was primarily attributed to the formation of oxyanions-substituted ettringite at alkaline conditions as suggested by many studies [3,4,72,73].

Like Type I and II, for the Type III behavior, adsorption tends to inhibit leaching of the oxyanions at more acidic pH conditions than other pH range. The missing data at pH < ~4 for the CFAs with Type III behavior were caused by the strong acid-buffering capacity of these alkaline ashes. However, according to the pH-dependent leaching test carried out on another strongly alkaline CFA “PPB_U” (§2.4.2) with improved data covering the strongly acidic pH range (to pH < 2), concentrations of oxyanions increased when pH was lower than ~4, similar to Type I and II behaviors controlled by adsorption.

Besides the three typical types (Type I/II/III) of leaching behaviors where the primary controlling mechanisms can be clearly identified, the controlling mechanisms for oxyanion leaching sometimes cannot be clearly distinguished solely based on the pH-dependent leaching curve. The reasons to cause ambiguity in distinguishing leaching behavior in these cases are (i) the boundary between different mechanisms is not rigid and (ii) multiple mechanisms can simultaneously interact within the same pH range. In some cases, leaching of oxyanions from several CFAs in the alkaline pH range cannot be confidently identified as either adsorption (A) or co-precipitation with Ca (C) due to the slight decrease in mobility. For example, the Type I behavior of Cr is characterized as an overall "V" shape typically controlled by adsorption; however, the slightly declining trend of Cr concentrations under alkaline pH conditions might also be caused by precipitation. Additionally, co-precipitation with a Ca mineral (C) or substitution into ettringite (E) are sometimes not easy to distinguish because they may coexist in the alkaline pH domain, so a primary controlling mechanism cannot be confidently identified solely based on the pH-dependent leaching curve. The leaching test results for cases where both A and C are likely was noted as A/C, while C/E was used to indicate that both C and E are possible mechanisms. Leaching test results controlled by A/C (except for the results of Cr) and C/E are provided in Figure A.2 (Appendix A.X).

Overall, three primary mechanisms were identified to control the leaching behavior of oxyanions based on typical types of leaching curve. Despite the uncertainties in differentiating leaching behavior of CFAs in a wide range of solid compositions, geochemical speciation modeling provides an approach to obtain insights into the underlying controlling processes reflected in the pH-dependent leaching curve. The primary phases likely to precipitate can be identified by geochemical speciation modeling using the solid sample composition and test conditions.

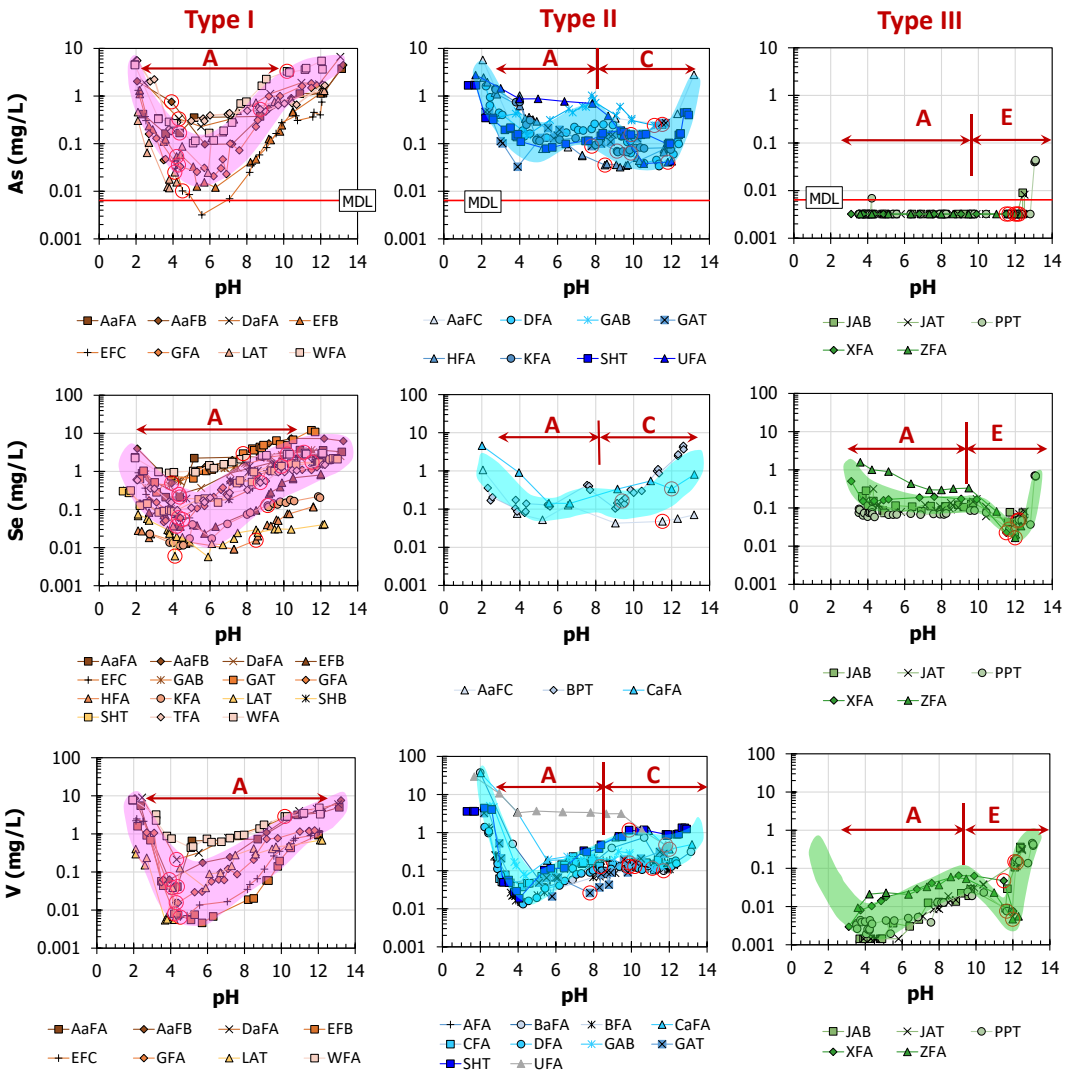

Figure 2.2 Three types of leaching behavior of As, Se, and V from coal fly ashes of the EPA database [11] controlled by different mechanisms. A: adsorption. C: co-precipitation with Ca. E: substitution in ettringite. MDL: method detection limit. The natural pH of each material is indicated by the red circled test data. The shaded area in each diagram is used to highlight the general shape of leaching behavior. General shape of V leaching behavior at pH lower than 4 was inferred based on the test results of reference CFAs carried out in this study (Figure 2.4).

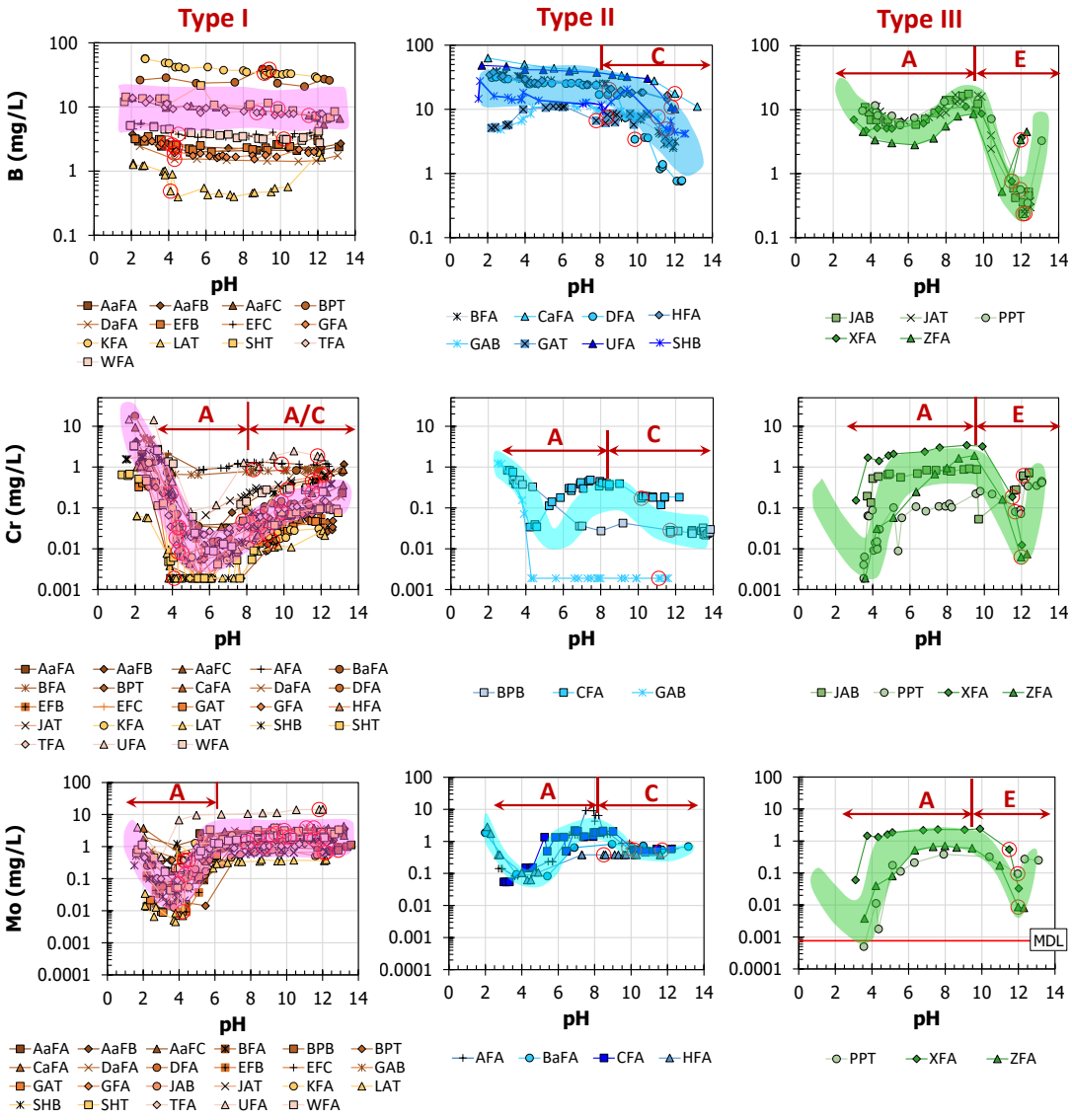

Figure 2.3 Three types of leaching behavior of B, Cr, and Mo from coal fly ashes of the EPA database [11] controlled by different mechanisms. A: adsorption. C: co-precipitation with Ca. E: substitution in ettringite. A/C: adsorption and/or co-precipitation with Ca. MDL: method detection limit. The natural pH of each material is indicated by the red circled test data. The shaded area in each diagram is used to highlight the general shape of leaching behavior. General shape of the leaching behavior of Cr and Mo at pH lower than 4 was inferred based on the test results of reference CFAs carried out in this study (Figure 2.5).

2.4.2 Leaching and chemical characterization of reference coal fly ashes

To evaluate how well the use of geochemical modeling can represent the identified primary mechanisms controlling oxyanion retention (i.e., adsorption, Ca mineral co-precipitation, and substitution in ettringite), geochemical speciation modeling was conducted on six reference CFAs exhibiting different types of leaching behavior, with leaching tests carried out with improved analytical fidelity: three CFAs ("EFA_U", "FFA_U", and "LAB_U") displaying Type I leaching behavior where adsorption has a predominant role; two CFAs ("KSP_AG" and "CDL_AG") that clearly show Type II behavior with decreased solubility of As, B, Se, and V at the alkaline pH range (Cr and Mo have low sensitivity to Ca precipitation); and one CFA ("PPB_U") with the minimal solubility at pH~12 for the selected constituents potentially caused by ettringite formation indicative of Type III behavior (Figure 2.4 and Figure 2.5). These reference ashes were hereafter referred to as Group I (EFA_U, FFA_U, and LAB_U); Group II (CDL_AG and KSP_AG); and Group III (PPB_U) CFAs for the convenience of results discussion.

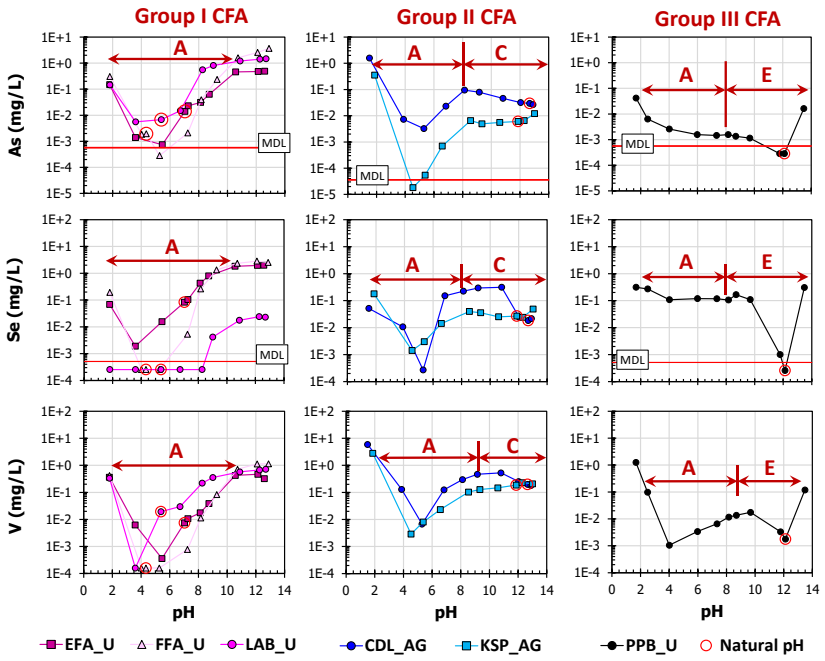

Figure 2.4 Leaching behavior of As, Se, and V from reference coal fly ashes used in geochemical speciation modeling. Samples were assigned to three groups (Group I, II, and III) based on different primary controlling mechanisms of leaching. A: adsorption. C: co-precipitation with Ca. E: substitution in ettringite. MDL: method detection limit. The natural pH of each material is indicated by the red circled test data.

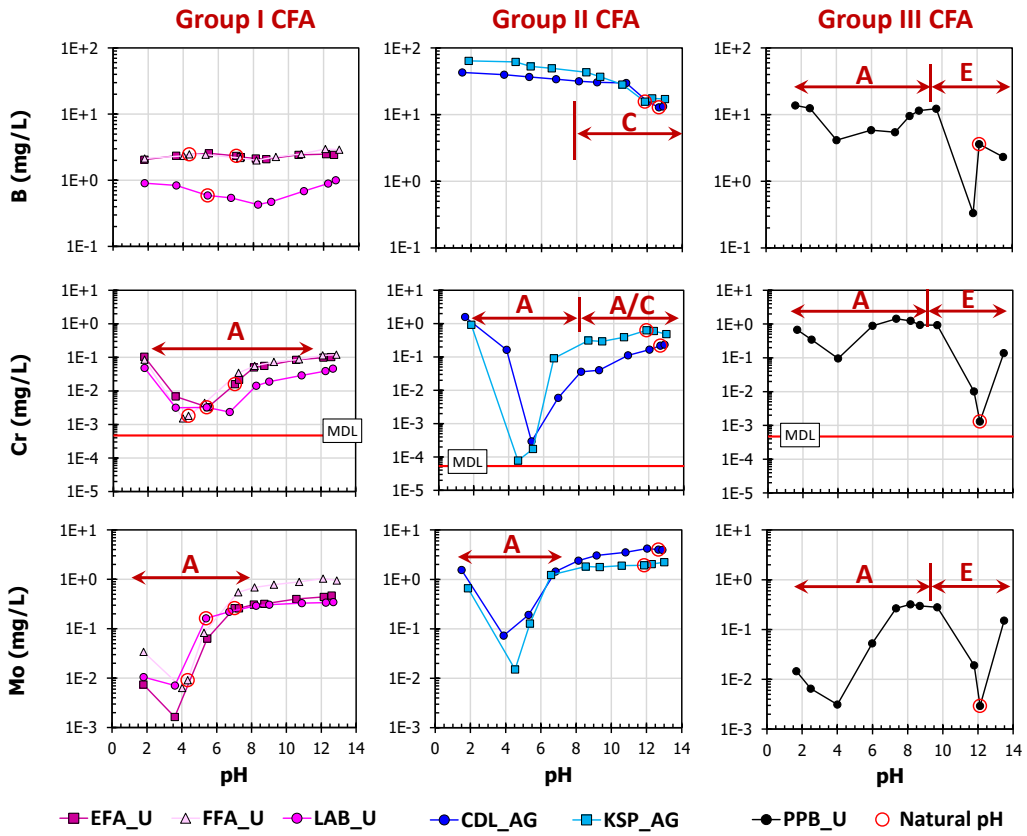

Figure 2.5 Leaching behavior of B, Cr, and Mo from reference coal fly ashes used in geochemical speciation modeling. Samples were assigned to three groups (Group I, II, III) based on different primary controlling mechanisms of leaching. A: adsorption. C: co-precipitation with Ca. A/C: adsorption and/or co-precipitation with Ca. E: substitution in ettringite. MDL: method detection limit. The natural pH of each material is indicated by the red circled test data.

The six reference CFAs showed variations in major chemical composition (Ca, Fe, and S), which also resulted in variations in natural pH (Figure 2.6; the data in this figure were adapted from Table A.16, Appendix A.XI). All the reference CFAs were derived from bituminous coal with exception of KSP_AG (50:50 blend of ash from bituminous and sub-bituminous coal sources) and PPB_U (from sub-bituminous coal source). The Group I CFAs (i.e., EFA_U, FFA_U, and LAB_U) are acidic ashes (natural pH: 4.3-7.0) with relatively low Ca (0.7-1.2 wt%) while Group II CFAs (CDL_AG and KSP_AG) have alkaline natural pH measurements (11.9-12.7) with moderate Ca of 5.9-9.0 wt%. The single Group III CFA (PPB_U) is strongly alkaline with the highest Ca (>20 wt%). Of all the CFAs, the Group II CFAs have the greatest Fe content (13-19 wt%). The alkaline ashes (Group II and III) also generally have higher content of S compared to

acidic samples (Group I).

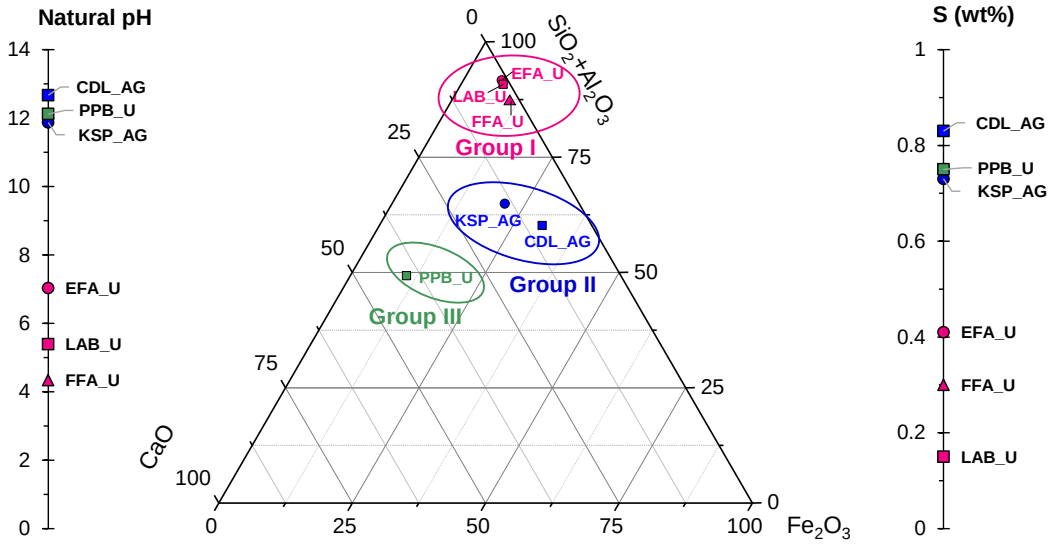

Figure 2.6 Ternary plot of major elemental composition (CaO, Fe_2O_3, SiO_2+Al_2O_3, wt%) and comparison of natural pH and S content of reference coal fly ashes used in geochemical modeling. The CFAs in the same class are indicated within ovals in the ternary diagram.

The XRD analysis on reference CFAs identified primary mineral phases (> ~1%) of mullite [$Al_6Si_2O_{13}$], quartz [SiO_2], hematite [Fe_2O_3] and magnetite [Fe_3O_4] (iron oxides), periclase [MgO], lime [CaO], anhydrite [$CaSO_4$], and calcium aluminates [e.g., $Ca_3Al_2O_6$] (Figure 2.7 and Table A.17, Appendix A.XI). The results are consistent with common phases reported in literature [74–79] (Table A.18, Appendix A.XI). While only two crystal types (mullite and quartz) were identified in Group I CFAs, additional Fe/Ca/Mg oxide crystal types were detected in Group II and Group III CFAs. The mineral phases obtained from XRD characterization were limited to a large extent by interference from the large portion (70-90 wt%) of glass and amorphous relics of clay in the CFAs [80].

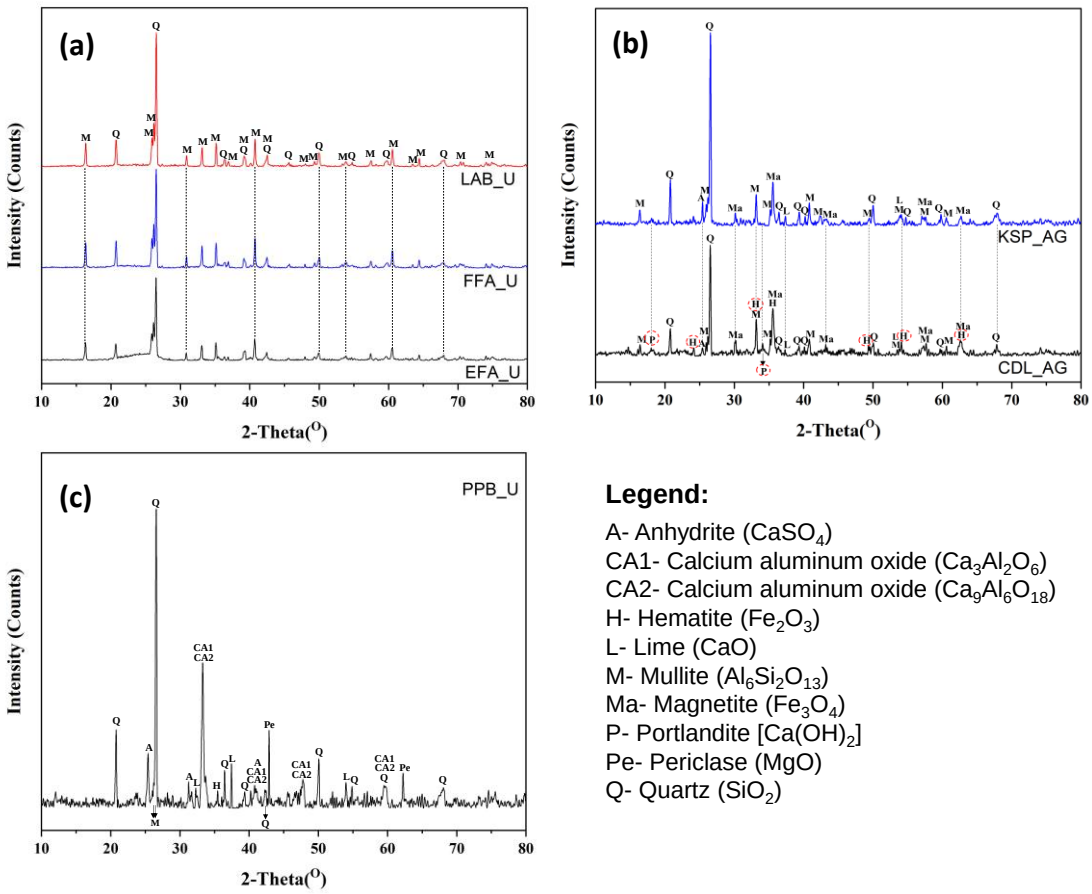

Figure 2.7 XRD patterns of (a) Group I coal fly ashes (EFA_U, FFA_U, and LAB_U); (b) Group II coal fly ashes (CDL_AG and KSP_AG); and (c) Group III coal fly ash (PPB_U)

2.4.3 Simulation results for major constituents

Prediction of Ca activity is fundamental to the description of trace constituent leaching because Ca controls the major ion chemistry of CFA leachates and may interact with the trace oxyanions through precipitation/dissolution reactions [3,9,70]. Modeling results of Ca are shown (Figure 2.8a) for EFA_U (Group I), KSP_AG (Group II), and PPB_U (Group III) while results for other reference CFAs are presented in Appendix A.XII (Figure A.5a). Also shown are representative results for S (Figure 2.8b and Figure A.5b). These results include model simulation of pH-dependent leaching compared to measured pH-dependent leaching test results (top) and indications of the solid and liquid partitioning phases that describe the pH-dependent simulation at L/S 10 and 1 L/kg (middle and bottom, respectively).

Within the pH range around the natural pH of each material (indicated by the circled leaching test data), the simulated pH-dependent leaching of Ca was in good agreement with experimentally determined concentrations at both L/S 1 and 10 L/kg (Figure 2.8a). The maximum release of Ca, obtained at pH <2, was greatest for Group III CFAs and least for Group I CFAs, consistent with but significantly less than the total content for these materials. Several primary phases including calcite and cementitious phases (e.g., monosulfates [C_4AsH_9/C_4AsH_{16} and $C_3(F,A)S_{0.84}H_{4.32}$]) were proposed to control solubility of Ca in the alkaline pH range. Ettringite and a calcium-silica-hydrate (C-S-H) solid solution were suggested as controlling phases in the strongly alkaline PPB_U (Group III) sample. At L/S 1 L/kg, simulations suggest that additional phases (e.g., gypsum) precipitate from the concentrated solution compared to less concentrated solution at L/S 10 L/kg.

Sulfur also exhibited different pH-dependent leaching behavior among CFA classes (Figure 2.8b). The greater available content of Ca and S in the Group II CFAs (e.g., KSP_AG) over that in Group I CFAs (e.g., EFA_U) resulted in the precipitation of monosulfates and decreased S concentrations at pH >8. In Group III CFAs (e.g., PPB_U), the elevated Ca and S available content would result in oversaturation of ettringite and the subsequent precipitation of S with the lowest solubility at 10<pH<12.

For Fe, leaching as a function of pH was consistent among the three CFA classes (Figure A.6, Appendix A.XII). Low solubility of Fe between pH ~6 and ~12 was primarily controlled by iron oxyhydroxide that dissolves in strongly acidic conditions. In addition, a weak increase in Fe concentrations was shown under strongly alkaline conditions. Such amphoteric leaching behavior was well described by the model. The leaching of Fe under more acidic pH conditions (pH < ~6) is related to the redox state of the leaching system. For example, the ash CDL_AG with relatively reduced condition during leaching (potentially due to the addition of anhydrous ammonia for NOx control prior to collection of ash) showed a more rapid increase of aqueous Fe concentrations than other CFAs when pH decreased from 6 to 4. The speciation diagrams of Fe suggest that the higher fraction of Fe(II) in leachate from CDL_AG than other CFAs contributes to the more soluble Fe at pH < ~6 (Figure A.10, Appendix A.XII; also includes speciation of other redox sensitive constituents including As, Cr, and Se). The prediction of pH-dependent leaching behavior of Fe is important to account for the change in the number of HFO adsorption sites with pH, as the total adsorption sites will decrease with the dissolution of Fe oxyhydroxide.

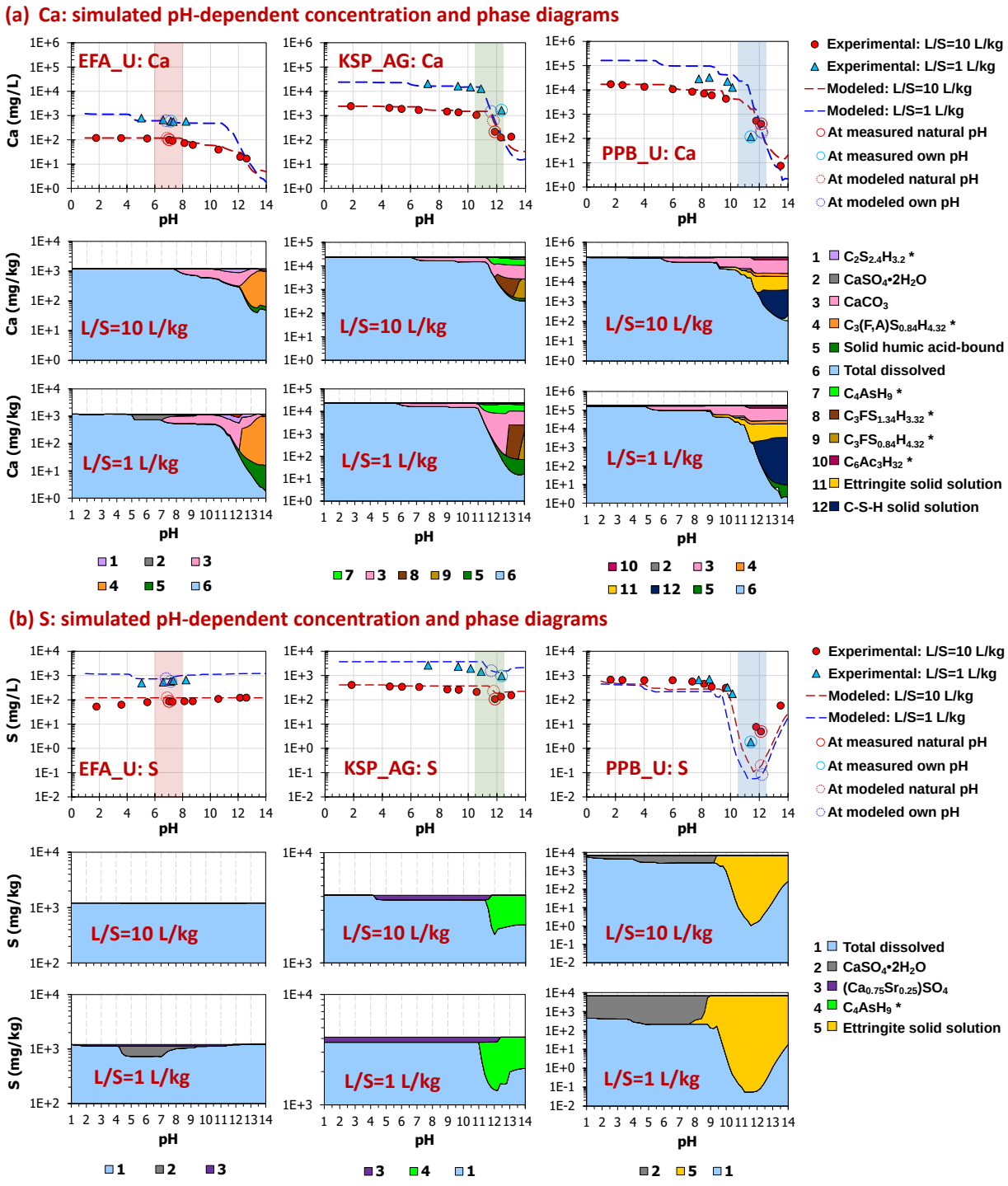

Figure 2.8 Geochemical speciation modeling of Ca and S from representative coal fly ashes Group I (EFA_U), Group II (KSP_AG), and Group III (PPB_U) (only primary phases shown). *Cement chemist notation was used to simplify the formulae of cement phases using C = CaO; S = SiO_2; A = Al_2O_3; F = Fe_2O_3; M = MgO; H = H_2O; c = CO_2; s = SO_3. A specific pH range around the natural and own pH conditions of each material is highlighted in pH-dependent concentration diagram.

2.4.4 Simulation results for trace constituents (Group I CFAs)

Since Group I CFAs (EFA_U, FFA_U, and LAB_U) are characterized by adsorption to iron (hydr)oxides as a primary retention mechanism for trace oxyanions, the ability of the DDL model to simultaneously describe the adsorption of oxyanions to HFO is an important evaluation. First, the impact of adsorption of major constituents (i.e., Ca, Mg, S, and Si) on simulation of trace constituents will be evaluated by comparison of pH-dependent leaching test results for As in the EFA_U sample to geochemical speciation model simulations with and without adsorption reactions of major constituents. A second evaluation will focus on the DDL model uncertainties based on the simultaneous simulation of multiple oxyanionic constituents (i.e., As, B, Cr, Mo, Se, and V) across the three Group I CFAs using the default reaction set of the DDL-HFO model.

2.4.4.1 Impact of adsorption of major constituents on simulation of oxyanionic constituents

The impact of adsorption of major constituents on simulated As leaching results are shown in Figure 2.9. Multicomponent simulations using the reported HFO adsorption reactions for major constituents (Ca, Mg, S, and Si) resulted in significant deviations of predicted As concentrations from experimental results. When Ca-HFO or Mg-HFO adsorption reactions are included in the model, eluate concentrations of As in EFA_U were significantly underestimated in the pH range 8<pH<13 (Figure 2.9a-b), while including S-HFO adsorption reactions led to overestimation of As concentrations at pH <6 (Figure 2.9c). The inclusion of Si-HFO sorption reactions had negligible influence on the simulation of As concentrations (Figure 2.9d).

The DDL model conceptualization is that of a surface plane within which specific surface complexation reactions occur and a diffuse layer with counterions to compensate the charge of surface plane [52]. Adsorption of positively charged cations including Ca^{2+} and Mg^{2+} onto the surface plane in the alkaline pH range increases the surface electrostatic potential, leading to a stronger adsorption of negatively charged oxyanions, such as $H_2AsO_4^-$, $HAsO_4^{2-}$, and AsO_4^{3-} [81,82]. Conversely, adsorption of SO_4^{2-} in the acidic pH range significantly decreases adsorption of other negatively charged oxyanions through direct competition for surface sites [81]. Although the electrostatic interactions between the adsorption surfaces and multiple adsorbates (cations and anions) are considered in the DDL model, the large uncertainties of the

reported HFO reaction sets of major constituents can be magnified in the simulation of partitioning by trace constituents. For the CFA leachate with relatively high concentrations of major ions, the application of the adsorption reactions for major constituents failed to simultaneously describe multiple oxyanion leaching.

Overall, the DDL-HFO adsorption model had limited ability to accurately describe the adsorption of trace constituents when adsorption reactions for both major and trace constituents were simultaneously considered. For simulation of major constituents, excluding HFO adsorption does not noticeably impact the simulation results because mineral precipitation/dissolution reactions were the primary controlling process (Figure A.4, Appendix A.XII). Subsequently, HFO adsorption reactions for major constituents (Ca, Mg, S, and Si) were not included when evaluating the HFO adsorption reactions for trace constituents (As, B, Cr, Mo, Se, and V).

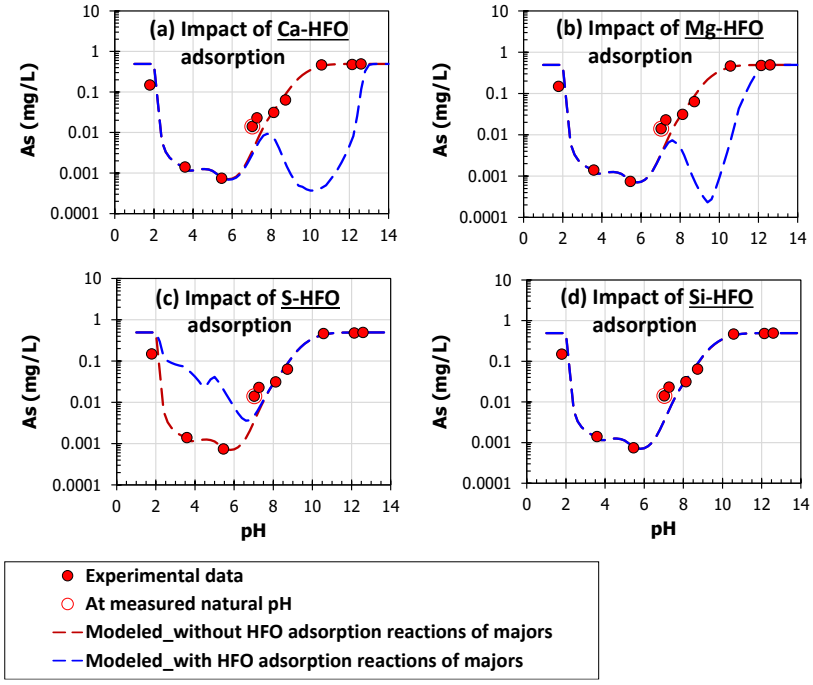

Figure 2.9 Impact on simulated leaching of As from the coal fly ash EFA_U by adding reported DDL-HFO adsorption reactions [52] of each major constituent (Ca, Mg, S, and Si). Simulated concentrations of As without adding HFO reactions of major constituents are compared to results with HFO adsorption reactions of (a) Ca, (b) Mg, (c) S, and (d) Si.

2.4.4.2 Uncertainty of HFO adsorption parameters for oxyanionic constituents

For all Group I acidic CFAs (EFA_U, FFA_U, and LAB_U), simulations of pH-dependent leaching of As, Mo, Se, and V using the DDL model indicated strong HFO adsorption at pH <10 (Figure 2.10). The maximum adsorption occurs in the acidic pH range because the available protonated surface sites for anion adsorption decrease under alkaline pH conditions and the negatively charged surface repels anions [9,52,68]. In contrast, weak adsorption to HFO was found for B and complexation of Cr with dissolved organic matter was important (Figure A.7, Appendix A.XII), consistent with previous studies [27,83]. Using the reported adsorption reaction constants in the DDL model [52], the leaching of As and Mo were well described across the three Group I samples at both L/S 1 and 10 L/kg conditions. However, the combination of the DDL model with reported adsorption constants failed to predict leaching concentrations of Se and V with a high degree of fidelity as both Se and V concentrations were consistently overestimated by up to three orders-of-magnitude in the range of 4<pH<10 for all Group I CFAs (Figure 2.10, dashed lines).

To improve the simulation fidelity of Se and V leaching from Group I CFAs, HFO adsorption reaction constants were calibrated to the leaching data (Table A.12, Appendix A.VIII). Simulated results of multiple oxyanions (As, Mo, Se, and V) with calibrated HFO adsorption reaction constants for Se and V were compared to results with reported reaction constants at both L/S 1 and 10 L/kg extraction conditions (Figure 2.10). The same calibrated HFO reaction set when applied to each of the three Group I CFAs (EFA_U, FFA_U, and LAB_U) significantly improved predictions for Se and V with minor influence on As and Mo. Moreover, the calibration of oxyanion reactions did not noticeably impact predictions of metals (e.g., Cu and Pb) for which adsorption was indicated as important (Figure A.9, Appendix A.XII).

Between pH 2 and 8, the simulated adsorption of Se was enhanced by increasing the reaction constant of log K_2 (Table A.12), which controls the formation of the surface species $\equiv FeOHSeO_4^{2-}$ between the HFO adsorption sites and the SeO_4^{2-} ion [52]. The value of log K_2 increased from the reported value of 0.8 to the calibrated value of 4.8.

For V, the only reported HFO adsorption reaction in the DDL model (log K_3 in Table A.12, Appendix A.VIII) primarily controls V adsorption in the neutral to alkaline pH range [52]. The reported adsorption reaction constant of 13.6 (log K_3) was developed from limited experimental

data that did not adequately cover the acidic pH range. However, strong adsorption of V at pH < 8 has been reported in CFAs [4,50]. Thus, using the V adsorption reaction in the DDL model leads to overestimation of V concentrations in the range of $4 \leq pH \leq 8$. The calibration of reaction constants includes the addition of two VO_4/HFO reactions ($\log K_1 = 28$ and $\log K_2 = 21.7$, Table A.12) to increase the observed uptake of V in the acidic pH range.

Considering the large uncertainties of reported HFO model parameters for simulating the leaching of oxyanions from CFAs and the example calibration of adsorption reactions shown for Se and V, an optimized HFO reaction set is needed to provide a more accurate description of the multiple oxyanion leaching from CFA. Based on the evaluation presented here, several uncertainties need to be considered when using the DDL-HFO model with published parameters for simulation of complex systems such as CFA: (i) the simplified assumptions of forming solely inner-sphere monodentate complexes in the DDL model can cause large uncertainties in simulating the adsorption of multiple constituents in a competitive environment [81]; (ii) the reported HFO reaction sets of major constituents have large uncertainties that can be magnified in the simulation of partitioning by trace constituents; (iii) adsorption behavior in a complex and competitive environment can deviate from predicted ideal adsorption behavior under a single-component condition; (iv) adsorption by HFO can be influenced by the structure and crystallinity of iron (hydr)oxides [59,61] but a single representation of HFO was used to approximate the combination of different phases potentially present (e.g., ferrihydrite, hematite, magnetite); and (v) adsorption onto HFO was used to represent all adsorptive mineral surfaces in addition to iron (hydr)oxides (e.g., aluminum oxides).

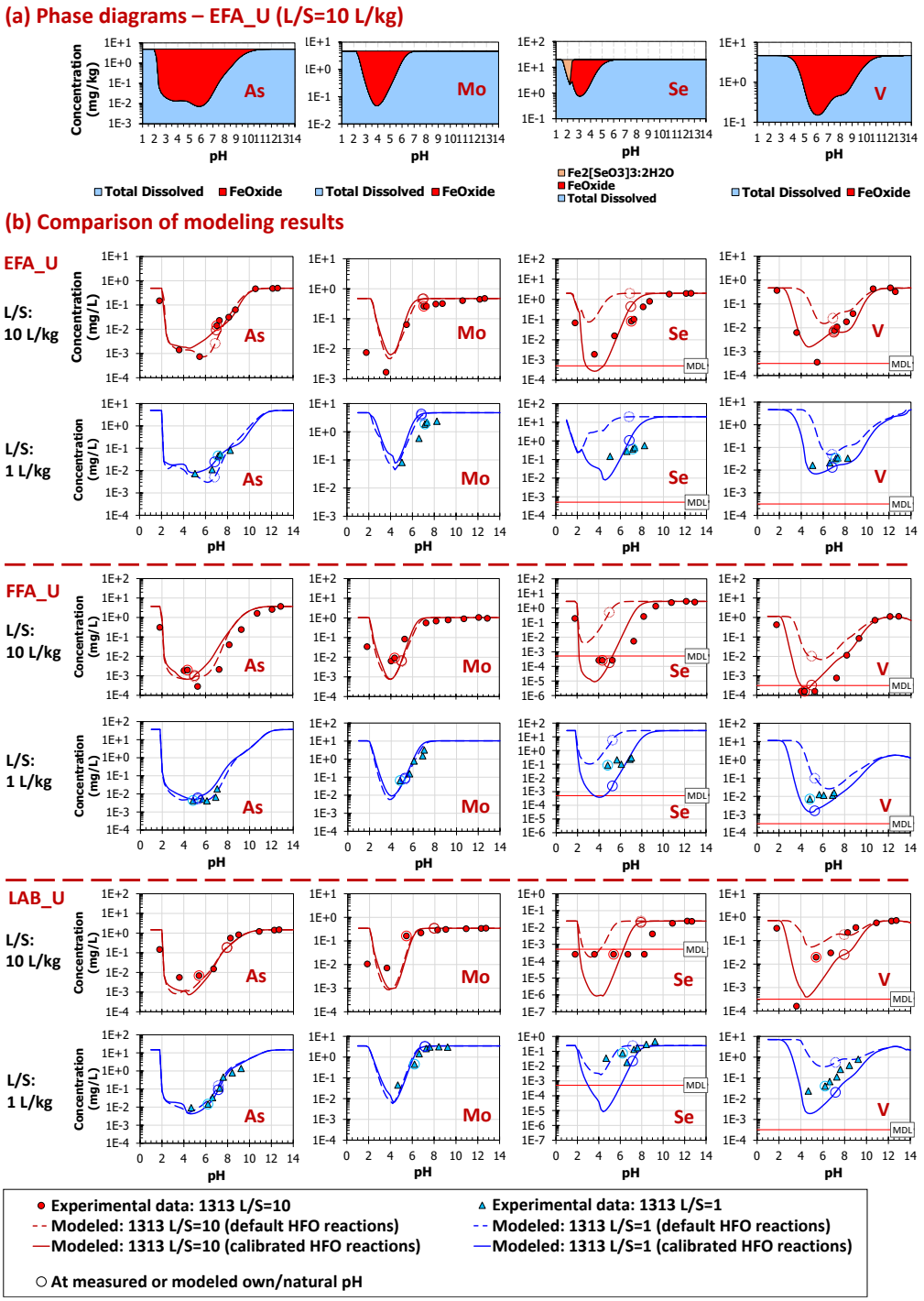

Figure 2.10 Comparison of leaching of trace constituents (As, Mo, Se, and V) from Group I coal fly ashes (EFA_U, FFA_U, and LAB_U) simulated by reported HFO adsorption reactions [52] and calibrated adsorption reaction sets. MDL: method detection limit. Phase diagrams in (a) are representative results using reported HFO adsorption reactions at L/S=10 L/kg for EFA_U. FeOxide: adsorbed onto hydrous ferric oxide (HFO); Fe2[SeO3]3:2H2O: $Fe_2(SeO_3)_3 \cdot 2H_2O$ mineral; Total dissolved: in dissolved phase, free ions.

2.4.5 Simulation results for trace constituents (Group II CFAs)

Important mechanisms controlling the retention and release of oxyanions for Group II CFAs (CDL_AG and KSP_AG) included both HFO adsorption at low pH and precipitation of Ca-bearing minerals at alkaline pH conditions. At pH values > 9 (natural pH condition for the CFAs), the solubility of Ca-oxyanion minerals generally simulated the observed decrease in aqueous concentrations of multiple oxyanions including As, Se, and V shown in Figure 2.11 and B and Cr shown in Figure A.8 (Appendix A.XII). Concentrations of Mo were not suggested to decease at alkaline pH range (Figure 2.11) due to the high solubility of Ca-molybdates [4]. For As leaching at pH > 9 and L/S 10 L/kg, the Ca-arsenates $Ca_3(AsO_4)_2 \bullet 2.25H_2O$ [42] and $Ca_5(OH)(AsO_4)_3$ [43] best fit pH-dependent leaching data in CDL_AG and KSP_AG, respectively. The primary controlling phases for V at pH > 10 in CDL_AG were $Ca_2V_2O_7$ and $Ca_3(VO_4)_2$.

2.4.5.1 Limitations of thermodynamic databases

For Se and V at pH > ~9, none of the mineral phases available in widely-used thermodynamic databases were adequate to capture the low solubility of V in KSP_AG and Se in both CDL_AG and KSP_AG, including the MINTEQA2_V4 [56], CEMDATA18 [84], THERMODDEM2011 [85], Lawrence Livermore National Laboratory (LLNL) [86], and ThermoChimie [87] databases. Therefore, experimental minerals $Ca_3(OH)_2(SeO_3)_2$, $Ca_3(OH)_2(SeO_4)_2$, and $Ca_5(OH)(VO_4)_3$ (Table A.7, Appendix A.VII) were postulated based on similarities in leaching behavior between oxyanions to overcome the limitations of the thermodynamic databases. The solubility product constants (K_{sp}) for the postulated minerals were calibrated to simulate leaching of Se and V for the Group II CFAs. Similarly, the experimental minerals, $Ca_3[OH]_2[CrO_4]_2$ and $Ca_5[OH][BO_3]_3$, were defined and calibrated to simulate leaching of B and Cr (Figure A.8).

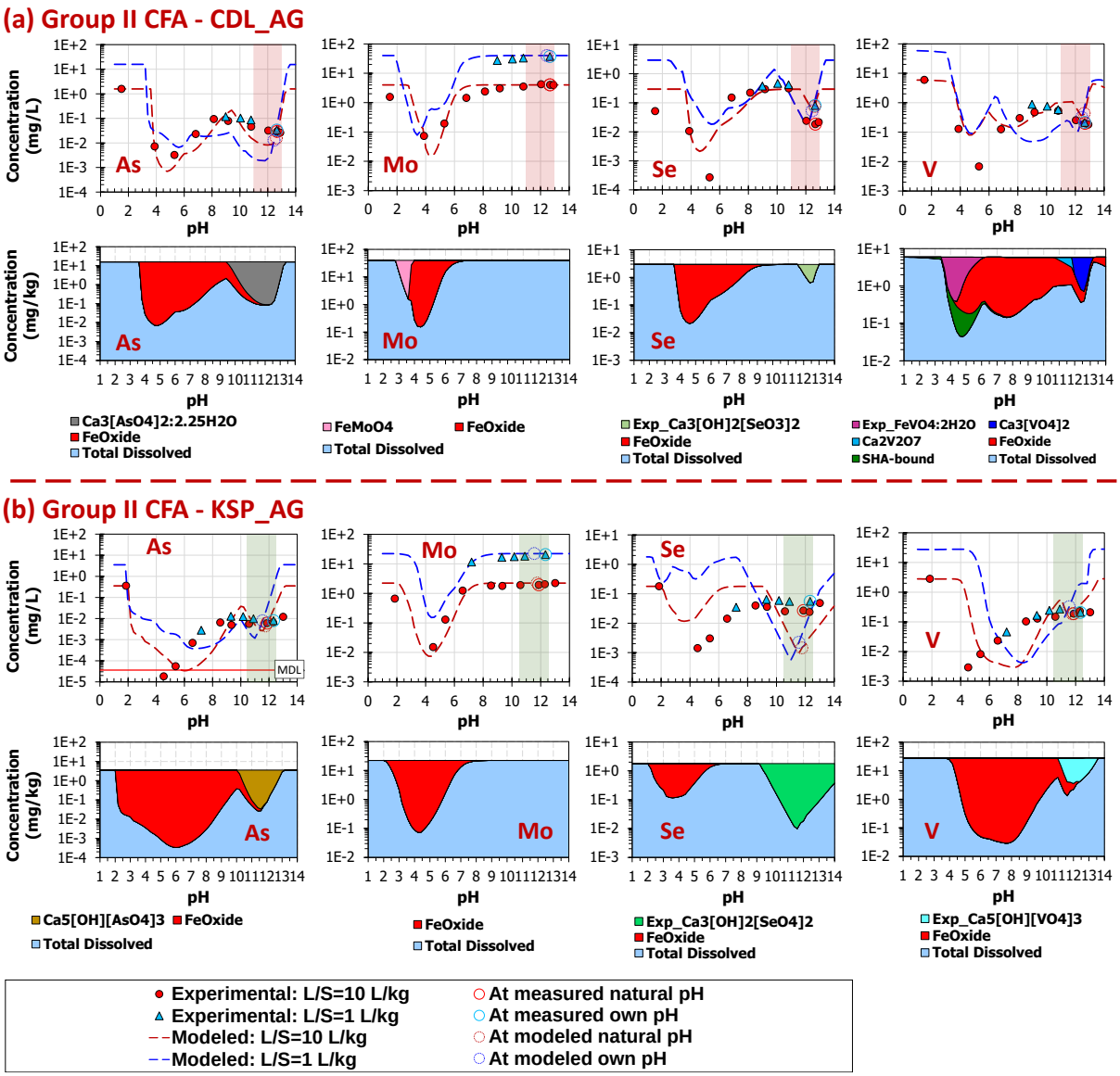

Figure 2.11 Geochemical speciation modeling of trace constituents (As, Mo, Se, and V) from Group II fly ashes (CDL_AG and KSP_AG). MDL: method detection limit. FeOxide: adsorbed onto hydrous ferric oxide (HFO); SHA-bound: solid humic acid bound; Phases with prefix of "Exp_" are experimental phases (postulated phases). Phase diagrams are representative results at L/S=10 L/kg. A specific pH range around the natural and own pH conditions of each material is highlighted in each pH-dependent concentration diagram.

2.4.5.2 Uncertainties of Ca-arsenate phases

The selection of the mineral assemblage for Group II CFAs was optimized using L/S 10 L/kg data and verified with L/S 1 L/kg data. Leaching of As and V at both the L/S 10 and 1 L/kg for KSP_AG were reasonably captured by the same Ca-arsenate or Ca-vanadate phase under the two different L/S conditions (Figure 2.11b). In some cases, however, discrepancies with the leaching data at L/S 1 L/kg were found when using the suggested mineral phases at L/S 10 L/kg, for example, the leaching of As from CDL_AG was underestimated at pH > ~9 (Figure 2.11a).

High uncertainties in reported thermodynamic values for laboratory-synthesized phases from different studies, even within the same study, can result in high uncertainties in simulated solution concentrations. Previous experimental studies [42,43] on the formation of Ca-arsenates included varied equilibrium pH and molar Ca/As ratio conditions. According to these studies, the observed precipitates from an alkaline solution primarily are $Ca_3(AsO_4)_2 \bullet xH_2O$, $Ca_4(OH)_2(AsO_4)_2 \bullet 4H_2O$, and $Ca_5(OH)(AsO_4)_3$. While some of these phases have been reported in the MINTEQA2_V4 [56], THERMODDEM2011 [85], LLNL [86], and ThermoChimie [87] databases, the pK_{sp} (-log K_{sp}) values reported for these phases can vary by orders of magnitude (Table A.10, XI-VII). Simulation results were compared using the minimum, median, and maximum pK_{sp} values observed for each of the three phases for CDL_AG and KSP_AG (Figure 2.12) which showed that the uncertainties of pK_{sp} for the same phase can result in variations of simulated concentrations up to two orders-of-magnitude.

Comparisons of simulated As concentrations in Figure 2.12 suggest that the mineral phases controlling As solubilities may have changed with the variations of solution compositions, L/S, and pH conditions. Interactions of As with Ca in the CFA leachate, along with other constituents, may be much more complicated than can be described by a reported pure phase covering varied leaching conditions (e.g., pH and L/S). For example, while $Ca_3(AsO_4)_2 \bullet xH_2O$ with a median pK_{sp} appeared to be a good fit for the CDL_AG data at L/S 10 L/kg, a lower pK_{sp} value (minimum in the reported range) better captured the data at L/S 1 L/kg (Figure 2.12a-c). For the sample KSP_AG, the solubility of $Ca_5(OH)(AsO_4)_3$ better described As leaching at the L/S 10 L/kg, but either $Ca_3(AsO_4)_2 \bullet xH_2O$ or $Ca_4(OH)_2(AsO_4)_2 \bullet 4H_2O$ better described the L/S 1 L/kg concentrations at pH <11, and $Ca_5(OH)(AsO_4)_3$ may instead have controlled leachate concentrations at pH >11 (Figure 2.12d-f). Similar effects were observed for a study on Ca-

antimonate [7] where a slight variation in the structure of Ca-antimonate was possible under different pH conditions, resulting in a significant change in leaching behavior. The results presented here further suggest that geochemical speciation modeling should be conducted in conjunction with experimental data obtained under a range of conditions to better identify uncertainties, and thus, to verify the applicability of model.

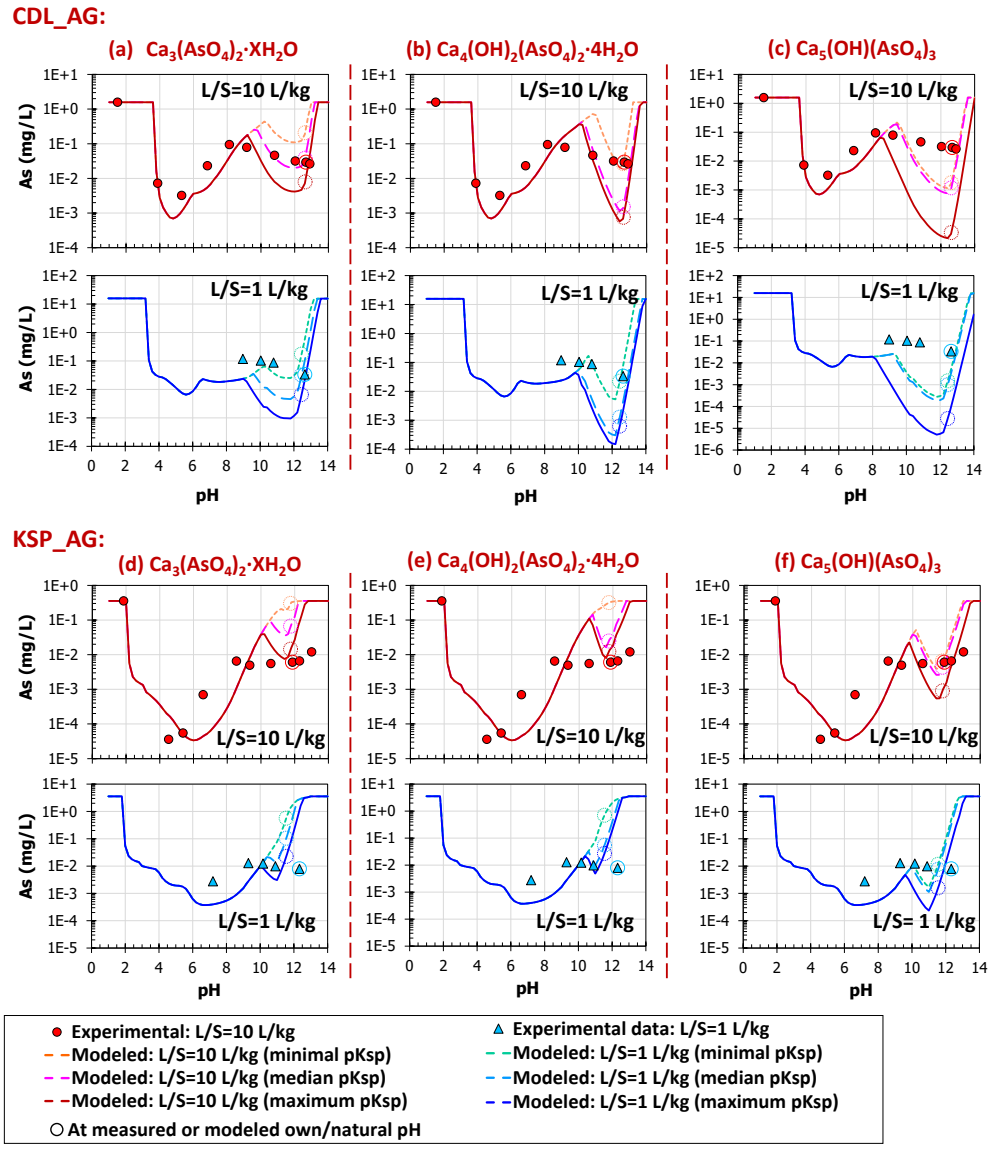

Figure 2.12 Comparison of simulated As leaching from Group II fly ashes (CDL_AG and KSP_AG) using three Ca-arsenates with the range of pK_{sp} values from multiple sources [42,43,56,85–87]

2.4.6 Simulation results for trace constituents (Group III CFA)

Leaching of As, Mo, Se, and V from the Group III CFA (PPB_U) was described by the formation of ettringite solid solutions at pH >9.5 (Figure 2.13). In addition, substitution into ettringite well represented the leaching behavior of Cr and B at pH > 9.5 (Figure A.8, Appendix A.XII). The formation of ettringite peaked at pH~12, near the natural pH condition of the PPB_U material. Either decreasing or increasing pH from pH~12 led to the dissolution of ettringite and release of the precipitated oxyanions. The structure of ettringite consists of columns of chemical units $[Ca_6(Al(OH)_6)_2 \cdot 24H_2O]^{6+}$ and anions(SO_4^{2-})/water molecules located within the intercolumn regions [70]. The simultaneous incorporation of multiple oxyanions [e.g., AsO_4^{3-}, $B(OH)_4^-$, CrO_4^{2-}, MoO_4^{2-}, SeO_4^{2-}, and VO_4^{3-}] into ettringite was reported to be preferential via substitution for SO_4^{2-} in the ettringite structure [70,71]. However, the thermodynamic data for simulating the leaching of oxyanions controlled by substitution into ettringite have not been reported extensively in literature.

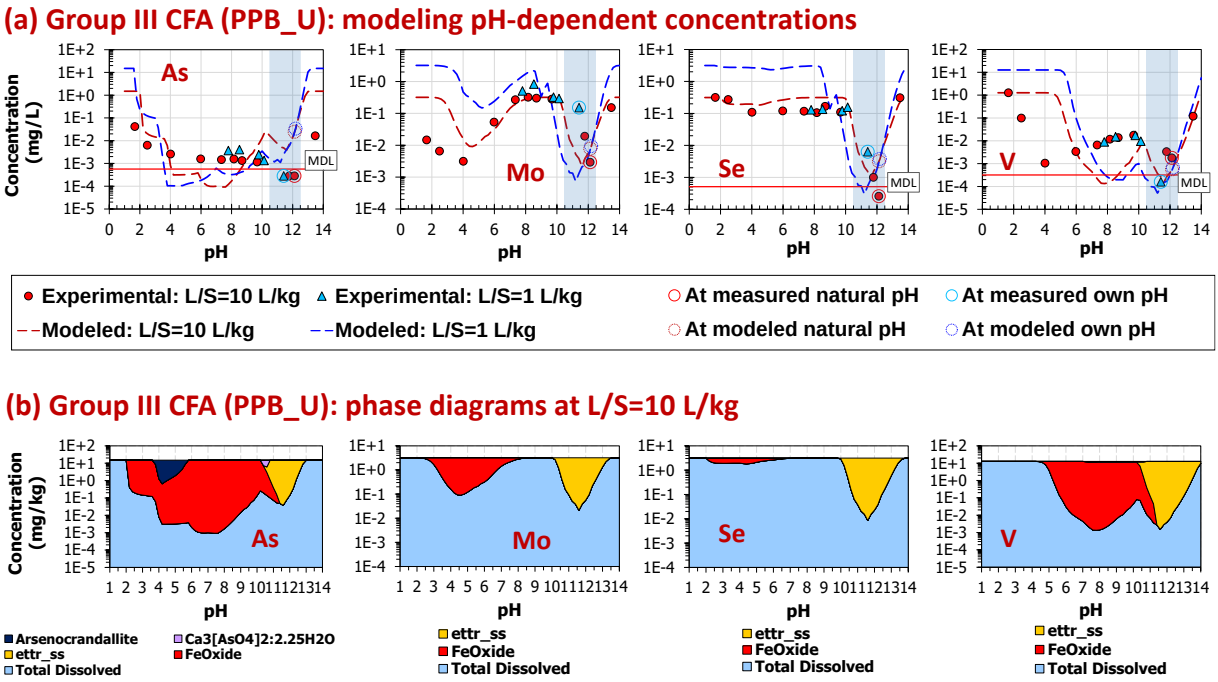

Figure 2.13 Geochemical speciation modeling of trace constituents (As, Mo, Se, and V) from Group III fly ash (PPB_U). MDL: method detection limit. Arsenocrandallite: $CaAl_3(AsO_4)(AsO_3OH)(OH)_6$; ettr_ss: ettringite solid solution; FeOxide: adsorbed onto hydrous ferric oxide (HFO). Phase diagrams are representative results at L/S=10 L/kg. A specific pH range around the natural and own pH conditions of the sample is highlighted in pH-dependent concentration diagram.

The development of oxyanion-substituted ettringite solid solutions was derived in this study from the modeling work on cement-based waste materials [88]. Uncertainties may reside in the assumption of an ideal solid solution that may not accurately represent reality; however, the reaction set successfully described mechanisms controlling the reduction of multiple constituent leaching (As, B, Cr, Mo, Se, and V) at pH > 9.5 for strongly alkaline CFAs.

2.5 Conclusions

The research presented in Chapter 2 identified primary mechanisms controlling retention/leaching of oxyanions based on leaching test results of 30 CFAs covering a wide range of solid compositions. This work also provides a systematic evaluation of the fidelity associated with geochemical modeling of oxyanion aqueous-solid partitioning during leaching. While the primary evaluations focus on leaching from "as-generated" CFAs under oxic conditions, more reducing conditions frequently exist at CFA disposal sites [45]. However, this study provides a basis for initial conditions prior to potential establishment of reducing conditions and insights as to which retention mechanisms may be impacted by redox changes (e.g., loss or reduction in adsorption surfaces). The main conclusions are summarized as:

- Multiple mechanisms control the retention and, hence, leaching of As, B, Cr, Mo, Se, and V, including adsorption to HFO or analogous surfaces, co-precipitation with Ca minerals, and substitution in ettringite. These mechanisms depend on the CFA composition (e.g., Ca and S) and the pH domain considered.
- The inclusion of DDL-HFO adsorption model from Dzombak and Morel (1990) generally described leaching behavior of oxyanions, but competition between adsorbates and nonideal adsorption surfaces contributes to the uncertainties of the HFO adsorption reaction sets developed for sorption onto pure HFO in single-component systems. Calibrated reaction sets for Se and V improved modeling predictions and indicated that more reliable adsorption models, based on multicomponent aqueous-solid partitioning data, are needed to simultaneously describe the leaching of multiple oxyanionic constituents from CFAs.
- Previously reported Ca-bearing phases reasonably described the decreased solubility of As

in the alkaline pH conditions for CFAs with relatively medium alkalinity. For B, Cr, Se and V, thermodynamic data for Ca-oxyanion minerals were inadequate and postulated experimental minerals were developed based on analogy to known minerals. However, the available pure phases from the thermodynamic databases and literature are limited and often inadequate to describe leaching of trace constituents with a high degree of fidelity for a wide range of L/S and pH conditions.

- For CFAs with high content of Ca and S (e.g., ash derived from sub-bituminous coal), the ettringite solid solution of As, B, Cr, Mo, Se, and V described the immobilization of oxyanions at pH >9.5 via assumed incorporation of trace elements into the ettringite structure.

For future leaching assessment on other CFAs, the calibrated reaction sets from modeling in this study provide a foundation for estimating concentrations of oxyanionic constituents in leachate in conjunction with leaching testing.

CHAPTER 3

THE INFLUENCE OF REDOX CONDITIONS ON AQUEOUS-SOLID PARTITIONING OF ARSENIC AND SELENIUM IN A CLOSED COAL ASH IMPOUNDMENT[2]

3.1 Abstract

A closed coal ash impoundment case study characterized the effects of field redox conditions on arsenic and selenium partitioning through monitoring of porewater and subsurface gas in conjunction with geochemical speciation modeling. When disposed coal ash materials and porewater were recovered for testing, oxidation during sample collection and testing led to lower arsenic and higher selenium concentrations in leaching test extracts compared to porewater measurements. Multiple lines of evidence suggest multiple mechanisms of arsenic retention are plausible and the concurrent presence of several redox processes and conditions (e.g., methanogenesis, sulfate reduction, and Fe(III)-reduction) controlled by spatial gradients and dis-equilibrium. Geochemical speciation modeling indicated that, under reducing field conditions, selenium was likely immobilized through the formation of insoluble precipitates Se(0) or FeSe while arsenic partitioning was likely affected by a progression of reactions including changes in arsenic speciation, reduction in adsorption due to dissolution and recrystallization of hydrous ferric oxides, and precipitation of arsenic sulfide minerals.

3.2 Introduction

The recent publication of national regulations regulating the operation and aftercare of disposal sites of coal ash (CA), which called for the end of CA wet disposal in unlined surface impoundments, is estimated to have impacted over 700 surface impoundments [89]. Given the large quantities of Cas stored in impoundments and landfills, attention has been focused on the

[2] This chapter is adapted from "The influence of redox conditions on aqueous-solid partitioning of arsenic and selenium in a closed coal ash impoundment " published in *Journal of Hazardous Materials* and has been reproduced with the permission of the publisher and my co-authors (A.C. Garrabrants, Z. Chen, H.A. van der Sloot, K.G. Brown, Q. Qiu, R. DeLapp, B. Hensel, and D.S. Kosson). *Journal of Hazardous Materials*. 428 (2022) 128255.

long-term environmental safety of CA disposal sites. Detailed information integrating pore gas and porewater compositions with leaching test results for Cas under post-closure scenarios is not publicly available or incomplete data sets can lead to conflicting interpretations. Thus, more robust characterization considering the critical factors influencing field leaching behaviors would improve the understanding of the performance of these impoundments.

Extensive laboratory leaching characterization over a broad range of materials [4,10,12,27,90–92] has established several environmental variables that control the composition of solid waste leachates. The variables include pH, reduction-oxidation (redox) potential, and the ratio between the total liquid volume and the dry mass equivalent of the solid material, also known as the liquid-to-solid ratio (L/S). Leachate pH and L/S are expressly considered within the Leaching Environmental Assessment Framework (LEAF) [12,15–20] developed for the United States Environmental Protection Agency (U.S. EPA); however, a standardized approach for evaluating the effects of redox conditions on leaching concentrations remains to be developed. Due to relatively high mobility coupled with toxicity compared to other redox-sensitive constituents in Cas [3,4,72], arsenic (As) and selenium (Se) have received significant attention.

In “as-generated” fly ash collected directly from electrostatic precipitators, the chemical speciation of As has been found mainly as arsenate [As(V)] associated with aluminosilicates glass phases and mineral matrix (e.g., calcium arsenates and iron oxides), either through As binding within the phases and/or adsorption onto mineral surfaces [13,22,93]. Selenium is mostly present as selenite [Se(IV)] adsorbed to metal oxides or aluminosilicate and to a lesser extent as elemental selenium [Se(0)] [22,94]. Speciation and leaching of As and Se are subject to change as a result of redox transformations in the field environment [23,95]. For example, the act of dredging an ash slurry from a river bank to a pond oxidized arsenite [As(III)] to As(V), decreasing its mobility due to stronger adsorption onto iron oxides [23]. In contrast, in a highly reducing environment such as in sediment, selenite [Se(IV)] or selenite species were reduced to selenium sulfide and organo-selenium with low solubility [95,96]. Both biotic and abiotic mechanisms, including reductive dissolution of hydrous ferric oxide (HFO), microbial sulfate reduction, and direct microbial oxidation through dissimilation or detoxification, may support the transformation of redox-sensitive constituents [21].

While many researchers aim to explain field leaching behavior with laboratory testing of the

material, maintaining or reproducing field redox and related conditions (e.g., microbial substrate and spatial gradients) in the laboratory remains difficult. For these studies, geochemical speciation modeling provides a useful approach to inform interpretation of leachability under varied laboratory conditions and relate the implications of redox changes on constituent release under field conditions [26,27].

Overall, leaching behavior of As or Se in the disposal site of CAs is closely related to the composition of the disposed material and in situ pH and redox conditions. Assessing field aqueous-solid partitioning and release of As and Se based solely on laboratory leaching characterization can be misleading especially when field redox conditions are strongly reducing, as well as when significant spatial heterogeneity is indicated. Therefore, the methodology to assess field release based on laboratory leaching characterization needs to consider the field environmental context, which, however, has usually been overlooked in previous studies. Also, the simultaneous consideration of geochemical speciation modeling, laboratory results, and field data on how major element chemistry and redox potential influence the retention and leaching of As and Se at CA disposal sites has not been reported.

In this work, a case study at a closed CA impoundment provides an opportunity to identify and assess the effects of field environmental conditions, especially for redox conditions, on the field liquid-solid partitioning (LSP) of As and Se. Other important trace constituents such as B, Mo, and V also were included for assessment. Generally, this study (i) compared the chemical composition between field-disposed ash and as-generated ashes; (ii) characterized ash stratigraphy in the field site by extraction tests on materials from different borehole locations and depths; (iii) estimated field redox states by porewater and subsurface gas monitoring; (iv) evaluated the impact of geochemical parameters (pH, L/S, and redox potential) on LSP of trace constituents by leaching characterization; and (v) identified mechanisms controlling the mobility of As and Se under a wide range of redox and pH conditions by geochemical speciation modeling. The obtained results and methodologies can guide the assessment of partitioning of trace constituents in disposal sites for a wide range of solid waste materials.

3.3 Materials and methods

3.3.1 Field sampling

3.3.1.1 Continuous borehole sampling

A sampling and monitoring campaign was carried out in July 2018 on a closed CA impoundment (~10 ha) that historically received a sluiced blend of primarily coal fly ash with some bottom ash. In June 2018, the impoundment was closed by removal of free water and construction of a geosynthetic cap consisting of a clay layer, a membrane liner, and engineered turf. The ash deposit varies from 3- to 6-m thick while the cap is about 1.5-m thick.

Three ash boring locations (VB1, VB2, and VB3) were selected to evaluate the pond area as indicated in Figure 3.1. After removing the top vegetation cover and geosynthetic cover, a Φ7.6 × 60 cm split spoon sampler was advanced at each location with the underlying native clay material was reached. Representative ash samples were collected for in-field extraction tests (see §3.3.2.1). The rest of the material was vacuum sealed, transported on ice to the laboratory, and stored at < 6ºC for subsequent laboratory testing.

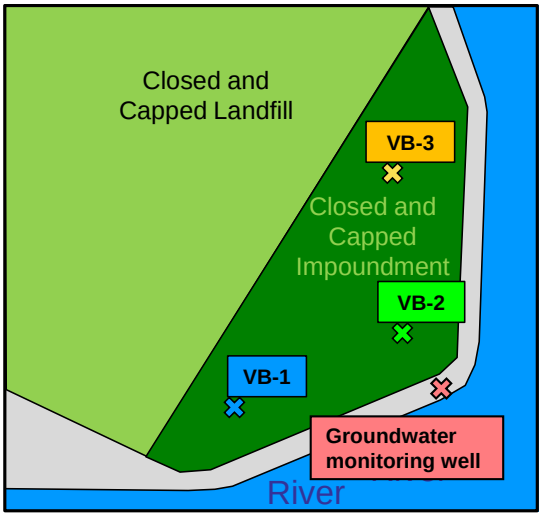

Figure 3.1 Layout of boreholes (VB1, VB2, and VB3) and the downgradient groundwater monitoring well.

3.3.1.2 Porewater, groundwater, and subsurface gas sampling

Following the ash sampling, at each borehole location, a porewater access well was established within the porewater between ~2.4 and ~3 m below the ash layer surface, and a gas access point was set within the vadose zone between ~0.6 and ~0.9 m below the ash layer surface to sample subsurface gas. Monthly porewater and subsurface gas sampling began in September 2018, allowing two months for the porewater to establish equilibrium with the ash deposit. Sampling continued until September 2019 (13 months). In addition, a downgradient monitoring well located ~20 m outside of the impoundment but near the impound outflow (Figure 3.1) was selected for groundwater sampling.

The pH, dissolved oxygen (DO), electrical conductivity (EC), oxidation-reduction potential (ORP), and temperature of porewater and groundwater samples were measured in-line with the low flow sampling pump using a multi-parameter sonde while turbidity was measured with a separate Hatch turbidity meter. Residence time of porewater in the well during pumping was estimated to be 8-50 min based on the water volume in the well and flow rate at 100-150 mL/min. Liquid samples were collected in duplicate for laboratory analysis, including one set of duplicates for carbon analysis (dissolved inorganic carbon (DIC) and dissolved organic carbon (DOC)) and anion analysis and another set that was acidified with Tracemetal® grade nitric acid (3% total acid addition) for metals analysis. Liquid samples were transported on ice and stored at < 6ºC prior to analysis.

Following porewater sampling, subsurface gas monitoring was conducted at the boreholes using a portable gas pump/meter (Vertis Pro 5, Industrial Scientific, Pittsburgh, PA). The meter was fitted to a valve at the top of the gas access point and the steady state concentrations of oxygen (O_2; 0-30%), carbon dioxide (CO_2; 0-5%), methane (CH_4; 0-5%), ammonia (NH_3; 0-500 ppm), and hydrogen sulfide (H_2S; 0-500 ppm) were recorded over up to three consecutive 3-min intervals. Details of the well installation and sampling procedures are provided in Appendix B.I.

3.3.2 Leaching characterizations

3.3.2.1 Batch extractions under field conditions

Field extraction testing was set up in the field to evaluate the use of leaching extractions with control of field redox conditions to estimate the field LSP of constituents. Grab samples of CA were extracted immediately after split spoon retrieval by placing approximately 150 g of ash into a high-density polyethylene (HDPE) bottle and filling the bottle with de-oxygenated 18 MΩ reagent water. The use of de-oxygenated water and minimal headspace in the set up aimed to preserve, to the extent possible, the original redox state of ash samples. The target L/S of the extraction was 1 L/kg-dry; however, the actual L/S values ranged between 1.7 and 3.3 L/kg-dry due to the moisture contents of different grab samples. Filled extraction bottles were brought to the laboratory and tumbled end-over-end for 24 hours at room temperature (20±2 ºC). Details of the procedures to set up field extractions are provided in Appendix B.II.

3.3.2.2 Batch extractions under laboratory conditions

Laboratory extraction testing was carried out (i) to understand the ash stratigraphy with well-controlled L/S in laboratory and (ii) to evaluate the impact of laboratory handling on leaching extraction results compared to the field LSP of constituents. The laboratory extractions were conducted on homogenized CA material from each split spoon under laboratory conditions using 35 g-dry CA and de-oxygenated reagent water at a fixed L/S of 1 L/kg-dry. The extractions were conducted after the determination of moisture content so that the L/S would be more consistent. Otherwise, the same tumbling, separation, and analysis procedures as the field extractions were used. Details of the procedures to set up laboratory extractions are provided in Appendix B.III.

3.3.2.3 pH-dependent leaching of ash composites at L/S = 10 and 1 L/kg-dry

Borehole composites (VB1, VB2, VB3) were made from homogenized split spoon materials located from the strata consistent with the porewater well screens (for details refer to Appendix B.IV). The three field composites were considered to represent the ash deposited near the associated porewater well screen at each sampling location. Each composite was subjected to

characterization of near-equilibrium LSP behavior as a function of pH using EPA Method 1313 [62] at L/S of 10 L/kg-dry and its variant at L/S of 1 L/kg (to approximate the L/S of field porewater), aiming to evaluate the effects of pH and L/S on the LSP of constituents and to serve as a basis for geochemical model development. Procedures of the pH-dependent leaching test followed same procedures as described in §2.3.3 of Chapter 2.

3.3.3 Eluate analysis

For eluates from field extractions, laboratory-extractions, and pH-dependent leaching tests, the pH and electronical conductivity were measured using an Accumet 20XL multimeter. The ORP was read through an ORPTestr 10 meter and converted to redox potential (Eh) by adding a correction factor (228V) of the standard reference electrode. The *pe*, which is defined in terms of the electron activity, was calculated by a conversion equation derived from the Nernst equation:

$$pe = \frac{F}{2.303RT}(Eh/1000)$$

where F is the Faraday constant (23,061 cal/ (V mol)),
R is the gas constant (1.987 cal/ (K mol)),
T is the temperature (K), and
1000 is for unit conversion (1,000 mV = 1 V).

For eluates from porewater and leaching characterizations (field extractions, laboratory-extractions, and pH-dependent leaching tests), major species and trace elements present at higher concentrations were determined using a Varian Model 720-ES ICP-OES (Agilent Technologies, Santa Clara, CA) following EPA Method 6010D [97]. For low-level trace analysis, concentrations were determined by ICP-MS using a Perkin Elmer Elan DRC II (Perkin Elmer, Waltham, MA) following EPA Method 6020B [98]. The method detection limit (MDL) and lower limits of quantitation (LLOQ) are listed in Table 3.1 for elements presented in this study.

The concentrations of anions were determined by ion chromatography (IC) using a Metrohm 881 Compact IC Pro (Metrohm USA, Riverview, FL) with a Metrosep A Supp 5 column and a conductivity detector following EPA Method 9056A [99]. Carbon analysis including DIC and DOC was conducted using a Shimadzu TOC-V CPH/CPN (Shimadzu Scientific Instruments,

Inc., Columbia, MD) by catalytic oxidation/non-dispersive infrared detection (NDIR) following EPA Method 9060A [100]. Details of analytical quality assurance (QA) and quality control (QC) can be referred to Appendix A.III.

Table 3.1 Methods, MDLs, and LLOQs for analysis of eluates by ICP-OES and ICP-MS

Analyte	Symbol	Method	MDL (mg/L)	LLOQ (mg/L)
Aluminum	Al	ICP-OES	0.0034	0.025
Antimony	Sb	ICP-MS	0.00008	0.001
Arsenic	As	ICP-MS	0.00057	0.001
Boron	B	ICP-OES	0.0023	0.025
Calcium	Ca	ICP-OES	0.0065	0.025
Chromium	Cr	ICP-MS	0.00047	0.001
Iron	Fe	ICP-OES	0.0022	0.025
Molybdenum	Mo	ICP-MS	0.00059	0.001
Phosphorus	P	ICP-OES	0.0068	0.025
Selenium	Se	ICP-MS	0.00051	0.001
Silicon	Si	ICP-OES	0.0038	0.025
Sulfur	S	ICP-OES	0.0058	0.025
Vanadium	V	ICP-MS	0.00032	0.001

3.3.4 Solid characterization

Subsamples of VB1, VB2, and VB3 composites were dried in a sealed container purged with continuous nitrogen flow prior to determination of solid sample composition. The major elemental composition was measured by X-ray fluorescence (XRF, Thermoscientific ARL ADVANT'X IntelliPowerTM 4200, Wilmington, DE, USA). The total contents of trace elements were determined by acid digestion following EPA Method 3052 [101] with a subsequent analysis of the digestion solution following EPA Method 6010B [102] by Eurofins TestAmerica (Nashville, TN).

A carbon analyzer (Shimadzu model TOC-LCPH with a SSM-5000 unit for solid samples) was used to measure total carbon (TC) and total inorganic carbon (TIC). Total organic carbon (TOC)

was computed as the difference between TC and TIC.

The amounts of amorphous and crystalline iron (hydr)oxides were determined through analysis of Fe concentrations in eluates from two selective extraction tests. The amorphous iron (hydr)oxides (Am_{FeOOH}) was extracted with ascorbic acid following the ISO Method 12782-1 [63]. The crystalline iron (hydr)oxides (Cry_{FeOOH}) was extracted with dithionite following the ISO Method 12782-2 [64]. Concentrations of Fe in eluates from the extraction tests were analyzed by ICP-OES following EPA Method 6010D [97].

The obtained results were used to understand the chemical composition of CA as it is closely related to the leaching behavior of trace constituents and to provide parameters (TIC, Am_{FeOOH}, and Cry_{FeOOH}) necessary for geochemical model development (§3.3.5).

3.3.5 Geochemical modeling approach

Geochemical speciation modeling was performed within the Objects Representing CHEmical Speciation and TRAnsport (ORCHESTRA) modeling framework [58] embedded in the software package LeachXS™ [65] to develop a virtual material that best described experimental results of pH-dependent leaching (EPA Method 1313) of the field ash composites. Virtual material definition is provided in §2.3.4 of Chapter 2. For modeling purposes, a system that included major constituents (i.e., Al, Ca, Fe, Si, S, and CO_3^{2-}) and oxyanionic constituents (i.e., As, Se, Mo, P, Sb, and V) was considered. As a first approximation, adsorption of As, Se, Mo, P, Sb, and V was modeled by the diffuse double-layer model developed for HFO with the same HFO adsorption parameters as reported by Dzombak and Morel [52], including the acidity constants, adsorption equilibrium constants, and specific surface area to ensure the internal consistency in modeling a multi-ion system.

In simulations of reducing conditions (e.g., field porewater conditions), the surface site density of HFO in the model was set at different values to show the sensitivity of changing HFO site density on simulated leaching concentrations of As and Se. The density of weak sites (major sites for adsorption) was decreased from the reported values of 0.2 [52] to 0.1 and 0.04 mol/mol-Fe, with decreasing ratios of 2 and 5, respectively. Similarly, the density of strong sites also was reduced from the reported values with the same decreasing ratios as weak sites. In the model, the number of adsorption surface sites is coupled and proportional to the amount of the selected iron

(hydr)oxide mineral phase accounting for the solubility of Fe in the model, allowing for the change of total HFO adsorption sites with the precipitation/dissolution of selected iron (hydr)oxides.

The available content (AC) of constituents (Table B.2, Appendix B.V) except CO_3^{2-} and Fe were determined as the maximum release (mg/kg) in the full pH range in EPA Method 1313 [18,19]. The AC of CO_3^{2-} was calibrated against the leaching behavior of Ca at pH > 8 with the upper limit constrained by measured TIC. The AC of Fe was calibrated within the range of measured amount of Am_{FeOOH} (lower limit) and Am_{FeOOH}+Cry_{FeOOH} (upper limit) to yield the minimum residual between simulation and experimental results of pH-dependent leaching of As and Se.

Aqueous reactions were based on the MINTEQA2_V4 database [56] at 20°C according to the laboratory temperature (20±2ºC) and mean porewater temperature (18.8°C). A set of minerals (Table B.3) was selected from the MINTEQA2_V4 [56], CEMDATA18 [84], and MINTEQA2 [103] databases, aiming to generally describe the pH-dependent leaching behavior of major constituents according to the common phases controlling leaching from CA as reported in literature [31,104,105]. Additional precipitates were included in the mineral assemblage to simulate the LSP of As and Se under field reducing conditions, including orpiment (As_2S_3), pyrite (FeS_2), elemental Se, and FeSe based on their occurrences in sulfate-reducing aquifer sediments [106] or in reduced coal ash [22,94].

3.4 Results and discussion

3.4.1 Chemical characterization of field-disposed coal ash

The CA material collected from the field impoundment is Class F fly ash likely co-disposed with a smaller portion of bottom ash. When compared with 26 as-generated bituminous fly ashes from an EPA database [11], the field material had relatively moderate Ca (~1.4 wt%) and high Fe (13.3 wt%) content (Table 3.2) while the total content of most trace elements was within reported ranges (Table B.5, Appendix B.VII).

Table 3.2 Total content of major elements analyzed by XRF and other properties (total organic carbon and total inorganic carbon) in as-generated bituminous fly ashes from the EPA report (EPA_FA) [11] and field ash composites (VB_FA), unit (%, w/w)

	EPA_FA (26 samples)			VB_FA (VB1, VB2, and VB3)
	10th Percentile [a]	Median [a]	90th Percentile [a]	Mean ± S.D. [b]
Si	18.89	23.38	26.41	21.93 ± 0.89
Al	10.52	13.26	15.2	11.76 ± 0.62
Ca	0.5	1.28	3.86	1.46 ± 0.06
Fe	2.38	4.71	11.75	13.26 ± 2.72
Mg	0.36	0.57	0.84	0.61 ± 0.03
S	0.22	0.42	0.92	0.04 ± 0.01
Na	0.17	0.32	0.82	0.72 ± 0.23
K	1.01	1.91	2.33	3.44 ± 0.44
P	0.03	0.09	0.25	0.64 ± 0.04
TOC	0.05	0.25	1.29	1.81 ± 0.10
TIC	0.51	4.87	12.67	0.09 ± 0.01

[a] Statistical parameters including the 10th percentile, median, and 90th percentile were given for 26 fly ashes combusted from bituminous coal in the EPA report [11]. Because results from the populations have large variations, medians were reported instead of means.

[b] Mean value (between VB1, VB2, and VB3) ± Sample standard deviation.

The total content has been reported not to be an adequate predictor of leaching behavior [12]. Therefore, the available content of constituents in the field composites, typically determined as the maximum leachable amount from the pH-dependent leaching test [18,19], was compared to the range of as-generated EPA ashes (Figure 3.2). Results showed that sluicing removed a significant fraction of soluble oxyanionic constituents including B, Mo, Sb, Se, and V from the solid matrix. In contrast, the available content of As in the field ash indicated that leachable As was enriched relative to as-generated EPA ashes and was not affected by the sluicing process.

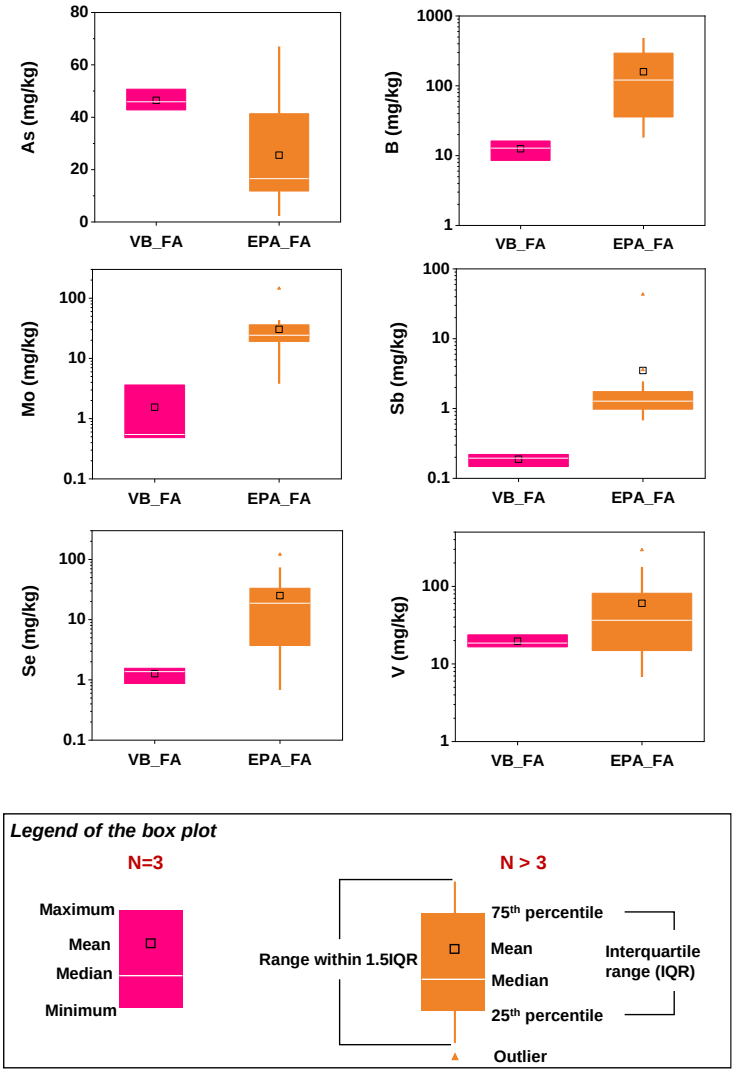

Figure 3.2 Available content of As, B, Mo, Sb, Se, and V in field ash composites (VB_FA) from each borehole (VB1, VB2, and VB3) and in as-generated bituminous fly ash from the EPA report (EPA_FA) [11]. Available content is defined as the maximum leaching amount from the EPA 1313 leaching test [18,19].

3.4.2 Ash stratigraphy in the field site

Results of laboratory extraction tests with well-controlled L/S conditions were used to inform the ash stratigraphy as a function of sampling depths and borehole locations. Vertical profiles of *pe* and concentrations of Fe from VB2 and VB3 showed the influences of overlying soil and underlying clay materials on the leaching of ash samples near the interfaces due to the

penetration or mixing of soil or clay, while the collection of samples at VB1 was centered on the ash layer with a more consistent response with depth than VB2 and VB3 (Figure 3.3). However, a one-way analysis of variance on the confirmed ash samples (excluding samples potentially influenced by cover soil and bottom clay materials) indicated no statistically significant difference in mean values (p-value > 0.05) among the three borehole locations for geochemical parameters (i.e., EC and *pe*) and eluate concentrations of major (i.e., Ca, Fe, and S) and trace constituents (i.e., As, Se, Cr, Mo, and B) (Figure 3.3; Figure B.2-Figure B.3 and Table B.6 in Appendix B.VII).

The *pe* values of materials were found to be closely correlated to the leaching of Se, Sb, V, and Fe. The Se, Sb, and V tended to be immobilized when *pe* < ~5.4 (Figure 3.4) and their concentrations increased accordingly as *pe* increased from 5.4 to 6.2. Such a relationship suggested lower solubilities of Se, Sb, and V under reducing redox conditions than under oxidizing conditions, which was likely attributed to the precipitation of Se, Sb, and V into insoluble phases, such as metal Se(0) or FeSe [22,94], Sb_2O_3 or Sb_2S_3 [107,108], and V(IV)-bearing minerals (e.g., $CaV_2(PO_4)_2(OH)_4 \cdot 3H_2O$) [109,110]. Conversely, higher dissolved Fe concentrations were observed for samples with lower *pe* values (< ~5.4) likely because of the conversion of insoluble Fe(III) in iron hydroxides to soluble Fe (II) under reducing conditions [21]. Eluate concentrations of As and Cr did not show explicit correlations with *pe* values of laboratory-extracted materials. For As, the potential reason is because that As leaching is primarily controlled by HFO adsorption under suboxic to oxic conditions [4,13] and the adsorption is influenced by combined factors including the number of adsorption sites, available content of As, and pH/*pe* conditions [68,111]. Therefore, the concentration of As was not sensitive to solely *pe* (4.8-6.2) at the laboratory characterization conditions. For Cr, the leaching in this *pe* range (4.8-6.2) is mainly controlled by organic matter complexation and a greater amount of solid organic matter results in a lower Cr aqueous concentration [27,112], which is supported by the negative correlation between Cr and DOC, where increased DOC is reflective of greater solid organic matter (Figure 3.4).

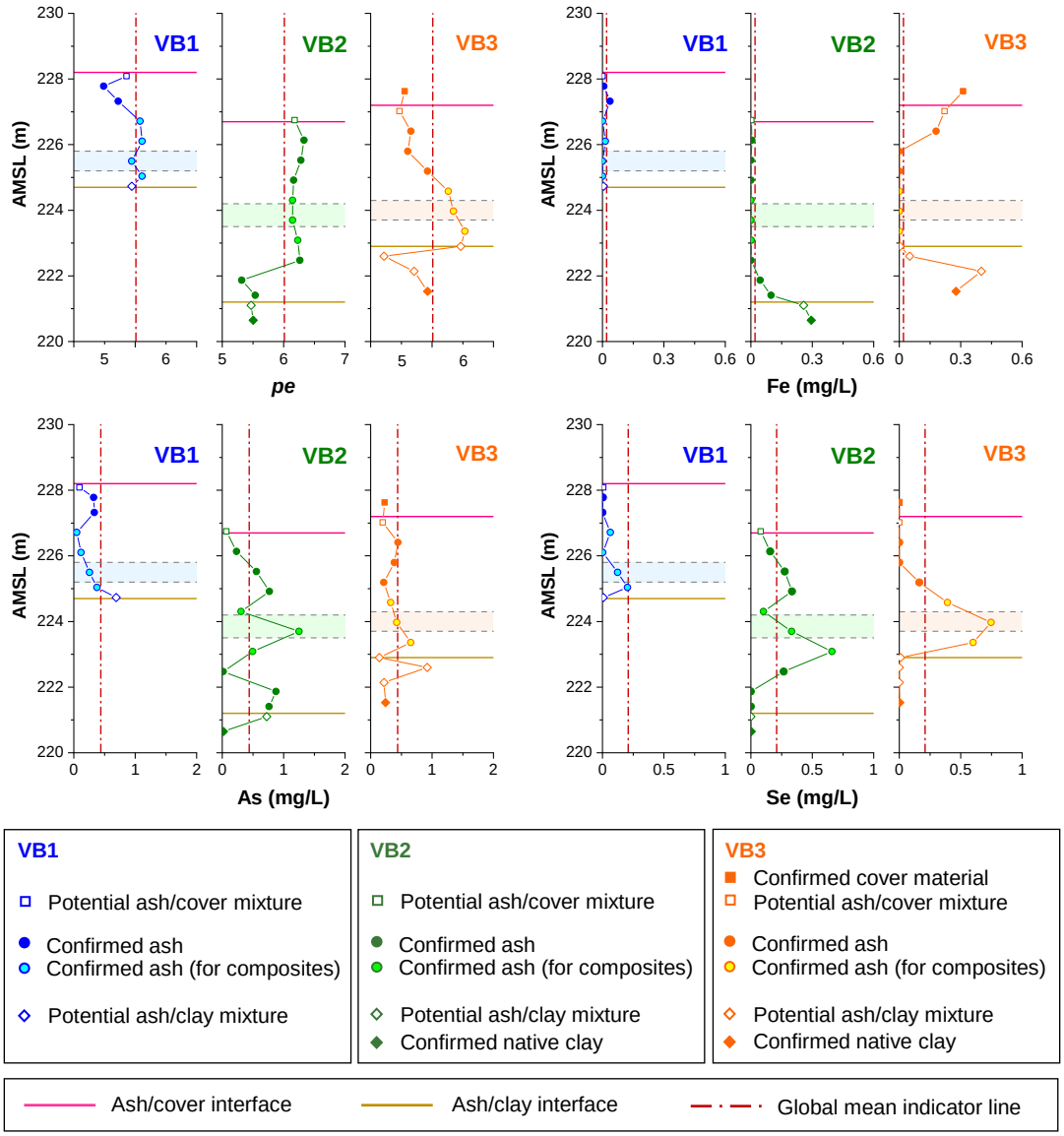

Figure 3.3 Depth profiles of *pe*, Fe, As, and Se concentrations at VB1, VB2, and VB3. The elevations of two interfaces (in pink and brown) were determined from geologist notes. The global mean of each parameter was calculated only based on confirmed ash from three boreholes excluding the confirmed cover soil (■), native clay (♦), potential cover/ash mixtures (□), and ash/clay mixtures (◊). The shaded areas correspond to porewater-screening depth intervals. Bulk ash samples collected from the strata consistent with the porewater well screens were composited for EPA Method 1313 laboratory leaching tests.

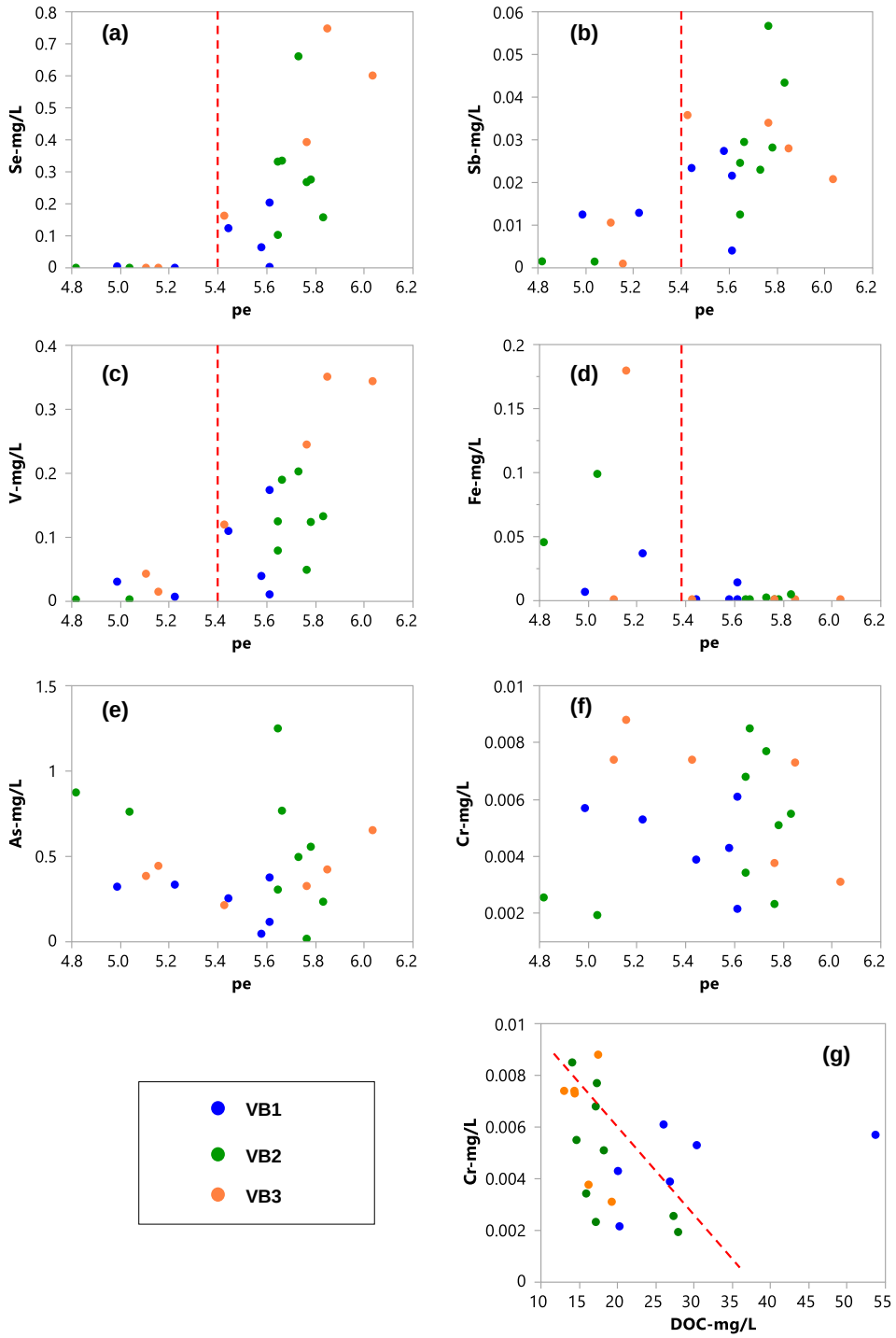

Figure 3.4 (a)-(f) Concentrations of Se, Sb, V, Fe, As, and Cr as a function *pe* and (g) concentrations of Cr as a function of DOC concentrations in laboratory extraction tests on individual coal ash samples from different depths at VB1, VB2, and VB3. Dashed lines: reference lines to help indicate the relationships between variables.

3.4.3 Impacts of geochemical parameters on leaching of arsenic and selenium

3.4.3.1 Comparison of ranges of pH, *pe*, and pH+*pe* between laboratory extractions, field extractions, and porewater

In this section, results from field and laboratory extractions on individual ash core samples and pH-dependent leaching tests on field ash composites were compared with porewater compositions to evaluate the relationships between leaching under different conditions and the extent to which leaching assessment methodologies reflect field leaching behaviors. For the field and laboratory extractions on individual split spoon material, only samples from the locations close to porewater well screens were included for the comparison. The domains of controlling geochemical parameters (i.e., pH, *pe*, and pH+*pe*) in Figure 3.5 help to characterize the redox conditions in each environment.

The *pe* values from both laboratory and field extraction tests indicated a suboxic environment, while the *pe* in porewater extended into an anoxic zone with *pe* ranging from 1.0 (10th percentile) to 3.5 (90th percentile). Compared to laboratory extractions with more exposure to air during homogenization and testing, the field extractions had much wider distributions of pH, *pe*, and pH+*pe*. The range of *pe* in field extractions (3.6-5.8, 10th-90th percentile) compared to *pe* in laboratory extractions (5.5-6.0, 10th-90th percentile) indicated that leaching tests set up in the field limited O_2 contact with samples and helped preserve the redox states of materials but remained at much higher *pe* than porewater. Additionally, a clear and consistent trend of a progressive decrease in median pH from porewater (~8.0) to field extractions (~7.5) to laboratory extractions (~7.1) was observed. The difference of pH was statistically significant (p-value < 0.0001) and was likely caused by the H^+ produced by oxidation reactions of primary reduced species (e.g., Fe^{2+} and HS^-) in coal ash leaching system when the materials were recovered for the field and laboratory extraction tests.

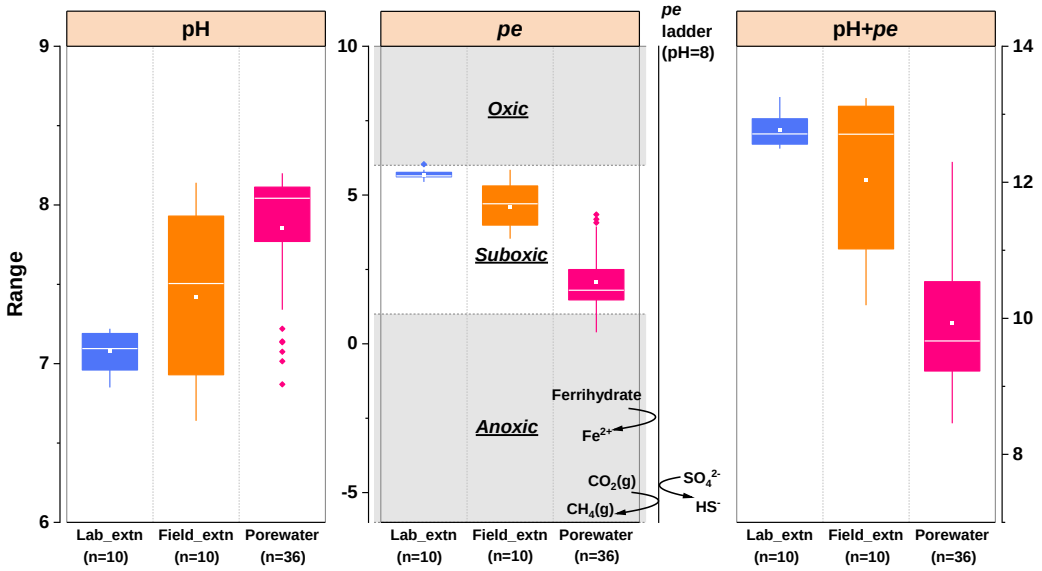

Figure 3.5 The ranges of pH, *pe*, and pH+*pe* in laboratory extractions, field extractions, and in porewater. Lab_extn: laboratory extraction. Field_extn: field extractions. Redox environments (oxic, suboxic, and anoxic) were classified according to the pH+*pe* values used by Borch et al. [21] for each environment. To calculate the redox ladder, the activity of Fe^{2+} in the half reaction was set at 1E-5 mol/L. Redox couples for the sulfate and CO_2 reduction reactions were indicated when the corresponding chemical species were at the same chemical activity to illustrate the *pe* of transition.

From subsurface gas compositions (Figure 3.6) monitored throughout the year, methane exceeding the calibration limit (5 vol.%) was recorded from all boreholes and H_2S was detected at VB2 and VB3. The formation of CH_4 (methanogenesis) and reduction of sulfate to H_2S are indicators of a strongly reducing environment mediated by microorganisms [113]. Correlation to seasonal temperature variations (Figure B.4, Appendix B.VII) showed that a more oxic environment appeared to be generated at VB1 during colder weather (December to May), likely due to lower microorganism activity, which resulted in higher pH + *pe* values. However, no such relationships were evident at VB2 and VB3.

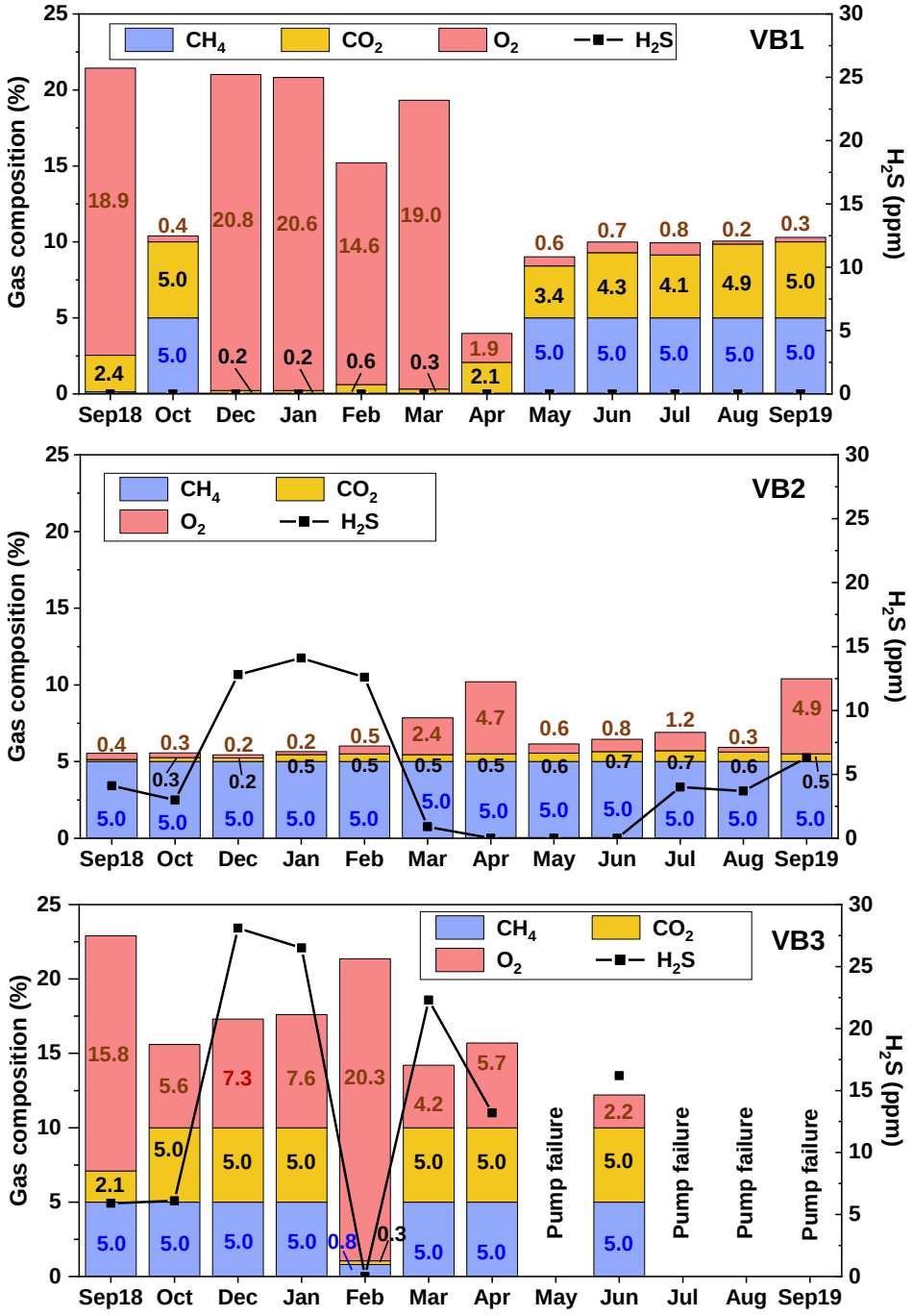

Figure 3.6 Temporal variations of subsurface gas compositions (CH_4, CO_2, O_2, and H_2S) at VB1, VB2, and VB3. No readings were taken during November for all wells because of a sampling schedule conflict. No measurements on VB3 in May, July, Aug., and Sep. 2019 due to a pump failure. The upper calibration limit for CH_4 and CO_2 is 5.0 vol.%.

The *pe* ladder in Figure 3.5 compares the domains of selected redox couples that are important to identify the dominating biogeochemical leaching processes. Although the exact redox sequence is determined by multiple factors (e.g., chemical compositions of the system and selected redox couples), the shown ladder gives rough *pe* levels for the reactions to occur. The measured *pe* of porewater appeared not to be sufficiently low to support anaerobic methanogenesis. Given the residence time of porewater in the well during pumping (8-50 min), the porewater sample might have been oxidized when in contact with oxygen remaining in the sampling equipment or with air introduced into the well during pumping because of the potential of a relatively large surface area for porewater-air contact in the well. The discrepancy between subsurface gas compositions and *pe* measurement makes it reasonable to argue that porewater sampling in the field is still suffering from exposure of samples to air to some extent, and the resulting field *pe* measurement can be problematic [114].

3.4.3.2 Comparison of leaching concentrations in the field and in leaching tests

The impacts of geochemical parameters (i.e., pH, redox potential, and L/S) on determining leaching behavior in different environmental scenarios were evaluated (i) through the modified EPA 1313 test at L/S = 1 L/kg with respect to the effect of pH (6-8); (ii) through the comparisons between extraction tests (in field and in laboratory) and porewater compositions with respect to the effect of redox potential; and (iii) through the comparisons between field extractions (L/S=1.7-2.4 L/kg) and porewater (L/S ~0.67 L/kg) with respect to the effect of L/S. The porewater L/S was estimated from the mean porosity (0.64) of ash core samples and dry density (2.65 kg/L) assuming full saturation at stagnant conditions.

Arsenic concentrations up to 4.1 mg/L were observed in field porewater from this study, in comparison to the 90th percentile concentration of 0.78 mg/L in porewater from other CA impoundments [2]. In contrast, As concentrations in the downgradient groundwater well located ~20 m away from the impoundment were less than 0.001 mg/L. The average As concentration was greatest in porewater, followed by field extractions, and was the lowest in laboratory extractions (Figure 3.7).

The greatest As concentration in porewater compared to in other extraction tests cannot be caused by the L/S and pH effects. Comparing leaching in the laboratory at L/S=1 and L/S=10

L/kg (Figure B.5, Appendix B.VII), a lower L/S did not significantly decrease apparent equilibrium concentrations of As but decreased the total mass released. However, the mass released of As in porewater with a lower L/S (~0.67 L/kg) compared to field extractions (L/S=1.7-2.4 L/kg) was not decreased (Figure B.6, Appendix B.VII). Furthermore, although the higher porewater pH may increase leachable As concentration compared to in field and laboratory extractions as indicated by pH-dependent leaching results, such an increase is not adequate to account for the high porewater As concentrations. Therefore, the greatest As concentrations in porewater were attributed to the influence of other geochemical parameters, which likely led to a more reducing environment in the field porewater compared to that in the extraction tests and modified EPA Method 1313 leaching [5]. The strongly reducing environment in the field was supported by the CH_4 detection (Figure 3.6) and higher concentrations of Fe in porewater compared to leaching tests (Figure B.11, Appendix B.VII). The lower concentrations of As in porewater for VB3 compared to VB1 and VB2 may have been caused by redox heterogeneity in the field.

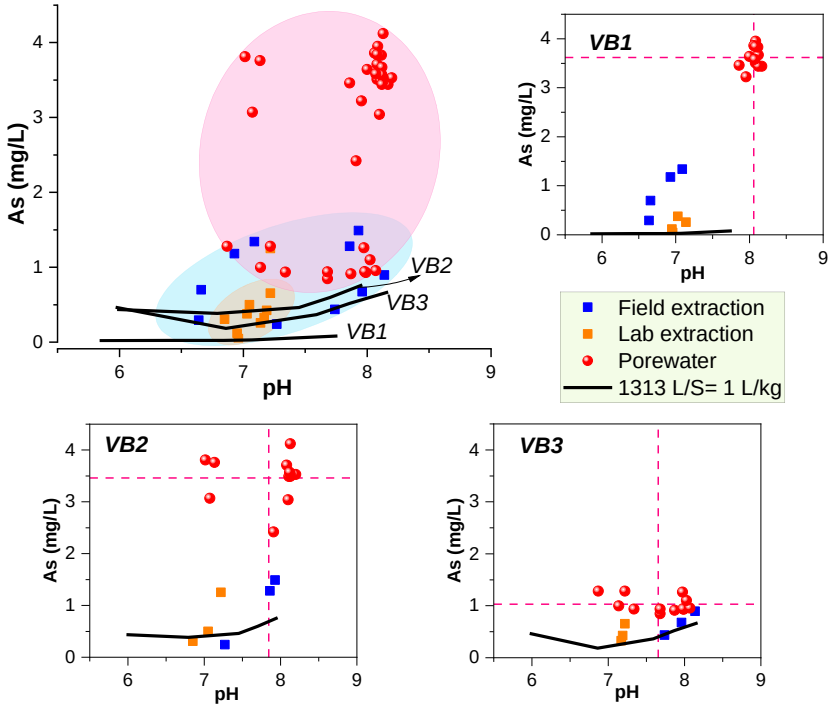

Figure 3.7 Arsenic concentrations as a function of pH from the field extractions, laboratory extractions, modified EPA Method 1313 test at L/S = 1 L/kg, and in field porewater at VB1, VB2, and VB3. Porewater was sampled monthly from September 2018 to September 2019. Mean of porewater pH and As concentrations are indicated by vertical and horizontal red dash lines, respectively.

For Se, the average aqueous concentration decreased with the reducing environment, from 0.32 mg/L in laboratory extractions to 0.08 mg/L in field extractions and below the detection limit (<0.0005 mg/L) in porewater (Figure 3.8). The change in aqueous concentrations is attributed to variations of redox conditions because the effects of pH and L/S cannot explain the significant change of leaching behavior. The mechanisms accounting for the leaching variations of As and Se are further discussed based on insights from geochemical speciation modeling in §3.4.4.

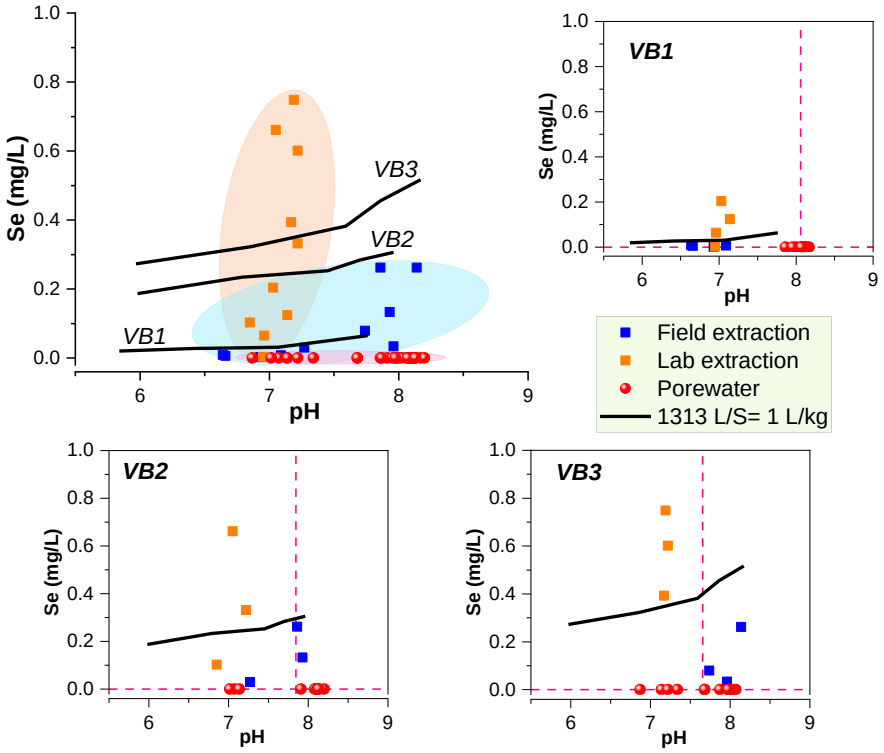

Figure 3.8 Selenium concentrations as a function of pH from the field extractions, laboratory extractions, modified EPA Method 1313 test at L/S = 1 L/kg, and in field porewater at VB1, VB2, and VB3. Porewater was sampled monthly from September 2018 to September 2019. Mean of porewater pH and Se concentrations are indicated by vertical and horizontal red dash lines, respectively.

The comparisons between the field study and laboratory leaching characterization indicated the important role of redox conditions in influencing leaching of As and Se. At each sampling location, the concentrations of As and Se in porewater were found to be temporally stable with only a slight variation of As concentrations and consistently low Se concentrations < 0.0005 mg/L over 13 months, indicating that the partitioning of As and Se was near steady state and

primarily controlled by thermodynamic equilibrium although kinetics may play a role in local stratification of microbial processes. In addition, other redox-sensitive constituents such as Sb and V were in low concentrations in porewater (Figure B.8Figure B.9) similar to Se. Such behavior was consistent with observations from spatial variations on individual split spoon samples (refer to §3.4.2), as Se, Sb, and V were more soluble in samples with higher *pe*. Yet, the leaching of B and Mo was relatively independent of redox conditions (Figure B.12-B.13). Boron appeared to show sorption between pH 6 and 8 in the pH-dependent test (Figure B.13). However, such an effect on controlling the dissolved concentrations of B was minor compared to the effect of L/S, because the porewater with the lowest L/S value showed the highest B concentrations. Also, similar total released mass of B was obtained in porewater, field extractions, and laboratory extractions (Figure B.14), indicating B as a highly soluble element.

3.4.4 Mechanisms controlling the LSP of arsenic and selenium

3.4.4.1 Development of geochemical speciation models for the materials under laboratory test conditions

Geochemical speciation modeling was applied to (i) facilitate understanding the leaching variations of As and Se between laboratory tests and in the field, (ii) evaluate potential mechanisms reported in literature, and (iii) identify model uncertainties when predicting field leaching behaviors based on laboratory leaching characterizations.

The field composites from VB2 and VB3 were near replicates in the pH-dependent leaching, and VB1 was slightly different from these two samples; therefore, two separate models were developed for VB1 and VB2/3 (merged results of VB2 and VB3). The ORCHESTRA model used the HFO adsorption approach of Dzombak and Morel [52] with adsorption reaction constants for As adjusted within reported uncertainty to best fit the data from Method 1313 (Table B.4). Model parameterization was focused on the pH range of 6-8 at L/S = 1 L/kg to optimize the simulation near the natural pH range and estimate porewater compositions. In each model, a fixed value of pH + *pe* (VB1: pH + *pe* = 13.9; VB2/3: pH + *pe* = 13.7) was set across different pH test positions according to the pH and *pe* measurements at the natural pH condition. Samples characterized in the EPA 1313 test were somewhat reducing (suboxic) as indicated by

the pH+*pe* level.

The pH-dependent leaching behaviors of As and Se at two L/S conditions (10 and 1 L/kg) were fairly well described by simulation results (Figure 3.9). Leaching of As and Se between pH 2 and 10 were characterized as adsorption-controlled onto metal oxides [4,9] represented by HFO in the model (Figure 3.10). The HFO adsorption decreases as pH increases from 4 because of decreased availability of protonated surface sites for anion adsorption. Ca-arsenates were shown not to precipitate given the limited amount of soluble Ca present in the studied ash.

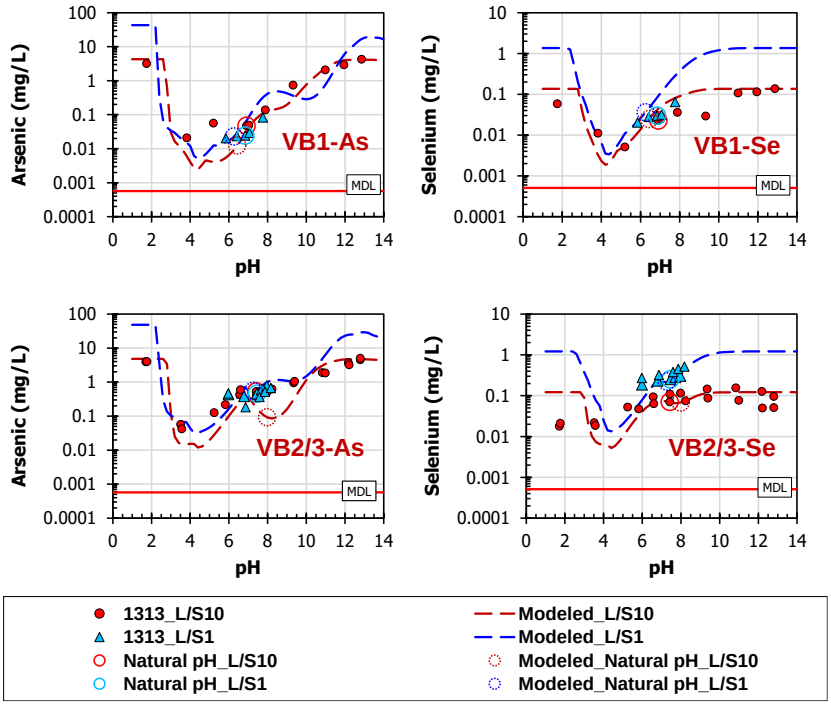

Figure 3.9 Simulated leaching concentrations of As and Se as a function of pH compared to the EPA Method 1313 at L/S = 10 L/kg and modified Method 1313 at L/S = 1 L/kg for the field ash composites (VB1 and merged results of VB2 and VB3 as VB2/3). VB1: pH + *pe* = 13.9; VB2/3: pH + *pe* = 13.7. MDL: method detection limit.

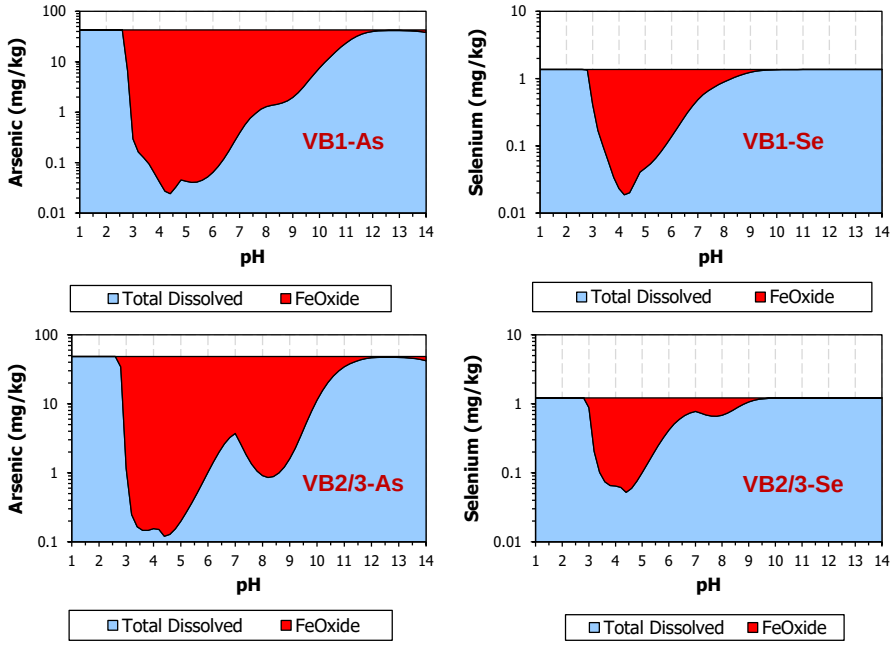

Figure 3.10 Phase diagrams of As and Se as a function of pH according to the EPA Method 1313 at L/S = 10 L/kg for the field ash composites (VB1 and merged results of VB2 and VB3 as VB2/3). VB1: pH + *pe* = 13.9; VB2/3: pH + *pe* = 13.7. FeOxide: adsorbed onto hydrous ferric oxide.

Simulated results of other elements (i.e., Al, Ca, Si, Fe, P, Mo, S, V, and Sb) and the corresponding phase diagrams were shown in Figure B.15 and Figure B.16. With the HFO equilibrium adsorption constants reported by Dzombak and Morel [52], the concentrations of trace elements including V and Sb were over predicted in the pH range of 2-10. Insufficient experimental datasets used by Dzombak and Morel to develop the reported reaction constants for Sb and V appeared to be primary uncertainties [115].

3.4.4.2 Response of model predictions to the field environmental conditions

The geochemical speciation model developed and calibrated using laboratory test results and conditions was then used to simulate porewater composition based on field conditions. Sensitivity cases were used to evaluate the effects of HFO surface site density and redox conditions. The pH and L/S were fixed at 8.0 and 0.67 L/kg, respectively, according to the field characterization results. As discussed in §3.4.3, actual *pe* in the field may be lower (more

reducing) than the porewater measurements, so a range of *pe* starting from a suboxic condition (*pe* = 5) to an anoxic condition (*pe* = -8) was applied.

Arsenic. Figure 3.11 provides the comparison between the results of simulations, laboratory leaching on ash composites (modified EPA Method 1313 at natural pH and L/S=1 L/kg), and porewater measurements. Even though the differences in pH and L/S between field and laboratory conditions were considered in the model, the simulation results at measured *pe* with reported HFO site density (weak site: 0.2 mol/mol-Fe; strong site: 0.005 mol/mol-Fe) [52] still underestimated the As concentrations in porewater at VB1/VB2. So, the effect of pH and L/S variations was insufficient to account for the increased porewater As concentrations at VB1/VB2 (up to 4.1 mg/L) compared to laboratory results.

In addition to pH and L/S effects, the redox state significantly impacts aqueous As concentrations through multiple mechanisms. A decrease of *pe* from 5 to -8, caused reduction of arsenate to arsenite, decreases of number of adsorption sites by ferrihydrite dissolution and recrystallization, and caused sulfide precipitation (As_2S_3). The reduction of arsenate to arsenite (*pe* < 0; Figure 3.12) did not lead to greater release of arsenic into solution, even though arsenite has been generally reported to have weaker adsorption to HFO than arsenate [5,22]. However, the relative adsorption of arsenate and arsenite on HFO is pH dependent. The adsorption of arsenate on HFO is stronger in the acidic pH range versus neutral to alkaline conditions, while the adsorption of arsenite is stronger in the pH range of 6-9 than in other pH conditions [68,116,117]. Therefore, adsorption of arsenite can be comparable or greater than arsenate at porewater pH of 8. After arsenite became the dominant species (*pe* < -2; Figure 3.12), the amount of adsorbed arsenite as $\equiv H_2AsO_3$ was greater than the adsorbed arsenate as $\equiv OHAsO_4^{3-}$.

When a fixed HFO adsorption site density was assumed, the decrease in adsorption sites by the dissolution of ferrihydrite as *pe* decreased from around 2 to -5 did not increase the predicted aqueous As concentrations (Figure 3.11). Subsequently, further reducing *pe* to < -5.5 resulted in a substantial increase of As concentrations (over one order of magnitude) but was accompanied by the dissolution of over 80 mol.% ferrihydrite, which, however, was inconsistent with low dissolved Fe concentrations measured in porewater (Figure B.17). Also, using both field porewater and laboratory extraction results, the As:Fe molar release ratio was calculated (Appendix B.VI) as 140 and 120 mol/mol for VB1 and VB2, respectively. However, if the

release of As is primarily attributed to HFO dissolution, the maximum As:Fe molar release ratio will only be 0.2 mol/mol given the site density of 0.005 (strong site) and 0.2 (weak site) mol/mol-Fe from the reported HFO model [52]. As such, there appears to be mechanisms in addition to HFO dissolution that are responsible for the high concentrations of As in porewater.

The high concentrations of As in porewater can be explained if recrystallization of iron (hydr)oxide under the reducing environment was assumed because the recrystallization can cause a decrease in HFO site density and then release adsorbed As to porewater. Such an assumption was based on the results reported by [118]. Specifically, the HFO weak site density was suggested to decrease from 0.2 to ~0.01 mol/mol-Fe due to the transformation of a ferrihydrite-like mineral to a magnetite-like mineral as the environment became more reducing, and the decreased site density led to an extensive release of As. The recrystallization of iron oxides also has been reported to have implications on the incongruent release of As during HFO reductive dissolution in anoxic aquifers [119,120].

In this study, the effects of changing surface site density on the dissolved As concentrations were simulated (Figure 3.11). A decrease of the major weak site density from 0.2 (laboratory conditions) to 0.1 mol/mol-Fe (porewater conditions) resulted in agreement between simulated and measured porewater As concentrations of ~3 mg/L in the *pe* range between -1 and 0 (*pe* conditions estimated from porewater Fe concentrations at VB1 and VB2 as shown in Figure B.17). Given that almost all of the available content of As present in the system was adsorbed at $pe > -5.5$ (Figure 3.12), a relatively small decrease in HFO site density (from 0.2 to 0.1 mol/mol-Fe) can lead to a disproportionately large release of As into solution (i.e., much greater aqueous As concentrations).

The presence of strong methanogenesis suggested $pe < -5$, where arsenic sulfide precipitated (Figure 3.11) and was consistent with the detection of hydrogen sulfide in subsurface gas. However, the measured S concentrations in porewater did not support a condition of $pe < -5$ (Figure B.18), because at such low *pe* the simulated S solubility controlled by pyrite precipitation was much lower than the measured S concentrations. Also, the measured Fe concentrations were much lower than the simulated Fe concentrations at $pe < -5$ (Figure B.17). The apparent contradiction of observations of methanogenesis with dissolved porewater S and Fe concentrations was likely caused by the concurrent presence of multiple redox processes and

conditions (e.g., methanogenesis, sulfate reduction, and Fe(III)-reduction) controlled by spatial gradients and dis-equilibrium [121–123].

Lower As porewater concentrations were observed at VB3 compared to VB1/VB2, potentially because of sulfide precipitation as orpiment at *pe* < -5 indicated by methanogenesis. Alternatively, from the comparison of simulated and measured Fe concentrations in porewater (Figure B.17), a value of *pe* around -1.5 was suggested at VB3 compared to *pe* between -1 and 0 at VB1/VB2, which also could cause lower As concentrations at VB3 compared to VB1/VB2. Thus, multiple mechanisms of As retention are plausible given the multiple lines of competing evidence and can result in the same observed As concentrations in porewater (Figure 3.11).

Selenium. Mechanisms controlling retention and leaching of Se were far less complex than for As. Unlike As, the porewater concentrations of Se were controlled by reduction of selenite to insoluble Se(0) and selenide (FeSe) indicated from simulations. For Se, adsorbed $\equiv SeO_3^-$ on HFO was the major phase for Se speciation under suboxic conditions (Figure 3.12). Precipitation of metallic selenium occurred when *pe* < 2 and was followed by transformation to FeSe(-II) mineral when *pe* < -1, resulting in the gradual decrease of dissolved Se concentrations as *pe* decreased. Low solubilities of the two minerals caused Se to be immobile; the resulting concentrations were too low to be detected under suboxic to anoxic environments. The transformation of Se speciation under different redox environments resulting the change of leaching behavior is consistent with literature [22].

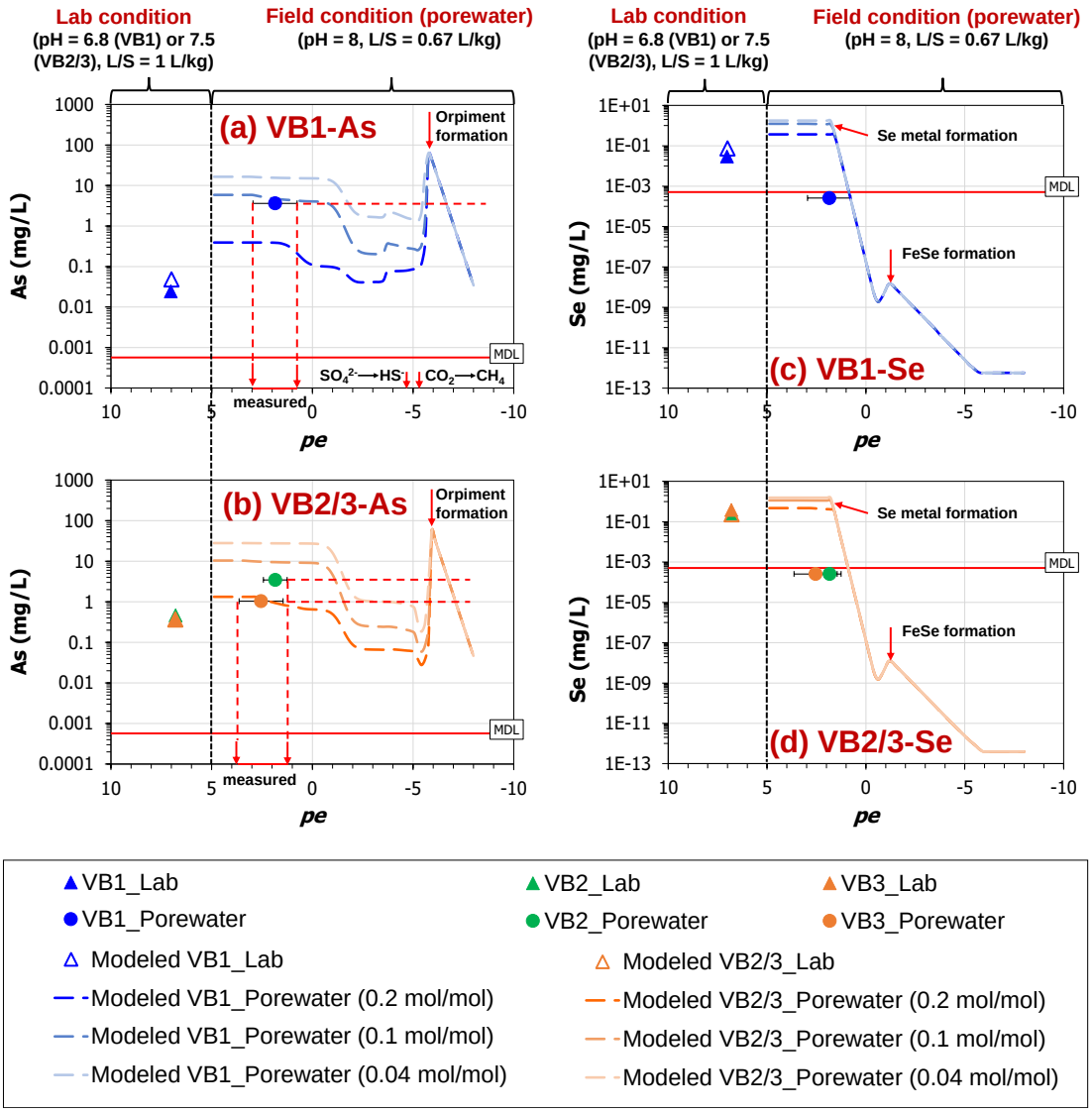

Figure 3.11 Simulated leaching concentrations of As and Se as a function of *pe* compared to measurements from laboratory test conditions and field porewater conditions. The laboratory test condition refers the natural pH condition (pH = 6.8 for VB1, pH = 7.5 for VB2 and VB3) of the modified EPA Method 1313 at L/S = 1 L/kg. Field porewater condition was simulated using pH = 8 for VB1, VB2 and VB3 and L/S = 0.67 L/kg. HFO site density was indicated in parentheses for each porewater case. Concentrations of Se in porewater are below the method detection limit (MDL) and set as half of the MDL.

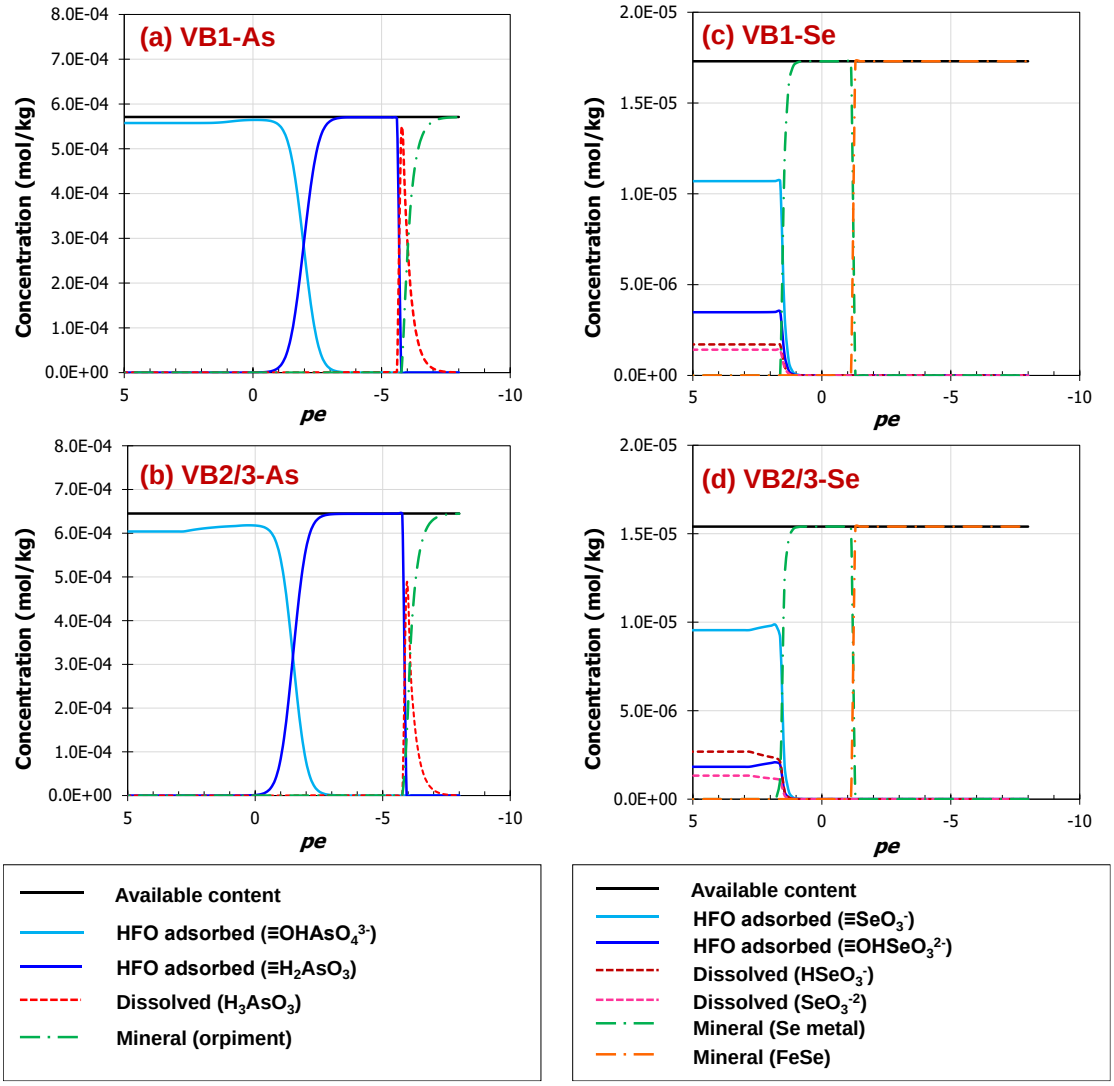

Figure 3.12 The speciation of As and Se as a function of *pe* in the simulation of field porewater conditions. Densities of HFO adsorption sites were set at reported values (weak site: 0.2 mol/mol-Fe; strong site: 0.005 mol/mol-Fe) [52].

3.4.4.3 Speciation of arsenic and selenium under a wide range of environmental conditions

The predominance diagrams in Figure 3.13 incorporated the HFO adsorption phases of the As and Se species in addition to the dissolved and precipitated phases; therefore, these diagrams can help identify the reactions influencing the release and uptake of elements under a wide range of pH and *pe* conditions. Adsorption controls the speciation of As between pH 2 and 12 under the oxic environment (pH + *pe* > 14). Dissolution of ferrihydrite in strongly acidic pH condition

releases adsorbed As as $H_2AsO_4^-$ under suboxic conditions (~9 < pH + *pe* < ~14). Using the reported HFO site density [52] across the full pH and *pe* ranges in Figure 3.13(a) indicated that both As(V) and As(III) adsorbed strongly onto HFO primarily as $\equiv OHAsO_4^{3-}$ and $\equiv H_2AsO_3$, respectively. The dissolved As species ($H_2AsO_4^-$ and H_3AsO_3) became predominant phases under relatively acidic and reducing conditions as a result of ferrihydrite dissolution. However, using a decreased adsorption site density under the anoxic environment (pH + *pe* < 9) in Figure 3.13(c) generated a re-mobilization zone of As between pH 6 and 8 when ~7 < pH + *pe* < ~9, caused by the release of adsorbed $\equiv OHAsO_4^{3-}$ from HFO to porewater. Under strongly anoxic (~0 < pH + *pe* < ~6) conditions, the formation of orpiment is suggested to precipitate As in more acidic to neutral pH conditions compared to the alkaline region, likely accompanied by methanogenesis.

For Se, immobilization by precipitation reactions occurs at relatively more oxic environments (pH + *pe* < 7-11, depending on pH) compared to As, covering strongly acidic to alkaline conditions. Different adsorption affinities between Se and As are reflected in Figure 3.13(b) as the HFO-adsorbed part only dominates the speciation of Se over a limited pH range. The stronger adsorption of Se(IV) on HFO compared to Se(VI) also was reported to help immobilize Se in a more reduced environment than aerobic conditions [5]. The Se(VI) is adsorbed strongly by HFO between a narrow pH range of ~2 to 5 and is leachable as SeO_4^{2-} at higher pH conditions, while the reduced Se(IV) is adsorbed mainly between a wider pH range of ~2 to 9. The speciation of Se was not noticeably impacted by using a decreased HFO adsorption site density under the anoxic environment (pH + *pe* < 9) in Figure 3.13(d) compared to using a fixed value in Figure 3.13(b), because the precipitation of Se as less soluble phases controls the leaching of Se under such conditions.

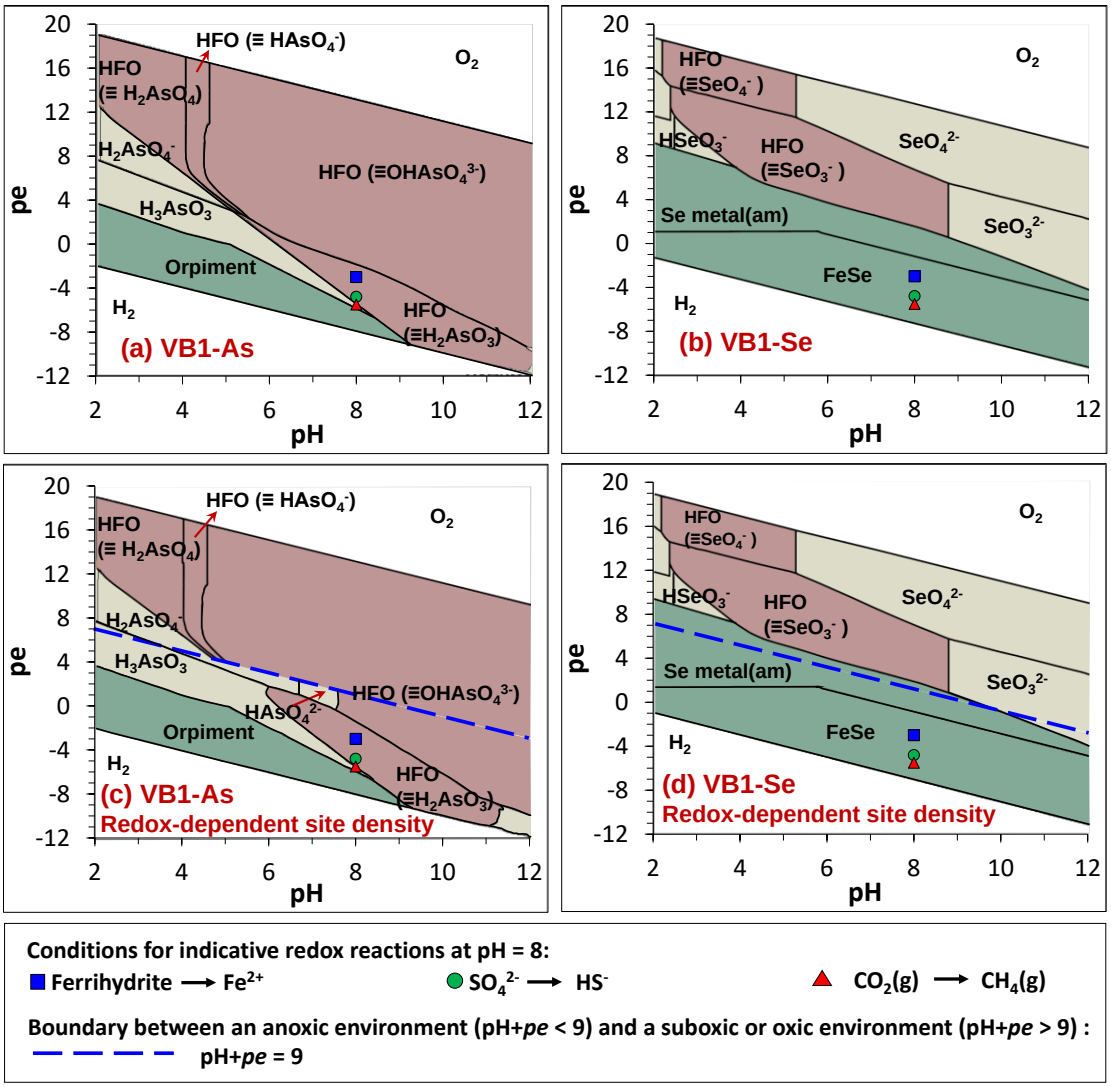

Figure 3.13 *pe*-pH predominance diagrams of As and Se species at L/S = 0.67 L/kg for VB1 sample. For (a) As and (b) Se, simulation with the reported HFO site density (weak site: 0.2 mol/mol-Fe; strong site: 0.005 mol/mol-Fe) [52] across the full pH and *pe* ranges. For (c) As, and (d) Se, simulation with the reported HFO site density under a suboxic or oxic environment (pH + *pe* > 9) and with a decreased site density (weak site: 0.04 mol/mol-Fe; strong site: 0.001 mol/mol-Fe) under an anoxic environment (pH + *pe* < 9). To calculate the transition *pe* values of indicative redox reactions, activity of Fe^{2+} in the half reaction for ferrihydrite reduction was set at 1E-5 mol/L, and chemical species were at the same chemical activity for sulfate and CO_2 reduction reactions.

Composition has been found to play a vital role in determining equilibrium speciation [106]. For example, a different equilibrium speciation may be obtained by changing the S/As and Fe/As

molar ratios, as increasing the ratio of S/As expanded the dominating area of As precipitated by sulfides over adsorbed by HFO, and increasing the ratio of Fe/As had the opposite effect (Figure B.19). The selection of phases such as orpiment versus realgar also is a model uncertainty.

Overall, the geochemical speciation modeling in this study provides insights for important mechanisms, including both HFO adsorption and mineral precipitation, on controlling the releases of As and Se in response to redox and pH changes. Such mechanisms are applicable to a wide range of scenarios and materials. For example, the measured pH + *pe* of groundwater in the downgradient well ranged from 8.5 to 11.2 (10th percentile to 90th percentile), suggesting no obvious change of redox conditions from the porewater with pH + *pe* ranging from 8.8 to 11.3. However, the more acidic pH condition (~4.8) in groundwater compared to in porewater (pH ~8) can lead to attenuation of As by enhanced adsorption on HFO, resulting in low As concentrations (< 0.001 mg/L) in the downgradient groundwater.

3.5 Conclusions

This study of a closed impoundment combining different leaching characterizations, field subsurface gas and porewater measurements, and geochemical speciation modeling provided direct evidence for the complex mechanisms controlling the leaching of As and Se under field conditions. Key findings are as follows:

- The strongly reducing environment in the closed impoundment has been indicated from methanogenesis and sulfate reduction observed in subsurface gas, due to active microbial reduction of organic substances (e.g., organic debris in the ash deposit, residual unburnt carbon from coal, or organic matter from the processing water).
- Laboratory leaching extractions with more oxidized conditions than present in the field are not sufficient to understand leaching of redox sensitive constituents (As, Se, Sb, and V) under reducing field conditions.
- Redox heterogeneity in the field site caused spatial variations on the release of As. Both pH dependent adsorption and redox conditions (altering As speciation and decreasing HFO adsorption capacity by solubilization and recrystallization) need to be considered to explain the greater field porewater concentrations of As compared to laboratory test results. Released

As can be re-stabilized by precipitation as arsenic sulfides under strongly reducing conditions as indicated by geochemical speciation modeling.

- Selenium solubility under field conditions was much lower than under laboratory conditions, likely because of the transformation from soluble Se(IV) (oxidized laboratory conditions) to minerals of Se(0)/FeSe (reduced field conditions).
- The concentrations of B and Mo in porewater and extraction tests were not sensitive to redox states and mainly depended on L/S.

CHAPTER 4

LEACHING AND GEOCHEMICAL EVALUATION OF OXYANION PARTITIONING WITHIN AN ACTIVE COAL ASH MANAGEMENT UNIT[3]

4.1 Abstract

Field porewater and subsurface gas monitoring combined with laboratory leaching characterization and geochemical speciation modeling were used to identify important geochemical parameters and controlling mechanisms of the equilibrium leaching of oxyanions from coal ash in a disposal site. The site consisted of dry stacked ash on top of a former surface impoundment. Constituents leached from the dry stacked ash served as sources for the soluble fractions of constituents in underlying impoundment ash. Weathering of field ash was evidenced by the identification of calcite and ettringite. Porewater concentrations of As, B, and V in the field pH range (9-11) were primarily controlled by Ca-bearing precipitates (Ca-arsenate, B-substituted carbonate solid solution, Ca-vanadate, and V-substituted ettringite solid solution). Incorporation of Mo into ettringite decreases Mo solubility at pH >8, but the leachable fraction of Mo was primarily limited by the available content in the solid, with aqueous concentrations of Mo being a function of L/S. Leaching behavior of Cr and Se was sensitive to the redox changes during field ash collection and laboratory leaching tests, including oxidative dissolution of insoluble Cr(III)-oxides and conversion of Se(0) in the solid and dissolved Se(IV)/Se(VI).

4.2 Introduction

On average, 47% (by mass) of the coal ash (CA) produced in the U.S. over the decade from 2011 to 2020 was stored in disposal sites, including landfills and surface impoundments [1]. The mobility of oxyanions (As, B, Cr, Mo, Se, and V) from CA have been extensively assessed using batch leaching tests such as the toxicity characteristic leaching procedure (TCLP; EPA Method

[3] The results from this chapter have been incorported into a manuscript "Leaching and geochemical evaluation of oxyanion partitioning within an active coal ash management unit" and submitted to *Chemical Engineering Journal*. X. Wang, A.C. Garrabrants, H.A. van der Sloot, Z. Chen, K.G. Brown, B. Hensel, and D.S. Kosson.

1311) or the synthetic precipitation leaching procedure (SPLP; EPA Method 1312) [124–126]. More recently, a more comprehensive leaching characterization of CA has been conducted using EPA Method 1313 (pH-dependent leaching test) and EPA Method 1314 (percolation column) [36,115,127]. Leaching characterization in the laboratory is often used directly as the basis for prediction of the leachability of constituents in a field disposal facility. However, the accuracy of laboratory-based leaching tests to provide an estimate of leaching under a wide variety of diverse field conditions is not well documented [18].

Laboratory leaching tests cannot account for spatial and temporal variability in field conditions that often control constituent leaching and alter material parameters that may result in oxyanion speciation changes, especially for the redox-sensitive oxyanions Cr, As, and Se [5,22,128]. In a previous study focused on a closed impoundment of sluiced CA (Chapter 3), the field data suggested that the partitioning of As and Se between the deposited ash and impoundment porewater was strongly impacted by anoxic field conditions due to substantial microbial activity that were not present during standard laboratory leaching tests [45]. However, field conditions may differ drastically due to material composition (e.g., alkalinity, organic carbon content) impacted by site-specific configurations found in CA landfills and impoundments; therefore, there is a need to assess material leaching test results in the context of measured or anticipated site conditions to better predict the environmental performance of CA disposal facilities.

Another field parameter that is difficult to address directly through laboratory batch testing is the low liquid-to-solid ratio (L/S) often found in disposal facilities. For example, the L/S of a closed impoundment [45] was estimated to be approximately 0.7 L/kg-dry, whereas most regulatory leaching tests (e.g., TCLP, SPLP) are conducted at L/S values > 20 L/kg-dry. Leaching tests that specifically vary L/S ratio (e.g., EPA Methods 1314 and 1316) [129,130] evaluate the leaching at near equilibrium conditions at L/S values as low as 0.2 L/kg-dry; however, the results of these tests may also not be predicative of field performance. Even in the absence of redox differences between laboratory and field conditions, the chemistry of porewater at low L/S may be significantly different than high L/S due to (i) changes in ionic strength which can impact electrostatic interactions of adsorbing surfaces [131,132] and (ii) chemical saturation of mineral phases that would dissolve at higher L/S [133]. Thus, laboratory leaching characterization of CA intended for assessment of field release needs to consider the prevailing field porewater L/S and, to the extent possible, be verified with the field porewater data.

The gaps between field conditions and laboratory leaching may be minimized using geochemical speciation modeling to project standardized test data over field conditions. Past studies on the equilibrium leaching of constituents at CA disposal sites have focused on relating constituent concentrations in groundwater adjacent to the disposal facility to measured CA geochemical parameters including pH, alkalinity, and oxidation-reduction potential [23,24,73,134]. In several studies, geochemical speciation modeling was used to identify potential solubility-controlling mechanisms assuming a saturation state in pore solutions relative to constituents (e.g., Cu, Cr, etc.) [73,134]. However, these geochemical speciation modeling studies have not been able to achieve quantitative estimation of equilibrium leaching concentrations of constituents in field porewater. Overall, the integration of (i) material leaching characterizations; (ii) assessment of field conditions and porewater compositions; and (iii) quantitative multi-component geochemical speciation modeling to evaluate the field equilibrium leaching of multiple oxyanions (As, B, Cr, Mo, Se, and V) has been rarely reported.

In this study, a comprehensive large-scale field study was performed on a CA management unit comprised of dry-stacked CAs overlying a former sluiced ash impoundment. The interaction between unsaturated condition in the fresh, dry-stacked CA and saturated ash of the impoundment led to distinctly different site conditions and major chemical composition of CAs compared to the previously studied closed impoundment [45]. Leaching tests were conducted on CA samples collected during the establishment of porewater wells into the saturated impoundment. In addition, gas access points (GAPs) established throughout the unsaturated dry stack allowed for monitoring of subsurface gas composition over 8 months. The link between field conditions and laboratory testing results was demonstrated through geochemical speciation modeling of CA composition materials. The objectives of this study were (i) to identify important environmental parameters of the field porewater and mechanisms that control oxyanion concentrations in the unsaturated stacked CA and in the saturated impounded ash and (ii) to evaluate the relationships between laboratory leaching characterization and field subsurface observations.

4.3 Materials and methods

4.3.1 Field sampling

A field sampling and monitoring campaign was initiated in March 2019 on an active coal ash management unit (~45 ha). The profile of the disposal unit includes approximately 17 m of dry-stacked CA placed over a historical clay-lined CA impoundment that is approximately 14 m in depth (Figure 4.1a). A 0.5-m layer of bottom ash was used as a capillary break to separate the dry stack coal ash from the wet-handled ash in the impoundment.

The underlying CA impoundment was originally constructed in 1969 and then divided into a bottom ash sluicing/consolidation pond and other two sections, i.e., a dry fly ash stack and a separate gypsum disposal unit with both built above the historic impoundment. The dry fly ash stack started operation in 1996 to primarily receive fly ash from combustion of bituminous coal but also received smaller amounts of bottom ash, process wastewater, and (historically) air pollution control gypsum.

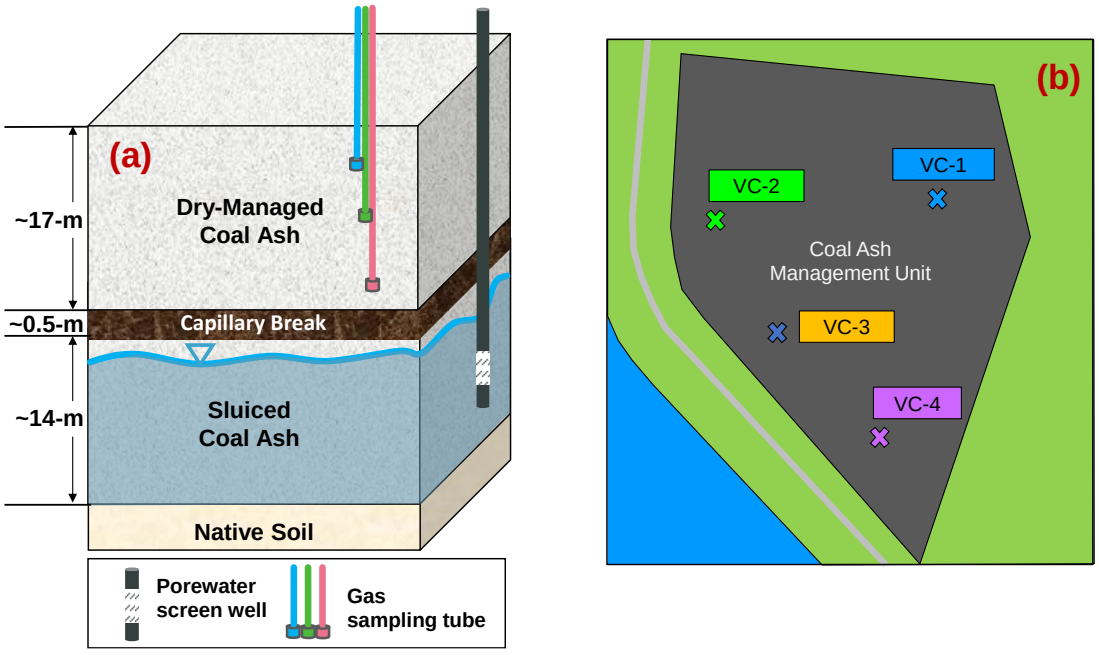

Figure 4.1 (a) Cross-section of the disposal unit and (b) layout of boreholes (VC-1, VC-2, VC-3, and VC-4)

4.3.1.1 Bulk ash sampling and compositing

Bulk ash materials were collected at discrete intervals from four boring locations (VC-1, VC-2, VC-3, VC-4) on the management unit (Figure 4.1b). Sample collection started at approximately 1.5-m below ground surface (BGS) and proceeded at 3-m intervals (1.5, 4.5, 7.5, and 13.5-m BGS) in the dry stacked CA. Samples were collected using a 7.6-cm diameter (Φ) × 60-cm long split spoon sampler. Once the borehole was advanced past the capillary break at approximately 17 m BGS (Figure 4.1a), split spoon sampling was used to retrieve 3 to 5 wet CA samples at 3-m intervals between 21 and 26 m BGS. As each split spoon was retrieved, the core was inspected by a licensed geologist prior to release to the sample collection team. Grab samples of the ash in each split spoon sample were collected for (i) determination of field moisture content (20 g) and (ii) field extractions (120 g) using a novel low L/S extractor (§4.3.2.1). The remainder of the material in the split spoon was vacuum-sealed into plastic bags and stored on ice for transport to the laboratory for testing where all samples were stored at < 6ºC prior to compositing for material characterization (§4.3.2.2, 4.3.2.3, and 4.3.3).

In the laboratory, composite samples for each borehole were generated by homogenizing equal portions (dry mass) of CAs from BGS levels near the porewater well screen. Material homogenization and compositing procedures were conducted in a nitrogen-purged environment as described in Appendix C.III. The four composites (VC-1, VC-2, VC-, and VC-4) served as representative CA samples associated with the pore solution collected at depth from each porewater well. In addition, a single global composite representing the dry-stacked CAs (referred to as “Dry”) was created using equal portions (dry mass) of homogenized ash collected above capillary break from all the four boreholes. All composites were stored at < 6°C prior to characterization.

4.3.1.2 Porewater and subsurface gas sampling

At the final depth of each borehole (21 to 26 m BGS), a 1.5-m porewater screen in a 5-cm Φ PVC tube was set into the saturated ash impoundment layer and the borehole was filled with expanding bentonite. During backfilling, gas access points (GAPs) were installed at discrete depths within the dry stack layer at 1.5 m and 4.5 m BGS in all boreholes and at additional 15 m

BGS in VC-1 and VC-3 (Figure 4.2). Each GAP consisted of a 6-mm stainless steel tube set in a 0.3-m bed of river rock. The GAP tubing was run to the surface outside of the PVC well and was capped with a valve for easy access for monitoring subsurface pore gas. Details of well installation and elevations are provided in Appendix C.I.

Monthly sampling of porewater and monitoring of subsurface gas composition began in June 2019, three months after completion of boring activities, and ended in January 2020. Porewater samples were collected using low-flow (70-200 mL/min) sampling techniques with in-line measurement of pH, dissolved oxygen (DO), electrical conductivity (EC), oxidation-reduction potential (ORP), and water temperature using a sonde and periodic turbidity measurements using a dedicated Hatch meter. Once the pH and turbidity stabilized, duplicate filtered (0.45 µm) porewater samples were collected in 125-mL HDPE bottles with one bottle for analysis of dissolved organic carbon (DOC) and dissolved inorganic carbon (DIC) and the other bottle acidified with HNO_3 (1% final concentration) for ICP-OES/ICP-MS analysis (eluate analysis details in Appendix C.IV). At each GAP, the concentration of the subsurface gases (i.e., O_2, CO_2, CH_4, NH_3, and H_2S) were measured using a Ventis® Pro 5 portable gas pump/meter following the sampling procedure described in a previous field study [45].

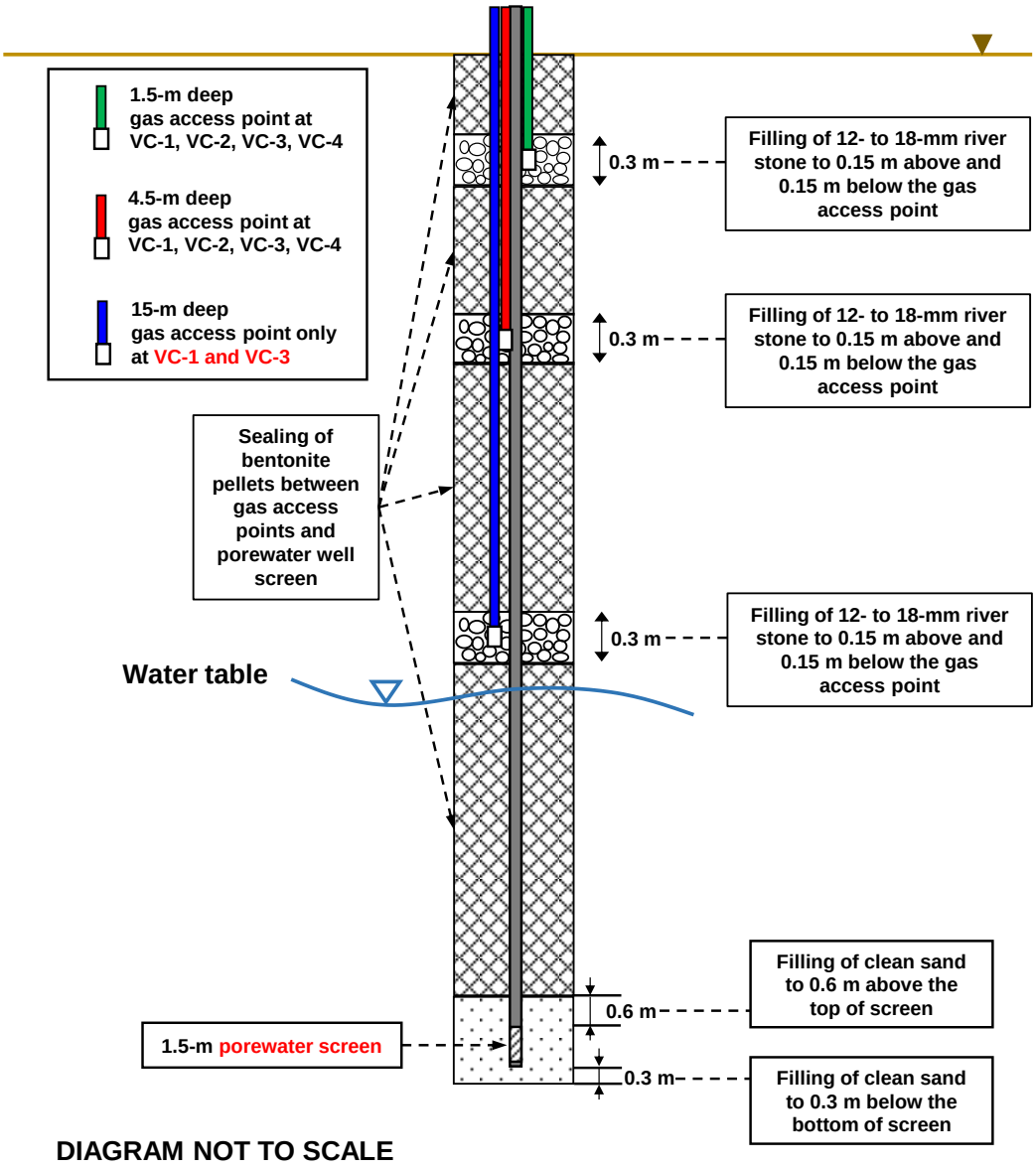

Figure 4.2 Schematic presentation of the porewater well screen and gas access points installation.

4.3.2 Leaching characterization

An initial low L/S extraction was conducted on grab samples from each split spoon retrieved from saturated CA during boring for groundwater wells. In addition, composite materials created from collected split spoon material (§4.3.1.1) were characterized using standard EPA methods. Details of the EPA method (Method 1313) are presented in a previous publication [45].

4.3.2.1 Low L/S field extractions

Representative split-spoon ash samples from the impoundment were selected for field extractions using a low L/S extractor designed specifically for this study (Figure C.2, Appendix C.II). The low L/S extractor aimed to efficiently express pore solution of CAs immediately after exposure to the atmosphere to preserve, to the extent possible, the original redox state of CA. Approximately 120 g of ash from a split spoon was packed into the extractor as soon after the split spoon was released to the sampling team. In parallel, a 20-g sample of ash was collected and stored for determination of moisture content, i.e., to determine the amount of porewater in the extractor sample. To preserve redox conditions, each extractor was immediately sealed with plastic caps and stored in a container purged with argon gas at the end of each sampling session. The sealed extractors were stored under argon at < 6°C for 24 to 48 hours to ensure equilibrium between solids and liquid. The equilibrated extractors were inserted into 250-mL centrifuge bottles under a nitrogen environment and centrifuged at 4,500 rpm for 5 minutes to separate pore solution from the CA solid. An aliquot of the eluate was used to measure pH, EC, and ORP under nitrogen while the remaining eluate was filtered (0.45-µm) for ICP-OES, IC, and carbon analysis (Appendix C.IV).

4.3.2.2 pH-dependent leaching test of ash composites at L/S of 10 and 1 L/kg-dry

The near-equilibrium leaching behavior of the five composite samples (VC-1, VC-2, VC-3, VC-4 and Dry) was determined as a function of pH following EPA Method 1313 [62]. For each composite, Method 1313 was conducted as specified, at an L/S of 10 L/kg-dry over the final pH range of $2 \leq pH \leq 13$ and also at an L/S of 1 L/kg-dry over a limited final pH range of $6 \leq pH \leq 13$. For both tests, an extraction was conducted without added acid or base, denoted the “natural pH” at L/S 10 L/kg-dry and the “own pH” at L/S 1 L/kg-dry. The lower L/S method allows for evaluation of equilibrium leaching of constituents at the L/S condition approximating porewater and serves as a verification case for development of a geochemical model describing the leaching of oxyanions from CA materials [115]. For eluates from both leaching tests, final extract pH, EC, and concentrations of cationic constituents, anions, DIC, and DOC were measured based on methods described in Appendix C.IV.

4.3.2.3 Percolation leaching of ash composites as a function of L/S

The five ash composites (VC-1, VC-2, VC-3, VC-4, and Dry) were characterized for leaching as a function of L/S using the EPA Method 1314 percolation column test [129], to facilitate identification of controlling mechanisms for oxyanion release as infiltration continues through the dry-stack CA. Approximately 400 g-dry (equivalent) of composite ash was moderately packed into a glass column of 5-cm Φ × 30-cm long. The column was initially saturated with deionized water (DIW) and equilibrated for 24 hours prior to the start of testing. During the percolation test, the DIW was pumped through the material at a flowrate 0.75±0.25 L/S per day in an up-flow direction to minimize channeling. Column eluates were collected at nine pre-determined cumulative L/S (ΣL/S) values of 0.2, 0.5, 1, 1.5, 2, 2.5, 4.5, 5, 9.5, and 10 L/kg-dry. The pH, EC, and concentrations of cationic constituents, anions, DIC, and DOC of each eluate was measured and plotted as a function of ΣL/S (Appendix C.IV).

4.3.3 Solid phase characterization

Subsamples of each composite (VC-1, VC-2, VC-3, VC-4, or Dry) were dried to constant mass in containers purged with a continuous flow of nitrogen. Dried samples were ground for (i) determination of total content of major constituents by X-ray fluorescence (XRF) and trace constituents by digestion following EPA Method 3052 [101]; (ii) measurement of total organic carbon (TOC) by EPA Method 9060 [100]; (iii) measurement of total inorganic carbon (TIC) by thermogravimetric analysis combined with mass spectrometry (TGA/MS) and also a carbon analyzer; (iv) characterization of crystalline structures by X-ray diffraction (XRD); and (v) quantitative analysis of amorphous iron (hydr)oxides and crystalline iron (hydr)oxides by ISO Method 12782-1 and 12782-2 [63,64]. Details of these characterization methods can be found in Appendix A.I.

4.3.4 Geochemical modeling

The LeachXS-ORCHESTRA modeling platform [58] was used to develop a representative virtual material for the field ash composites from the impoundment. A virtual material is

geochemical description of a material that provides simulated leaching test data consistent with pH-dependent and L/S-dependent testing and consists of (i) constituent available contents (Table C.3, Appendix C.VI); (ii) mineral assemblages approximating the geochemistry controlling the laboratory leachates and porewater within the material (Table C.4, Appendix C.VI); and (iii) parameters representing adsorption surface parameters (Table C.3) and adsorption reaction sets. The development of virtual materials was informed by the pH-dependent leaching test data at L/S 10 L/kg-dry and subsequently refined/verified by the pH-dependent leaching test results at L/S 1 L/kg-dry. The virtual material was then used to simulate the equilibrium leaching of constituents in porewater at corresponding field L/S and redox conditions (Table C.3). Because of obvious similarities in pH-dependent leaching behavior of the four field ash composites, the leaching data of two samples (VC-1 and VC-4) were merged to create a single "VC-1/VC-4" virtual material, representative for the field ash composites from the impoundment.

The aqueous speciation and mineral reactions were derived from the MINTEQA2_V4 database [56] at 20 °C and supplemented by data from literature [42] as well as the CEMDATA18 [84], THERMODDEM2011 [85], and ThermoChimie [87] databases. Previously calibrated mineral phases [115] also were included to describe the leaching data. The selection of solubility-controlling minerals and solid solutions that form the mineral assemblages was informed by minerals identified using XRD or reported in literature [31,42] along with previous modeling work on coal fly ashes [115]. The adsorption of oxyanions onto organic matter was calculated using the general adsorption reactions in the NICA-Donnan model [66,67], while adsorption of oxyanions onto iron (hydr)oxides was estimated using the diffuse double-layer model for hydrous ferric oxides (HFO) [52]. Details of the modeling approach and parameterization are presented in a previous study [115].

4.4 Results and discussion

4.4.1 Subsurface field geochemical conditions

The measured porewater pH from monthly sampling of the four porewater wells ranged from 9.8 to 11.1, indicating moderately alkaline porewater in the field disposal unit (Figure 4.3). The field pH generally agrees with the range of own pH (from modified Method 1313 test at L/S of 1 L/kg-dry) from 10.0 to 10.7 from CA composites (Table 4.1). The porewater *pe* (derived from ORP, Appendix C.IV) ranged from -0.2 to 3.6 with higher median *pe* at VC-4 (~2.5) and lower median *pe* at VC-2 (~1.1). The sum of pH and *pe* (pH+*pe*), which represents the overall redox condition in geochemical modeling, was between 10.3 and 14.0 suggesting suboxic field conditions in the saturated impoundment [18,21]. There was no correlation at any of the boreholes between porewater temperature and the redox component of pH+*pe* determined as *pe*/pH+*pe*. The lack of correlation infers no significant seasonal variations in subsurface redox conditions. However, an overall decrease in pH+*pe* values with sampling time was observed at VC-1, VC-3, and VC-4 (Figure C.3, Appendix C.VII), suggesting the gradual development of suboxic conditions in the subsurface following the establishment of the porewater well. No such relationships were observed at VC-2 likely as a result of well casing damage due to landfill activities in September 2019 and restoration of the well casing in November.

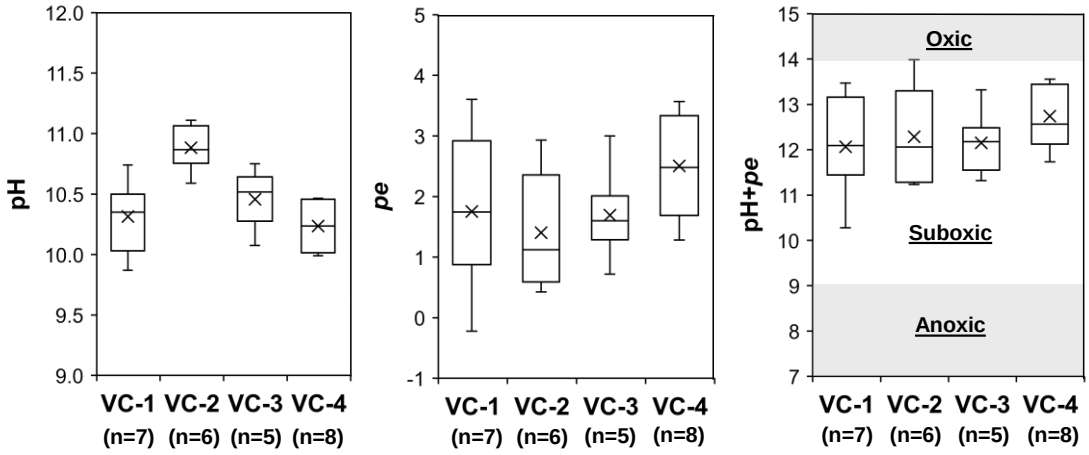

Figure 4.3 The ranges of pH, *pe*, and pH+*pe* in porewater from the field site.

Pore gas profiles consistently showed subsurface O_2 concentrations less the 21% (volume) O_2 content in air (Figure 4.4). Depletion of O_2 with depth in the subsurface was observed as a gradual decrease in each borehole. Beyond 8 months after establishing the well, subsurface O_2 concentrations stabilized at <1% (volume) in the GAPs at 15-m BGS at VC-1 and VC-3. These trends in O_2 monitoring data support the existence of suboxic conditions in the impoundment.

The field geochemical conditions (pH and redox state) and subsurface gas compositions observed at the field site were distinct from conditions previously characterized on a closed coal ash impoundment that had near neutral porewater pH (~8) and anoxic redox conditions [45]. In this study, significant gaseous CO_2 generally was not detected below 4.5-m BGS, compared to the CO_2 concentrations up to > 5 vol.% (calibration limit) in the other closed impoundment. In addition, CH_4 only was detected at VC-1 at low concentrations (< 1 vol.%) likely because of localized decay of organic matter, while much greater CH_4 concentrations (> 5 vol.%) and the detection of H_2S in the closed impoundment suggested methanogenesis and sulfate reduction. The development of a suboxic environment in this study rather than an anoxic environment is potentially due to the moderately alkaline pH environment (pH >10) that is not favorable for microbial activities but favorable for chemical reduction processes [21].

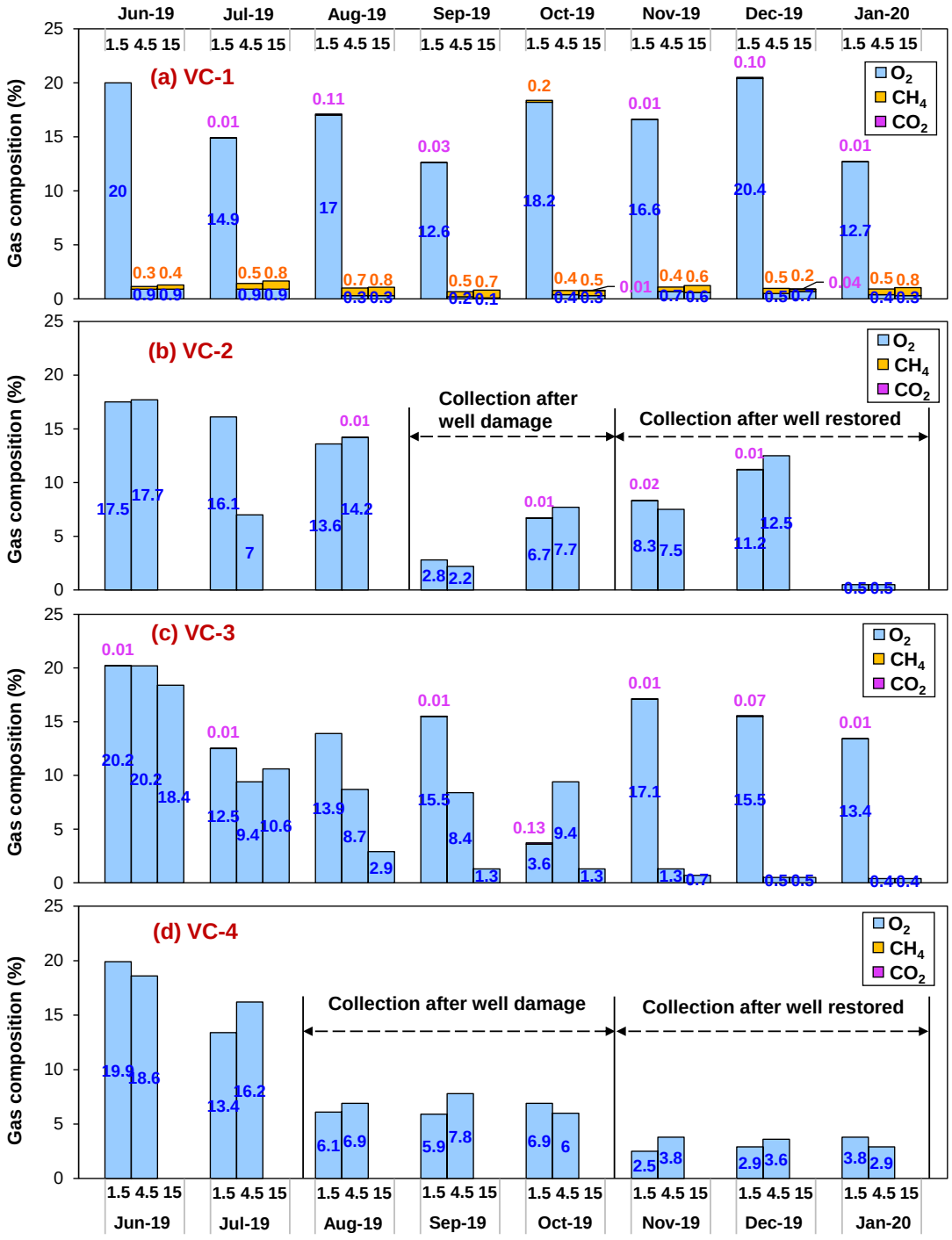

Figure 4.4 Temporal variations of subsurface gas compositions (O_2, CH_4, and CO_2) at VC-1, VC-2, VC-3, and VC-4. Three gas profiles from 1.5-, 4.5-, and 15-m deep below ground surface were taken at (a) VC-1 and (c) VC-3, while two gas profiles from 1.5- and 4.5-m deep below the ground were taken at (b) VC-2 and (d) VC-4. Sampling wells at VC-2 and VC-4 were damaged due to operations on the landfill from September 2019 and August 2019, respectively, but restored in November 2019.

4.4.2 Comparisons of leaching results for coal ash composites

Calcium and Sulfur. Field ashes from the site have moderate total content of Ca ranging between 4.1-6.4% (by mass; from the lowest to highest value in Table 4.1), in comparison to the range of 0.6-12.1% (10th-90th percentile) for 30 coal fly ashes showing a wide range of solid compositions [11,115]. The available contents of Ca and S for the dry-stacked CA composite (Dry) are higher than in the four saturated CA composites (VC-1/2/3/4). The higher leachable concentrations of major constituents may also impact the leaching of oxyanions. In the pH dependent leaching test, the Dry composite showed greater concentrations of Ca and S at alkaline pH (pH >8) than in VC-1/2/3/4, consistent with the greater Ca and S concentrations in the initial eluates (up to L/S ~5 L/kg-dry) from the Dry composite in the column test (Figure 4.5a-b). In all five composites, the XRD analysis identified the weathered mineral product, calcite [$CaCO_3$], which is a potential controlling phase for Ca solubility at pH > 8 [25,27,31] (Figure 4.6). Therefore, lower DIC concentrations at pH > 8 may indicate less aging and result in a higher solubility of Ca in the Dry composite than in other composites, especially near the natural pH condition (Figure C.5, Appendix C.IX). Also, gypsum [$CaSO_4 \cdot H_2O$] was identified in the Dry composite (Figure 4.6), which contributes to the overall greater total and available contents of Ca and S in the Dry composite (Table 4.1 and Table C.6, Appendix C.VIII).

Table 4.1 Natural and own pH and major chemical composition of the field ash composites

	VC-1 Composite	VC-2 Composite	VC-3 Composite	VC-4 Composite	VC Average (±S.D.) [c]	Dry composite
Natural pH [a]	10.4	10.3	10.7	10.4	10.5(±0.2)	10.2
Own pH [a]	10.7	10.6	10.7	10.3	10.6(±0.2)	10.0
Si (wt.%)	20.6	22.0	20.2	20.3	20.8(±0.8)	19.6
Al (wt.%)	7.99	7.91	7.49	8.05	7.86(±0.25)	7.74
Ca (wt.%)	4.73	4.18	6.42	4.08	4.85(±1.08)	5.53
Fe (wt.%)	17.4	15.3	16.1	18.4	16.8(±1.36)	17.6
Mg (wt.%)	0.58	0.70	0.72	0.60	0.65(±0.07)	0.64
S (wt.%)	0.30	0.23	0.49	0.22	0.31(±0.13)	0.85
Na (wt.%)	0.89	1.02	1.00	1.16	1.02(±0.11)	0.91
K (wt.%)	2.55	3.29	2.98	2.37	2.80(±0.42)	2.34
P (wt.%)	0.44	0.48	0.47	0.47	0.47(±0.02)	0.42
TOC (wt.%C)	1.87	1.77	1.66	1.78	1.77(±0.08)	2.00
TIC-C (wt.%C) [b]	0.097	0.094	0.101	0.108	0.100(±0.006)	0.094
TGA-C (wt.%C) [b]	1.31	1.11	1.35	1.38	1.29(±0.12)	1.43

[a] Natural pH and own pH are defined as the pH responses to deionized water extractions for 24 hours at liquid-to-solid ratios of 10 L/kg-dry and 1 L/kg-dry, respectively.

[b] TIC-C refers to the total inorganic carbon (TIC) measured by the carbon analyzer, while TGA-C is the TIC measured by TGA/MS. The TGA/MS results are shown in Figure C.4, Appendix C.VIII.

[c] VC Average is the mean value of the results of VC-1, V-2, VC-3, and VC-4 composites. Sample standard deviation is indicated in parenthesis.

Boron. Of all the oxyanions, B, Mo, and V were in relatively greater concentrations at the natural pH of CA composites than As, Cr, and Se. Compared to the Dry composite, the composites from the saturated CA impoundment did not show significant depletion in oxyanion total or available contents (Table C.5 and Table C.6, Appendix C.VIII). This result is in contrast to the previous study [45] where sluiced ash in the impoundment exhibited significant oxyanion depletion compared to “as-generated” ash. Boron leaching showed similar leaching behavior as a function of pH in the Dry composite and four VC composites, which was attributed to (i) the movement of soluble B from the upper dry stack ash into the impoundment, probably as a result of natural infiltration and deposition of process water and (ii) the subsequent transformation of infiltrating B into less soluble B-bearing minerals (e.g., co-precipitation or substitution into carbonates) in the older, weathered impoundment ash [135,136]. The percolation column results

(Figure 4.5d) show higher B concentrations at low L/S and a longer wash-off interval of B in the Dry composite ($\Sigma L/S \leq 10$ L/kg-dry) than in the VC composites ($\Sigma L/S \leq 2$ L/kg-dry). The pH-dependence of the batch leaching results of B in the VC composites and the relatively steady column concentrations of B at $\Sigma L/S > 2$ L/kg-dry (Figure 4.5d) point to eluates limited by chemical saturation of B associated with mineral solubility [19], sometimes referred to as "solubility-controlled leaching" [19,137].

Molybdenum. Mo is typically a soluble constituent in CAs over the alkaline pH range [4]; however, Mo concentrations in Method 1313 results indicate a decrease in Mo concentration at pH > 8 in all CA composites except VC-2 (Figure 4.5e). This decrease may be a result of incorporation of Mo into ettringite [$Ca_6Al_2(SO_4)_3(OH)_{12}\bullet 25H_2O$], which was identified by XRD in all field ashes (Figure 4.6). The association of Mo with ettringite is supported by literature [70,115,138]. In VC-2, XRD exhibited a weaker ettringite XRD signal than for other composites (Figure 4.6), thus it is likely that Mo may not have co-precipitated with ettringite to the same degree, resulting in higher Mo eluate concentrations than in other composites. The results of batch testing were consistent with results of column leaching, as VC-2 showed the highest Mo concentrations at $\Sigma L/S < 6$ L/kg-dry and the fastest wash-off of Mo at $\Sigma L/S > 6$ L/kg-dry than other composites. In contrast, column concentrations of Mo in all other composites appeared to be controlled by an initial rapid flush of a soluble fraction at $\Sigma L/S < 2$ L/kg-dry and then accompanied by relatively steady concentrations in the order of VC-4 > VC-1 > Dry > VC-3, consistent with the Mo concentrations at natural pH from Method 1313.

Arsenic, Selenium, and Vanadium. At natural pH of the five composites, the logarithmic Se concentrations [$\log(C_{Se})$] were inversely proportional to the summed logarithmic concentrations of Ca and OH^- [$\log(C_{Ca}) + \log(C_{OH^-}) = \log(C_{Ca} x C_{OH^-})$] (Figure C.6, Appendix C.IX), implying the potential for a $Ca_x(OH)_x(Se)_z$ phase to control the equilibrium leaching of Se. The identification of controlling phases will be refined through geochemical speciation modeling in §4.4.3. The Method 1313 data also show that concentrations of As (Figure 4.5c) and V (Figure C.5, Appendix C.IX) were relatively consistent at natural pH in all composites. The potential controlling mechanisms for As and V will be discussed through geochemical speciation modeling in §4.4.3.

In summary, when taken in context of the site configuration of dry stack of CA on top of a historical impoundment, leaching data indicated the downward movement of constituents leached from the fresh, dry stack CA into the underlying saturated materials. The leached fraction of constituents can be retained in the saturated CA through mineralization reactions (e.g., carbonation). However, differences in major constituent (i.e., Ca, S, and DIC) chemistry and speciation of oxyanions (e.g., B) between unsaturated and saturated CAs can lead to differences in long-term leaching behavior of constituents. These differences are supported by the percolation column test results that can be related to long-term leaching if the rate of infiltration (L/S of infiltration per time) can be estimated [2]. For example, assuming a 30-m depth under a post-closure scenario with a 0.3-m vegetated soil cover, the ΣL/S of 10 L/kg-dry at the end of the percolation column test equates to approximately 2,000 years based on an estimated infiltration rate of 250 mm/y during humid season [139].

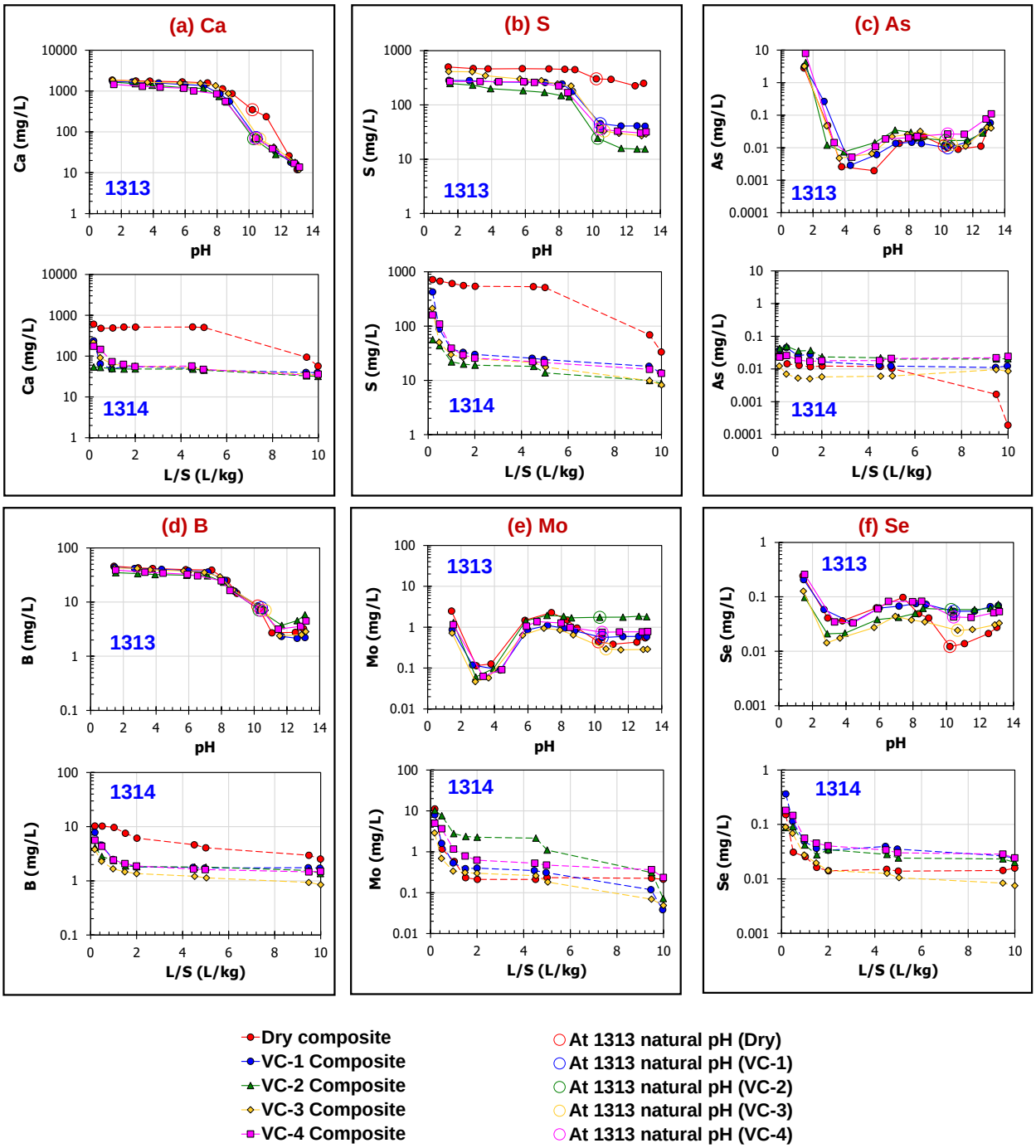

Figure 4.5 Comparison of pH-dependent (EPA Method 1313) and L/S-dependent (EPA Method 1314) leaching of (a) Ca, (b) S, (c) As, (d) B, (e) Mo, and (f) Se from the field ash composites.

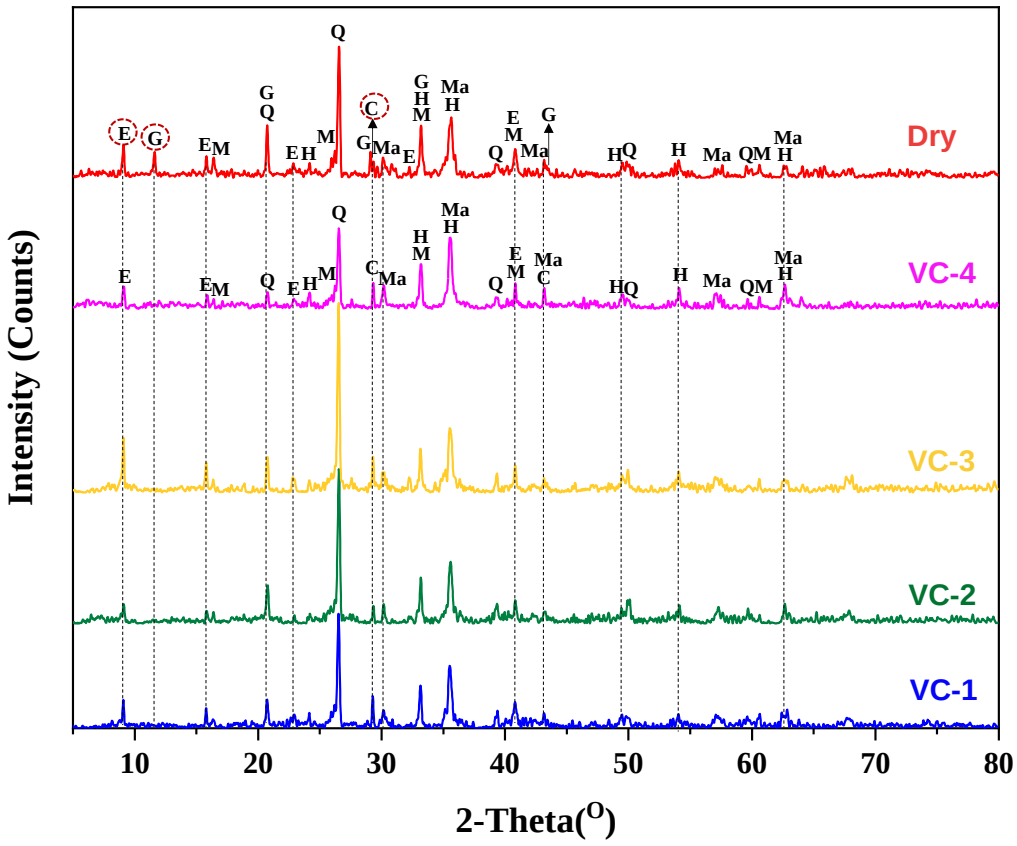

Figure 4.6 XRD patterns of the field ash composites. C= Calcite [$CaCO_3$]; E= Ettringite [$Ca_6Al_2(SO_4)_3(OH)_{12}•25H_2O$]; G= Gypsum [$CaSO_4•H_2O$]; H= Hematite [$Fe_2O_3$]; M= Mullite [$Al_6Si_2O_{13}$]; Ma= Magnetite [$Fe_3O_4$]; Q= Quartz [$SiO_2$)].

4.4.3 Controlling mechanisms of leaching identified by testing and geochemical speciation modeling

Effects of important geochemical parameters (pH, L/S, and redox potential) to control the partitioning of As, B, Cr, Se, Mo, and V under field conditions were demonstrated by comparing porewater well concentrations to the results of (i) low L/S field extractions of saturated CA and (ii) laboratory pH-dependent leaching on saturated ash composites (Figure 4.7). In addition, geochemical speciation modeling was used to simulate porewater concentrations and laboratory batch leaching of representative field ash composites (VC-1/VC-4) at L/S 1 and 10 L/kg-dry, to provide insights regarding controlling mechanisms for the leaching behavior of oxyanions. The evaluation of modeling results was focused on the alkaline pH range, especially for 9≤pH≤11,

i.e., the pH range around the ash natural pH and porewater pH conditions. Modeling results for oxyanions (i.e., As, B, Cr, Mo, Se, and V) are provided in Figure 4.8 and Figure 4.9, while results for major constituents (i.e., Al, Ca, Fe, Na, S, and Si) are in Figure C.10 (Appendix C.XI).

4.4.3.1 Solubility-controlled leaching behavior: arsenic, boron, and vanadium

Porewater concentrations of As, B, and V were well approximated by field extractions and laboratory batch leaching at low L/S of 1 L/kg-dry (Figure 4.7(a, b, f)). Also, eluate concentrations of As, B, and V are strong functions of both pH and L/S at pH >9 based on results of batch leaching at L/S of 1 and 10 L/kg-dry. Such comparisons suggested that the field equilibrium leaching of As, B, and V was controlled by mineral solubilities (e.g., Ca-coprecipitations) [9,10,115] with negligible influence from the field suboxic environment; therefore, both field extractions and laboratory batch leaching at low L/S can reasonably reflect the porewater concentrations at an estimated L/S of ~0.6 L/kg-dry. Similarly, major constituents including Al, Ca, Si, and Fe showed solubility-controlled leaching as porewater concentrations aligned well with field extraction results and the pH-concentration curves in batch leaching at L/S of 1 L/kg-dry (Figure C.7, Appendix C.X).

Arsenic. As suggested by geochemical speciation modeling, solubility of As at $9 \leq pH \leq 11$ was described primarily by the precipitation/dissolution of Ca-arsenates [$Ca_5(OH)(AsO_4)_3$] [42] with minor contributions from adsorption/desorption onto HFO (Figure 4.8). Decreasing the simulation L/S to 1 L/kg-dry resulted in increased concentrations of As at pH >10, due to the effects of increased ionic strength (Figure C.9, Appendix C.XI), which impacted the thermodynamic activities of major constituents and the oxyanions. The response of simulations at L/S 10 and 1 L/kg-dry were in good agreement with the leaching data that showed an increase in As concentrations at pH >9 for L/S 1 L/kg-dry over that at L/S 10 L/kg-dry (Figure 4.7a and Figure 4.8). However, further decrease of L/S toward L/S 0.6 L/kg-dry, the estimated porewater L/S condition based on moisture content, had negligible impact on As concentrations. This L/S analysis supports the use of batch leaching at L/S of 1 L/kg-dry as a practice laboratory extraction that can serve as an estimate of porewater concentrations. Furthermore, a difference in the pH+*pe* parameter between simulations (pH+*pe*=12.9) and laboratory batch leaching (pH+*pe*=17.9) was not sufficient to induce a speciation change in As from the dominant As(V).

Boron. Screening of minerals from thermodynamic databases (published mineral phases) cannot describe the experimentally determined concentrations of B; however, the equilibrium leaching of B in porewater and in laboratory batch leaching as functions of pH and L/S conditions were well represented by a proposed experimental B-substituted carbonate solid solution (Figure 4.8 and Table C.4, Appendix C.VI) based on the detection of $CaCO_3$ in all the field materials (Figure 4.6) and the reported substitution of B oxyanions into carbonates [135]. According to the mechanism reported by Hemming and Hanson [135], the CO_3^{2-} site in calcite can be substituted by the HBO_3^{2-} ion in a 1:1 stoichiometry. In addition to B, the simultaneous incorporation of multiple constituents into a carbonate solid solution was indicated by the decrease in eluate concentrations of alkaline earth metals (i.e., Ba and Sr) at pH > 8, which has been reported to be caused by the formation of a (Ca, Ba, Sr)-CO_3 solid solution instead of pure $BaCO_3$ or $SrCO_3$ in weathered solid waste [140]. Thus, a carbonate solid solution was included in the simulation, with end member reactions for the formation of calcite ($CaCO_3$), magnesite ($MgCO_3$), strontianite ($SrCO_3$), witherite ($BaCO_3$), and $Ca(HBO_3)$ (Table C.4). Reaction constants for the Ca/Mg/Sr/Ba-carbonates are from the MINTEQ2_V4 database, while the reaction constant for $Ca(HBO_3)$ was calibrated due to the lack of a reported value. Including the ideal carbonate solid solution reasonably described the concentration variations of B, Ba, and Sr (results of Ba and Sr are in Figure C.11, Appendix C.XI) in response to changes in pH (pH < 11) and L/S.

Vanadium. Similar to As, the combination of mineral precipitation/dissolution and adsorption/desorption to HFO sufficiently describes the leaching behavior of V (Figure 4.8). Specifically, in the range between pH 8 and 10, the mineral phase calcium vanadate [$Ca_2V_2O_7$] controls solubility of V. The V-substituted ettringite, a solid solution developed over a broad range of cementitious waste materials [88] and verified for fly ash by modeling [115], dominates V leaching at pH > 10. In addition, adsorption to HFO also was indicated to contribute to the retention of V within the focused pH range ($9 \leq pH \leq 11$).

4.4.3.2 Available content-limited leaching behavior: molybdenum

Concentrations of Mo were significantly impacted by L/S, as lower L/S values in porewater (L/S ~0.6 L/kg-dry) and in field extractions (L/S ~0.3-0.6 L/kg-dry) contributed to greater eluate concentrations than in batch leaching at L/S of 1 and 10 L/kg-dry around the natural pH range

(9-11) (Figure 4.7d); however, similar total released mass (mg/kg) was obtained from porewater, field extractions, and the batch leaching at different L/S (Figure C.8, Appendix C.X). The results suggest that the total released mass of Mo is primarily limited by the available content in the solid (i.e., "available content-limited" equilibrium leaching behavior), while eluate concentrations (mg/L) are influenced by the specific L/S condition. Such available content-limited leaching behavior is typical for highly soluble constituents [19] such as Mo and K and consistent with results observed for a previously characterized coal ash impoundment [45].

Despite the overall high solubility of Mo at pH >8, the slight decrease of Mo concentrations at pH >8 and L/S 10 L/kg-dry for material VC-1/3/4 was not captured by any mineral phases from available thermodynamic databases or HFO adsorption that dominates at pH < 7 (Figure 4.8). However, concentrated Mo in porewater and in laboratory batch leaching at L/S of 1 L/kg-dry led to the predicted precipitation of Mo-substituted ettringite using a previously reported ettringite solid solution (Table C.4) [88,115], indicating that the formation of Mo-substituted ettringite in weathered field ash is possible. The substitution of Mo in ettringite was not significant for the L/S of 10 L/kg-dry simulation and, therefore, slightly overestimated the measured concentrations. This discrepancy may result from uncertainties of end member reaction sets, which were calibrated from other waste materials and have not been extensively verified on field coal ash because of limited experimental data. Since Mo is typically highly soluble in as-generated ash collected directly from electrostatic precipitators [4], the incorporation of Mo in ettringite as secondary mineral formation would be important for the retention of Mo during field disposal, noting that the material VC-2 without such incorporation (into ettringite) showed much greater Mo concentrations in porewater (~30 mg/L) than concentrations from VC-1/3/4 (5-10 mg/L) (Figure 4.8).

4.4.3.3 Redox-sensitive leaching behavior: chromium and selenium

The field leaching of Cr and Se, two redox-sensitive constituents [5,22,26,141], are likely controlled by the field suboxic conditions as suggested by (i) insoluble Cr in porewater ($< 5.3 \times 10^{-5}$ mg/L) but much greater concentrations (0.001-0.1 mg/L) in field and in laboratory batch extractions with more oxidized conditions, consistent with the reported higher mobility of Cr in Cr(VI) than reduced Cr(III) [26,142]; (ii) relatively large variations of porewater Se

concentrations ranging from 0.03 to 0.24 mg/L and greater Se concentrations observed at VC-4 with overall higher *pe*/pH+*pe* values than other boreholes; and (iii) elevated Se concentrations in field extractions (oxic conditions with pH+*pe* of 14.8-15.8) compared to in porewater (suboxic conditions with pH+*pe* of 10.3-14.0), in agreement with the reported increase in Se solubility under a more oxidized environment (Figure 4.7(c, e)) [5,22]. Previous studies on an anoxic coal ash impoundment revealed that the leaching of As and Se both were sensitive to redox variations [45], but this study identified such effects only with respect to Se rather than As because the suboxic conditions discussed here were not sufficiently reducing to affect As speciation and leaching [21].

Chromium. Cr leaching was sensitive to the pH+*pe* value used in simulations, resulting from the dissolution/precipitation of a Cr(III) oxide mineral (Cr_2O_3, eskolaite), which was likely a predominant Cr phase in field fly ashes [93] (Figure 4.9a). For the oxic laboratory condition with pH+*pe* of 17.9, Cr_2O_3 was suggested to precipitate at pH < 8 while a postulated Ca-bearing Cr(VI) mineral [$Ca_3(OH)_2(CrO_4)_2$] derived from previous simulations on fly ashes [115] was used to capture the decreased Cr solubilities with pH at pH > 8. For the suboxic porewater environment at alkaline natural pH range (9-11), a pH+*pe* value of 12.9 led to the transformation of Cr(VI) to Cr(III) and the subsequent precipitation into Cr_2O_3 (eskolaite), resulting in lower solubilities of Cr (< 0.00005 mg/L) in porewater than Cr concentrations at laboratory batch leaching (0.001-0.1 mg/L).

According to a sensitivity study of eluate Cr concentrations with *pe* changes, Cr_2O_3 dissolved rapidly as *pe* increased from ~4 to ~5, consistent with the significantly greater Cr concentrations in field extractions (*pe* ~5) and laboratory batch leaching (*pe* > 6) compared to in porewater (*pe* < 4) (Figure 4.9b). The sensitivity study suggested that the Cr leaching was impacted by rapid oxidation of insoluble Cr(III)-bearing oxides to more soluble Cr(VI) during field sampling and laboratory handling.

Selenium. Se leaching in response to variations of redox conditions between the field and laboratory environment appeared to involve Se species in several valence states including Se(0), Se(IV), and Se(VI). Selection of calcium selenate [$Ca_3(OH)_2(SeO_4)_2$] as a Se-controlling phase, as reported in literature [115] generally captured the laboratory batch leaching 9≤pH≤11 (Figure 4.9a). This controlling phase is consistent with the suggestion in §4.4.2 that Se concentrations

may be associated with $Ca_x(OH)_x(Se)_z$.

However, geochemical modeling at a lower porewater pH+*pe* (12.9) compared to laboratory pH+*pe* (17.9) predicted the reduction of Se(VI) to selenite [Se(IV)], which failed to describe Se concentrations in the porewater. In the model, a calcium selenite phase [$Ca_3(OH)_2(SeO_3)_2$] from a previous modeling study on as-generated fly ashes was used [115]. Using this calcium selenite phase overestimated porewater Se concentrations. A missing selenite phase from reported thermodynamic databases is suggested to adequately describe the porewater Se concentrations.

Alternatively, the lower Se solubility measured in porewater relative to simulated concentrations may be caused by further reduction of Se to insoluble Se(0), which was not reflected in our simulations based on a redox equilibrium assumption. The sensitivity of Se concentrations with *pe* by geochemical modeling indicates two critical transitions for Se speciation: (i) the gradual oxidation of insoluble Se(0) to more soluble Se(IV) with increasing *pe* through *pe* -1.5 (corresponding to a pH+*pe* of 8.9) and (ii) Se(IV) oxidization to Se(VI) between *pe* ~3.1 (pH+*pe* of 13.5) and *pe* ~4.1 (pH+*pe* of 14.5), accompanied by a decrease in Se concentrations. The calculated porewater pH+*pe* between ~10.9 and ~13.7 indicates Se(IV) as the dominate state by equilibration calculations. However, the co-existence of insoluble Se(0) with Se(IV), as reported in literature [93,94], implies that redox disequilibrium is possible and could potentially explain the overestimation of simulated porewater Se concentrations. Previous field studies also suggested the formation of Se(0) in field ash as an important control for Se leaching [45], albeit at significantly more reducing conditions.

Therefore, the oxidation of ash during field sampling may result in oxidative dissolution of Se(0) in field ashes, leading to increased solubilities of Se in field extractions compared to porewater concentrations observed at all borehole locations (Figure 4.7e and Figure 4.9b). The subsequent precipitation of oxidized Se into a Ca-Se(VI) phase under laboratory batch leaching may decrease the leaching of Se, reflected by the lower Se concentrations in laboratory leachates compared to in field extractions at some boreholes (i.e., VC-3 and VC-4).

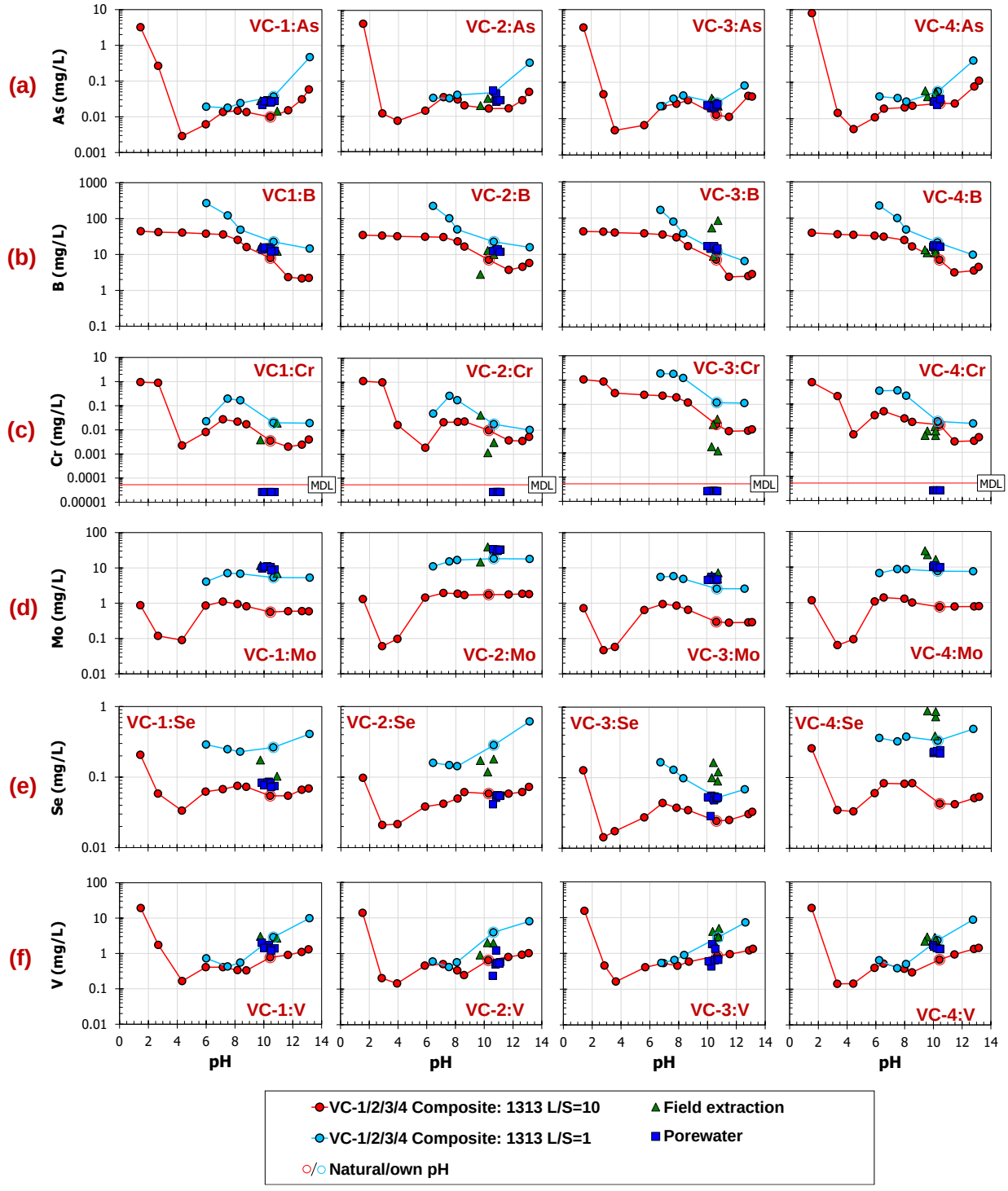

Figure 4.7 Concentrations of As, B, Cr, Mo, Se, and V in porewater and in field extractions compared to laboratory pH-dependent leaching at L/S of 1 and 10 L/kg-dry for the field ash composites. Concentrations less than the method detection limit (MDL) are plotted as one half of the MDL.

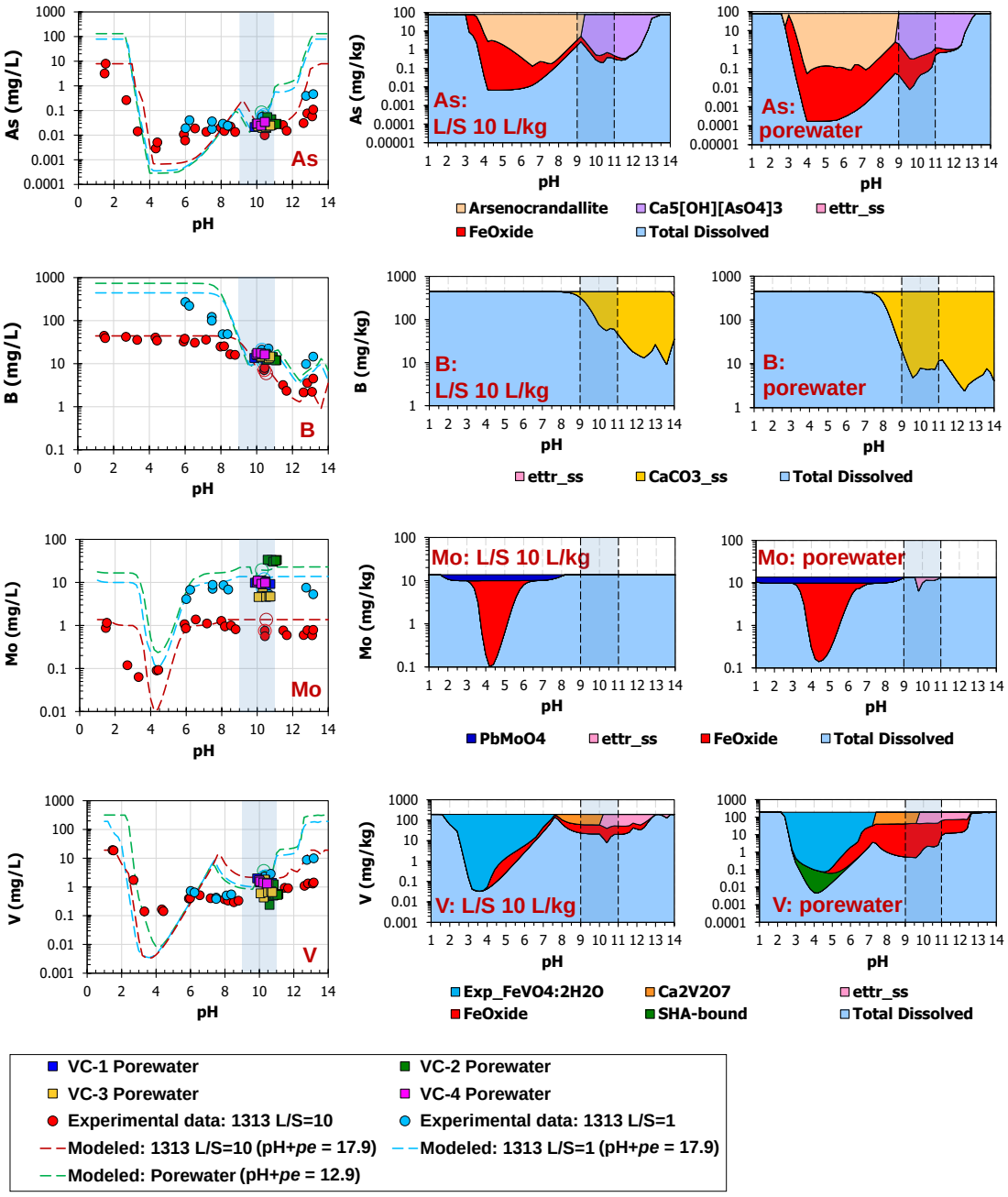

Figure 4.8 Geochemical speciation modeling of As, B, Mo, and V under laboratory pH-dependent leaching at L/S of 1 and 10 L/kg-dry and under field porewater conditions at estimated L/S of 0.6 L/kg-dry. Phase diagrams are shown for laboratory leaching at L/S=10 L/kg-dry (EPA 1313) and porewater conditions. Arsenocrandallite: $CaAl_3(AsO_4)(AsO_3OH)(OH)_6$; FeOxide: adsorbed onto hydrous ferric oxide; CaCO3_ss: carbonate solid solution; ettr_ss: ettringite solid solution; Exp_FeVO4:2H2O: postulated mineral phase $FeVO_4 \cdot 2H_2O$; SHA-bound: solid humic acid bound; Total dissolved: in dissolved phase, free ions. A specific pH range around the natural pH condition of field ash is highlighted.

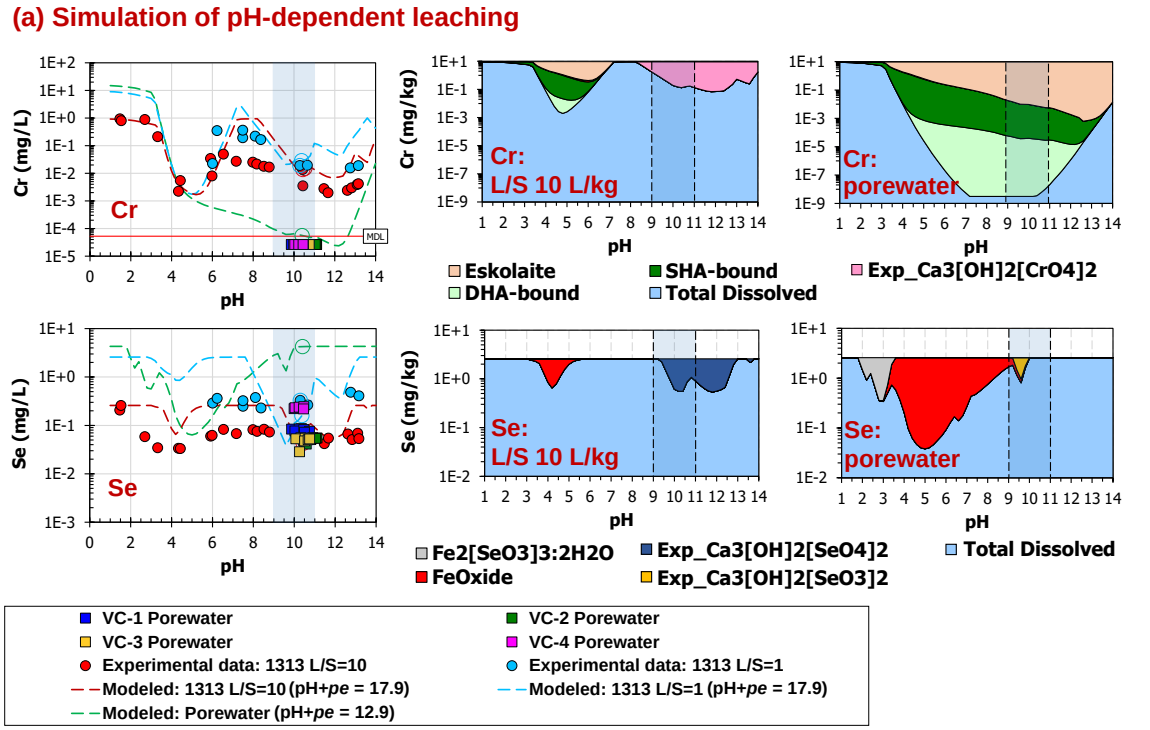

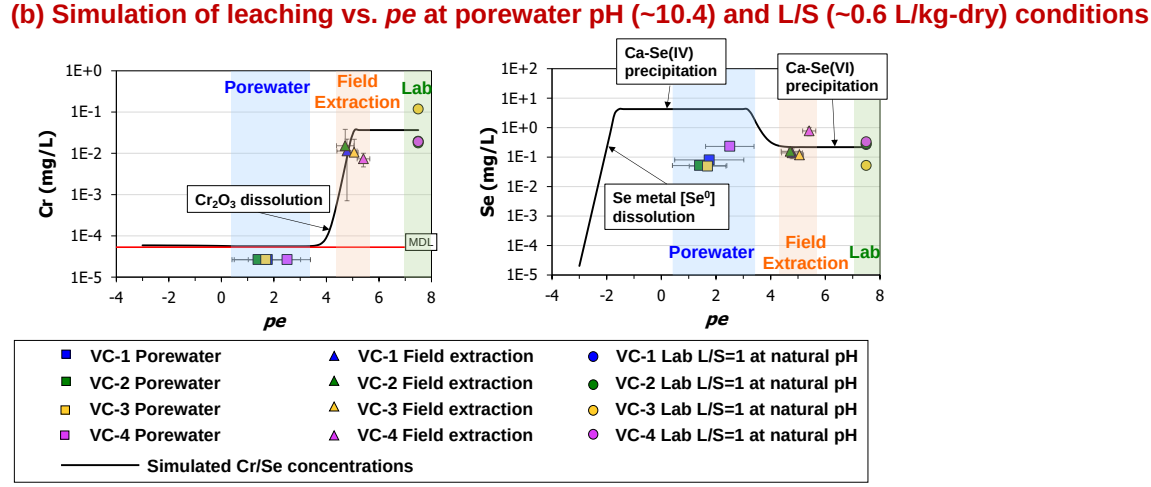

Figure 4.9 (a) Geochemical speciation modeling of Cr and Se under laboratory pH-dependent leaching at L/S of 1 and 10 L/kg-dry and under field porewater conditions at estimated L/S of 0.6 L/kg-dry and (b) simulated leaching as a function of *pe* at natural pH (pH=10.4) and L/S=0.6 L/kg-dry. Chromium concentrations below than method detection limit (MDL) are indicated as half of the MDL. Phase diagrams in (a) are shown for laboratory leaching at L/S=10 L/kg-dry (EPA 1313) and porewater conditions. Eskolaite: Cr_2O_3 mineral; Mineral phases with prefix of "Exp_" are postulated, experimental phases; SHA-bound: solid humic acid bound; DHA-bound: dissolved humic acid bound; Total dissolved: in dissolved phase, free ions; FeOxide: adsorbed onto hydrous ferric oxide. A specific pH range around the natural pH condition of field ash is highlighted in (a).

4.5 Conclusions

In conclusion, field characterization results in this study in conjunction with another study on a closed coal ash impoundment [45] (Chapter 3) serve as two reference cases to provide insights into controlling mechanisms of leaching in coal ash disposal sites. The primary controls of field leachate compositions were suggested as the major constituent composition, field geochemical parameters (pH, L/S, redox potential), and other critical factors (site configuration and weathering effects).

Results from the long-term field monitoring of porewater and subsurface gas compositions suggest that the field environment in this site is moderately alkaline and suboxic. In contrast to the near neutral pH and anoxic environment accompanied by methanogenesis and sulfate reduction in the closed impoundment, the strongly alkaline pH condition observed in this study does not support significant microbial reduction activity and, therefore, has a less reducing environment.

Mechanisms controlling the field leaching of oxyanions are significantly different between the two field disposal sites. In this study, geochemical speciation modeling indicated that the solubilities of As, B, and V in porewater (pH~10) were primarily controlled by a Ca-arsenate phase [$Ca_5(OH)(AsO_4)_3$], a proposed B-substituted carbonate solid solution, and a V-substituted ettringite solid solution, respectively. Porewater concentrations of Mo were primarily limited by its available content in the solid with minor contributions from the substitution in ettringite at pH > 8; the porewater concentrations of Cr and Se were controlled by solubilities of Cr(III)-oxides and Se(IV)/Se(0) phases. In the closed impoundment (Chapter 3), HFO adsorption/desorption and sulfide mineral precipitation were indicated to be important for the sluiced ash containing less calcium, low alkalinity, and having near neutral pH conditions.

Leaching tests used to understand field leaching should be evaluated in context with site-specific conditions for each oxyanion of interest. In this study, the leaching of As, B, V, and Mo was not subject to change from the suboxic field condition to the oxic laboratory condition, therefore, laboratory leaching tests at low L/S (modified EPA Method 1313) can be used to approximate the field porewater concentrations of As, B, V, and Mo. However, sample oxidation that occurred in the laboratory leaching test led to different leaching behavior of Cr and Se compared to field porewater. For the closed impoundment studied earlier, the strongly anoxic field

environment was oxidized to a suboxic environment during laboratory leaching tests, which resulted in changes of As and Se speciation and, therefore, under- and over-estimated As and Se concentrations compared to porewater measurements, respectively.

CHAPTER 5

LONG-TERM ASSESSMENT OF LEACHING FROM COAL ASHES

5.1 Introduction

The long-term assessment of the release of coal ash constituents under field disposal scenarios is fundamental for decision making and proper site management with respect to protecting human health and environment from coal ash disposal sites. Compared to the assessment of constituent release at near-equilibrium conditions using batch leaching tests, the long-term dynamic leaching of constituents in a field site is controlled by both liquid-to-solid partitioning and mass transfer in the aqueous phase, where insights can be gained using a laboratory percolation column leaching test [28,143]. The EPA Method 1314 test is part of the Leaching Environmental Assessment Framework (LEAF) [17,19,20] developed for the United States Environmental Protection Agency (U.S. EPA) and has been used to characterize percolation leaching as a function of liquid-to-solid ratio (L/S) for L/S up to ~10 L/kg-dry. Accordingly, the Method 1314 test results can be used to estimate the long-term leaching of constituents considering that the L/S can be translated into a long-term leaching time depending on the estimated infiltration rate, the height of the disposal site, and dry bulk density of ash [28,144]. The potential for changing pH and redox conditions in response to disposed material isolation (e.g., by an impermeable cover), internal reactions (e.g., microbial activity, material aging, and mixing from co-disposal of different residues), and ingress of atmospheric carbon dioxide and oxygen also need to be considered.

Results from column studies on a broad range of solid wastes (e.g., municipal solid waste (MSW), MSW bottom ash, and coal ashes) suggest that the complex dynamic leaching of constituents in a column test is controlled by both flow conditions (e.g., dispersion) and chemical reactions occurring in the porous medium [10,27,28,137,145]. Therefore, coal ashes in various compositions can show distinct leaching behavior for constituents due to different controlling chemical reactions. Neupane et al. [10] reported two different leaching behaviors of As between

acidic and alkaline fly ashes, where bimodal L/S-dependent leaching behavior was observed for the acidic ash, in comparison to the low As concentrations during the entire column test for the alkaline ash. In contrast, the column test on another alkaline fly ash from Khodadoust et al. [143] showed continuously decreasing As concentrations after an initial period of concentration increase. The different experimental procedures and the lack of other supporting data (e.g., pH-dependent leaching test and modeling results) make it difficult to compare phenomena and mechanisms controlling the dynamic leaching behavior of constituents across different studies.

In addition, because of the relatively high cost of a column test compared to a batch leaching test, a systematic study focusing on the various L/S-dependent leaching behavior for a wide range of coal ashes has not been reported. The identification of controlling mechanisms during a column test is fundamental to understanding the leaching behavior and, therefore, to estimating the long-term release of constituents under field conditions.

So far, laboratory column leach testing has been primarily focused on "as-generated" coal ashes that were collected directly from electrostatic hoppers [4,10,28,29]; however, the results obtained have limitations to reasonably represent the field release of constituents, in part, due to in-field handling (e.g., sluicing with process water) and weathering of ash under exposure to the field environment. For coal ash in impoundments, depletion of alkali-contributing constituents (e.g., Ca and Mg) and the internal mineral formation and dissolution related to ettringite, gibbsite, aluminosilicates, and Ca-carbonates have been reported to result in the progressive acidification of porewater [25,73]. Therefore, the mobility of constituents may change with pH during the weathering process.

In addition, the formation of secondary phases (e.g., Fe-oxides, carbonates, and clay minerals) in weathered ash can impact the chemical mobility of constituents via precipitation, adsorption, and co-precipitation [24,28,146]. For example, the carbonation of alkaline steel slag, MSW bottom ash, and cementitious waste forms has been suggested to reduce the leaching of Ba, Sr, Cr, and Sb(III) [7,34,140]. Such effects of carbonation may also affect the leaching of alkaline coal ashes at disposal sites where greater CO_2 partial pressure was measured (by Kim. et al. [24]) under post-closure conditions compared to an open disposal site. Therefore, leaching characterization carried out on both as-generated and field-disposed ash is necessary to understand the mechanisms controlling the long-term leaching behavior of constituents, which has had only

limited consideration in previous studies.

Aside from the weathering effects on field ashes, our previous studies also show impacts of field redox conditions on the leaching behavior of redox-sensitive oxyanionic constituents (e.g., As, Cr, Se, and V) [45,147] (Chapter 3&4). For scenarios where strongly reducing conditions are present in the field, the laboratory leaching column test may not well represent the field leaching behavior of redox-sensitive constituents due to the different redox conditions between the field and laboratory conditions. Thus, understanding the potential impacts of redox conditions on the long-term field release of constituents is vital to fill the gaps with respect to the long-term leaching assessment at coal ash disposal sites.

In this study, the L/S-dependent leaching behavior of As, B, Cr, Mo, Se, and V was characterized using the EPA 1314 column test for a range of as-generated ashes and field-disposed ashes, including six as-generated ashes in a wide range of solid compositions (from Chapter 2); field ashes from a closed impoundment (from Chapter 3); and field ashes from another coal ash management unit with a dry landfill cap on top of an impoundment (from Chapter 4). Method 1314 results also are compared to leaching tests using flexible wall permeameters that sought to preserve the physical and redox integrity of field core samples during testing. Experimental and modeling results (pH-dependent leaching tests, solid phase characterization, and geochemical speciation modeling) from previous studies [45,115,147] also were used to help identify mechanisms controlling the dynamic leaching behavior during column testing. A series of comparisons of column test results aim to evaluate the impacts of different chemical reactions (i.e., adsorption/desorption and mineral precipitation/dissolution reactions), field weathering reactions, and redox conditions on the L/S-dependent leaching of the oxyanions. Finally, based on field hydrologic conditions from a hydrologic model [139] and the column test results, a field conceptual scenario of an impoundment under post-closure conditions is used to estimate the long-term release of constituents for a specific disposal scenario.

5.2 Materials and methods

5.2.1 Materials and sample preparation

The 14 coal ash samples, for which the chemical composition and pH-dependent leaching behavior of oxyanions were characterized and described in previous studies [45,115,147], were included in the long-term leaching assessment (Table 5.1). These samples consisted of a range of as-generated fly ashes [115] (Chapter 2) and field coal ashes [45,147] (Chapter 3 and Chapter 4). Among the six as-generated fly ashes (i.e., EFA_U, FFA_U, LAB_U, PPB_U, KSP_AG, and CDL_AG) from different facilities, the KSP_AG and CDL_AG were respectively collected "as generated" from the facility where disposal Site 1 and Site 2 were located. For Site 1, the three field-disposal ashes KSP_VB1/VB2/VB3 were similar sluiced ash composites from three borehole locations (VB1, VB2, and VB3) at a closed impoundment. For Site 2, the CDL_Dry ash represents blended ash composites from different depths of a dry coal ash stack, while CDL_VC1/VC2/VC3/VC4 are the four ash composites from each of four borehole locations (VC1, VC2, VC3, and VC4) in the underlying impoundment.

Table 5.1 Summary of coal ash samples included in the long-term leaching assessment

Sampling facility	Sample type	Sample ID
Facility E	As-generated ash	EFA_U
Facility F		FFA_U
Facility L		LAB_U
Facility P		PPB_U
Site 1	As-generated ash	KSP_AG
	Field ash: sluiced pond	KSP_VB1, KSP_VB2, KSP_VB3
Site 2	As-generated ash	CDL_AG
	Field ash: dry stack	CDL_Dry
	Field ash: sluiced pond	CDL_VC1, CDL_VC2, CDL_VC3, CDL_VC4

In addition, intact ash cores were collected by Φ7.6 × 91 cm thin-wall sampling tubes (Osterberg sampler) from the closed impoundment on Site 1, with the intent of maintaining the physical and chemical properties for hydraulic conductivity and leach testing. For analysis of the saturated hydraulic conductivity (test was carried out at University of Virginia), sections of undisturbed

coal ash were extruded from the sampling tubes and cut into 76-mm long specimens. For leaching testing, the remaining ashes were stored in plastic bags and transported back to Vanderbilt University for the percolation leaching test by EPA Method 1314 (§5.2.2.1). Before the leaching test, the ash cores were quickly homogenized in the plastic bag by hand and then used in the packing procedures for the percolation test.

Three samples collected by the Osterberg sampler were included in this study, i.e., KSP_VB1_OST (738.8), KSP_VB2_OST (737.9), and KSP_VB3_OST (738.8), which included one ash core sample from each borehole location. The number in parentheses at the end of each sample ID represents the bottom elevation (above mean sea level) of the sample interval.

5.2.2 Leaching characterization

5.2.2.1 Percolation leaching by EPA Method 1314

An up-flow percolation column leaching test was carried out on the 14 coal ash samples (Table 5.1) and the three additional Osterberg ash samples from Site 1. The leaching test method followed EPA Method 1314 [129], which aims to evaluate the L/S-dependent leaching behavior of constituents during water percolation through a column. Generally, about 250-400 g ash (dry basis) was loosely packed in a glass column (Φ5×30 cm) and then saturated with deionized water (DIW). After equilibrating for ~24 hours, DIW was pumped at a low flow rate (0.75±0.25 L/S per day) through the material in an up-flow direction to minimize air entrainment and flow channeling. Eluates were collected at predetermined cumulative L/S (ΣL/S) values (i.e., 0.2, 0.5, 1, 1.5, 2, 2.5, 4.5, 5, 9.5, and 10 L/kg-dry). The eluates were measured for pH, electrical conductivity (EC), and concentrations of cationic constituents, anions, DIC, and DOC. Details of eluate analysis methods can refer to previous studies [45,115,147] in Chapter 2 to 4 (Appendix A.III).

5.2.2.2 Percolation leaching from hydraulic conductivity test

For the three Osterberg ash samples (KSP_VB1_OST (738.8), KSP_VB2_OST (737.9), and KSP_VB3_OST (738.8)), eluate concentrations from the hydraulic conductivity (HC) test were

measured as a function of ΣL/S. The concentrations of constituents in HC eluates were compared with the results from EPA Method 1314 (§5.2.2.1) to compare the leaching behavior of oxyanions between column tests carried out on intact field ash samples with minimal exposure to air and homogenized field samples exposed to air.

Hydraulic conductivity tests were conducted in flexible-wall permeameters following the methods in ASTM D5084-16 at the University of Virginia [148]. DIW was used as the permeant solution. Effluent samples were collected from the tests and stored in Teflon sample bottles with minimal headspace. The collected eluate samples were shipped under chain of custody to Vanderbilt University for chemical analysis (pH, EC, and concentrations of cationic constituents). The analytical methods are the same as eluate analysis in §5.2.2.1. Details of the hydraulic conductivity test methods are provided in another study [149].

5.2.3 Geochemical speciation modeling

The geochemical speciation models previously developed for the as-generated ashes (Chapter 2) and field-disposed ashes (Chapter 3&4) were used to help identify potential controlling phases during the percolation test. For simulating the phase distribution of constituents in column porewater at a specific ΣL/S during percolation leaching, the available content of constituents in the geochemical virtual material was adjusted by subtracting the cumulative release of constituents at this ΣL/S from the initial available content prior to leaching.

5.2.4 Hydrologic model

For long-term leaching assessment, the discharge of water from a conceptual coal ash impoundment under different stages of pre-closure and post-closure conditions has been predicted by Benson et. al. [139] using a hydrologic model. In this study, the discharge rate under post-closure stages from the hydrologic model was used to estimate the water discharge as a function of time for a conceptual impoundment in post-closure periods. Thus, at a specific time (t, y) following site closure, the cumulative water percolated through the ash on the basis of the dry ash mass (ΣL/S, L/kg-dry) was converted based on the cumulative water discharge at time t

(Q_t, mm), the height of the impoundment (h, m), and the bulk ash dry density (ρ, g/cm^3) with Equation 5-1.

$$\Sigma L/S = \frac{Q_t}{h \times \rho \times 1000} = \frac{\int_0^t q dt}{h \times \rho \times 1000} \quad \text{Equation 5-1}$$

In Equation 5-1, the Q_t was calculated by integrating the water discharge rate (q, mm/y) (from the hydrologic model) with respect to time. The impoundment was assumed to be 10 m deep (h = 10 m), which was consistent with the value used in the hydrologic model. The dry bulk density was selected as 1.15 g/cm^3 (ρ = 1.15 g/cm^3) according to the measured value of the field intact core samples from Site 1.

The water discharge results used in this study were for a conceptual impoundment located above the groundwater table. One dimensional flow in a vertically downward direction was simulated considering the large area of an impoundment relative to the depth. Three types of coal ashes with different saturated hydraulic conductivity (K_s) values were considered, including less permeable ash with K_s of 5.0×10^{-6} cm/s, typical ash with K_s of 5.5×10^{-5} cm/s, and more permeable ash with K_s of 6.0×10^{-4} cm/s. In addition, two scenarios with different final top covers were included in the model, i.e., an earthen cover with a percolation rate of 250 mm/y (under humid climates) and a geosynthetic cover with a percolation rate of 3 mm/y (under humid climates). Herein, the results from the hydrologic model on humic climates were used for the long-term leaching assessment to provide a conservative estimate.

5.3 Results and discussion

5.3.1 Typical types of percolation leaching behavior and the associated leaching-controlling mechanisms

The oxyanions exhibited different dynamic leaching behaviors from a wide range of coal ashes primarily attributed to different leaching-controlling mechanisms. A previous study [115] identified three primary controlling mechanisms to control the near-equilibrium partitioning of As, B, Cr, Mo, Se, and V under static conditions: adsorption to hydrous ferric oxide (or analogous surfaces); co-precipitation with Ca-containing minerals; and substitution in ettringite. These mechanisms are important when evaluating the percolation leaching process of oxyanions.

The variation of eluate concentrations of oxyanions as a function of L/S showed distinctions between ash groups wherein different controlling mechanisms were identified (Figure D.1-Figure D.6, Appendix D.I). Representative results of oxyanions with typical L/S-dependent leaching behaviors are discussed in detail (Figure 5.1-Figure 5.3). In addition, results from the column tests were compared with the pH-dependent leaching test results to assist in understanding the controlling processes during percolation leaching.

(a) Adsorption to HFO

In the batch leaching test, several oxyanionic constituents (i.e., As, Cr, Se, Mo, and V) from the as-generated ash "LAB_U" were strongly adsorbed by iron (hydr)oxides or analogous surfaces at the natural pH condition, leading to adsorption-controlled leaching during the percolation test where the pH conditions were close to the natural pH. Concentrations of As, Cr, Mo, Se, and V in the first eluate from the column test agreed well with the near-equilibrium concentrations from the pH-dependent leaching curve under the low L/S condition (1 L/kg), indicating that the initial leaching of these oxyanions was likely controlled by the local adsorption equilibrium (Figure 5.1(a2/b2/c2/d2/f2)). Subsequently, the concentrations of As, Cr, Mo, Se, and V were relatively steady with the increase of ΣL/S from 0.5 to 10 L/kg (Figure 5.1(a2/b2/c2/d2/f2)). During the entire column test, the pH change of eluates for LAB_U was approximately within 1.1 pH units (Figure D.7a, Appendix D.I), which appeared to result in slight fluctuations in column eluate concentrations of oxyanions where eluate concentrations followed the pH-dependent concentration curve from the batch leaching test (Figure 5.1(a1/b1/c1/d1/f1)).

The consistency between concentrations from the column test and pH-dependent batch leaching test further supports the importance of adsorption equilibrium in controlling the percolation leaching behavior of oxyanions for acidic ashes where adsorption is a controlling phenomenon for leaching. In another column study on rocks [150], the pseudo-steady leaching of As also was suggested to be associated with adsorption. According to Wang et al. [151], sand columns loaded with iron hydroxides can effectively increase the retention of As by adsorption under near-neutral or slightly acidic environments. For coal ashes used in the column experiments, the role of adsorption in controlling the leaching behavior depends on the characteristics of the ash such as the pH and the number of adsorption surfaces, which should first be evaluated using other

tests (e.g., the pH-dependent leaching test) to assess the degree of adsorption for different oxyanions.

An increase in As concentrations at late stages of the column test sometimes was observed for acidic ashes. For example, the acidic ash "EFA_U" with strong adsorption effects observed for As, Cr, Se, and V showed a significant increase in As concentrations from ~0.002 mg/L at ΣL/S < 2 L/kg to 0.2 mg/L at ΣL/S of 10 L/kg (Figure D.1b, Appendix D.I), while not for other oxyanions. Some studies ascribed the increased leaching of trace elements at higher L/S to the diffusion of these elements from the interiors of ash particles to the surface resulting from glass dissolution [10]. However, this reasoning cannot explain the increased concentrations only for As observed in this study. Another possible explanation is that the depletion of Ca at high L/S decreased the adsorption of As due to the less positively charged surface, therefore, leading to increased eluate As concentrations [81,82]. The released fraction of available content of Ca from the ash EFA_U reached a plateau of ~63% at ΣL/S of 2 L/kg, ranked the highest released fraction among the acidic ashes.

Unlike the oxyanions with strongly pH-dependent adsorption effects, the concentrations of B, Ca, Na, and S showed a weak pH-dependency but were a strong function of L/S in the batch leaching tests (B in Figure 5.1(e1); Ca, Na, S in Figure D.8, Appendix D.I), which is typical for available content-limited leaching behavior. Accordingly, these constituents exhibited a rapid decrease in eluate concentrations with the increase of ΣL/S at ΣL/S < 2 L/kg in the column test, indicating a rapid depletion of the soluble fraction during the percolation leaching (B in Figure 5.1(e2); Ca, Na, S in Figure D.8). The fast release of B in the column experiments on fly ashes has been commonly reported in other studies [10,36]. The fractional cumulative release from the column test relative to the available content was 60% for B, 40% for Ca, 88% for S, and 54% for Na, which well matched the released fractions at the natural pH condition from the batch leaching test (at L/S of 10 L/kg) (B in Figure 5.1(e3); Ca, Na, and S in Figure D.8). These fractions represent the readily soluble fractions of content that are available to leach under the natural pH condition.

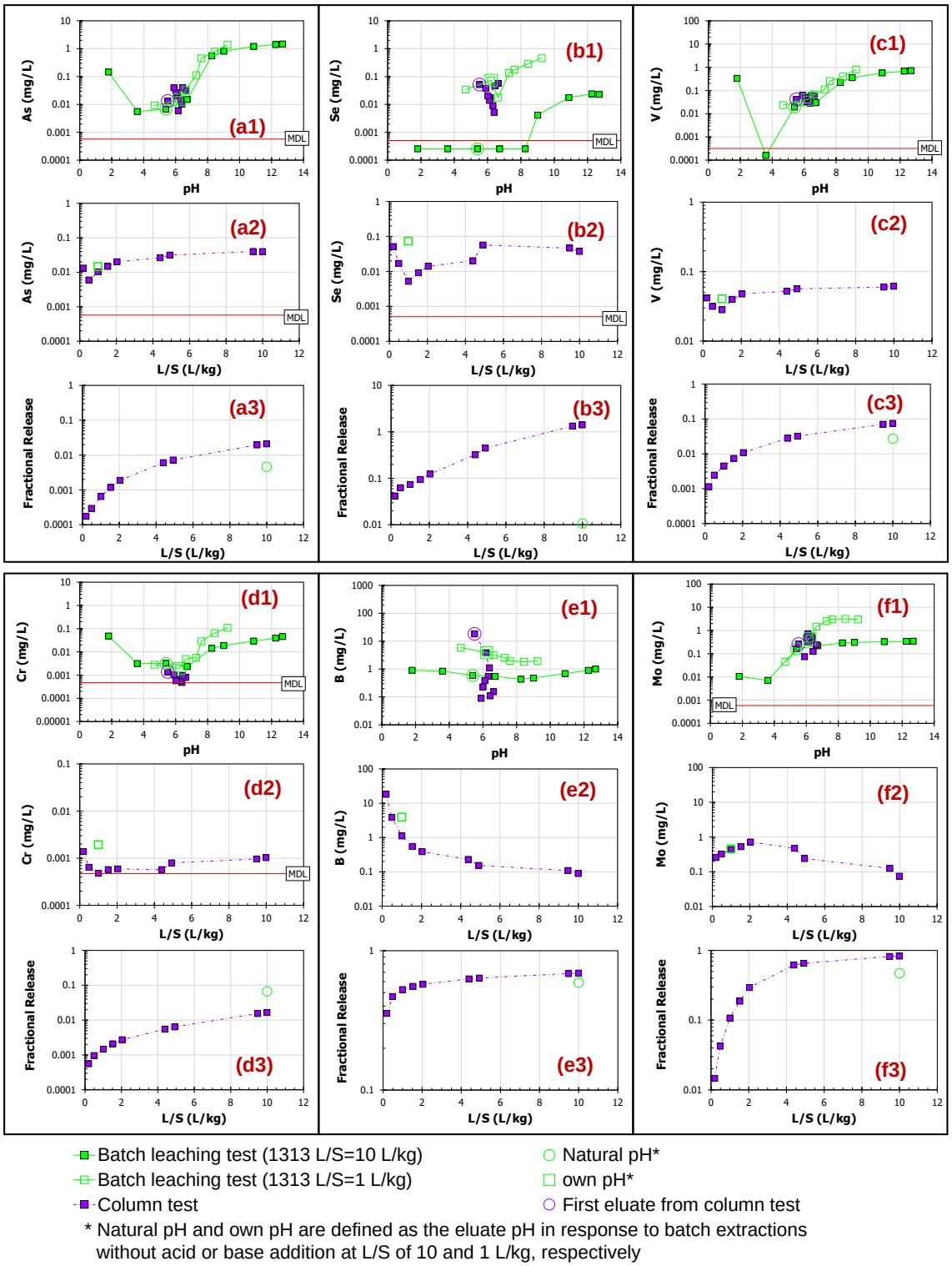

Figure 5.1 The pH- and L/S-dependent leaching test results of As, B, Cr, Se, Mo, and V for the acidic as-generated fly ash LAB_U. The fractional release is the fraction of cumulative release relative to the available content (i.e., the maximum release in the pH-dependent leaching test). Concentrations less than the method detection limit (MDL) are plotted as one half of the MDL.

(b) Co-precipitation with Ca-containing minerals

For the alkaline as-generated ash "CDL_AG", the eluate concentrations of B, Cr, and Se decreased substantially (greater than one order of magnitude) from the initial condition to ΣL/S between 2-5 L/kg, but were relatively constant at ΣL/S conditions above 5 L/kg (Figure 5.2(b2/d2/e2)). The initial rapid wash-off behavior was because of the depletion of readily soluble fractions, ranging from 6 to 10% (relative to the available content) for B, Cr, and Se. For example, the initial release of relatively soluble Se(VI) fraction compared to the less soluble Se(IV) fraction. Subsequently, the relatively constant concentrations at low values were likely controlled by mineral solubilities. According to the pH-dependent batch leaching test, Ca-coprecipitation could decrease the respective solubilities of B, Cr, and Se at pH > 10 (Figure 5.2(b1/d1/e1)). The results imply that mineral solubilities control the long-term release of B, Cr, and Se from the alkaline ash, where the mineral phase continues to release the contained oxyanions at low release rate.

The eluate concentrations of Mo decreased continuously from 40 mg/L at the initial collected L/S condition to 1 mg/L at ΣL/S of 10 L/kg in the column test (Figure 5.2(f2)), which was consistent with the leaching behavior of highly soluble Na (Figure D.9, Appendix D.I). Among the oxyanions, Mo was the most soluble, and almost the entire available content was depleted at ΣL/S of 10 L/kg (Figure 5.2(f3)), while for other oxyanions less than 10% of the available content was released (Figure 5.2(a3-e3)). The highly soluble characteristic of Mo has been widely acknowledged in earlier studies because Mo primarily deposits on the surfaces of ash particles [4].

For As and V, the solubilities were strongly controlled by mineral precipitation and dissolution, with less wash-off effects observed when compared to B, Cr, Mo, and Se. The initial concentration of V (0.1 mg/L) was close to the near-equilibrium state (0.2 mg/L) from batch testing and the concentration of V during the entire column test was relatively steady (0.06 – 0.1 mg/L) (Figure 5.2(c1/c2)). This distinct leaching behavior indicated the presence of a V-bearing mineral that continuously released V to the pore solution under local equilibrium conditions. The geochemical modeling results of batch leaching under the L/S of 10 and 1 L/kg both suggested $Ca_3(VO_4)_2$ was a potential controlling phase (Figure 2.11, Chapter 2).

For As, the eluate concentrations were approximately 0.02 mg/L at ΣL/S less than 5 L/kg, but

gradually decreased to 0.001 mg/L at greater ΣL/S (Figure 5.2(a2)). The decrease in As concentrations at ΣL/S > 5 L/kg suggests the depletion in Ca available content (~20 %) (Figure D.9(a3)) altered the phases controlling the solubility of Ca and, therefore, caused the simultaneous concentration decrease of Ca and As. The As in fly ash could be closely associated with matrices of Ca-bearing minerals as identified in other studies [13]. Given the correlation among the percolation leaching behaviors of As, Ca, and S, the high concentrations of As, Ca, and S at ΣL/S < 5 L/kg are attributed to the dissolution of relatively soluble gypsum (based on the XRD analysis results; Chapter 4) and the associated fraction of As; at ΣL/S > 5 L/kg, the gypsum appeared to be depleted and Ca came to be primarily controlled by other phases with low solubility (e.g., calcite), resulting in low concentrations for both Ca and the associated As. According to a study by Khodadoust et al. [143], the leaching of Ca from a fly ash also initially was controlled by a calcium sulfate phase but was subsequently controlled by carbonate and bicarbonate phases in the long-term. The change of Ca leaching behavior also impacted the leached As [143].

Overall, the effects of Ca coprecipitation reactions on controlling the elution curves of oxyanions are suggested to be constituent-specific depending on the solubility of different metalate precipitates and the kinetics of phase formation and dissolution. The strong congruent leaching of As and V with Ca in comparison to B, Cr, Mo, and Se is consistent with the finding from the earlier study, where the leaching of As and V was found most sensitive to the variation of Ca content in comparison to other oxyanions from a wide range of fly ashes (§2.4.1, Chapter 2).

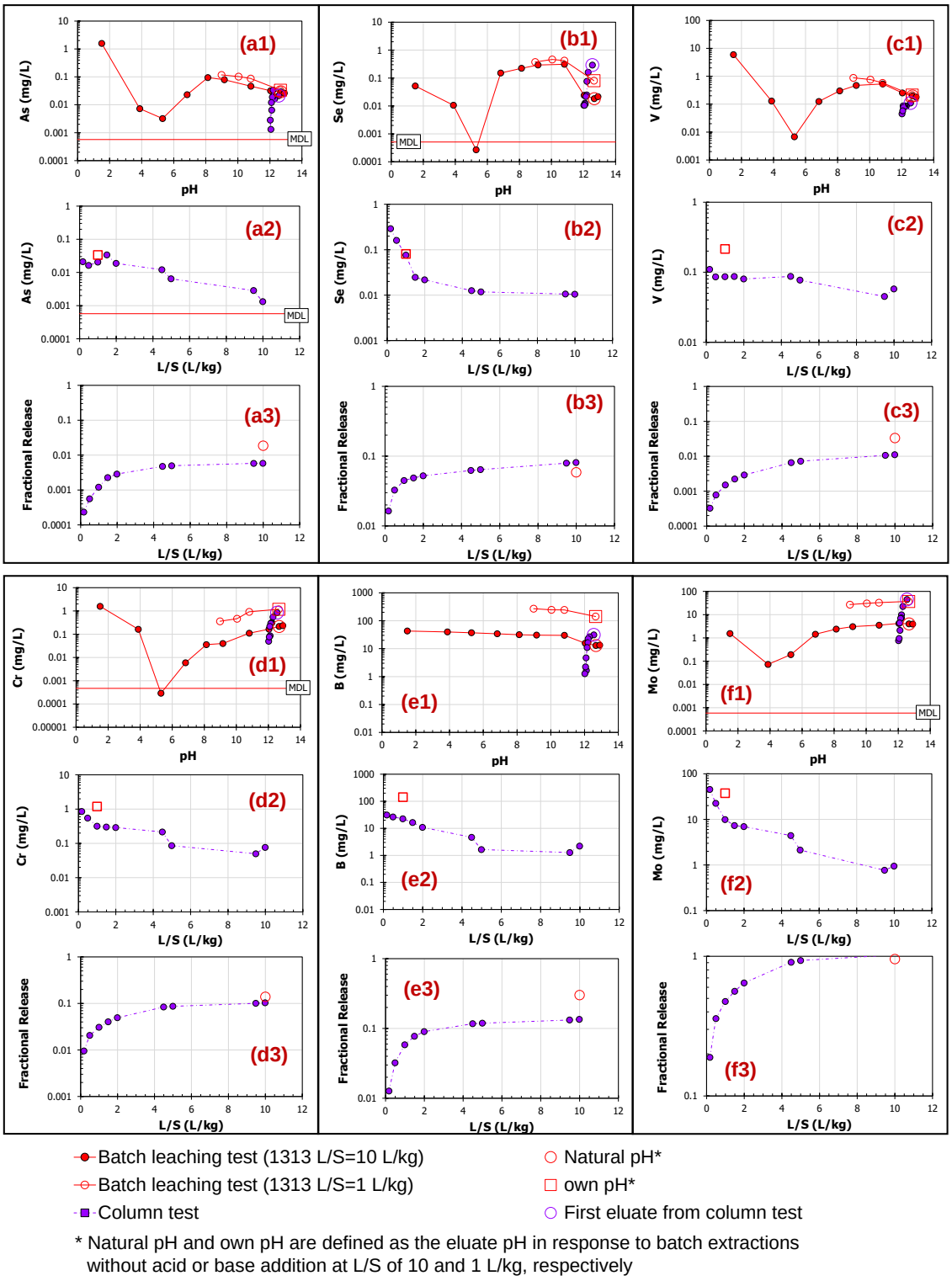

Figure 5.2 The pH- and L/S-dependent leaching test results of As, B, Cr, Se, Mo, and V for the alkaline as-generated fly ash CDL_AG. The fractional release is the fraction of cumulative release relative to the available content (i.e., the maximum release in the pH-dependent leaching test). Concentrations less than the method detection limit (MDL) are plotted as one half of the MDL.

(c) Substitution in ettringite

For the strongly alkaline ash "PPB_U", the L/S-dependent leaching behavior of the oxyanions (i.e., As, B, Cr, Mo, Se, and V) was strongly associated with the solubility of ettringite, which is highly sensitive to the pH of the leaching system. According to the geochemical speciation modeling results, the formation of ettringite was predominantly favored at pH range of 11-12, while a deviation from this pH range could lead to significant ettringite dissolution and release of co-precipitated oxyanions (§2.4.6, Chapter 2). During the column test, the initial high pH of 12.8 from the fast dissolution of alkali-contributing constituents (e.g., CaO and MgO from XRD measurements, Figure 2.7 in Chapter 2) was not favorable for ettringite precipitation, but the progressive decrease of pH to a steady value of ~11.5 at ΣL/S > 2 L/kg (Figure D.7, Appendix D.I) could result in precipitation of oxyanions through the formation of an ettringite solid solution. Consequently, the L/S-dependent concentrations of all oxyanions were characterized as a sharp decrease when ΣL/S increased from 0.2 to ~2 L/kg and then were relatively steady for B, Cr, Mo, and V or less than the method detection limit (MDL) for As and Se at L/S greater than 4 L/kg (Figure 5.3(b2/b2/c2/d2/e2/f2)). The change in solubilities of oxyanions caused by ettringite formation/dissolution with the pH evolution has been suggested by Stefaniak et al. [73] in a field study on coal ash disposal sites.

In addition, the concentrations of oxyanions and major constituents (i.e., Ca, S, and Si) in the column effluents were in alignment with the pH-dependent solubility curve from the batch leaching test (Figure 5.3(b1/b1/c1/d1/e1/f1); Ca, S, and Si in Figure D.10), suggesting that the dynamic leaching behavior of constituents in the percolation test for PPB_U was controlled by the solubility of the ettringite solid solution.

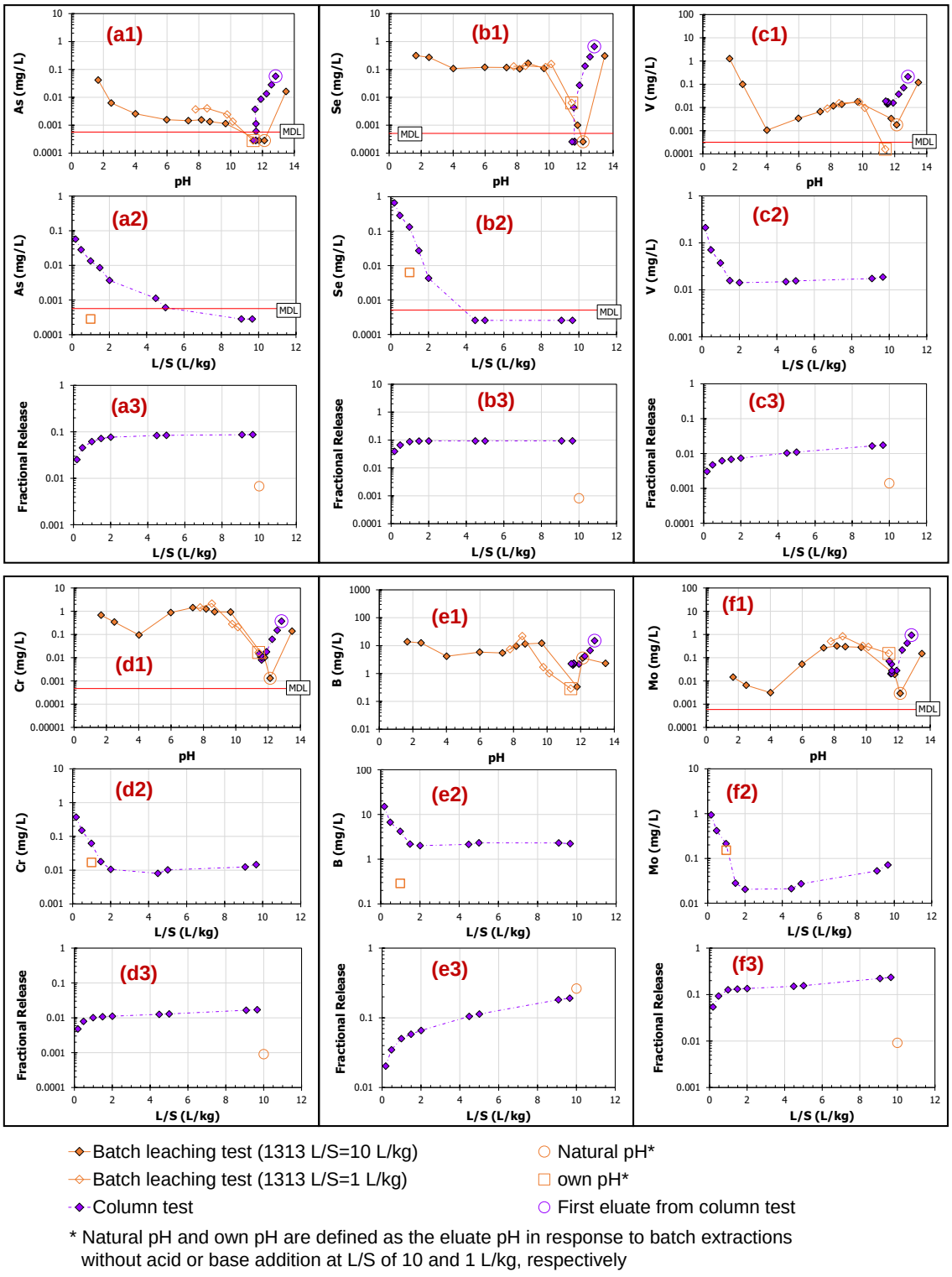

Figure 5.3 The pH- and L/S- dependent leaching test results of As, B, Cr, Se, Mo, and V for the alkaline as-generated fly ash PPB_U. The fractional release is the fraction of cumulative release relative to the available content (i.e., the maximum release in the pH-dependent leaching test). Concentrations less than the method detection limit (MDL) are plotted as one half of the MDL.

5.3.2 Impacts of field weathering on percolation leaching of coal ashes (Site 2)

In the field study on the active coal ash management unit (where an active landfill was built above a historical impoundment; Chapter 4), both as-generated ash ("CDL_AG") and field ashes ("CDL_Dry" from the upper dry stack and "CDL_VC" from the underlying impoundment) were collected from the same facility. The comparison of leaching results among the three ashes helps to elucidate the changes in long-term leaching of oxyanions from field weathered ash and the underlying controlling mechanisms. Compared to the as-generated ash, the field-disposed ashes showed a significant change in pH-dependent leaching behavior of major constituents and trace oxyanions from the batch test, primarily resulting from mineralogical transformations as informed by the geochemical modeling results (Figure 5.4).

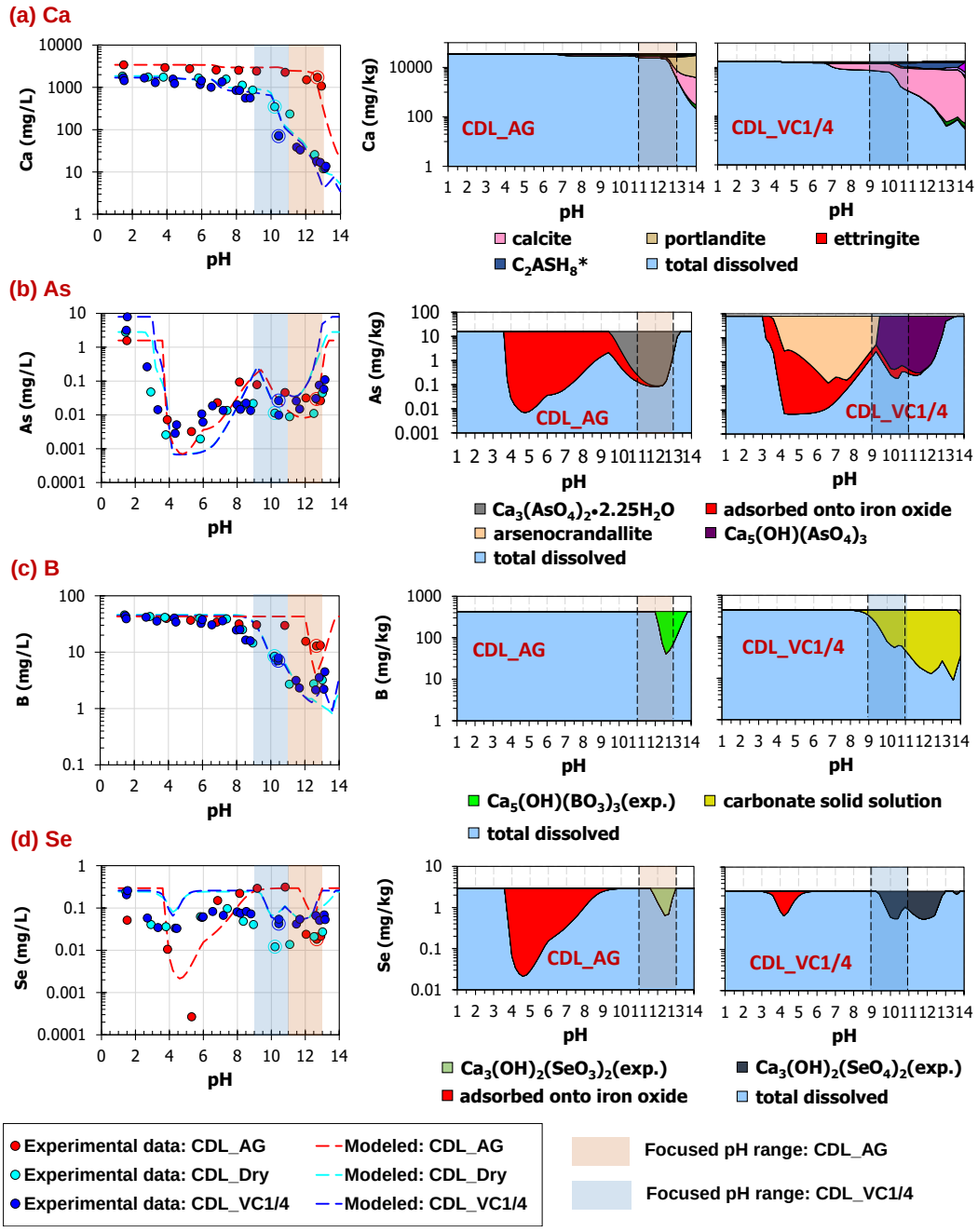

Figure 5.4 Comparisons of pH-dependent leaching and geochemical speciation models for As, B, Ca, and Se between as-generated ash (CDL_AG) and field ashes (CDL_Dry and CDL_VC1/4) from the field study on an active coal ash management unit. Phase diagrams are shown for CDL_AG and representative field ash CDL_VC1/4. *Cement chemist notation was used to simplify the formulae of cement phases using C = CaO; S = SiO_2; A = Al_2O_3; H = H_2O. Arsenocrandallite: $CaAl_3(AsO_4)(AsO_3OH)(OH)_6$. Ettringite: $Ca_6Al_2(SO_4)_3(OH)_{12}•25H_2O$. Calcite: $CaCO_3$. Mineral phases with the suffix "(exp.)" are postulated experimental phases. Specific pH ranges around the natural pH conditions of the as-generated and field ashes are highlighted.

(a) Impact of carbonation

The natural pH of the field ashes CDL_Dry and CDL_VC1 (pH ~10.5) was lower than that of the as-generated ash CDL_AG (pH ~12.5), which was mainly attributed to the carbonation of the field ashes. The total inorganic carbon measured by thermogravimetric analysis was 1.4 and 1.3 wt% C for the field ashes CDL_Dry and CDL_VC1, respectively, in comparison to the 0.6 wt% C for the as-generated ash CDL_AG. Geochemical modeling suggested that carbonation also caused the decrease in solubilities of Ca and B at pH > 8 for the field ashes because of the formation of carbonate phases (Figure 5.4a). Compared to the relatively constant Ca concentrations between pH 8 and 12 for the as-generated ash (CDL_AG), the two field ashes showed a decrease in Ca concentrations by two orders of magnitude from pH 8 to 12, due to higher fractions of carbonate in the field ashes relative to the available content of Ca. According to modeling results, the molar ratio of available content between CO_3^{2-} and Ca was the highest in the field impoundment ash (CDL_VC1) with a value of 0.38, followed by the field dry stack ash (CDL_Dry) of 0.32, and was the lowest in the as-generated ash (CDL_AG) of 0.12.

In the percolation test, the eluate concentrations of Ca from the three ashes were steady at ΣL/S of 1-5 L/kg in the sequence: CDL_AG > CDL_Dry > CDL_VC1, corresponding to the lowest carbonation degree in CDL_AG and the highest carbonation degree in CDL_VC1 (Figure D.12, Appendix D.II). The dry stack ash seemed to be in the process of transforming from as-generated ash to strongly weathered ash. The CDL_VC1 released a much lower fraction of Ca available content (~2%) than either CDL_AG or CDL_Dry (~20%), suggesting that carbonation of the impoundment ash (CDL_VC1) with a long disposal history contributed to the immobilization of Ca (Figure D.12 (a3)).

Similar to Ca, the field ashes showed a greater decrease in B concentrations at pH > 8 compared to the as-generated ash in the batch leaching test, which is due to the carbonation of field ashes as suggested by geochemical modeling (Figure 5.4c). Although the field ashes and as-generated ash had similar available content of B, the release of B during the percolation test was less in field ashes than in the as-generated ash. Specifically, the fractional cumulative release of B at ΣL/S of 10 L/kg from the impoundment ash CDL_VC1 (~4%) was less than that from the as-generated ash CDL_AG and dry stack ash CDL_Dry (~10%), indicating a more refractory fraction of B in the impoundment ash likely from the stabilization by a carbonate solid solution

(Figure 5.5(e3)). For the impoundment ash CDL_VC1, the concentrations of B were steady at ΣL/S > 1 L/kg, suggesting that the percolation leaching of B was strongly controlled by the solubility of B-containing carbonates. However, for the as-generated ash CDL_AG and dry stack ash CDL_Dry, the percolation leaching of B was observed to be minimally controlled by the solubility of minerals because the eluate concentration of B continued to decrease until ΣL/S of 5 L/kg (Figure 5.5(e2)).

(b) Impact of Ca depletion

Generally, after the initial surface wash of loosely bound fractions (i.e., ΣL/S > ~2 L/kg), multiple oxyanions (i.e., As, B, Se, Cr, and V) from the percolation test of the field impoundment ash CDL_VC1 eluted at fairly constant concentrations, potentially controlled by solubility of Ca-bearing mineral phases (Figure 5.5(a2-e2)). The cumulative releases of oxyanions (i.e., As, B, Se, Cr, and V), Ca, and S at the ΣL/S of 10 L/kg from CDL_VC1 were less than 20% of the initial available content. The results of using the reduced amount of available content at the ΣL/S of 10 L/kg in geochemical speciation modeling suggested no change of phases controlling the solubility of the oxyanions compared to the initial porewater conditions.

However, for the as-generated ash (CDL_AG) and dry stack ash (CDL_Dry), the leaching behavior of As, Ca, and S was observed to be highly consistent, i.e., their concentrations were relatively steady at ΣL/S < 5 L/kg but significantly decreased at ΣL/S > 5 L/kg (As in Figure 5.5(a2); Ca and S in Figure D.12(a2)). For both ashes, the available content of Ca and S is depleted by 10-20% and 40-50%, respectively, at ΣL/S > 5 L/kg. The concentration decreases of Ca and S at ΣL/S > 5 L/kg were likely because of the depletion of relatively soluble gypsum considering that gypsum was detected in both CDL_AG and CDL_Dry while not in CDL_VC1. After the depletion of gypsum, the leaching of Ca mainly was controlled by phases with low solubilities, leading to the low concentration of Ca at ΣL/S of 10 L/kg. Accordingly, given the strong correlation of As to Ca-bearing phases in ashes [13], the leaching behavior of As showed similar L/S-dependent leaching behavior to Ca.

(c) Impact of ettringite

Based on the batch leaching test results, the leaching concentration of Mo at natural pH from the as-generated ash (CDL_AG) was approximately one order of magnitude greater than that from the field ashes (CDL_Dry and CDL_VC1) (Figure 5.5(f1)), which was potentially attributed to the immobilization of Mo by substitution into ettringite because: (i) ettringite was detected in the field ashes but not in the as-generated ash [147] (Chapter 4) and (ii) the Ca molybdate mineral was unlikely to stabilize Mo due to its highly solubility [4]. During the hydration of alkaline field ashes in disposal sites, ettringite is likely to form as a secondary mineral with the progressive acidification of porewater from a strongly alkaline environment (pH > 12) in as-generated ash to the pH range of 10-11 in the field porewater as reported in other studies [25]. The role of ettringite in Mo retention was pronounced during the percolation test, as the eluate concentration of Mo from the field ashes was much lower than that from the as-generated ash (Figure 5.5(f2)). Accordingly, the available content of Mo was completely released for the as-generated ash, while the released fractions for the field ashes were less than 40% (Figure 5.5(f3)). In terms of the cumulative release, the release of Mo from as-generated ash was reduced by approximately 90% for the two field ashes, suggesting weathering has been contributing to the immobilization of typically highly soluble Mo in the long-term field leaching process.

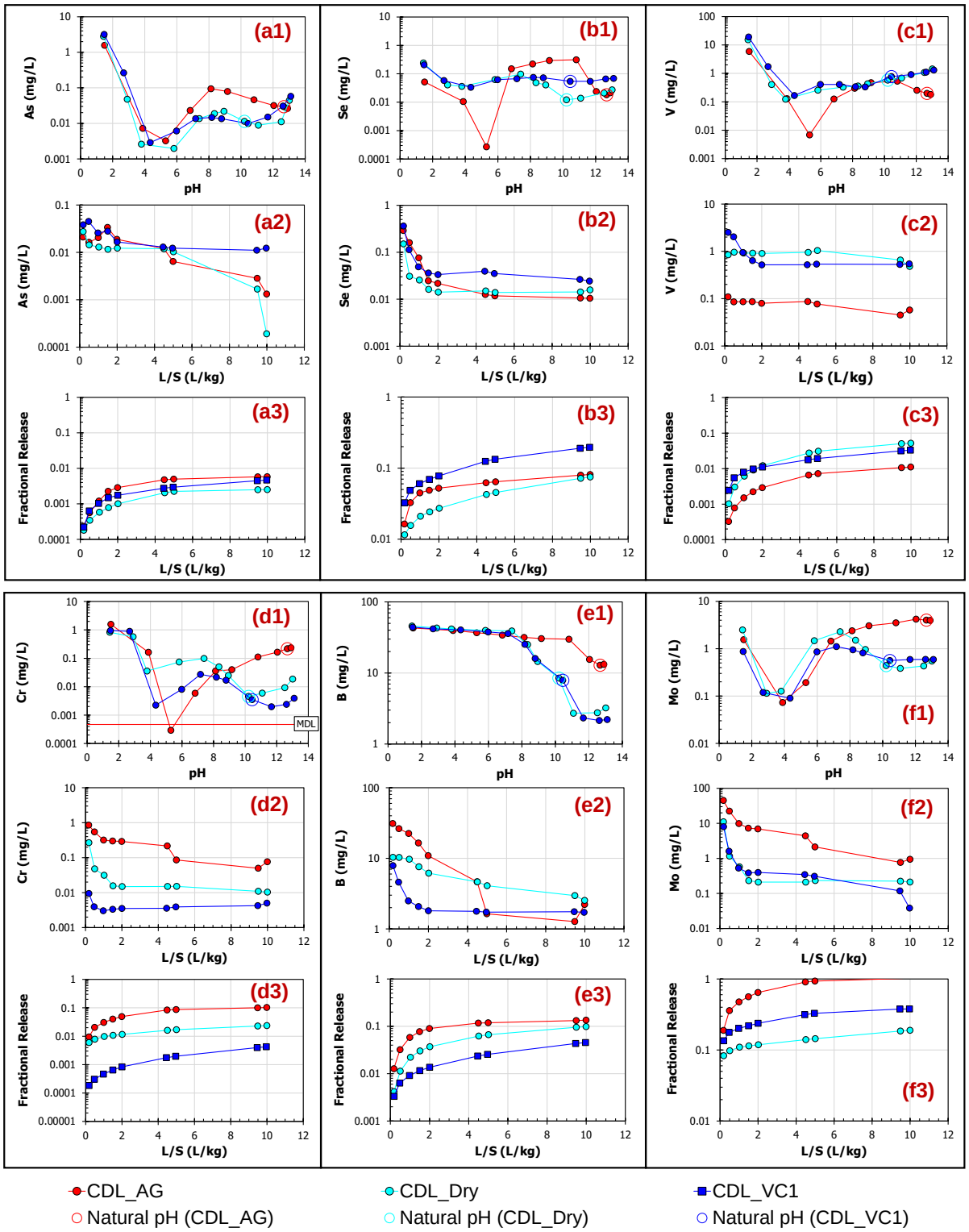

Figure 5.5 Comparison of the pH- and L/S-dependent leaching test results of As, B, Cr, Se, Mo, and V between the as-generated ash (CDL_AG) and field ashes (CDL_Dry and CDL_VC1) from the field study on an active coal ash management unit. Concentrations less than the method detection limit (MDL) are plotted as one half of the MDL.

5.3.3 Impacts of redox conditions on percolation leaching of coal ashes (Site 1)

Based on the previous field study of a closed impoundment [45], coal ash was identified to be in a strongly reducing environment under field scenarios but was subject to oxidation during field sampling and laboratory testing. Comparison of the constituent concentrations in the eluates from intact field cores with relatively well-preserved redox conditions (hydraulic conductivity test: HC test) and repacked columns (EPA Method 1314) provides insights into the influence of redox conditions on the dynamic leaching of different oxyanions from coal ashes.

(a) Redox-insensitive oxyanions (B and Mo)

The soluble oxyanions including B and Mo showed similar leaching behavior between the HC test and the Method 1314 column test, indicating their leaching behavior was not sensitive to the different redox conditions between the two percolation tests. The batch leaching of B and Mo for the field ashes (KSP_VB1/VB2/VB3) indicated that the partitioning of B and Mo was primarily limited by their available contents, indicated by the near-equilibrium concentrations being strong functions of L/S conditions (Figure D.13, Appendix D.III). Specifically, the eluate concentration of B and Mo at any pH position of the pH-dependent leaching curve with L/S of 1 L/kg was approximately 10 times the concentration at the corresponding pH position with L/S of 10 L/kg.

For these two soluble oxyanions with typical available content-limited leaching behavior, the L/S-dependent leaching in both the HC and column tests was characterized as a fast dissolution of available content into the porewater followed by a wash-off of the dissolved mass in porewater with continuous water flow. Specifically, the initial concentration decrease of B and Mo was about one to two orders of magnitude during ΣL/S up to 2 L/kg and continued to decrease in eluate concentrations with increasing L/S (Figure 5.6(a-b)). The primary factors controlling the leaching behavior of B and Mo during the percolation test were not chemical reactions but the physical characteristics of the column such as the longitudinal dispersion.

For samples including KSP_VB1_OST (738.8) and KSP_VB2_OST (737.9), the leaching curves of B and Mo from the HC and Method 1314 column tests were very similar, implying minimal differences in the physical retention ability between the intact cores used in the HC test and the repacked columns in the Method 1314 column test for these samples. The L/S-dependent leaching curves from the HC and Method 1314 column tests did not overlap for the other sample

(KSP_VB3_OST (738.8)), which might be attributed to the slightly different flow conditions (fluid velocity and dispersivity of the packed bed) impacting advection-dispersion during leaching of conservative constituents [28,152]. For example, similar to Na (a typical soluble constituent), the more rapid decreases in B and Mo concentrations at ΣL/S > 2 L/kg were observed in the HC test compared to the Method 1314 column test for the sample KSP_VB3_OST (738.8). The general consistency in elution responses between B, Mo, and Na also was observed for other samples.

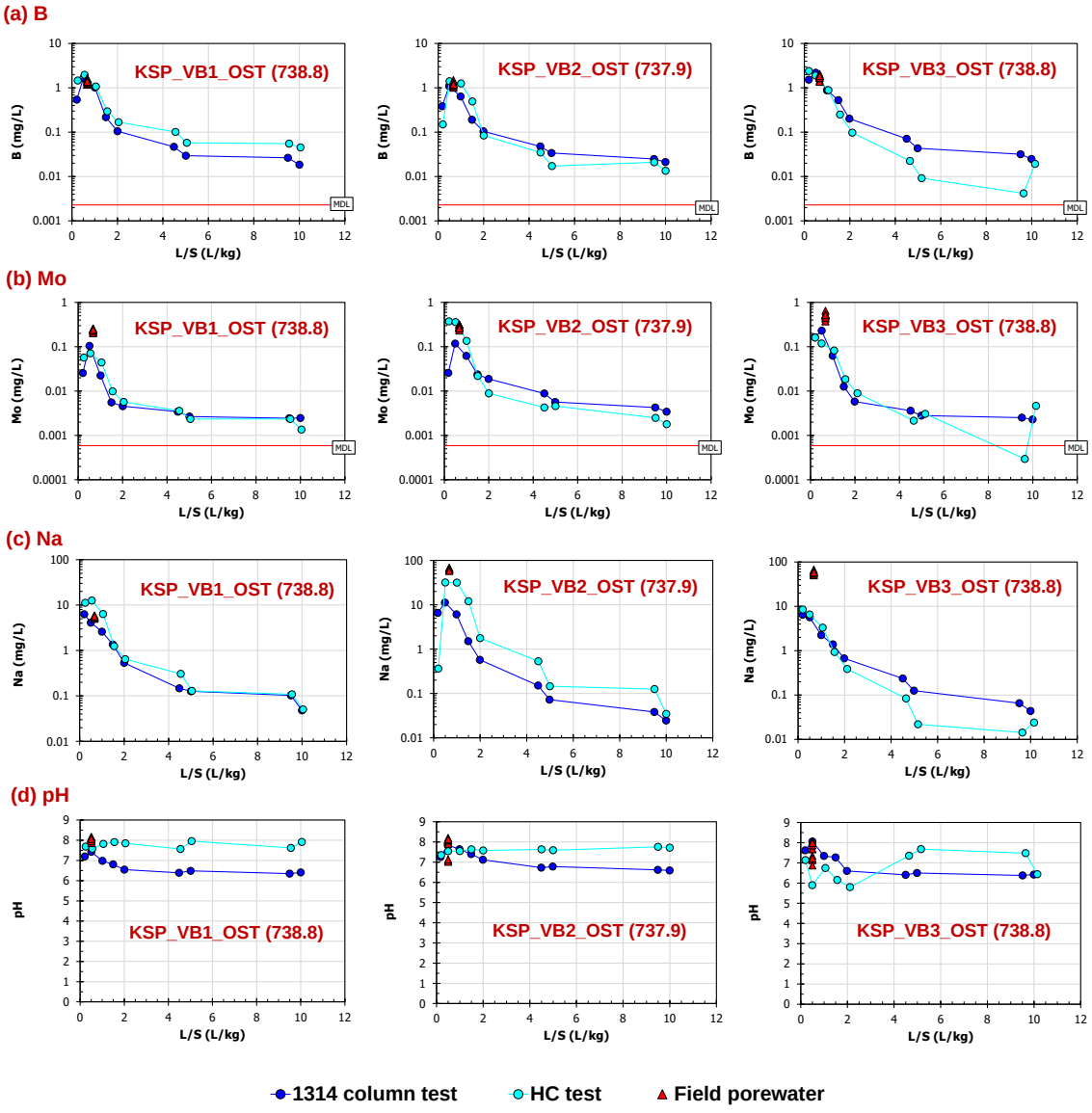

Figure 5.6 Comparison of the L/S-dependent leaching results of B, Mo, Na, and pH between the Method 1314 column test and the hydraulic conductivity (HC) eluates from intact core samples of the closed impoundment. Concentrations less than the method detection limit (MDL) are set as one half of the MDL.

(b) Redox-sensitive oxyanions (As, Cr, Se, and V)

Redox conditions indicated by iron. The coal ashes in the HC test generally exhibited more reducing initial conditions than ashes in the Method 1314 column test, which led to different leaching behavior between the two methods for As, Se, and V. The reducing environment in the HC test, especially for initial conditions in the columns, was evidenced by the greater Fe concentrations in eluates from the HC test compared to the Method 1314 column test, because Fe species in reduced form [Fe(II)] are more soluble than in oxidized form [Fe(III)] [21]. For all samples in the HC test, Fe concentrations at ΣL/S less than 4 L/kg were between 0.01 and 1 mg/L and generally showed a decreasing trend in eluate concentrations as elution progressed. In contrast, Fe concentrations in most eluates from the Method 1314 column test were less than the MDL of 0.002 mg/L (Figure 5.7a). The relationships between dissolved Fe concentrations and *pe* (Figure 5.8a) suggest that a one-order-of-magnitude increase in Fe concentration was accompanied by a decrease of 1 unit of *pe* at the fixed pH condition due to the increased fraction of soluble Fe(II). Also, the pH condition could impact the Fe(II)/Fe(III) redox equilibrium, as decreasing pH by 1 unit could result in greater Fe concentrations (up to three orders of magnitude) at a fixed *pe* condition.

For the HC test, the decrease in eluate Fe concentrations with the increase of ΣL/S was likely caused by the progressive oxidation of ash because of dissolved oxygen introduced by the influent (Figure 5.7(a)). The three Osterberg samples had relatively constant pH during the HC test with the initial and end point pH between 7 and 8 (Figure 5.6(d)). The leaching of As, Se, and V (three redox-sensitive oxyanions) was significantly impacted by the redox changes that occurred throughout the HC test.

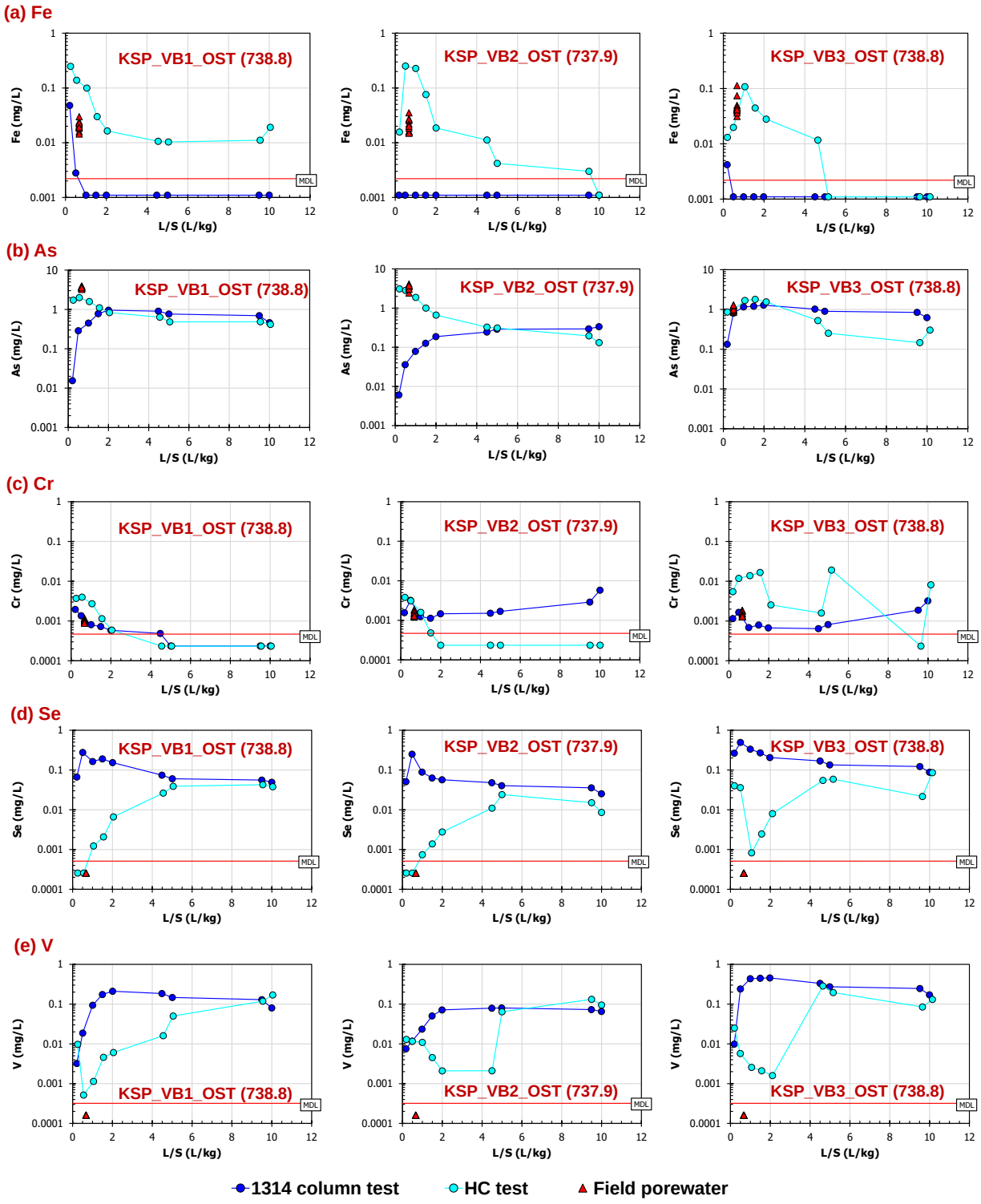

Figure 5.7 Comparison of the L/S-dependent leaching results of Fe, As, Cr, Se, and V between the Method 1314 column test and the hydraulic conductivity (HC) eluates from intact core samples of the closed impoundment. Concentrations less than the method detection limit (MDL) are set as one half of the MDL.

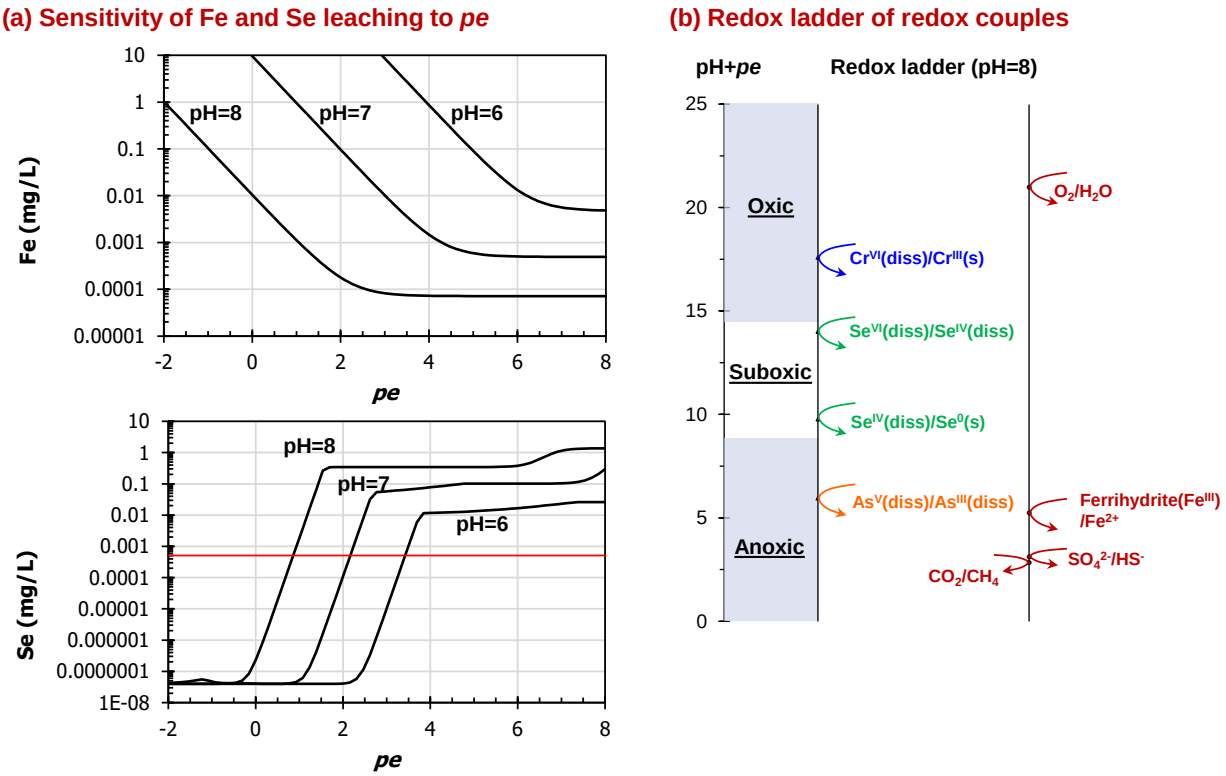

Figure 5.8 (a) Sensitivity of Fe and Se leaching to *pe* changes based on the developed geochemical speciation model of Site 1 field ash [45] and (b) the redox ladder of important redox couple reactions at pH of 8. Redox environments (oxic, suboxic, and anoxic) were classified according to the pH + *pe* values used by Borch et al. (2010) for each environment. To calculate the redox ladder, the activity of Fe^{2+} in the half reaction was set at 1E-5 mol/L. Redox couples for the other reactions were indicated when the corresponding chemical species were at the same chemical activity to illustrate the *pe* of transition.

Selenium and Vanadium. For Se, the field characterization in Chapter 3 indicated low Se concentrations (less than the MDL of 0.0005 mg/L) under a reducing field environment due to the precipitation of insoluble elemental Se or FeSe mineral, whereas oxidative dissolution of Se-bearing minerals caused a rapid increase in Se solubilities during the laboratory batch leaching characterizations. During the HC test on the field retrieved cores, two samples including KSP_VB1_OST (738.8) and KSP_VB2_OST (737.9) showed low concentrations of Se (less than the MDL) in the first two HC eluates that were consistent with the low concentrations in field porewater. The Se concentrations in HC eluates then gradually increased to the concentration range between 0.01-0.1 mg/L (Figure 5.7(d)). This leaching behavior of Se was

consistent with the overall more reducing conditions at the earlier stage of the HC test than the later stage as supported by the Fe concentration decrease (Figure 5.7(a)).

The other sample KSP_VB3_OST (738.8) also had an overall increasing trend of Se concentrations from low values (near the MDL of 0.0005 mg/L) at low ΣL/S to 0.01-0.1 mg/L at ΣL/S higher than 5 L/kg for the HC test despite the first two eluates showing Se concentrations of ~0.04 mg/L. The relatively high Se concentrations in the first two HC eluates suggest that surface oxidation may have occurred during storage because this sample had been stored for a longer time than the other two samples before the testing. In contrast to the increasing Se mobility during the HC test, the Method 1314 column test with more oxidized conditions had much greater eluate Se concentrations at ΣL/S < 2 L/kg and then declined at higher L/S (Figure 5.7d). Overall, the Se concentrations during the entire Method 1314 column test were greater than that from the HC test. The cumulative release of Se at ΣL/S of 10 L/kg from the Method 1314 column test was between 0.5 and 1.7 mg/kg for the three samples, which is 3 to 5 times as much as the cumulative release from the HC test (0.1-0.3 mg/kg).

Overall, the change of Se concentrations of up to three orders of magnitude during the HC test indicates that Se can be a strongly sensitive redox indicator. According to Figure 5.8(a), the increase of Se concentrations from less than 0.0005 mg/L (MDL) to 0.1 mg/L can occur rapidly within a *pe* increase of 1 to 2 units under a constant pH environment. Within such a *pe* change, Fe concentrations were predicted to decline by one to two orders of magnitude. Figure 5.9(e) further suggested that the two samples KSP_VB1_OST (738.8) and KSP_VB2_OST (737.9) were likely oxidized from a *pe* condition of 1 to 2 with pH between 7.5-8 during the HC test, while the sample KSP_VB3_OST (738.8) was subject to oxidation from *pe* of 2 to 4 with more acidic pH conditions (pH of 5.5-7.5).

Vanadium showed synchronous concentration changes with Se during the HC test for the three Osterberg samples, as lesser concentrations were observed in earlier eluates (ΣL/S < 5 L/kg) than at greater ΣL/S conditions (Figure 5.7(e)). The previous study on this site [45] detected low V concentrations, less than the MDL of 0.00032 mg/L in the field porewater with strongly reducing conditions. The lower V concentrations in the HC test compared to in the Method 1314 column test within the ΣL/S range of 1-5 L/kg were assumed to be driven by the more reducing environment in the HC test during the early stage of the test. Also, the positive correlation

between Se and V concentrations in the HC eluates from the three samples (Figure 5.9(c)) suggests that the large variations of Se and V during the HC test were primarily driven by redox changes.

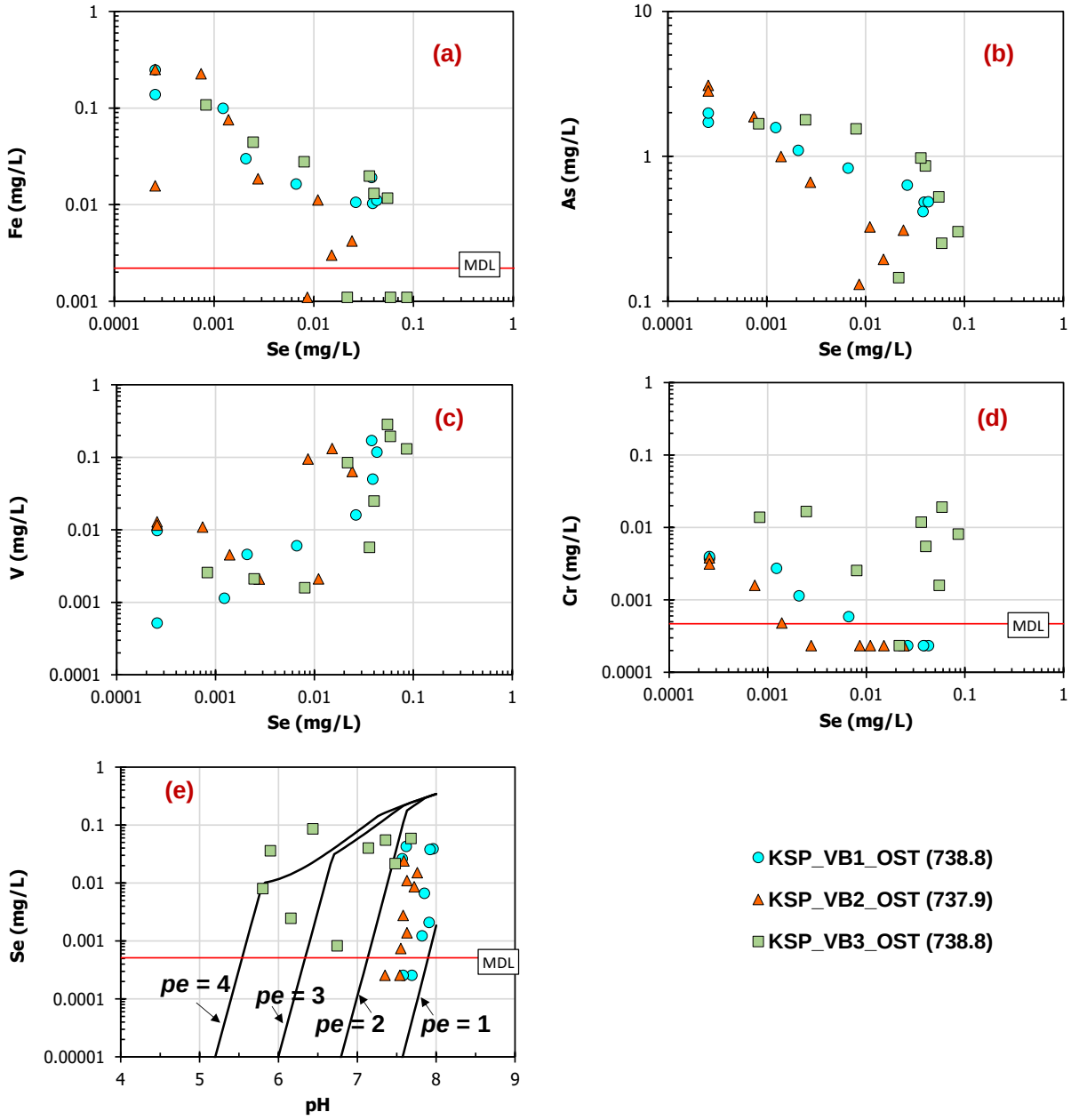

Figure 5.9 Relationships between eluate concentration of Se and (a) Fe, (b) As, (c) V, and (d) Cr for the three core samples during the hydraulic conductivity test; (e) concentrations of Se with pH for the three core samples during the hydraulic conductivity test (reference lines indicating Se concentration at different *pe* conditions based on the developed geochemical speciation model of Site 1 field ash [45]). Concentrations less than the method detection limit (MDL) are set as one half of the MDL.

Arsenic. For As, the initial eluates from the HC test with more reducing conditions seemed to show higher mobility into the solution compared to the Method 1314 column test (Figure 5.7(b)), which was the opposite to the behavior of Se and V as As concentrations were negatively correlated to Se concentrations (Figure 5.9(b)). The As concentrations in the first two HC eluates from the three samples were between 1-3 mg/L, close to the near-equilibrium concentrations in the reduced field porewater (Figure 5.7(b)). This result suggests that the core samples in the HC test appear to have well-preserved redox conditions of the field ashes with respect to As leaching. With the continuous increase of ΣL/S, eluate As concentrations from the HC test gradually decreased, while the Method 1314 column test results showed the reverse trend. The declining As concentrations in the HC test was likely because of the oxidation of As(III) to As(V) which enhanced the adsorption of As on the iron oxides or analogous surfaces. Therefore, As concentrations approached similar values between the HC test and the Method 1314 column test in the end, as As concentrations were controlled by adsorption equilibrium of As(V) at high ΣL/S for both tests. The wash-off effects are not likely to cause a significant decrease in As concentrations during the percolation test for cases where the adsorption-equilibrium is the primary controlling mechanism of As leaching (§5.3.1a).

Chromium. Unlike As, Se, and V, the impacts of the variations in redox conditions between the HC test and the Method 1314 column test were not readily observed for Cr. Concentrations of Cr in the eluates from both tests were generally less than 0.01 mg/L and fluctuated with ΣL/S without a discernible pattern (Figure 5.7(c)). Although often regarded as a redox-sensitive constituent, Cr in ash from this field site had low mobility under both reducing field porewater environment and oxidized laboratory leaching test conditions, consistent with the leaching behavior of Cr shown in the percolation tests. Additionally, only a weak correlation between Se concentrations (significantly impacted by redox changes) and Cr concentrations was observed for the HC eluates (Figure 5.9(d)).

The reason for the negligible impacts of redox conditions on Cr leaching for ash from this site is that the sample oxidation from an anoxic field environment to a suboxic laboratory leaching environment was not sufficient to cause a change in Cr speciation, and Cr was primarily as Cr(III) in both environments. The redox ladder in Figure 5.8(b) suggests that the transformation from Cr(III) to Cr(VI) happens under the oxic condition, while the oxidation reactions between

Fe(II)/Fe(III), As(III)/As(VI), and Se(0)/Se(IV) occur preceding Cr oxidation when strongly reduced ashes are retrieved and oxidized during the testing. The insensitivity of Cr leaching to redox changes shown here may not apply to other scenarios where the field ash is suboxic and then tested under an oxic leaching environment.

Overall, the HC test on field retrieved intact cores showed better preserved field redox conditions than the samples in repacked columns of the Method 1314 test. The redox conditions of samples significantly impacted the leaching of redox-sensitive oxyanions. Therefore, the results of percolation tests need to be carefully interpreted under the context of field conditions for field leaching estimation. For strongly reduced ash, a percolation test using field intact cores with redox conditions well preserved is recommended to better estimate the leaching of constituents under field scenarios. Also, based on the virtual material description of ashes tested under a laboratory oxidized environment, geochemical modeling is useful to infer the field release with the estimated field redox conditions.

5.3.4 Long-term leaching assessment of a coal ash impoundment under conceptual post-closure conditions

Knowledge of the hydrologic conditions at coal ash disposal sites is necessary for long-term leaching assessment, because the time required to reach a specific ΣL/S condition during percolation leaching can be estimated based on the discharge rate from hydrologic analysis. However, due to the wide variety of site configurations (e.g., impoundments, landfills, and combination of an impoundment with a landfill) and diverse climate conditions at different disposal sites, the time frame to reach a specific ΣL/S condition can be very different between sites and may have large uncertainties. According to an EPA report [2], the time required to reach the ΣL/S of 1 L/kg can range from 24.4 (5th percentile) to 5,087 years (95th percentile) for an open landfill based on the landfill depth and the estimated infiltration rate. The ΣL/S of 10 L/kg, the end-point condition in the percolation test, is equivalent to the discharge of 244 to 50,870 years (corresponding to 5th and 95th percentile). Compared to landfills with relatively dry conditions, impoundments under post-closure conditions are initially more saturated and are expected to have greater discharge through the base in early stages, which may result in greater

environmental risk in the early stage following the site closure.

Therefore, because of the broad range of hydrologic conditions at coal ash disposal sites, a site-specific hydrologic model should be coupled with leaching test results for long-term leaching assessment. Herein, an assessment example is provided for a conceptual impoundment by combining the results from a hydrologic model and the percolation leaching tests. The evaluation focuses on post-closure conditions, and the percolation test results are for the field ash collected one month after the closure of an impoundment (Site 1; Chapter 2) [45].

Hydrologic condition for a conceptual impoundment. In a coal ash impoundment after site closure, percolation of water into the site will be constrained by the final cover used to close the site, resulting in a variation of water discharge rate with time. The discharge process generally includes two periods: (i) an initial transient state with the drain down of porewater along with gradual decrease of water content and (ii) a steady state with the constant water content profile within the ash stack [139]. Initially, the water discharge rate is relatively high because of high water saturation at the beginning of post-closure period. In the transient state, the recharge rate from the cover is less than the discharge rate, leading to the water loss from the ash stack. Such decrease in water saturation will in turn lead to a decrease in discharge rate because of declining hydraulic conductivity. Finally, a steady state will be reached when the discharge rate is equal to the recharge rate, resulting in a constant water saturation for the ash stack.

According to the hydrologic model [139], the time frame for the transient and steady state of water discharge depends on the type of cover and the hydraulic properties of the ash. For an earthen cover with high percolation rate (250 mm/y), the time to reach steady state of water discharge after site closure is ~2 years for more permeable ash, ~3 years for typical ash, and ~4 years for less permeable ash. For a geosynthetic cover with low percolation rate under humid conditions (3 mm/y), a long transient period is required to reach the steady state water discharge, i.e., ~40 years for more permeable ash, ~80 years for typical ash, and ~200 years for less permeable ash. After the transient period, the long-term (i.e., steady state) discharge rate is 250 mm/y and 3 mm/y for the earthen cover and geosynthetic cover, respectively, equivalent to the recharge rate from each of the final cover.

The ΣL/S converted into post-closure leaching time indicates a significant distinction between scenarios with an earthen cover (Figure 5.10(a)) and a geosynthetic cover (Figure 5.10(b)). For

an earthen cover (Figure 5.10(a)), 2-4 years are needed to reach water discharge steady state, and the cumulative water discharge at the end of the transient state is approximately ΣL/S of 0.1-0.2 L/kg for ashes with a range of hydraulic conductivities (K_s: 5.0×10^{-6} – 6.0×10^{-4} cm/s). During subsequent steady state, the annual water discharge represents an L/S of approximately 0.022 L/kg; therefore, ~450 years would be required to reach an ΣL/S of 10 L/kg.

For a geosynthetic cover (Figure 5.10(b)), the water discharge during 40-200 years of transient state contributes to an ΣL/S of 0.1-0.4 L/kg, similar to the ΣL/S condition for the earthen cover. Due to the low percolation rate from the geosynthetic cover, the steady state has an annual water discharge of only 0.0003 L/kg. Thus, it takes a substantially longer time (~40 thousand years) to reach an ΣL/S of 10 L/kg. The amounts of time required to reach the ΣL/S of 1 and 10 L/kg for the relatively permeable earthen cover and less permeable geosynthetic cover are respectively close to the lower boundary and upper boundary of the time range from the EPA report (i.e., the time range from the EPA report is in purple bar in Figure 5.10) [2]. The three types of ashes with different hydraulic conductivities have slight variations in the cumulative water discharge during the transient state, while similar long-term cumulative water discharge is approached under steady state conditions.

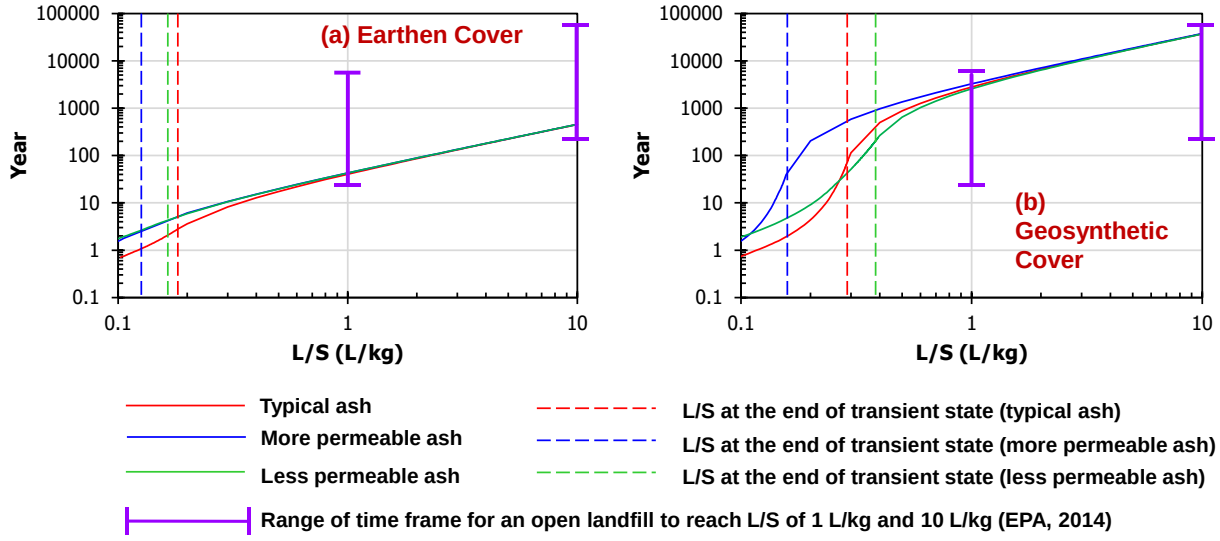

Figure 5.10 Relationships between post-closure leaching time and L/S for an impoundment closed with (a) an earthen cover and (b) a geosynthetic cover.

The relationship between field cumulative L/S and leaching time under post closure conditions is based on a simplified system with several assumptions. First, the hydrologic model assumes a cover that remains intact during time interval, which may underestimate the water infiltration rate due to potential cover damage or degradation. Also, the model assumes uniform hydrologic properties within the site, but heterogeneity in field conditions is possible which can result in preferential flow. The preferential flow would lead to locally higher L/S conditions. Additionally, the geological controls such as by an aquitard below the impoundment can reduce the discharge rate in comparison to the herein assumed scenario without a geological control.

Therefore, the assumptions for the simplified system may cause uncertainties for the translation of field L/S condition to leaching time, especially for the projection into time intervals greater than thousands of years in future where uncertainties can be magnified. As a result, the evaluation of long-term leaching is focused on the leaching time within one thousand years.

Boron and Molybdenum. The long-term leaching behavior of oxyanions from the coal ash impoundment under post-closure conditions is evaluated using the percolation test results of field ash from Site 1 as an example. For highly soluble constituents B and Mo, which typically show rapid concentration drop within ΣL/S of 2 L/kg, the decrease in B and Mo concentrations by one order of magnitude can last for ~100 years for an earthen cover (Figure 5.11(a)) and more than one thousand years for a geosynthetic cover (Figure 5.11(b)). For this early stage, the release rate of B and Mo is greater than the late stage due to the greater eluate concentrations.

Chromium. For Site 1, the laboratory leaching tests with suboxic conditions compared to the field anoxic conditions have not shown to impact the leaching results of Cr (§5.3.3). Therefore, the results of Cr from the laboratory percolation test on the field ash are assumed to be representative for the long-term field leaching behavior of Cr. Compared to highly soluble B and Mo, Cr shows relatively constant concentrations as controlled by adsorption equilibrium during the entire evaluated period. As a result, Cr release gradually increases with time with a relatively consistent rate. However, because of the low Cr concentrations (< 0.01 mg/L) under the test conditions, the cumulative release from the transient state period only contributes < 0.1% of the available content and < 0.001% of the total content. The total release fraction at the end of the evaluated period (~400 years for an earthen cover and 1,000 thousand years for a geosynthetic cover) is still small (less than 1% of the available content and 0.1% of the total content).

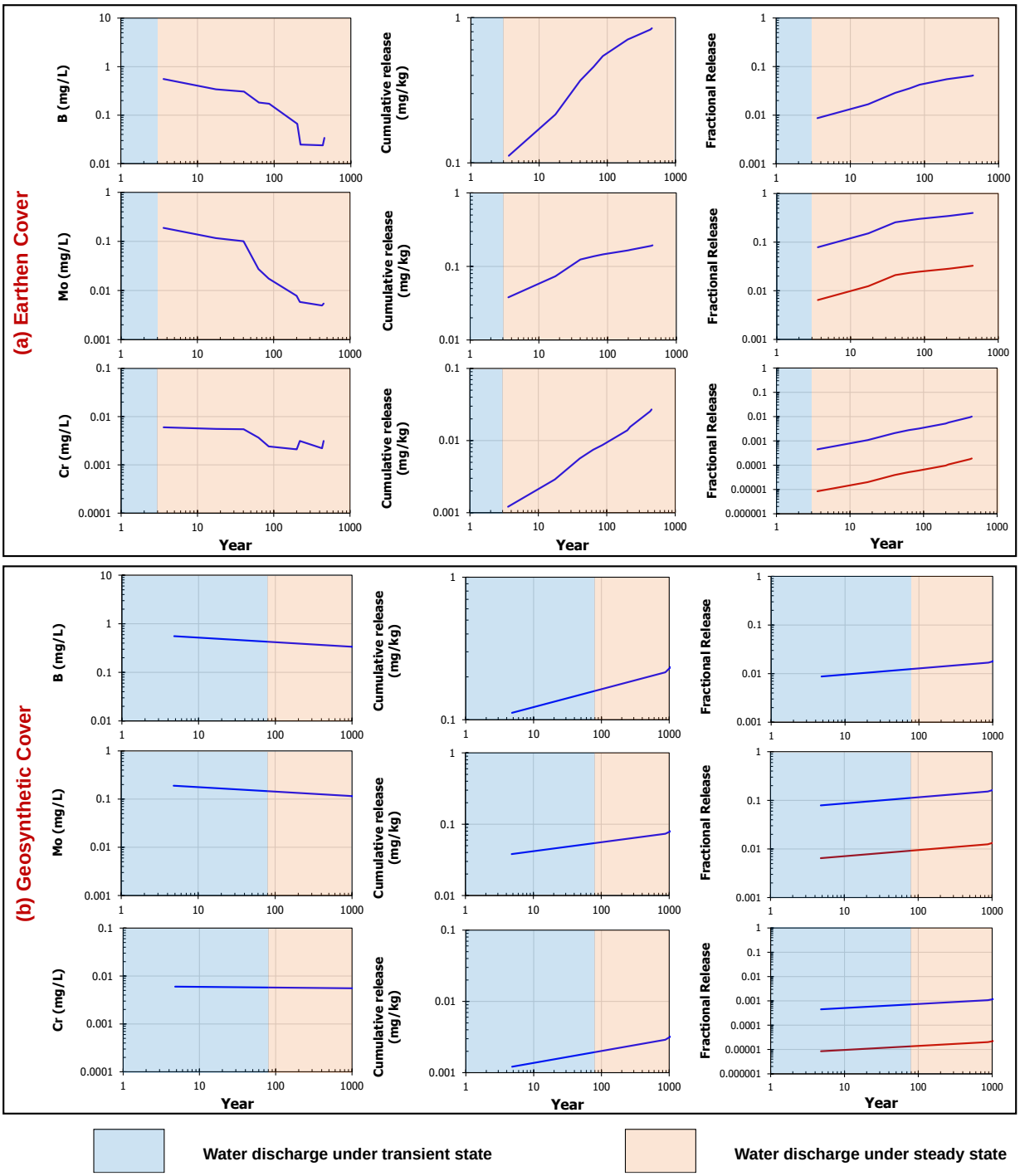

Figure 5.11 Concentration and release of B, Mo, and Cr as a function of time under post-closure conditions for a conceptual impoundment closed with (a) an earthen cover and (b) a geosynthetic cover. Fractional release (blue lines): the fraction of cumulative release relative to the available content (i.e., the maximum release in the pH-dependent leaching test). Fractional release (red lines): the fraction of cumulative release relative to total content. Total content of B is not available. Water discharge is shown for coal ash with typical hydraulic conductivity.

Arsenic, Selenium, and Vanadium. Previous studies have suggested that the leaching behaviors of As, Se, and V in laboratory leaching tests are significantly different from their field leaching behaviors because of ash sample oxidation from an anoxic field environment to a suboxic laboratory test environment. Thus, the results from laboratory percolation tests may not be good indicators of the field leaching assessment of a coal ash impoundment. Therefore, the measured concentrations of As, Se, and V in the field porewater are included to estimate the long-term release. The release from the two scenarios provides bounding cases for oxidized conditions in the laboratory (solid line in Figure 5.12) and assumed anoxic conditions present during the entire evaluation period after site closure (dashed line in Figure 5.12).

For As, the laboratory percolation test under oxidized conditions indicated relatively consistent concentrations between 0.4 and 0.6 mg/L during transient and steady state water discharge, resulting in a fractional release (relative to available content) of ~0.2% at the end of the transient state period and ~15% at 400 years for an earthen cover and 0.5% at 1,000 years for a geosynthetic cover. However, the one-year field sampling starting from ~1 month after the site closure suggested that the field anoxic environment was established quickly (i.e., within 1 month) after the final cover was placed. Under an anoxic environment, steady As concentrations as high as ~3 mg/L were measured in the field porewater due to desorption [45]. By assuming constant As concentration in porewater at the measured value, the total fractional release of As based on available content was estimated as ~75% at 400 years for an earthen cover and 4% at 1,000 years for a geosynthetic cover, which was significantly greater than the results (15% and 0.5%) estimated based on laboratory percolation test results.

In contrast to the case for As, the field anoxic environment inhibited the release of Se and V compared to the release under the laboratory oxidized environment. Under laboratory oxidized conditions, the Se appeared to be highly soluble, and the V was primarily controlled by adsorption equilibrium during the entire evaluated period. Thus, the total release of Se (based on available content) at the end of the evaluated steady state period approached 100% and 20%, respectively, for the earthen cover and geosynthetic cover scenarios, while the total release of V was much lower at ~8% and 0.4% for the two scenarios. However, under the field reducing conditions, both Se and V were well stabilized, potentially because of the precipitation of Se metal, FeSe, and V(IV)-bearing minerals, resulting in concentrations less than the MDL (0.0005 and 0.00032 mg/L for Se and V, respectively) [45]. Accordingly, the fractional release of Se and

V under the field reducing conditions was substantially less than the estimated release under the laboratory oxidized conditions. For example, for the earthen cover scenario, the fractional release (based on the available content) of Se and V was respectively 0.5% and 0.02% at the end of the evaluated steady state period (400 years after site closure).

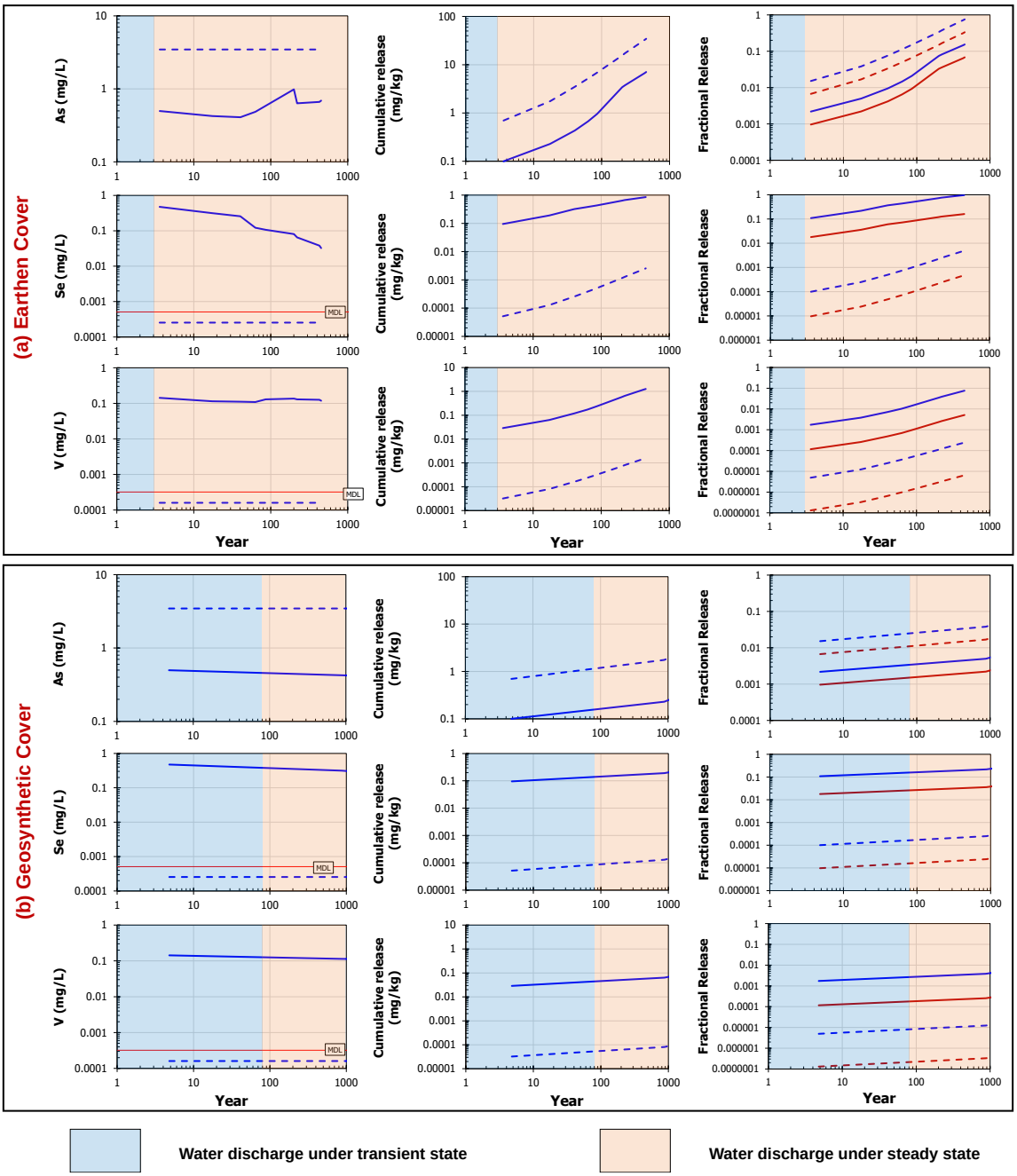

Figure 5.12 Concentration and release of As, Se, and V as a function of time under post-closure conditions for a conceptual impoundment closed with (a) an earthen cover and (b) a geosynthetic cover. Solid lines: under laboratory conditions (suboxic). Dashed lines: under field conditions (anoxic). Fractional release (blue lines): the fraction of cumulative release relative to the available content (i.e., the maximum release in the pH-dependent leaching test). Fractional release (red lines): the fraction of cumulative release relative to total content. Total content of B is not available. Water discharge is shown for coal ash with typical hydraulic conductivity. Concentrations of Se and V less than the method detection limit (MDL) are set as one half of the MDL.

5.4 Conclusions

This study identified important phenomena and key factors impacting the long-term release of As, B, Cr, Mo, Se, and V in coal ash disposal sites. The percolation test results for a range of as-generated ashes and field ashes were used to evaluate the leaching of oxyanions, assisted by the batch leaching testing and geochemical speciation modeling results presented in previous studies [45,115,147]. Major conclusions from this study are:

- Both adsorption and mineral coprecipitation reactions are important retention mechanisms controlling the percolation leaching behavior of oxyanions through local chemical equilibrium. The batch leaching test is necessary for the identification of chemical equilibrium controlling reactions, which can be further verified by geochemical speciation modeling.
- For leaching of oxyanions where adsorption or mineral coprecipitation reactions have minimal impact, the initial leaching period within ΣL/S of 2 L/kg is of most concern due to the rapid release of these oxyanions. Under post-closure conditions, it can take more than 100 years to reach an ΣL/S of 2 L/kg. The highly soluble oxyanions such as B and Mo are more readily leached than other oxyanions, as exhibited for several coal ash samples.
- The field weathering process of alkaline ashes such as carbonation and formation of ettringite can effectively reduce the leaching of oxyanions. Based on the field study on a coal ash management site (Site 2), the cumulative release of B from field weathered ashes was reduced by 90% at the ΣL/S of 2 L/kg and by 60% at the ΣL/S of 10 L/kg compared to the release from as-generated ash with similar available content of B, potentially due to the formation of a B-containing carbonate solid solution. Similarly, the cumulative release of Mo from field weathered ashes was reduced by 90% at both the ΣL/S of 2 and 10 L/kg conditions compared to the as-generated ash.
- Field ashes are more reducing compared to the as-generated ash, potentially impacting the leaching of redox-sensitive oxyanions (e.g., As, Cr, Se, and V). The impacts of redox conditions need to be evaluated for site-specific conditions. For the alkaline ash disposal landfill, the release rate of Cr from field ashes was greatly reduced (by 90%) compared to the as-generated ash. Due to the potential sample oxidation in the laboratory test, the percolation test carried out under well-controlled redox conditions using the intact field

cores is suggested to better represent the leaching behavior of redox-sensitive oxyanions under field conditions, in comparison to the standard percolation test with samples subject to oxidation during collection and repacking in the laboratory.

- The long-term leaching assessment of coal ash disposal sites requires estimation of the site-specific hydrologic conditions, which have large uncertainties depending on the site configuration, the type of final cover, and climate conditions. The time frame to reach an ΣL/S of 10 L/kg can take ~100 to ~10,000 years after site closure. For a conceptual closed impoundment, at ΣL/S of 10 L/kg (equivalent to 400 years for the earthen cover and 40 thousand years for the geosynthetic cover), the total release of relatively soluble B and Mo was estimated as ~7 and ~40%, respectively (relative to the available content); the total release of Cr, Se, and V was estimated as ~1, 0.5, and 0.02%, respectively, because of their low concentrations under reducing field conditions. The total release of As could be up to 71% due to desorption of As under strongly reducing conditions.

CHAPTER 6

CONCLUSIONS AND FUTURE WORK

This dissertation characterized the effects and mechanisms of important variables (material major chemical composition and field environmental conditions) on the leaching of oxyanionic constituents (As, B, Cr, Mo, Se, and V) from coal ash at disposal sites. The main conclusions are summarized here concerning (i) primary mechanisms controlling and distinctions between the oxyanion leaching from as-generated and field-disposed ashes, (ii) evaluation of the use of laboratory leaching characterization for the estimation of oxyanion partitioning in field porewater, (iii) methodologies for the development of a geochemical speciation model for leaching assessment, and (iv) methodologies for long-term leaching assessment. Details for each conclusion are presented as follows:

- Three primary mechanisms have been identified that control the leaching of oxyanions from coal fly ash, depending on the major composition (e.g., Ca and S) and the pH domain considered. These mechanisms include (i) adsorption to iron oxides or analogous surfaces, (ii) co-precipitation with Ca-bearing minerals, and (iii) substitution into ettringite; these mechanisms are suggested as important retention mechanisms controlling the dynamic leaching behavior of oxyanions in percolation tests through local chemical equilibrium. Therefore, these mechanisms should be considered important for the assessment of long-term release of oxyanions in coal fly ash.

- Weathering of coal ashes during field disposal such as carbonation and ettringite formation as observed in the study of the Site 2 coal management unit (i.e., a dry-handled landfill on top of a historical ash impoundment) changes the mechanisms controlling the equilibrium leaching and dynamic leaching behavior of oxyanions.

    - Through the formation of a less soluble carbonate solid solution, the carbonation reaction decreases B concentrations at natural pH in the batch leaching test compared to the as-generated ash. Correspondingly, the cumulative release of B was reduced

substantially (by 60% at the L/S of 10 L/kg-dry of column test) from the field ashes in comparison to the release from as-generated ashes.

  - Ettringite can form as a secondary mineral phase during hydration of alkaline ashes at pH > 9.5. Ettringite formation decreases solubility by the incorporation of oxyanions into the ettringite solid solution. At Site 2, for example, ettringite was suggested to decrease the mobility of Mo (a typical highly soluble constituent in as-generated coal ashes) in field ashes, resulting in a reduction of the release rate from the column tests of 90%.

- Laboratory leaching tests at a low liquid-to-solid ratio (L/S), a modification of the EPA Method 1313, can be used to approximate the field porewater concentrations of non-redox-sensitive constituents, such as B and Mo. However, results from standard laboratory leaching tests reflected more oxidized conditions than are present in the field. Thus, laboratory leaching extractions alone may not be sufficient to understand the leaching of redox-sensitive constituents (e.g., As, Se, Sb, and V) under reducing field redox conditions.

  - The field study on a closed coal ash impoundment (Site 1) showed that sluiced ash with neutral pH supports biological activity, resulting in a strongly reducing field condition (as supported by observations of methanogenesis and sulfate reduction). The pore gas composition indicated lower in situ redox than porewater measurements. Such field-reducing environments stabilize Se as insoluble minerals (Se metal or FeSe). Spatially heterogeneous concentrations of As in porewater vary with local redox potential, where ferric oxide desorption and sulfide precipitation appear to control As leaching in reducing environments. During testing under laboratory conditions, the strongly anoxic field environment was oxidized to a suboxic condition, which resulted in a change in As and Se speciation and, therefore, under- and over-estimated As and Se concentrations, respectively, compared to porewater measurements.

  - Field redox conditions vary by the chemical composition of the disposed material and the configuration of the site; therefore, results of laboratory leaching tests for estimating field leaching behavior should be interpreted in the context of the specific site conditions and constituent behavior. Compared to the strongly reducing field

environment (anoxic) at Site 1 with sluiced ash and near neutral pH, the strongly alkaline pH condition observed at Site 2 did not support significant microbial reduction activity and, therefore, had a less reducing environment (suboxic). At Site 2, the sample oxidation from the suboxic field condition to the oxic laboratory condition resulted in the oxidative dissolution of insoluble Cr(III) oxides and conversion of Se(0) in the solid and dissolved Se(IV)/Se(VI) but did not lead to a change of As speciation between the laboratory test eluates and field porewater as observed at Site 1.

  - The two field studies in this dissertation cover two typical field conditions for coal ash disposal sites, including (i) strongly reducing conditions potentially developed in closed impoundments, and (ii) suboxic conditions in landfills with a more alkaline environment. The key factor controlling the field redox conditions is suggested as the field pH environment, as a near neutral pH condition can facilitate the rapid development of a reducing field environment by microbial activity in comparison to the alkaline pH condition that can result in a suboxic field environment because of the absence of microbial activity. Therefore, a reducing field environment may be common for coal ash disposal sites with near neutral pH condition at the time of site closure. A suboxic field environment is expected to be maintained for a substantially long time at disposal sites with alkaline ashes, given the long time frame to transform from an initial alkaline pH to a near neutral pH condition through natural abiotic processes (e.g., calcium leaching and carbonation).

- Geochemical speciation models developed from laboratory leaching test results are a useful tool for estimating equilibrium leaching of oxyanions in field porewater, as well as to evaluate the change of concentration in response to the range of field geochemical parameters (pH, L/S, and redox potential). To improve model fidelity, several model uncertainties need to be considered in the use of the reported adsorption model and mineral reaction set.

  - The widely-used diffuse double-layer adsorption model for hydrous ferric oxide caused substantial deviations in predicted leaching from the measured concentrations of Se and V due to uncertainties from the nonideal adsorption surfaces and competitive

adsorption effects. Calibration of adsorption reaction sets improved the simultaneous description of leaching for multiple oxyanions.

  - For the assessment of leaching from alkaline ashes, the reported solubility product for a mineral phase (e.g., Ca-arsenate) has a wide reported range. Therefore, the selection of phases should be verified with experimental data under a range of conditions to better identify uncertainties. In addition, postulated experimental phases were necessary to predict B, Cr, Se, and V leaching due to the limitation of reported thermodynamic databases.

  - For a typically strongly alkaline fly ash, the use of a calibrated reaction set of an oxyanion-substituted ettringite solid solution successfully captured the simultaneous retention of all oxyanionic constituents at pH > 9.5. The reaction set was originally developed from other cement-based waste materials and is applicable to both as-generated and field-disposed coal ashes.

- The long-term release of oxyanionic constituents in disposal sites can be estimated by laboratory leaching testing in conjunction with a hydrologic model.

  - Laboratory leach testing (EPA Method 1313 at L/S of 10 and 1 L/kg-dry and EPA Method 1314) is necessary for the identification of chemical equilibrium controlling reactions for the leaching of oxyanions, while the percolation test carried out under well-controlled redox conditions using the field intact cores is suggested to better represent the leaching behavior of redox-sensitive constituents under field conditions. Geochemical speciation modeling is an alternative approach to estimate the field release with estimated field redox conditions.

  - The time frame to reach an L/S of 2 and 10 L/kg-dry (i.e., the end-point L/S condition in EPA Method 1314 test), respectively, can take *ca.* 100-6,000 years and 400-40,000 years under post-closure conditions, depending on the type of final cover and climate conditions for a conceptual impoundment. Based on testing, the period up to a cumulative L/S to 2 L/kg-dry is of most concern considering the rapid release of readily soluble constituents.

For future work, the geochemical speciation model developed in this study should be coupled with a reactive transport model for predicting oxyanion leaching from the percolation test. Therefore, the reactive transport modeling results can provide an estimation of long-term oxyanion leaching as a function of time.

RERFERENCES

[1] American Coal Ash Association, 2020 Production and Use Survey Results News Release, (2020). https://acaa-usa.org/wp-content/uploads/2021/12/News-Release-Coal-Ash-Production-and-Use-2020.pdf (accessed August 4, 2022).

[2] U.S. EPA, Human and Ecological Risk Assessment of Coal Combustion Residuals, US EPA, 2050-AE81, Washington, DC, 2014.

[3] G. Cornelis, C.A. Johnson, T. van Gerven, C. Vandecasteele, Leaching mechanisms of oxyanionic metalloid and metal species in alkaline solid wastes: A review, Applied Geochemistry. 23 (2008) 955–976. https://doi.org/10.1016/j.apgeochem.2008.02.001.

[4] M. Izquierdo, X. Querol, Leaching behaviour of elements from coal combustion fly ash: An overview, Int J Coal Geol. 94 (2012) 54–66. https://doi.org/10.1016/j.coal.2011.10.006.

[5] L. Ruhl, A. Vengosh, G.S. Dwyer, H. Hsu-Kim, A. Deonarine, Environmental impacts of the coal ash spill in Kingston, Tennessee: An 18-month survey, Environ Sci Technol. 44 (2010) 9272–9278. https://doi.org/10.1021/es1026739.

[6] J. Hudson, Santee cooper's coal ash impoundment closure challenge: Risk reduction through recycling, in: Sustainable Electricity II: A Conversation on Tradeoffs, 2018. https://doi.org/10.1007/978-3-319-95696-1_10.

[7] G. Cornelis, T. van Gerven, C. Vandecasteele, Antimony leaching from MSWI bottom ash: Modelling of the effect of pH and carbonation, Waste Management. 32 (2012) 278–286. https://doi.org/10.1016/j.wasman.2011.09.018.

[8] S. v. Vassilev, C.G. Vassileva, A new approach for the classification of coal fly ashes based on their origin, composition, properties, and behaviour, Fuel. 86 (2007) 1490–1512. https://doi.org/10.1016/j.fuel.2006.11.020.

[9] T. Wang, J. Wang, Y. Tang, H. Shi, K. Ladwig, Leaching characteristics of arsenic and selenium from coal fly ash: Role of calcium, Energy and Fuels. 23 (2009) 2959–2966. https://doi.org/10.1021/ef900044w.

[10] G. Neupane, R.J. Donahoe, Leachability of elements in alkaline and acidic coal fly ash samples during batch and column leaching tests, Fuel. 104 (2013) 758–770. https://doi.org/10.1016/j.fuel.2012.06.013.

[11] D. Kosson, F. Sanchez, P. Kariher, L.H. Turner, R. DeLapp, P. Seignette, Characterization of Coal Combustion Residues from Electric Utilities – Leaching and Characterization Data, EPA-600/R-09/151, US EPA, Research Triangle Park, NC, 2009.

[12] S.A. Thorneloe, D.S. Kosson, F. Sanchez, A.C. Garrabrants, G. Helms, Evaluating the fate of metals in air pollution control residues from coal-fired power plants, Environ Sci Technol. 44 (2010) 7351–7356. https://doi.org/10.1021/es1016558.

[13] A. Deonarine, A. Kolker, A.L. Foster, M.W. Doughten, J.T. Holland, J.D. Bailoo, Arsenic Speciation in Bituminous Coal Fly Ash and Transformations in Response to Redox Conditions, Environ Sci Technol. 50 (2016) 6099–6106. https://doi.org/10.1021/acs.est.6b00957.

[14] L. Zhao, S. Dai, R.B. Finkelman, D. French, I.T. Graham, Y. Yang, J. Li, P. Yang, Leaching behavior of trace elements from fly ashes of five Chinese coal power plants, Int J Coal Geol. 219 (2020) 103381. https://doi.org/10.1016/J.COAL.2019.103381.

[15] A. Garrabrants, D. Kosson, L. Stefanski, R. DeLapp, Interlaboratory Validation of the Leaching Environmental Assessment Framework (LEAF) Method 1314 and Method 1315, EPA/600/R/12/706, US EPA, Washington, DC, 2012.

[16] A. Garrabrants, D. Kosson, L. Stefanski, R. DeLapp, Interlaboratory Validation of the Leaching Environmental Assessment Framework (LEAF) Method 1313 and Method 1316, EPA/600/R/12/623, US EPA, Washington, DC, 2012.

[17] D.S. Kosson, H.A. van der Sloot, F. Sanchez, A.C. Garrabrants, An Integrated Framework for Evaluating Leaching in Waste Management and Utilization of Secondary Materials, Environ Eng Sci. 19 (2002) 159–204. https://doi.org/10.1089/109287502760079188.

[18] D. Kosson, H. van der Sloot, A. Garrabrants, P. Seignette, Leaching Test Relationships, Laboratory-to-Field Comparisons and Recommendations for Leaching Evaluation using the Leaching Environmental Assessment Framework, EPA/600/R-14/061, US EPA, Cincinnati, OH, 2014.

[19] U.S. EPA, Leaching Environmental Assessment Framework (LEAF) How-To Guide: Understanding the LEAF Approach and How and When to Use It, US EPA, SW-846 Update VII, 2019.

[20] A.C. Garrabrants, D.S. Kosson, K.G. Brown, D.P. Fagnant, G. Helms, S.A. Thorneloe, Methodology for scenario-based assessments and demonstration of treatment effectiveness using the Leaching Environmental Assessment Framework (LEAF), J Hazard Mater. 406 (2021) 124635. https://doi.org/10.1016/J.JHAZMAT.2020.124635.

[21] T. Borch, R. Kretzschmar, A. Skappler, P. van Cappellen, M. Ginder-Vogel, A. Voegelin, K. Campbell, Biogeochemical redox processes and their impact on contaminant dynamics, Environ Sci Technol. 44 (2010) 15–23. https://doi.org/10.1021/es9026248.

[22] G.E. Schwartz, N. Rivera, S.W. Lee, J.M. Harrington, J.C. Hower, K.E. Levine, A. Vengosh, H. Hsu-Kim, Leaching potential and redox transformations of arsenic and selenium in sediment microcosms with fly ash, Applied Geochemistry. 67 (2016) 177–185. https://doi.org/10.1016/j.apgeochem.2016.02.013.

[23] A.J. Bednar, D.E. Averett, J.M. Seiter, B. Lafferty, W.T. Jones, C.A. Hayes, M.A. Chappell, J.U. Clarke, J.A. Steevens, Characterization of metals released from coal fly ash during dredging at the Kingston ash recovery project, Chemosphere. 92 (2013) 1563–1570. https://doi.org/10.1016/j.chemosphere.2013.04.034.

[24] K. Kim, S.H. Kim, S.M. Park, J. Kim, M. Choi, Processes controlling the variations of pH, alkalinity, and CO2 partial pressure in the porewater of coal ash disposal site, J Hazard Mater. 181 (2010) 74–81. https://doi.org/10.1016/j.jhazmat.2010.04.089.

[25] S. Stefaniak, E. Miszczak, J. Szczepańska-Plewa, I. Twardowska, Effect of weathering transformations of coal combustion residuals on trace element mobility in view of the environmental safety and sustainability of their disposal and use. I. Hydrogeochemical processes controlling pH and phase stability, J Environ Manage. 156 (2015) 128–142. https://doi.org/10.1016/j.jenvman.2015.03.046.

[26] Z. Chen, P. Zhang, K.G. Brown, J.L. Branch, H.A. van der Sloot, J.C.L. Meeussen, R.C. Delapp, W. Um, D.S. Kosson, Development of a Geochemical Speciation Model for Use in Evaluating Leaching from a Cementitious Radioactive Waste Form, Environ Sci Technol. 55 (2021) 8642–8653. https://doi.org/10.1021/acs.est.0c06227.

[27] H.A. van der Sloot, D.S. Kosson, A. van Zomeren, Leaching, geochemical modelling and field verification of a municipal solid waste and a predominantly non-degradable waste landfill, Waste Management. 63 (2017) 74–95. https://doi.org/10.1016/j.wasman.2016.07.032.

[28] L. Tiruta-Barna, Z. Rakotoarisoa, J. Méhu, Assessment of the multi-scale leaching behaviour of compacted coal fly ash, J Hazard Mater. 137 (2006) 1466–1478. https://doi.org/10.1016/j.jhazmat.2006.04.039.

[29] W. Wang, Y. Qin, D. Song, K. Wang, Column leaching of coal and its combustion residues, Shizuishan, China, Int J Coal Geol. 75 (2008) 81–87. https://doi.org/10.1016/J.COAL.2008.02.004.

[30] H.A. van der Sloot, J.C.L. Meeussen, D.S. Kosson, O. Hjelmar, Use of chemical speciation and reactive transport to predict leaching from coal combustion residues, in: 2nd International

Conference on Sustainable Construction Materials and Technologies, Ancona, Italy, 2010: pp. 28–30.

[31] S. Hareeparsad, L. Tiruta-Barna, C.J. Brouckaert, C.A. Buckley, Quantitative geochemical modelling using leaching tests: Application for coal ashes produced by two South African thermal processes, J Hazard Mater. 186 (2011) 1163–1173. https://doi.org/10.1016/j.jhazmat.2010.11.127.

[32] M. Loncnar, H.A. van der Sloot, A. Mladenovič, M. Zupančič, L. Kobal, P. Bukovec, Study of the leaching behaviour of ladle slags by means of leaching tests combined with geochemical modelling and mineralogical investigations, J Hazard Mater. 317 (2016) 147–157. https://doi.org/10.1016/j.jhazmat.2016.05.046.

[33] B. Du, J. Li, W. Fang, Y. Liu, S. Yu, Y. Li, J. Liu, Characterization of naturally aged cement-solidified MSWI fly ash, Waste Management. 80 (2018) 101–111. https://doi.org/10.1016/j.wasman.2018.08.053.

[34] P. Zhang, Z. Chen, K.G. Brown, A.C. Garrabrants, R. Delapp, J.C.L. Meeussen, H.A. van der Sloot, D.S. Kosson, Impact of carbonation on leaching of constituents from a cementitious waste form for treatment of low activity waste at the DOE Hanford site, Waste Management. 144 (2022) 431–444. https://doi.org/10.1016/J.WASMAN.2022.04.009.

[35] G.E. Schwartz, J.C. Hower, A.L. Phillips, N. Rivera, A. Vengosh, H. Hsu-Kim, Ranking Coal Ash Materials for Their Potential to Leach Arsenic and Selenium: Relative Importance of Ash Chemistry and Site Biogeochemistry, Environ Eng Sci. 35 (2018) 728–738. https://doi.org/10.1089/ees.2017.0347.

[36] L. Zhao, S. Dai, R.B. Finkelman, D. French, I.T. Graham, Y. Yang, J. Li, P. Yang, Leaching behavior of trace elements from fly ashes of five Chinese coal power plants, Int J Coal Geol. 219 (2020) 103381. https://doi.org/10.1016/J.COAL.2019.103381.

[37] ASTM C618-19, Standard Specification for Coal Fly Ash and Raw or Calcined Natural Pozzolan for Use in Concrete, ASTM International, West Conshohocken, PA, 2019.

[38] S. Zhao, Z. Chen, J. Shen, J. Kang, J. Zhang, Y. Shen, Leaching mechanisms of constituents from fly ash under the influence of humic acid, J Hazard Mater. 321 (2017) 647–660. https://doi.org/10.1016/J.JHAZMAT.2016.09.054.

[39] K. Komonweeraket, B. Cetin, A. Aydilek, C.H. Benson, T.B. Edil, Geochemical Analysis of Leached Elements from Fly Ash Stabilized Soils, Journal of Geotechnical and Geoenvironmental Engineering. 141 (2015) 04015012. https://doi.org/10.1061/(ASCE)GT.1943-5606.0001288.

[40] Y. Zhang, B. Cetin, W.J. Likos, T.B. Edil, Impacts of pH on leaching potential of elements from MSW incineration fly ash, Fuel. 184 (2016) 815–825. https://doi.org/10.1016/J.FUEL.2016.07.089.

[41] M. Mahedi, B. Cetin, A.Y. Dayioglu, Leaching behavior of aluminum, copper, iron and zinc from cement activated fly ash and slag stabilized soils, Waste Management. 95 (2019) 334–355. https://doi.org/10.1016/J.WASMAN.2019.06.018.

[42] Y.N. Zhu, X.H. Zhang, Q.L. Xie, D.Q. Wang, G.W. Cheng, Solubility and stability of calcium arsenates at 25°C, Water Air Soil Pollut. 169 (2006) 221–238. https://doi.org/10.1007/s11270-006-2099-y.

[43] J. v. Bothe, P.W. Brown, Arsenic immobilization by calcium arsenate formation, Environ Sci Technol. 33 (1999) 3806–3811. https://doi.org/10.1021/es980998m.

[44] E.E. van der Hoek, P.A. Bonouvrie, R.N.J. Comans, Sorption of As and Se on mineral components of fly ash: Relevance for leaching processes, Applied Geochemistry. 9 (1994) 403–412. https://doi.org/10.1016/0883-2927(94)90062-0.

[45] X. Wang, A.C. Garrabrants, Z. Chen, H.A. van der Sloot, K.G. Brown, Q. Qiu, R. DeLapp, B. Hensel, D.S. Kosson, The influence of redox conditions on aqueous-solid partitioning of arsenic

and selenium in a closed coal ash impoundment, J Hazard Mater. 428 (2022) 128255. https://doi.org/10.1016/J.JHAZMAT.2022.128255.

[46] T. Su, J. Wang, Modeling batch leaching behavior of arsenic and selenium from bituminous coal fly ashes, Chemosphere. 85 (2011) 1368–1374. https://doi.org/10.1016/j.chemosphere.2011.08.002.

[47] J. Wang, T. Wang, J.G. Burken, C.C. Chusuei, H. Ban, K. Ladwig, C.P. Huang, Adsorption of arsenic(V) onto fly ash: A speciation-based approach, Chemosphere. 72 (2008) 381–388. https://doi.org/10.1016/j.chemosphere.2008.02.045.

[48] J.O. Leckie, M.M. Benjamin, K. Hayes, G. Kaufman, S. Altman, Adsorption/Coprecipitation of Trace Elements from Water with Iron Oxyhydroxide, EPRI-CS-1513, EPRI, Palo Alto, CA, 1980.

[49] G. Neupane, R.J. Donahoe, Y. Arai, Kinetics of competitive adsorption/desorption of arsenate and phosphate at the ferrihydrite-water interface, Chem Geol. 368 (2014) 31–38. https://doi.org/10.1016/j.chemgeo.2013.12.020.

[50] T. Hua, R.J. Haynes, Y.F. Zhou, Competitive adsorption and desorption of arsenate, vanadate, and molybdate onto the low-cost adsorbent materials alum water treatment sludge and bauxite, Environmental Science and Pollution Research. 25 (2018) 34053–34062. https://doi.org/10.1007/s11356-018-3301-7.

[51] K.D. Hristovski, J. Markovski, Engineering metal (hydr)oxide sorbents for removal of arsenate and similar weak-acid oxyanion contaminants: A critical review with emphasis on factors governing sorption processes, Science of The Total Environment. 598 (2017) 258–271. https://doi.org/10.1016/J.SCITOTENV.2017.04.108.

[52] D.A. Dzombak, F. Morel, Surface Complexation Modeling: Hydrous Ferric Oxide, John Wiley & Sons, 1990.

[53] L. Wang, Q. Chen, I.A. Jamro, R. Li, Y. Li, S. Li, J. Luan, Geochemical modeling and assessment of leaching from carbonated municipal solid waste incinerator (MSWI) fly ash, Environmental Science and Pollution Research. 23 (2016) 12107–12119. https://doi.org/10.1007/s11356-016-6320-2.

[54] J.A. Davis, R.O. James, J.O. Leckie, Surface ionization and complexation at the oxide/water interface. I. Computation of electrical double layer properties in simple electrolytes, J Colloid Interface Sci. 63 (1978) 480–499. https://doi.org/10.1016/S0021-9797(78)80009-5.

[55] T. Hiemstra, W.H. Van Riemsdijk, A surface structural approach to ion adsorption: The charge distribution (CD) model, J Colloid Interface Sci. 179 (1996) 488–508. https://doi.org/10.1006/jcis.1996.0242.

[56] U.S. EPA, MINTEQA2/PRODEFA2, A geochemical assessment model for environmental systems: user manual supplement for version 4.0, US EPA, Athens, Georgia, 1998.

[57] D.L. Parkhurst, C.A.J. Appelo, Description of input and examples for PHREEQC version 3: a computer program for speciation, batch-reaction, one-dimensional transport, and inverse geochemical calculations, US Geological Survey, No. 6-A43, 2013.

[58] J.C.L. Meeussen, Orchestra: An object-oriented framework for implementing chemical equilibrium models, Environ Sci Technol. 37 (2003) 1175–1182. https://doi.org/10.1021/es025597s.

[59] H.I. Adegoke, F.A. Adekola, O.S. Fatoki, B.J. Ximba, Sorptive interaction of oxyanions with iron oxides: A Review, Pol J Environ Stud. 22 (2013) 7–24.

[60] S. Gypser, F. Hirsch, A.M. Schleicher, D. Freese, Impact of crystalline and amorphous iron- and aluminum hydroxides on mechanisms of phosphate adsorption and desorption, J Environ Sci (China). 70 (2018) 175–189. https://doi.org/10.1016/j.jes.2017.12.001.

[61] J. Liu, R. Zhu, L. Ma, H. Fu, X. Lin, S.C. Parker, M. Molinari, Adsorption of phosphate and

cadmium on iron (oxyhydr)oxides: A comparative study on ferrihydrite, goethite, and hematite, Geoderma. 383 (2021) 114799. https://doi.org/10.1016/j.geoderma.2020.114799.

[62] U.S. EPA, Test Method 1313 (SW-846): Liquid-Solid Partitioning as a Function of Extract pH Using a Parallel Batch Extraction Procedure, Washington, DC, 2017.

[63] ISO, Soil quality — Parameters for geochemical modelling of leaching and speciation of constituents in soils and materials — Part 1: Extraction of amorphous iron oxides and hydroxides with ascorbic acid, ISO 12782-1:2012, 2012.

[64] ISO, Soil quality — Parameters for geochemical modelling of leaching and speciation of constituents in soils and materials — Part 2: Extraction of crystalline iron oxides and hydroxides with dithionite, ISO 12782-2:2012, 2012.

[65] Vanderbilt University, LeachXS - Leaching Assessment Tool, (2022). http://leachxs.vueinnovations.com/leachxs/ (accessed March 28, 2022).

[66] C.J. Milne, D.G. Kinniburgh, W.H. Van Riemsdijk, E. Tipping, Generic NICA - Donnan model parameters for metal-ion binding by humic substances, Environ Sci Technol. 37 (2003) 958–971. https://doi.org/10.1021/es0258879.

[67] C.J. Milne, D.G. Kinniburgh, E. Tipping, Generic NICA-Donnan model parameters for proton binding by humic substances, Environ Sci Technol. (2001). https://doi.org/10.1021/es000123j.

[68] A.M.A. Pintor, B.R.C. Vieira, S.C.R. Santos, R.A.R. Boaventura, C.M.S. Botelho, Arsenate and arsenite adsorption onto iron-coated cork granulates, Science of the Total Environment. 642 (2018) 1075–1089. https://doi.org/10.1016/j.scitotenv.2018.06.170.

[69] L. Tian, Z. Shi, Y. Lu, A.C. Dohnalkova, Z. Lin, Z. Dang, Kinetics of Cation and Oxyanion Adsorption and Desorption on Ferrihydrite: Roles of Ferrihydrite Binding Sites and a Unified Model, Environ Sci Technol. 51 (2017) 10605–10614. https://doi.org/10.1021/acs.est.7b03249.

[70] M. Zhang, E.J. Reardon, Removal of B, Cr, Mo, and Se from wastewater by incorporation into hydrocalumite and ettringite, Environ Sci Technol. 37 (2003) 2947–2952. https://doi.org/10.1021/es020969i.

[71] B. Guo, S. Nakama, Q. Tian, N.D. Pahlevi, Z. Hu, K. Sasaki, Suppression processes of anionic pollutants released from fly ash by various Ca additives, J Hazard Mater. 371 (2019) 474–483. https://doi.org/10.1016/j.jhazmat.2019.03.036.

[72] N. Wang, X. Sun, Q. Zhao, Y. Yang, P. Wang, Leachability and adverse effects of coal fly ash: A review, J Hazard Mater. 396 (2020) 122725. https://doi.org/10.1016/J.JHAZMAT.2020.122725.

[73] S. Stefaniak, E. Kmiecik, E. Miszczak, J. Szczepańska-Plewa, I. Twardowska, Effect of weathering transformations of coal combustion residuals on trace elements mobility in view of the environmental safety and sustainability of their disposal and use. II. Element release, J Environ Manage. 156 (2015) 167–180. https://doi.org/10.1016/j.jenvman.2015.03.047.

[74] J.J. Suloway, W.R. Roy, T.M. Skelly, D.R. Dickerson, R.M. Schuller, R.A. Griffin, Chemical and toxicological properties of coal fly ash, Environmental Geology No. 105. (1983).

[75] N. Rivera, N. Kaur, D. Hesterberg, C.R. Ward, R.E. Austin, O.W. Duckworth, Chemical composition, speciation, and elemental associations in coal fly ash samples related to the kingston ash spill, Energy and Fuels. 29 (2015) 954–967. https://doi.org/10.1021/ef501258m.

[76] N.T. Plaks, A.M. Palomino, B.E. Scheetz, G.D. Braun, Testing Framework for Analysis of Time-Dependent Behavior of Coal Combustion Products, Journal of Materials in Civil Engineering. 28 (2016) 06015004. https://doi.org/10.1061/(asce)mt.1943-5533.0001326.

[77] P.J. Tikalsky, R.L. Carrasquillo, The effect of fly ash on the sulfate resistance of concrete, University of Texas at Austin. Center for Transportation Research, 1989.

[78] B.G. Kutchko, A.G. Kim, Fly ash characterization by SEM-EDS, Fuel. 85 (2006) 2537–2544. https://doi.org/10.1016/j.fuel.2006.05.016.

[79] J.K. Tishmack, J. Olek, S. Diamond, Characterization of High-Calcium Fly Ashes and Their Potential Influence on Ettringite Formation in Cementitious Systems, Cement, Concrete, and Aggregates, CCAGDP. 21 (1999) 82–92. https://doi.org/10.1520/cca10512j.

[80] R.T. Chancey, P. Stutzman, M.C.G. Juenger, D.W. Fowler, Comprehensive phase characterization of crystalline and amorphous phases of a Class F fly ash, Cem Concr Res. 40 (2010) 146–156. https://doi.org/10.1016/j.cemconres.2009.08.029.

[81] M. Kanematsu, T.M. Young, K. Fukushi, P.G. Green, J.L. Darby, Arsenic(III, V) adsorption on a goethite-based adsorbent in the presence of major co-existing ions: Modeling competitive adsorption consistent with spectroscopic and molecular evidence, Geochim Cosmochim Acta. 106 (2013) 404–428. https://doi.org/10.1016/j.gca.2012.09.055.

[82] J. Antelo, F. Arce, S. Fiol, Arsenate and phosphate adsorption on ferrihydrite nanoparticles. Synergetic interaction with calcium ions, Chem Geol. 410 (2015) 53–62. https://doi.org/10.1016/j.chemgeo.2015.06.011.

[83] E. Van Eynde, J.C. Mendez, T. Hiemstra, R.N.J. Comans, Boron Adsorption to Ferrihydrite with Implications for Surface Speciation in Soils: Experiments and Modeling, ACS Earth Space Chem. 4 (2020) 1269–1280. https://doi.org/10.1021/acsearthspacechem.0c00078.

[84] B. Lothenbach, D.A. Kulik, T. Matschei, M. Balonis, L. Baquerizo, B. Dilnesa, G.D. Miron, R.J. Myers, Cemdata18: A chemical thermodynamic database for hydrated Portland cements and alkali-activated materials, Cem Concr Res. 115 (2019) 472–506. https://doi.org/10.1016/j.cemconres.2018.04.018.

[85] P. Blanc, A. Lassin, P. Piantone, M. Azaroual, N. Jacquemet, A. Fabbri, E.C. Gaucher, Thermoddem: A geochemical database focused on low temperature water/rock interactions and waste materials, Applied Geochemistry. 27 (2012) 2107–2116. https://doi.org/10.1016/j.apgeochem.2012.06.002.

[86] J.M. Delany, S.R. Lundeen, The LLNL thermodynamic database, UCRL-21658, Lawrence Livermore National Laboratory, Livermore, California, USA, 1990.

[87] E. Giffaut, M. Grivé, P. Blanc, P. Vieillard, E. Colàs, H. Gailhanou, S. Gaboreau, N. Marty, B. Madé, L. Duro, Andra thermodynamic database for performance assessment: ThermoChimie, Applied Geochemistry. 49 (2014) 225–236. https://doi.org/10.1016/j.apgeochem.2014.05.007.

[88] H.A. van der Sloot, D.S. Kosson, Estimates of mineral stability constants derived from pH dependence leaching test data, in: 5th International Workshop on "Mechanisms and Modelling of Waste/Cement Interactions," Karlsruhe, Germany, 2019.

[89] U.S. EPA, Hazardous and Solid Waste Management System; Disposal of Coal Combustion Residuals From Electric Utilities: Final Rule, Washington, DC, 2015.

[90] T. Astrup, J.J. Dijkstra, R.N.J. Comans, H.A. Van Der Sloot, T.H. Christensen, Geochemical modeling of leaching from MSWI air-pollution-control residues, Environ Sci Technol. 40 (2006) 3551–3557. https://doi.org/10.1021/es052250r.

[91] J.A. Meima, R.N.J. Comans, The leaching of trace elements from municipal solid waste incinerator bottom ash at different stages of weathering, Applied Geochemistry. 14 (1999) 159–171. https://doi.org/10.1016/S0883-2927(98)00047-X.

[92] L. Tosti, A. van Zomeren, J.R. Pels, J.J. Dijkstra, R.N.J. Comans, Assessment of biomass ash applications in soil and cement mortars, Chemosphere. 223 (2019) 425–437. https://doi.org/10.1016/j.chemosphere.2019.02.045.

[93] N. Rivera, D. Hesterberg, N. Kaur, O.W. Duckworth, Chemical Speciation of Potentially Toxic Trace Metals in Coal Fly Ash Associated with the Kingston Fly Ash Spill, Energy and Fuels. 31 (2017) 9652–9659. https://doi.org/10.1021/acs.energyfuels.7b00020.

[94] Y.T. Liu, T.Y. Chen, W.G. MacKebee, L. Ruhl, A. Vengosh, H. Hsu-Kim, Selenium speciation in

coal ash spilled at the tennessee valley authority kingston site, Environ Sci Technol. 47 (2013) 14001–14009. https://doi.org/10.1021/es4041557.

[95] M.A. Chappell, J.M. Seiter, A.J. Bednar, C.L. Price, D. Averett, B. Lafferty, R. Tappero, J.S. Stanley, A.J. Kennedy, J.A. Steevens, P. Zhou, E. Morikawa, G. Merchan, A. Roy, Stability of solid-phase selenium species in fly ash after prolonged submersion in a natural river system, Chemosphere. 95 (2014) 174–181. https://doi.org/10.1016/j.chemosphere.2013.08.061.

[96] M. Lenz, E.D. van Hullebusch, F. Farges, S. Nikitenko, C.N. Borca, D. Grolimund, P.N.L. Lens, Selenium Speciation Assessed by X-Ray Absorption Spectroscopy of Sequentially Extracted Anaerobic Biofilms, Environ Sci Technol. 42 (2008) 7587–7593. https://doi.org/10.1021/es800811q.

[97] U.S. EPA, Method 6010D (SW-846): Inductively Coupled Plasma-Atomic Emission Spectrometry, Revision 4. Washington, DC, 2014.

[98] U.S. EPA, Method 6020B (SW-846): Inductively Coupled Plasma-Mass Spectrometry, Revison 2. Washington, DC, 2014.

[99] U.S. EPA, Method 9056A (SW-846): Determination of Inorganic Anions by Ion Chromatography, Revision 4.Washington, DC, 2007.

[100] U.S. EPA, Method 9060A (SW-846): Total Organic Carbon, Revision 4.Washington, DC, 2004.

[101] U.S. EPA, Method 3052 (SW-846): Microwave Assisted Acid Digestion of Siliceous and Organically Based Matrices, Washington, DC, 1996.

[102] U.S. EPA, Method 6010B (SW-846): Inductively Coupled Plasma - Atomic Emission Spectrometry, Revision 2.Washington, DC, 1996.

[103] J.D. Allison, D.S. Brown, K.J. Novo-Gradac, MINTEQA2/PRODEFA2, a geochemical assessment model for environmental systems: version 3.0 user's manual, US EPA, Athens, Georgia, 1991.

[104] J.S. Fruchter, D. Rai, J.M. Zachara, Identification of Solubility-Controlling Solid Phases in a Large Fly Ash Field Lysimeter, Environ Sci Technol. 24 (1990) 1173–1179. https://doi.org/10.1021/es00078a004.

[105] G.M. Mudd, T.R. Weaver, J. Kodikara, Environmental geochemistry of leachate from leached brown coal ash, Journal of Environmental Engineering. 130 (2004) 1514–1526. https://doi.org/10.1061/(ASCE)0733-9372(2004)130:12(1514).

[106] P.A. O'Day, D. Vlassopoulos, R. Root, N. Rivera, The influence of sulfur and iron on dissolved arsenic concentrations in the shallow subsurface under changing redox conditions, Proceedings of the National Academy of Sciences. 101 (2004) 13703–13708. https://doi.org/10.1073/pnas.0402775101.

[107] F. Liu, G. Zhang, S. Liu, Z. Fu, J. Chen, C. Ma, Bioremoval of arsenic and antimony from wastewater by a mixed culture of sulfate-reducing bacteria using lactate and ethanol as carbon sources, Int Biodeterior Biodegradation. 126 (2018) 152–159. https://doi.org/10.1016/j.ibiod.2017.10.011.

[108] C.A. Abin, J.T. Hollibaugh, Dissimilatory antimonate reduction and production of antimony trioxide microcrystals by a novel microorganism, Environ Sci Technol. 48 (2014) 681–688. https://doi.org/10.1021/es404098z.

[109] I. Ortiz-Bernad, R.T. Anderson, H.A. Vrionis, D.R. Lovley, Vanadium respiration by Geobacter metallireducens: Novel strategy for in situ removal of vanadium from groundwater, Appl Environ Microbiol. 70 (2004) 3091–3095. https://doi.org/10.1128/AEM.70.5.3091-3095.2004.

[110] B. Zhang, Y. Li, Y. Fei, Y. Cheng, Novel Pathway for Vanadium(V) Bio-Detoxification by Gram-Positive Lactococcus raffinolactis, Environ Sci Technol. 55 (2021) 2121–2131. https://doi.org/10.1021/acs.est.0c07442.

[111] Y. Kong, J. Kang, J. Shen, Z. Chen, L. Fan, Influence of humic acid on the removal of arsenate and arsenic by ferric chloride: effects of pH, As/Fe ratio, initial As concentration, and co-existing solutes, Environmental Science and Pollution Research. 24 (2017) 2381–2393. https://doi.org/10.1007/s11356-016-7994-1.

[112] G. Choppala, A. Kunhikrishnan, B. Seshadri, J.H. Park, R. Bush, N. Bolan, Comparative sorption of chromium species as influenced by pH, surface charge and organic matter content in contaminated soils, J Geochem Explor. 184 (2018) 255–260. https://doi.org/10.1016/j.gexplo.2016.07.012.

[113] K.C. Misra, Oxidation-reduction reactions, in: Introduction to Geochemistry : Principles and Applications, Wiley-Blackwell, 2012: pp. 167–194.

[114] U.S. EPA, Field Measurement of Oxidation-Reduction Potential (ORP), USSESDPROC-113-R2, Athens, Georgia, 2017.

[115] X. Wang, H.A. van der Sloot, K.G. Brown, A.C. Garrabrants, Z. Chen, B. Hensel, D.S. Kosson, Application and uncertainty of a geochemical speciation model for predicting oxyanion leaching from coal fly ash under different controlling mechanisms, J Hazard Mater. 438 (2022) 129518. https://doi.org/10.1016/J.JHAZMAT.2022.129518.

[116] M.L. Pierce, C.B. Moore, Adsorption of arsenite and arsenate on amorphous iron hydroxide, Water Res. 16 (1982) 1247–1253. https://doi.org/10.1016/0043-1354(82)90143-9.

[117] Q. Xue, Y. Ran, Y. Tan, C.L. Peacock, H. Du, Arsenite and arsenate binding to ferrihydrite organo-mineral coprecipitate: Implications for arsenic mobility and fate in natural environments, Chemosphere. 224 (2019) 103–110. https://doi.org/10.1016/j.chemosphere.2019.02.118.

[118] H.B. Jung, B.C. Bostick, Y. Zheng, Field, experimental, and modeling study of arsenic partitioning across a redox transition in a bangladesh aquifer, Environ Sci Technol. 46 (2012) 1388–1395. https://doi.org/10.1021/es2032967.

[119] H.D. Pedersen, D. Postma, R. Jakobsen, Release of arsenic associated with the reduction and transformation of iron oxides, Geochim Cosmochim Acta. 70 (2006) 4116–4129. https://doi.org/10.1016/j.gca.2006.06.1370.

[120] D. Zhang, H. Guo, W. Xiu, P. Ni, H. Zheng, C. Wei, In-situ mobilization and transformation of iron oxides-adsorbed arsenate in natural groundwater, J Hazard Mater. 321 (2017) 228–237. https://doi.org/10.1016/j.jhazmat.2016.09.021.

[121] D. Postma, F. Larsen, N.T. Minh Hue, M.T. Duc, P.H. Viet, P.Q. Nhan, S. Jessen, Arsenic in groundwater of the Red River floodplain, Vietnam: Controlling geochemical processes and reactive transport modeling, Geochim Cosmochim Acta. 71 (2007) 5054–5071. https://doi.org/10.1016/j.gca.2007.08.020.

[122] R. Jakobsen, D. Postma, Redox zoning, rates of sulfate reduction and interactions with Fe-reduction and methanogenesis in a shallow sandy aquifer, Romo, Denmark, Geochim Cosmochim Acta. 63 (1999) 137–151. https://doi.org/10.1016/S0016-7037(98)00272-5.

[123] T. Yu, P.L. Bishop, Stratification of microbial metabolic processes and redox potential chance in an aerobic biofilm studied using microelectrodes, Water Science and Technology. 37 (1998) 195–198. https://doi.org/10.1016/S0273-1223(98)00104-8.

[124] G. Akar, M. Polat, G. Galecki, U. Ipekoglu, Leaching behavior of selected trace elements in coal fly ash samples from Yenikoy coal-fired power plants, Fuel Processing Technology. 104 (2012) 50–56. https://doi.org/10.1016/J.FUPROC.2012.06.026.

[125] V. Tsiridis, P. Samaras, A. Kungolos, G.P. Sakellaropoulos, Application of leaching tests for toxicity evaluation of coal fly ash, Environmental Toxicology: An International Journal. 21 (2006) 409–416. https://doi.org/10.1002/tox.20187.

[126] A.G. Kim, P. Hesbach, Comparison of fly ash leaching methods, Fuel. 88 (2009) 926–937.

https://doi.org/10.1016/J.FUEL.2008.11.013.

[127] S. Zhang, S. Dai, R.B. Finkelman, I.T. Graham, D. French, J.C. Hower, X. Li, Leaching characteristics of alkaline coal combustion by-products: A case study from a coal-fired power plant, Hebei Province, China, Fuel. 255 (2019) 115710. https://doi.org/10.1016/J.FUEL.2019.115710.

[128] C. Wang, M. Huang, W. Lou, W. Xiang, T. Zhou, J. Mao, F. Zan, X. Wu, Citric ligand manipulated efficient spatially-separated reduction and immobilization of Cr(VI) upon electron-rich copper-iron oxides, Chemical Engineering Journal. 434 (2022) 134575. https://doi.org/10.1016/J.CEJ.2022.134575.

[129] U.S. EPA, Test Method 1314 (SW-846): Liquid-Solid Partitioning as a Function of Liquid-Solid Ratio for Constituents in Solid Materials Using An Up-Flow Percolation Column Procedure, Washington, DC, 2017.

[130] U.S. EPA, Test Method 1316 (SW-846): Liquid-Solid Partitioning as a Function of Liquid-to-Solid Ratio in Solid Materials Using a Parallel Batch Procedure, Washington, DC, 2017.

[131] T. Wang, W. Liu, L. Xiong, N. Xu, J. Ni, Influence of pH, ionic strength and humic acid on competitive adsorption of Pb(II), Cd(II) and Cr(III) onto titanate nanotubes, Chemical Engineering Journal. 215–216 (2013) 366–374. https://doi.org/10.1016/J.CEJ.2012.11.029.

[132] Y. Zhang, C. Zhu, F. Liu, Y. Yuan, H. Wu, A. Li, Effects of ionic strength on removal of toxic pollutants from aqueous media with multifarious adsorbents: A review, Science of The Total Environment. 646 (2019) 265–279. https://doi.org/10.1016/J.SCITOTENV.2018.07.279.

[133] R. Barna, Z. Rethy, L. Tiruta-Barna, Release dynamic process identification for a cement based material in various leaching conditions. Part I. Influence of leaching conditions on the release amount, J Environ Manage. 74 (2005) 141–151. https://doi.org/10.1016/j.jenvman.2004.06.016.

[134] K. Kim, S.M. Park, J. Kim, S.H. Kim, Y. Kim, J.T. Moon, G.S. Hwang, W.S. Cha, Arsenic concentration in porewater of an alkaline coal ash disposal site: Roles of siderite precipitation/dissolution and soil cover, Chemosphere. 77 (2009) 222–227. https://doi.org/10.1016/j.chemosphere.2009.07.029.

[135] N.G. Hemming, G.N. Hanson, Boron isotopic composition and concentration in modern marine carbonates, Geochim Cosmochim Acta. 56 (1992) 537–543. https://doi.org/10.1016/0016-7037(92)90151-8.

[136] J.R. Farmer, O. Branson, J. Uchikawa, D.E. Penman, B. Hönisch, R.E. Zeebe, Boric acid and borate incorporation in inorganic calcite inferred from B/Ca, boron isotopes and surface kinetic modeling, Geochim Cosmochim Acta. 244 (2019) 229–247. https://doi.org/10.1016/J.GCA.2018.10.008.

[137] M. di Gianfilippo, G. Costa, I. Verginelli, R. Gavasci, F. Lombardi, Analysis and interpretation of the leaching behaviour of waste thermal treatment bottom ash by batch and column tests, Waste Management. 56 (2016) 216–228. https://doi.org/10.1016/J.WASMAN.2016.07.034.

[138] A. Vollpracht, W. Brameshuber, Binding and leaching of trace elements in Portland cement pastes, Cem Concr Res. 79 (2016) 76–92. https://doi.org/10.1016/J.CEMCONRES.2015.08.002.

[139] C. Benson, Y. Tan, M. Benavides, Hydrogeochemical Assessment of Long-Term Leaching Characteristics at Coal Combustion Product Sites: Hydrologic Analysis of Disposal Basins for Coal Combustion Products, 3002023682, EPRI, Palo Alto, CA, 2022.

[140] W.J.J. Huijgen, R.N.J. Comans, Carbonation of steel slag for CO2 sequestration: Leaching of products and reaction mechanisms, Environ Sci Technol. 40 (2006) 2790–2796. https://doi.org/10.1021/es052534b.

[141] K. Chalastara, G.P. Demopoulos, Selenate Se(VI) reduction to elemental selenium on heterojunctioned rutile/brookite nano-photocatalysts with enhanced charge utilization, Chemical

Engineering Journal. 437 (2022) 135470. https://doi.org/10.1016/J.CEJ.2022.135470.

[142] H. Li, Y. Yang, W. Zheng, L. Chen, Y. Bai, Immobilization of high concentration hexavalent chromium via core-shell structured lightweight aggregate: A promising soil remediation strategy, Chemical Engineering Journal. 401 (2020) 126044. https://doi.org/10.1016/J.CEJ.2020.126044.

[143] A.P. Khodadoust, P. Naithani, T.L. Theis, I.P. Murarka, Leaching characteristics of arsenic from aged alkaline coal fly ash using column and sequential batch leaching, Ind Eng Chem Res. 50 (2011) 2204–2213. https://doi.org/10.1021/ie100909n.

[144] S. Sarkar, D.S. Kosson, H. van der SLOOT, J. MEEUSSEN, K. Brown, A. GARRABRANTS, A Dual Regime Reactive Transport Model for Simulation of High Level Waste Tank Closure Scenarios-13375, in: WM2013 Conference, February, Citeseer, 2013: pp. 24–28.

[145] J.J. Dijkstra, J.C.L. Meeussen, H.A. van der Sloot, R.N.J. Comans, A consistent geochemical modelling approach for the leaching and reactive transport of major and trace elements in MSWI bottom ash, Applied Geochemistry. 23 (2008) 1544–1562. https://doi.org/10.1016/J.APGEOCHEM.2007.12.032.

[146] R.J. Donahoe, Secondary mineral formation in coal combustion byproduct disposal facilities: Implications for trace element sequestration, Geol Soc Spec Publ. 236 (2004) 641–658. https://doi.org/10.1144/GSL.SP.2004.236.01.36.

[147] X. Wang, A.C. Garrabrants, H.A. van der Sloot, Z. Chen, K.G. Brown, B. Hensel, D.S. Kosson, Leaching and geochemical evaluation of oxyanion partitioning within an active coal ash management unit, Chemical Engineering Journal. In Review. (2022).

[148] EPRI, Leaching, geotechnical, and hydrologic characterization of coal combustion products from a closed coal ash impoundment: capped unit, 3002017363, EPRI, Palo Alto, CA, 2020.

[149] C.H. Benson, J.N. Chen, T.B. Edil, W.J. Likos, Hydraulic Conductivity of Compacted Soil Liners Permeated with Coal Combustion Product Leachates, Journal of Geotechnical and Geoenvironmental Engineering. 144 (2018) 04018011. https://doi.org/10.1061/(asce)gt.1943-5606.0001855.

[150] T. Arima, R. Sasaki, T. Yamamoto, C.B. Tabelin, S. Tamoto, T. Igarashi, Effects of environmental factors on the leaching and immobilization behavior of arsenic from mudstone by laboratory and in situ column experiments, Minerals. 11 (2021). https://doi.org/10.3390/min11111220.

[151] Y. Wang, L. Sun, T. Han, Y. Si, R. Wang, Arsenite and arsenate leaching and retention on iron (hydr)oxide-coated sand column, J Soils Sediments. 16 (2016) 486–496. https://doi.org/10.1007/s11368-015-1230-3.

[152] D. Pedretti, B. Vriens, E.K. Skierszkan, P. Baják, K.U. Mayer, R.D. Beckie, Evaluating dual-domain models for upscaling multicomponent reactive transport in mine waste rock, J Contam Hydrol. 244 (2022) 103931. https://doi.org/10.1016/J.JCONHYD.2021.103931.

[153] B. Lothenbach, F. Winnefeld, Thermodynamic modelling of the hydration of Portland cement, Cem Concr Res. 36 (2006) 209–226. https://doi.org/10.1016/j.cemconres.2005.03.001.

[154] L.L. Willard, Chemical equilibria in soils, Chichester, UK: John Wiley & Sons, 1979.

[155] R.M. Asmussen, A.R. Lawter, J.R. Stephenson, M.E. Bowden, N.M. Washton, J.J. Neeway, Y. Du, C.I. Pearce, R.E. Clayton, S.A. Saslow, Getter Incorporation into Cast Stone and Solid State Characterizations, Pacific Northwest National Lab.(PNNL), Richland, WA, 2016.

APPENDIX A

SUPPLEMENTARY MATERIAL FOR CHAPTER 2

A.I Solid sample characterization

Total elemental and crystalline structure analysis. The major elemental concentrations in reference CFAs were measured by X-ray fluorescence (XRF) using an ARL ADVANT'X IntelliPower^{TM} Series 4200 sequential XRF spectrometer (Thermoscientific, Wilmington, DE, USA). Crystalline structures were analyzed by X-ray diffraction (XRD, X'Pert PRO PANalytical B.V., Almelo, the Netherlands).

Total carbon analysis. Total carbon analysis of solid CFA samples was conducted using a Shimadzu model TOC-LCPH with an SSM-5000 unit for solid samples to measure total carbon (TC) and total inorganic carbon (TIC) with total organic carbon (TOC) computed as the difference between TC and TIC. The TIC also was estimated by thermogravimetric analysis combined with mass spectrometry (TGA/MS), using a TA Instruments Q600 SDT analyzer (New Castle, Delaware, USA) and a MS unit. About 50 mg of ground and sieved sample (passing No. 100 mesh sieve) was loaded for analysis. Each test sample was heated under a continuous flow of nitrogen from 30 °C to 1000 °C at a rate of 10.0 °C/min. During the heating, the current of m/e=44 (CO_2 peak) was collected by the MS unit to determine the appropriate temperature range of CO_2 release. The TIC content was calculated based on the mass loss of the sample in the corresponding temperature range (~500 - ~900 °C).

Iron (hydr)oxide content. The amounts of iron (hydr)oxides in reference CFAs were determined through analysis of Fe concentrations in eluates from two selective extraction tests. The amorphous iron (hydr)oxides (Am_{FeOOH}) were extracted with ascorbic acid following the ISO Method 12782-1 [63]. The crystalline iron (hydr)oxides (Cry_{FeOOH}) were extracted with dithionite following the ISO Method 12782-2 [64].

A.II Details of pH-dependent leaching test (EPA Method 1313)

EPA Method 1313 [62] is a standardized parallel batch extraction method used to evaluate the

liquid-solid partitioning (LSP) of inorganic constituents as a function of eluate pH. The general procedure consists of nine batch extractions of a particle-size reduced subsample material contacted with leaching solution at a liquid-to-solid ratio (L/S) of 10 L/kg-dry material and tumbled end-over-end at 28±2 revolutions per minute (rpms) over a specified contact interval. The leaching solution is reagent water with additions of predetermined amount of nitric acid (2 N HNO_3) or potassium hydroxide (1 N KOH) to adjust the final pH of the eluate to nine specific target pH values (i.e., pH values of 2, 4, 5.5, 7, 8, 9, 10.5, 12, and 13 with a tolerance of ± 0.5 to each target pH except for the pH of 2 condition). The schedule of acid and base additions is formulated from a pre-test acid/base titration curve of each sample. Another extraction without addition of acid or base is carried out to analyze constituent leaching at the "natural pH" of the material. Additional extractions at other pH conditions may be carried out to better resolve pH-dependent leaching curves for geochemical speciation modeling. The extraction contact time depends on the maximum particle size of the material (e.g., for CFAs with a natural particle size of 85 wt% less than 300 µm, the extraction contact time is specified as 24 hours). After tumbling, the solid and liquid phases are separated by settling or centrifugation, and the pH and electrical conductivity (EC) of the clarified eluate are measured. The remaining slurry is vacuum-filtered through 0.45-µm pore size polypropylene membranes prior to chemical analysis by inductively coupled plasma spectrometry (ICP), ion chromatography (IC), and carbon analysis. Titration curves that show the amount of acid or base added to obtain the target pH values of eluate samples are provided in Figure A.1.

As the method specifies, three method blanks (reagent water, acid blank, and base blank) generated without solids are prepared in parallel with test extractions with the analytical results to be used for quality assurance/quality control (QA/QC purposes).

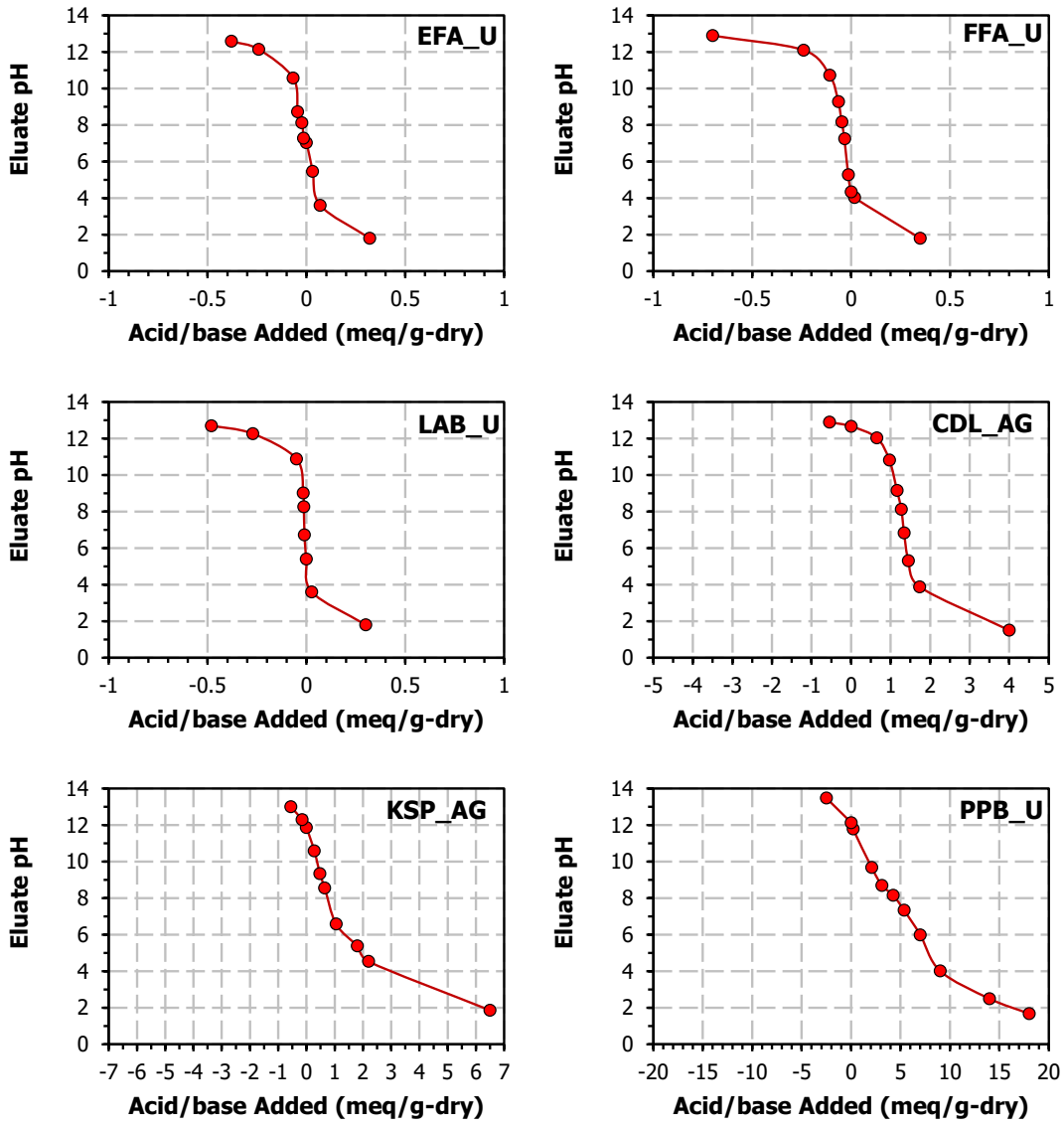

Figure A.1 Acid/base titration curves of reference coal fly ashes. Positive and negative values of x-axis represent acid and base additions, respectively.

A.III Eluate analysis

Analysis of pH and electrical conductivity (EC). For eluates from the leaching tests, the pH and EC were measured on aliquots (~5 mL) of eluate using an Accumet 20XL multimeter. Prior to testing, the pH electrode was calibrated with two National Institute of Standards and Technology (NIST) traceable pH buffer solutions that bounded the anticipated range of pH to be measured. A third mid-range NIST buffer was used to verify the calibration. Conductivity of all

leaching test eluates was determined using a standard conductivity probe calibrated to an appropriate standard conductivity solution for the conductivity range of concern.

Analysis by inductively coupled plasma spectrometry. The concentrations of most inorganic trace constituents were determined by a combination of inductivity coupled plasma-optical emission spectrometry (ICP-OES) following EPA Method 6010D [97] and inductivity coupled plasma-mass spectrometry (ICP-MS) following EPA Method 6020B [98].

ICP-OES was conducted using an Agilent Technologies Model 720-ES spectrometer (Agilent Technologies, Santa Clara, CA) calibrated to a 5-point standard curve with an analytical range of 25 to 25,000 μg/L. For some high-concentration elements (e.g., Ca, Mg, Na, K), the standard curve was extended up to 500,000 μg/L using a 7-point standard curve. The concentrations of select low-level constituents (see Table A.1) were determined using a Perkin Elmer Elan DRC II ICP-MS (Perkin Elmer, Waltham, MA) calibrated to a 5-point standard curve with range between approximately 1 and 250 μg/L and extended, when necessary, with a 7-point calibration curve to 500 μg/L for some constituents. Multi-elemental standards from SPEX CertiPrep were used to calibrate the instruments for the continuing calibration verification and for matrix spikes. Certified multi-elemental standards from AccuStandard were used for the initial calibration verification.

Analytical QA/QC included initial and continuing calibration checks and blanks, matrix spikes, and method blanks. Calibration check standards and matrix blanks were evaluated every 10 to 20 samples with the requirements that check standards were within 15% of the specified value and blanks were below the method detection limit (MDL). Matrix spikes were required to have recoveries within 20% of the calculated concentration considering the spiked mass. Initial and continuing calibration check standards for ICP-OES and ICP-MS were 0.5 mg/L and 0.050 mg/L, respectively. Analyte concentrations measured at less than MDLs were reported as <MDL and graphed at one-half the MDL to indicate that the measurement was conducted. The MDLs and lower limits of quantitation (LLOQs) were listed in Table A.1.

Table A.1 Methods, MDLs, and LLOQs for analysis of eluates by ICP-OES and ICP-MS

	EFA_U, FFA_U, LAB_U, PPB_U			CDL_AG, KSP_AG		
Analyte	Method	MDL (mg/L)	LLOQ (mg/L)	Method	MDL (mg/L)	LLOQ (mg/L)
Al	ICP-OES	0.0034	0.025	ICP-OES	0.0034	0.025
Sb	ICP-MS	0.000082	0.001	ICP-MS	0.000013	0.001
As	ICP-MS	0.00057	0.001	ICP-MS	0.000036	0.001
Ba	ICP-MS	0.00044	0.001	ICP-OES	0.0016	0.025
Be	ICP-MS	0.00042	0.001	ICP-MS	0.000035	0.001
B	ICP-OES	0.0023	0.025	ICP-OES	0.0023	0.025
Cd	ICP-MS	0.00019	0.001	ICP-MS	0.00018	0.001
Ca	ICP-OES	0.0065	0.025	ICP-OES	0.0065	0.025
Cr	ICP-MS	0.00047	0.001	ICP-MS	0.000053	0.001
Co	ICP-MS	0.00041	0.001	ICP-MS	0.000023	0.001
Cu	ICP-MS	0.00054	0.001	ICP-MS	0.00004	0.001
Fe	ICP-OES	0.0022	0.025	ICP-OES	0.0022	0.025
Pb	ICP-MS	0.00022	0.001	ICP-MS	0.000027	0.001
Li	ICP-OES	0.0047	0.025	ICP-OES	0.0047	0.025
Mg	ICP-OES	0.0035	0.025	ICP-OES	0.0035	0.025
Mn	ICP-MS	0.00031	0.001	ICP-MS	0.000032	0.001
Mo	ICP-MS	0.00059	0.001	ICP-OES	0.0018	0.025
Ni	ICP-MS	0.00047	0.001	ICP-MS	0.000032	0.001
P	ICP-OES	0.0068	0.025	ICP-OES	0.0068	0.025
K	ICP-OES	0.0032	0.025	ICP-OES	0.0032	0.025
Se	ICP-MS	0.00051	0.001	ICP-MS	0.000062	0.001
Si	ICP-OES	0.0038	0.025	ICP-OES	0.0038	0.025
Na	ICP-OES	0.0056	0.025	ICP-OES	0.0056	0.025
Sr	ICP-OES	0.0037	0.025	ICP-OES	0.0037	0.025
S	ICP-OES	0.0058	0.025	ICP-OES	0.0058	0.025
Tl	ICP-MS	0.00047	0.001	ICP-MS	0.000019	0.001
V	ICP-MS	0.00032	0.001	ICP-OES	0.0012	0.025
Zn	ICP-MS	0.000065	0.001	ICP-MS	0.000091	0.001

Analysis by ion chromatography. The concentrations of anions were determined by IC using a Metrohm 881 Compact IC Pro (Metrohm USA, Riverview, FL) with a Metrosep A Supp 5 column and a conductivity detector following EPA Method 9056A [99]. A 7-anion calibration standard from SPEX CertiPrep was diluted to form a 5-point calibration curve with the MDLs and LLOQs shown in Table A.2. Since the calibration standards were diluted from a bulk multi-analyte standard, the calibration range differed for each analyte (e.g., 0.050-50 mg/L for Cl^- and 0.150-150 mg/L for SO_4^{2-}). Calibration check standards were required to be within 15% of the specified value, while acceptable analytical blanks were measured below the MDLs. A second multi-anion certified standard from VeriSpec was used for the initial calibration verification.

Table A.2 MDLs and LLOQs for analysis of eluates by IC

Analyte	Symbol	MDL (mg/L)	LLOQ (mg/L)
Bromide	Br^-	0.0064	0.025
Chloride	Cl^-	0.0101	0.05
Fluoride	F^-	0.0063	0.02
Nitrate	NO_3^-	0.0112	0.1
Nitrite	NO_2^-	0.0108	0.05
Phosphate	PO_4^{3-}	0.0247	0.15
Sulfate	SO_4^{2-}	0.0254	0.15

Carbon analysis. Carbon analysis including dissolved inorganic carbon (DIC) and dissolved organic carbon (DOC) was conducted by catalytic oxidation/non-dispersive infrared detection (NDIR) following EPA Method 9060A [100] using a Shimadzu TOC-V CPH/CPN (Shimadzu Scientific Instruments, Inc., Columbia, MD). In this analysis, total carbon in the eluate is converted to carbon dioxide via oxidation or decomposition and carried by a zero-CO_2 air stream into the NDIR. For DIC analysis, liquid samples are acidified with 2-M hydrochloric acid to liberate carbonates and other forms of inorganic carbon from solution as carbon dioxide, which is sparged from the liquid sample into the NDIR by the zero-CO_2 carrier gas. DOC is determined by measuring the total carbon (TC) of a sample after purging of inorganic carbon.

The instrument was calibrated using sodium carbonate and potassium hydrogen phthalate over a 5-point calibration curve for DIC and DOC, respectively. The resultant analytical range was between 0.1 and 100 mg/L, with MDL and LLOQ values shown in Table A.3. Checks on

QA/QC at a frequency of every 10 to 20 analytical samples included calibration checks with a required recovery within 15% of the specific value and method blanks with a requirement that the concentration was less than the MDL. Certified standards from Sigma Aldrich were used to calibrate the instrument and for the continuing calibration verification. LabChem certified standards were used for the initial calibration verification.

Table A.3 MDLs and LLOQs for eluate analysis of carbon

Analyte	Symbol	MDL (mg/L)	LLOQ (mg/L)
Dissolved inorganic carbon	DIC	0.15	0.5
Dissolved organic carbon	DOC	0.18	0.5

A.IV Model calibration and parameterization

Available content. The available contents of simulated constituents (mg/kg-dry) are summarized in Table A.4 (Appendix A.V). For all constituents, except CO_3^{2-} and Fe, available content was determined as the maximum eluate concentration (mg/L) over the entire pH domain of the EPA Method 1313 multiplied by the EPA Method 1313 L/S of 10 L/kg-dry [18,19]. The available content of CO_3^{2-} was initialized using the TIC content of the solid material and adjusted, as needed, to fit the Ca LSP at pH > 8, because the TIC analysis often is not a sufficiently accurate measurement of CO_3^{2-} concentration. In this pH range, calcite [$CaCO_3$] was often the solid phase controlling Ca concentrations. The available content of Fe in the virtual materials was calibrated to yield the minimum residual between simulation and experimental results of pH-dependent leaching of As, Mo, and V, due to their high affinity to hydrous ferric oxide (HFO).

Redox condition. The *pe* [-log(electron activity)] is an indicator of the tendency of a solution to donate or accept electrons when it is subject to change by introduction of a new species. However, the solution pH can also impact the reduction/oxidation reaction between species in different valence states; therefore, the sum of pH and *pe* (pH + *pe*) is an important modeling parameter to represent the overall impact of pH and redox potential on the leaching of redox-sensitive constituents. In the geochemical model, the redox condition is represented by the pH + *pe*. For geochemical speciation simulation of EPA Method 1313 data, a constant value of pH + *pe* across the whole pH range was calibrated specifically for the leaching system of each fly ash and is summarized in Table A.5 (Appendix A.VI). As a first estimation, the pH + *pe* parameter in the model was calibrated to fit the LSP of Fe at 2 < pH < 6. This estimate acknowledges the sensitivity of Fe (a redox-sensitive major constituent) leaching to redox conditions under the acidic pH range [27]. Aside from Fe, Cr is also used as a redox indicator to further verify and refine the redox condition estimation of the leaching system because the leaching behavior of Cr at relatively high pH range of 6-12 is highly sensitive to pH + *pe* value [26].

Mineral phases. A potential set of mineral phases (Table A.6-8, Appendix A.VII) was derived by simulating pH-dependent leaching data (EPA Method 1313 at L/S 10 L/kg). Aqueous speciation reactions and selected minerals were taken from the MINTEQA2_V4 database [56] at 20°C. Additional mineral reactions also were considered from literature [42,43,153,154] and other databases [CEMDATA18 [84], THERMODDEM2011 [85], Lawrence Livermore National

Laboratory (LLNL) [86], ThermoChimie [87]]. Solid solution reactions assumed formation of an ideal solid solution and the fraction of each end member represented its activity. Based on analogous chemistry between constituents, postulated ettringite solid solution and experimental minerals were considered to describe leaching data for some elements. The possible solubility-controlling minerals and solid solutions were selected in an iterative process to fit eluate concentrations over the test pH range for each material. A MATLAB substitution algorithm was used to conduct sequential instances of ORCHESTRA to facilitate selection of similar mineral phases from a combination of thermodynamic databases. The selection of phases aimed to minimize the residual of simulation results under the laboratory test conditions. The log-squared residual between the pH-dependent leaching concentration (C_e) and modeled result (C_m) at each pH point over the pH range of interest was calculated and then summed according to the Equation A-1 to get the summed log-squared residuals (logRSS):

$$logRSS = \sum(\log\left(\frac{C_m}{C_e}\right))^2 \qquad \text{Equation A-1}$$

Additional minerals, which may form in CFA field sites under reduced environmental conditions as reported in reducing natural environments or solid waste materials, were collected from literature, and provided in Table A.9, Appendix A.VII.

Complexation to organic matter. Organic matter complexation is represented by an active fraction of the total organic matter (i.e., the humic acid or HA) by dividing HA into a solid humic acid (SHA) fraction and a dissolved humic acid (DHA) fraction (A.IX). A combination of total HA content and DHA description (Table A.13) was optimized to capture the concentration profiles of Cu, Pb, and Cr.

A.V Available content of virtual materials

Table A.4 Available content (mg/kg-dry) of constituents in geochemical virtual materials for reference coal fly ashes

Constituent	Group I			Group II		Group III
	EFA_U	FFA_U	LAB_U	CDL_AG	KSP_AG	PPB_U
Al	771	905	662	1,320	7,720	16,100
As	4.92	36.8	14.8	15.8	3.55	15.0
Ba	3.35	1.56	8.55	4.32	11.6	44.3
B	25.6	29.8	10.0	429	640	137
Ca	1,190	756	410	34,300	24,300	171,000
CO_3^{-2} [a]	878	1,300	1,500	6,000	12,000	185,000
Cl^-	21.9	3.30	3.29	3,000	48.3	1.19
Cr	1.05	1.21	0.482	15.7	9.20	14.3
Cu	2.23	3.77	3.75	6.50	7.14	38.2
Fe [b]	439	1,730	670	2,350	2,230	3,910
Pb	0.0515	0.104	0.184	3.13	0.547	1.88
Li	7.91	12.1	7.84	7.42	8.31	59.8
Mg	114	155	102	1,860	2,520	43,500
Mn	3.05	2.15	1.37	47.3	40.4	214
Mo	4.72	10.4	3.46	40.1	22.2	3.20
NO_3^-	7.34	4.72	1.81	0.056 [c]	0.056 [c]	0.870
P	5.07	11.4	10.7	123	276	216
K	100	234	216	573	451	900
Se	19.9	28.5	0.240	2.94	1.79	3.14
Si	394	406	531	1,280	2,740	3,560
Na	148	261	106	573	990	2,720
Sr	49.0	38.5	35.7	28.5	278	1,940
S	1210	1,630	322	4,800	4,110	6,790
V	4.70	11.5	7.15	59.4	28.1	12.7

[a] Available content of CO_3^{-2} was calibrated against the pH-dependent leaching behavior of calcium at pH > 8.

[b] Available content of Fe was calibrated to describe adsorption of As, Mo, and V by iron (hydr)oxide mineral in models.

[c] Values below the detection limit and set at one half of the detection limit.

A.VI pH and redox conditions in geochemical speciation model

Table A.5 Summary of natural pH and *pe*, and pH + *pe* in geochemical speciation model for simulating leaching of reference CFAs

Material ID	Natural pH [a]	*pe* [b]	pH + *pe* [c]
EFA_U	7.03	10.1	17.1
FFA_U	4.34	15.5	19.8
LAB_U	5.39	11.0	16.4
CDL_AG	12.7	-1.7	11.0
KSP_AG	11.9	5.0	16.9
PPB_U	12.1	7.0	19.1

[a] Measured natural pH is defined as the pH response to a deionized water extraction at a liquid-to-solid ratio of 10 L/kg-dry.

[b] Calibrated *pe* value for the test condition without acid or base addition at a liquid-to-solid ratio of 10 L/kg-dry. This calibrated *pe* value together with the measured natural pH value generated a constant pH + *pe* value to be used in the model simulation as described in section A.IV.

[c] The sum of pH and *pe* [-log(electron activity)] is a parameter to represent the overall redox condition from oxic (pH + *pe* > ~15) to mildly reducing (~10 < pH + *pe* < ~15) to anoxic (pH + *pe* < ~10) in the leaching system [18,21]. Most reference fly ashes (except CDL_AG) showed oxidized conditions during leaching with pH + *pe* > 15. Relative to the other materials, CDL_AG with a pH + *pe* of 11, may be somewhat reduced during leaching due to the addition of anhydrous ammonia for NOx control prior to collection.

A.VII Mineral sets of virtual materials

Table A.6 Mineral set identified in geochemical virtual materials for Group I CFAs

Phase ID in Database	Formula	Reaction	log K‡		
			EFA_U	FFA_U	LAB_U
AA_Magnesite [a]	$MgCO_3$	AA_Magnesite = 1 CO_3^{-2} + 1 Mg^{+2}	-9.33	-9.33	-9.33
AlOHSO4 [b]	$Al(OH)SO_4$	AlOHSO4 + 3 H_2O = 1 $Al[OH]_4^-$ + 3 H^+ + 1 SO_4^{-2}		-26.4	
CEM18_C3AFS0_84H4_32 [c]	$C_3(F,A)S_{0.84}H_{4.32}$*	CEM18_C3AFS0_84H4_32 + 2.32 H^+ = 1 $Al[OH]_4^-$ + 3 Ca^{+2} + 1 $Fe[OH]_4^-$ + 0.64 H_2O + 0.84 $H_2SiO_4^{-2}$	4.17	4.17	4.17
CEM18_Cal [c]	$CaCO_3$	CEM18_Cal = 1 CO_3^{-2} + 1 Ca^{+2}	-8.45	-8.45	-8.45
CEM18_chabazite [c]	$CaAl_2Si_4O_{12}$•$6H_2O$	CEM18_chabazite + 6 H_2O = 2 $Al[OH]_4^-$ + 1 Ca^{+2} + 8 H^+ + 4 $H_2SiO_4^{-2}$	-119		
CEM18_Cls [c]	$SrSO_4$	CEM18_Cls = 1 SO_4^{-2} + 1 Sr^{+2}	-6.63	-6.63	-6.63
CEM18_FeOOHmic [c]	$FeO(OH)$	CEM18_FeOOHmic + 2 H_2O = 1 $Fe[OH]_4^-$ + 1 H^+	-19.3	-19.3	-19.3
CEM18_Gp [c]	$CaSO_4$•$2H_2O$	CEM18_Gp = 1 Ca^{+2} + 2 H_2O + 1 SO_4^{-2}	-4.58	-4.58	
CEM18_M15SH [c]	$M_{1.5}SH_{2.5}$*	CEM18_M15SH + 1 H^+ = 2 H_2O + 1 $H_2SiO_4^{-2}$ + 1.5 Mg^{+2}	-4.28	-4.28	-4.28
CEM18_monocarbonate [c]	C_4AcH_{11}*	CEM18_monocarbonate + 4 H^+ = 2 $Al[OH]_4^-$ + 1 CO_3^{-2} + 4 Ca^{+2} + 9 H_2O	25.4		
CEM18_Tob_I [c]	$C_2S_{2.4}H_{3.2}$*	CEM18_Tob_I = 2 Ca^{+2} + 0.8 H^+ + 0.4 H_2O + 2.4 $H_2SiO_4^{-2}$	-28.7	-28.7	
Cu[OH]2[s] [b]	$Cu(OH)_2$	Cu[OH]2[s] + 2 H^+ = 1 Cu^{+2} + 2 H_2O	8.84		8.84
Fe2[SeO3]3:2H2O [b]	$Fe_2(SeO_3)_3$•$2H_2O$	Fe2[SeO3]3:2H2O + 9 H_2O = 2 $Fe[OH]_4^-$ + 14 H^+ + 3 SeO_4^{-2} + 6 e^-	-175		
LLNL_Alstonite [d]	$CaBa(CO_3)_2$	LLNL_Alstonite = 1 Ba^{+2} + 2 CO_3^{-2} + 1 Ca^{+2}			-18.2
PATCH_BaCaSO4[75%Ba] [e]	$(Ba_{0.75}Ca_{0.25})SO_4$	PATCH_BaCaSO4[75%Ba] = 0.75 Ba^{+2} + 0.25 Ca^{+2} + 1 SO_4^{-2}			-8.69
PATCH_BaSrSO4[50%Ba] [e]	$(Ba_{0.5}Sr_{0.5})SO_4$	PATCH_BaSrSO4[50%Ba] = 0.5 Ba^{+2} + 1 SO_4^{-2} + 0.5 Sr^{+2}	-8.22	-8.22	-8.22
PATCH_CaSrSO4[25%Sr] [e]	$(Ca_{0.75}Sr_{0.25})SO_4$	PATCH_CaSrSO4[25%Sr] = 0.75 Ca^{+2} + 1 SO_4^{-2} + 0.25 Sr^{+2}	-5.39	-5.39	-5.39
PbMoO4 [b]	$PbMoO_4$	PbMoO4 = 1 MoO_4^{-2} + 1 Pb^{+2}	-15.8	-15.8	-15.8
SiO2[am-ppt] [b]	SiO_2	SiO2[am-ppt] + 2 H_2O = 2 H^+ + 1 $H_2SiO_4^{-2}$	-26.0	-26.0	-26.0
Strengite [b]	$FePO_4$•$2H_2O$	Strengite + 2 H_2O = 1 $Fe[OH]_4^-$ + 4 H^+ + 1 PO_4^{-3}	-48.0	-48.0	-48.0
Strontianite [b]	$SrCO_3$	Strontianite = 1 CO_3^{-2} + 1 Sr^{+2}	-9.27	-9.27	-9.27
thermochem_Beidellite_Ca [f]	$Ca_{0.17}Al_{2.34}Si_{3.66}O_{10}(OH)_2$	thermochem_Beidellite_Ca + 12 H_2O = 2.34 $Al[OH]_4^-$ + 0.17 Ca^{+2} + 9.32 H^+ + 3.66 $H_2SiO_4^{-2}$			-127
THERMODDEM_Mullite [g]	$3Al_2O_3$•$2SiO_2$	THERMODDEM_Mullite + 19 H_2O = 6 $Al[OH]_4^-$ + 10 H^+ + 2 $H_2SiO_4^{-2}$	-135	-135	-135

Note: ‡ log K refers to dissolution reaction constant (solubility product constant).

Formula: Most mineral phases are presented in the chemical formula while some cementitious phases* are named according to the cement chemist notations using C = CaO; S = SiO_2; A = Al_2O_3; F = Fe_2O_3; M = MgO; H = H_2O; c = CO_2; s = SO_3.

Sources: [a] From literature [153]; [b] MINTEQA2_V4 database [56]; [c] CEMDATA18 database [84]; [d] LLNL database [86]; [e] Co-precipitations assuming ideal solid solution; [f] ThermoChimie database [87]; and [g] THERMODDEM2011 database [85].

Table A.7 Mineral set identified in geochemical virtual materials for Group II CFAs

Phase ID in Database	Formula	Reaction	log K[‡]	
			CDL_AG	KSP_AG
AA_Magnesite [a]	$MgCO_3$	AA_Magnesite = 1 CO_3^{-2} + 1 Mg^{+2}		-9.33
Brucite [b]	$Mg(OH)_2$	Brucite + 2 H^+ = 2 H_2O + 1 Mg^{+2}	17.2	
Ca2V2O7 [b]	$Ca_2V_2O_7$	Ca2V2O7 + 6 H^+ = 2 Ca^{+2} + 3 H_2O + 2 VO_2^+	18.0	
Ca3[AsO4]2:2.25H2O [c]	$Ca_3(AsO_4)_2$•2.25H_2O	Ca3[AsO4]2:2.25H2O = 2 AsO_4^{-3} + 3 Ca^{+2} + 2.25 H_2O	-21.4	
Ca3[VO4]2 [b]	$Ca_3(VO_4)_2$	Ca3[VO4]2 + 8 H^+ = 3 Ca^{+2} + 4 H_2O + 2 VO_2^+	39.8	
Ca4H[PO4]3:3H2O [b]	$Ca_4H(PO_4)_3$•3H_2O	Ca4H[PO4]3:3H2O = 4 Ca^{+2} + 1 H^+ + 3 H_2O + 3 PO_4^{-3}	-47.1	-47.1
Ca5[OH][AsO4]3 [d]	$Ca_5(OH)(AsO_4)_3$	Ca5[OH][AsO4]3 + 1 H^+ = 3 AsO_4^{-3} + 5 Ca^{+2} + 1 H_2O		-23.9
CEM18_AlOHam [e]	$Al(OH)_3$	CEM18_AlOHam + 1 H_2O = 1 $Al[OH]_4^-$ + 1 H^+	-13.8	-13.8
CEM18_C3FS0_84H4_32 [e]	$C_3FS_{0.84}H_{4.32}$*	CEM18_C3FS0_84H4_32 + 2.32 H^+ = 3 Ca^{+2} + 2 $Fe[OH]_4^-$ + 0.64 H_2O + 0.84 $H_2SiO_4^{-2}$		2.30
CEM18_C3FS1_34H3_32 [e]	$C_3FS_{1.34}H_{3.32}$*	CEM18_C3FS1_34H3_32 + 1.32 H^+ + 1.36 H_2O = 3 Ca^{+2} + 2 $Fe[OH]_4^-$ + 1.34 $H_2SiO_4^{-2}$		-13.1
CEM18_Cal [e]	$CaCO_3$	CEM18_Cal = 1 CO_3^{-2} + 1 Ca^{+2}	-8.45	-8.45
CEM18_Fe_monosulfate [e]	C_4FsH_{10}*	CEM18_Fe_monosulfate + 4 H^+ = 4 Ca^{+2} + 2 $Fe[OH]_4^-$ + 10 H_2O + 1 SO_4^{-2}	26.5	
CEM18_FeOOHmic [e]	FeO(OH)	CEM18_FeOOHmic + 2 H_2O = 1 $Fe[OH]_4^-$ + 1 H^+	-19.3	-19.3
CEM18_M15SH [e]	$M_{1.5}SH_{2.5}$*	CEM18_M15SH + 1 H^+ = 2 H_2O + 1 $H_2SiO_4^{-2}$ + 1.5 Mg^{+2}		-4.28
CEM18_Mg3AlC0_5OH [e]	$\frac{1}{2}M_6AcH_{13}$*	CEM18_Mg3AlC0_5OH + 4 H^+ = 1 $Al[OH]_4^-$ + 0.5 CO_3^{-2} + 6.5 H_2O + 3 Mg^{+2}	23.6	
CEM18_monosulfate9 [e]	C_4AsH_9*	CEM18_monosulfate9 + 4 H^+ = 2 $Al[OH]_4^-$ + 4 Ca^{+2} + 7 H_2O + 1 SO_4^{-2}		31.3
CEM18_monosulfate16 [e]	C_4AsH_{16}*	CEM18_monosulfate16 + 4 H^+ = 2 $Al[OH]_4^-$ + 4 Ca^{+2} + 14 H_2O + 1 SO_4^{-2}	27.7	
CEM18_Portlandite [e]	$Ca(OH)_2$	CEM18_Portlandite + 2 H^+ = 1 Ca^{+2} + 2 H_2O	23.2	
CEM18_Tob_I [e]	$C_2S_{2.4}H_{3.2}$*	CEM18_Tob_I = 2 Ca^{+2} + 0.8 H^+ + 0.4 H_2O + 2.4 $H_2SiO_4^{-2}$	-28.7	
Cr[OH]3[s] [b]	$Cr(OH)_3$	Cr[OH]3[s] + 1 H_2O = 1 CrO_4^{-2} + 5 H^+ + 3 e^-	-66.3	
Exp_Ca[OH]2.Cu[OH]2 [f]	$Ca(OH)_2$•$Cu(OH)_2$	Exp_Ca[OH]2.Cu[OH]2 + 4 H^+ = 1 Ca^{+2} + 1 Cu^{+2} + 4 H_2O	30.0	30.0
Exp_Ca3[OH]2[CrO4]2 [f]	$Ca_3(OH)_2(CrO_4)_2$	Exp_Ca3[OH]2[CrO4]2 + 2 H^+ = 3 Ca^{+2} + 2 CrO_4^{-2} + 2 H_2O	-1.00	
Exp_Ca3[OH]2[SeO3]2 [f]	$Ca_3(OH)_2(SeO_3)_2$	Exp_Ca3[OH]2[SeO3]2 + 2 H^+ = 3 Ca^{+2} + 2 H^+ + 2 SeO_4^{-2} + 4 e^-	-50.8	
Exp_Ca3[OH]2[SeO4]2 [f]	$Ca_3(OH)_2(SeO_4)_2$	Exp_Ca3[OH]2[SeO4]2 + 2 H^+ = 3 Ca^{+2} + 2 H_2O + 2 SeO_4^{-2}		0.52
Exp_Ca5[OH][BO3]3 [f]	$Ca_5(OH)(BO_3)_3$	Exp_Ca5[OH][BO3]3 + 7 H^+ = 5 Ca^{+2} + 3 H_2BO_3- + 1 H_2O	67.0[†]	64.0[†]
Exp_Ca5[OH][VO4]3 [f]	$Ca_5(OH)(VO_4)_3$	Exp_Ca5[OH][VO4]3 + 13 H^+ = 5 Ca^{+2} + 7 H_2O + 3 VO_2^+		66.0
Exp_PbHPO4 [f]	$PbHPO_4$	Exp_PbHPO4 = 1 H^+ + 1 PO_4^{-3} + 1 Pb^{+2}	-28.0	
Exp_FeVO4:2H2O [f]	$Fe(VO_4)_2$•2H_2O	Exp_FeVO4:2H2O + 2 H_2O = 1 $Fe[OH]_4^-$ + 1 VO_2^+	-23.5	
Fe2[SeO3]3:2H2O [b]	$Fe_2(SeO_3)_3$•2H_2O	Fe2[SeO3]3:2H2O + 9 H_2O = 2 $Fe[OH]_4^-$ + 14 H^+ + 3 SeO_4^{-2} + 6 e^-	-175	-175
FeMoO4 [b]	$FeMoO_4$	FeMoO4 + 4 H_2O = 1 $Fe[OH]_4^-$ + 4 H^+ + 1 MoO_4^{-2} + 1 e^-	-44.8	
LLNL_Cuprite [g]	Cu_2O	LLNL_Cuprite + 2 H^+ = 2 Cu^{+2} + 1 H_2O + 2 e^-	-7.24	
LLNL_Strontianite [g]	$SrCO_3$	LLNL_Strontianite = 1 CO_3^{-2} + 1 Sr^{+2}		-10.7
Manganite [b]	MnO(OH)	Manganite + 3 H^+ + 1 e^- = 2 H_2O + 1 Mn^{+2}	25.3	
MINTEQ_Laumontite [h]	$Ca(AlSi_2O_6)_2$•4H_2O	MINTEQ_Laumontite + 8 H_2O = 2 $Al[OH]_4^-$ + 1 Ca^{+2} + 8 H^+ + 4 $H_2SiO_4^{-2}$		-124
PATCH_alpha-TCP [i]	$Ca_3(PO_4)_2$	PATCH_alpha-TCP = 3 Ca^{+2} + 2 PO_4^{-3}	-25.6	-25.6
Pb[OH]2[s] [b]	$Pb(OH)_2$	Pb[OH]2[s] + 2 H^+ = 2 H_2O + 1 Pb^{+2}	8.32	8.32
Pb2V2O7 [b]	$Pb_2V_2O_7$	Pb2V2O7 + 6 H^+ = 3 H_2O + 2 Pb^{+2} + 2 VO_2^+	-1.82	
Strengite [b]	$FePO_4$•2H_2O	Strengite + 2 H_2O = 1 $Fe[OH]_4^-$ + 4 H^+ + 1 PO_4^{-3}	-48.0	-48.0
thermochem_Al[PO4][cr] [j]	$AlPO_4$	thermochem_Al[PO4][cr] + 4 H_2O = 1 $Al[OH]_4^-$ + 4 H^+ + 1 PO_4^{-3}	-45.5	-45.5

thermochem_Laumontite [k]	$Ca(AlSi_2O_6)_2 \cdot 4H_2O$	thermochem_Laumontite + 8 H_2O = 2 $Al[OH]_4^-$ + 1 Ca^{+2} + 8 H^+ + 4 $H_2SiO_4^{-2}$	-121

Note: [‡] log K refers to dissolution reaction constant (solubility product constant).

Formula: Most mineral phases are presented in the chemical formula while some cementitious phases[*] are named according to the cement chemist notations using C = CaO; S = SiO_2; A = Al_2O_3; F = Fe_2O_3; M = MgO; H = H_2O; c = CO_2; s = SO_3.

Sources: [a] From literature [153]; [b] MINTEQA2_V4 database [56]; [c] From literature [42]; [d] From literature [43]; [e] CEMDATA18 database [84]; [f] Experimental mineral; [g] LLNL database [86]; [h] MINTEQ database [103]; [i] From literature [154]; [j] Co-precipitation assuming ideal solid solution; and [k] ThermoChimie database [87].

Table A.8 Mineral set identified in geochemical virtual materials for Group III CFA (PPB_U)

Phase ID in Database	Formula	Reaction	log K[4]
Mineral phases			
AA_Magnesite [a]	$MgCO_3$	AA_Magnesite = 1 CO_3^{-2} + 1 Mg^{+2}	-9.33
Brucite [b]	$Mg(OH)_2$	Brucite + 2 H^+ = 2 H_2O + 1 Mg^{+2}	17.2
Ca3[PO4]2[beta] [b]	$Ca_3(PO_4)_2$	Ca3[PO4]2[beta] = 3 Ca^{+2} + 2 PO_4^{-3}	-29.1
Ca3[AsO4]2:2.25H2O [c]	$Ca_3(AsO_4)_2$•2.25H_2O	PATCH_Ca3[AsO4]2:2.25H2O = 2 AsO_4^{-3} + 3 Ca^{+2} + 2.25 H_2O	-21.4
CaHPO4[s] [b]	$CaHPO_4$	CaHPO4[s] = 1 Ca+2 + 1 H+ + 1 PO4-3	-19.4
CEM18_AlOHam [d]	$Al(OH)_3$	CEM18_AlOHam + 1 H_2O = 1 $Al[OH]_4^-$ + 1 H^+	-13.8
CEM18_C3AFS0_84H4_32 [d]	$C_3(F,A)S_{0.84}H_{4.32}$*	CEM18_C3AFS0_84H4_32 + 2.32 H^+ = 1 $Al[OH]_4^-$ + 3 Ca^{+2} + 1 $Fe[OH]_4^-$ + 0.64 H_2O + 0.84 $H_2SiO_4^{-2}$	4.17
CEM18_CAH10 [d]	CAH_{10}*	CEM18_CAH10 = 2 $Al[OH]_4^-$ + 1 Ca^{+2} + 6 H_2O	-7.29
CEM18_Cal [d]	$CaCO_3$	CEM18_Cal = 1 CO_3^{-2} + 1 Ca^{+2}	-8.45
CEM18_FeOOHmic [d]	$FeO(OH)$	CEM18_FeOOHmic + 2 H_2O = 1 $Fe[OH]_4^-$ + 1 H^+	-19.3
CEM18_Gp [d]	$CaSO_4$•2H_2O	CEM18_Gp = 1 Ca^{+2} + 2 H_2O + 1 SO_4^{-2}	-4.58
CEM18_M15SH [d]	$M_{1.5}SH_{2.5}$*	CEM18_M15SH + 1 H^+ = 2 H_2O + 1 $H_2SiO_4^{-2}$ + 1.5 Mg^{+2}	-4.28
CEM18_Mg3AlC0_5OH [d]	$\frac{1}{2}M_6AcH_{13}$*	CEM18_Mg3AlC0_5OH + 4 H^+ = 1 $Al[OH]_4^-$ + 0.5 CO_3^{-2} + 6.5 H_2O + 3 Mg^{+2}	23.6
CEM18_tricarboalu03 [d]	$\frac{1}{3}C_6Ac_3H_{32}$*	CEM18_tricarboalu03 + 1.332 H^+ = 0.667 $Al[OH]_4^-$ + 1 CO_3^{-2} + 2 Ca^{+2} + 10 H_2O	3.37
Cu[OH]2[s] [b]	$Cu(OH)_2$	Cu[OH]2[s] + 2 H^+ = 1 Cu^{+2} + 2 H_2O	8.84
Exp_Ca[OH]2.Cu[OH]2 [e]	$Ca(OH)_2$•$Cu(OH)_2$	Exp_Ca[OH]2.Cu[OH]2 + 4 H^+ = 1 Ca^{+2} + 1 Cu^{+2} + 4 H_2O	30.0
Exp_CuHPO4 [e]	$CuHPO_4$	Exp_CuHPO4 = 1 Cu^{+2} + 1 H^+ + 1 PO_4^{-3}	-26.0
Exp_Mn2SiO4 [e]	Mn_2SiO_4	Exp_Mn2SiO4 + 2 H^+ = 1 $H_2SiO_4^{-2}$ + 2 Mn^{+2}	-6.06
Exp_PbHPO4 [e]	$PbHPO_4$	Exp_PbHPO4 = 1 H^+ + 1 PO_4^{-3} + 1 Pb^{+2}	-28.0
MINTEQ_Laumontite [f]	$Ca(AlSi_2O_6)_2$•4H_2O	MINTEQ_Laumontite + 8 H_2O = 2 $Al[OH]_4^-$ + 1 Ca^{+2} + 8 H^+ + 4 $H_2SiO_4^{-2}$	-124
PATCH_BaCaSO4[25%Ba] [g]	$(Ba_{0.25}Ca_{0.75})SO_4$	PATCH_BaCaSO4[25%Ba] = 0.25 Ba^{+2} + 0.75 Ca^{+2} + 1 SO_4^{-2}	-5.56
Pb[OH]2[s] [b]	$Pb(OH)_2$	Pb[OH]2[s] + 2 H^+ = 2 H_2O + 1 Pb^{+2}	8.32
Strontianite [b]	$SrCO_3$	Strontianite = 1 CO_3^{-2} + 1 Sr^{+2}	-9.27
THERMODDEM_Arsenocrandallite [h]	$CaAl_3(AsO_4)(AsO_3OH)(OH)_6$	THERMODDEM_Arsenocrandallite + 6 H_2O = 3 $Al[OH]_4^-$ + 2 AsO_4^{-3} + 1 Ca^{+2} + 7 H^+	-96.5
Solid solutions			
CEM18_CSHQ_JenD [c]	-	CEM18_CSHQ_JenD + 1.67 H^+ = 0.67 CEM18_CSHQ_ss + 1.5 Ca^{+2} + 2.67 H_2O + 0.67 $H_2SiO_4^{-2}$	13.7
CEM18_CSHQ_JenH [c]	-	CEM18_CSHQ_JenH + 0.667 H^+ = 1 CEM18_CSHQ_ss + 1.333 Ca^{+2} + 1.5 H_2O + 1 $H_2SiO_4^{-2}$	-0.72
CEM18_CSHQ_TobD [c]	-	CEM18_CSHQ_TobD + 0.33 H^+ = 0.67 CEM18_CSHQ_ss + 0.83 Ca^{+2} + 1.33 H_2O + 0.67 $H_2SiO_4^{-2}$	-1.63
CEM18_CSHQ_TobH [c]	-	CEM18_CSHQ_TobH = 1 CEM18_CSHQ_ss + 0.667 Ca^{+2} + 0.667 H^+ + 0.1667 H_2O + 1 $H_2SiO_4^{-2}$	-14.9
AsO4_Ettringite_ss	-	AsO4_Ettringite_ss + 1 H^+ + 8 H_2O = 2 $Al[OH]_4^-$ + 3 AsO_4^{-3} + 6 Ca^{+2} + 1 ettr_ss	-26.8
Ba_Ettringite_ss [i]	-	Ba_Ettringite_ss + 4 H^+ + 8 H_2O = 2 $Al[OH]_4^-$ + 6 Ba^{+2} + 3 SO_4^{-2} + 1 ettr_ss	-4.01
BO3_Ettringite_ss [i]	-	BO3_Ettringite_ss + 7 H^+ + 8 H_2O = 2 $Al[OH]_4^-$ + 6 Ca^{+2} + 3 H_2BO_3- + 1 ettr_ss	46.9
CrO4_Ettringite_ss [i]	-	CrO4_Ettringite_ss + 4 H^+ + 8 H_2O = 2 $Al[OH]_4^-$ + 6 Ca^{+2} + 3 CrO_4^{-2} + 1 ettr_ss	8.59
Ettringite_ss [i]	-	Ettringite_ss + 4 H^+ + 8 H_2O = 2 $Al[OH]_4^-$ + 6 Ca^{+2} + 3 SO_4^{-2} + 1 ettr_ss	12.0
K_Ettringite_ss [i]	-	K-Ettringite_ss + 4 H^+ + 8 H_2O = 2 $Al[OH]_4^-$ + 5 Ca^{+2} + 2 K^+ + 3 SO_4^{-2} + 1 ettr_ss	6.70
MoO4_Ettringite_ss [i]	-	MoO4_Ettringite_ss + 4 H^+ + 8 H_2O = 2 $Al[OH]_4^-$ + 6 Ca^{+2} + 3 MoO_4^{-2} + 1 ettr_ss	9.59
Na_Ettringite_ss [i]	-	Na-Ettringite_ss + 4 H^+ + 8 H_2O = 2 $Al[OH]_4^-$ + 5 Ca^{+2} + 2 Na^+ + 3 SO_4^{-2} + 1 ettr_ss	7.70
PO4_Ettringite_ss [i]	-	PO4_Ettringite_ss + 1 H^+ + 8 H_2O = 2 $Al[OH]_4^-$ + 6 Ca^{+2} + 3 PO_4^{-3}	-39.1

		+ 1 ettr_ss	
SeO4-2_Ettringite_ss [i]	-	$SeO4^{-2}$_Ettringite_ss + 4 H^+ + 8 H_2O = 2 $Al[OH]_4^-$ + 6 Ca^{+2} + 3 SeO_4^{-2} + 1 ettr_ss	8.59
VO3_Ettringite_ss [i]	-	VO3_Ettringite_ss + 13 H^+ + 2 H_2O = 2 $Al[OH]_4^-$ + 6 Ca^{+2} + 3 VO_2^+ + 1 ettr_ss	53.8
Li_Ettringite_ss [i]	-	Li-Ettringite_ss + 4 H^+ + 8 H_2O = 2 $Al[OH]_4^-$ + 4 Ca^{+2} + 4 Li^+ + 3 SO_4^{-2} + 1 ettr_ss	-4.30

Note: [‡] log K refers to dissolution reaction constant (solubility product constant).

Formula: Most mineral phases are presented in the chemical formula while some cementitious phases[*] are named according to the cement chemist notations using C = CaO; S = SiO_2; A = Al_2O_3; F = Fe_2O_3; M = MgO; H = H_2O; c = CO_2; s = SO_3.

Sources: [a] From literature [153]; [b] MINTEQA2_V4 database [56]; [c] From literature [42]; [d] CEMDATA18 database [84]; [e] Experimental mineral; [f] MINTEQ database [103]; [g] Co-precipitation assuming ideal solid solution; [h] THERMODDEM2011 database [85]; and [i] Experimental mineral [88].

Table A.9 Potential minerals reported under a reducing environment from literature

Mineral Phase	Literature Source	Reaction	log K [a]
Pyrite [FeS_2] [b]	O'Day et al. [106]	Pyrite + 12 H_2O = 1 $Fe[OH]_4^-$ + 20 H^+ + 2 SO_4^{-2} + 15 e^-	-121
Vivianite [$Fe_3(PO_4)_2 \cdot 8H_2O$] [b]	Postma et al. [121]	Vivianite + 4 H_2O = 3 $Fe[OH]_4^-$ + 12 H^+ + 2 PO_4^{-3} + 3 e^-	-140
Siderite [$FeCO_3$] [b]	Postma et al. [121]	Siderite + 4 H_2O = 1 CO_3^{-2} + 1 $Fe[OH]_4^-$ + 4 H^+ + 1 e^-	-44.9
Orpiment [As_2S_3] [b]	O'Day et al. [106]	Orpiment + 20 H_2O = 2 AsO_4^{-3} + 40 H^+ + 3 SO_4^{-2} + 28 e^-	-244
Realgar [AsS] [b]	O'Day et al. [106]	Realgar + 8 H_2O = 1 AsO_4^{-3} + 16 H^+ + 1 SO_4^{-2} + 11 e^-	-94.0
FeSe [b]	Schwartz et al. [22]	FeSe + 8 H_2O = 1 $Fe[OH]_4^-$ + 12 H^+ + 1 SeO_4^{-2} + 9 e^-	-128
Semetal [Se] [b]	Schwartz et al. [22]	Semetal[am] + 4 H_2O = 8 H^+ + 1 SeO_4^{-2} + 6 e^-	-88.9
Eskolaite [Cr_2O_3] [c]	Asmussen et al. [155]	Eskolaite + 5 H_2O = 2 CrO_4^{-2} + 10 H^+ + 6 e^-	-148

Note: [a] log K refers to dissolution reaction constant (solubility product constant).

Database Sources: [b] MINTEQA2_V4 database [56]; [c] THERMODDEM2011 database [85].

Table A.10 Ca-arsenates [$Ca_4(OH)_2(AsO_4)_2 \cdot 4H_2O$, $Ca_5(OH)(AsO_4)_3$, and $Ca_3(AsO_4)_2 \cdot xH_2O$] reported by literature and thermodynamic databases

Mineral Phase	Database	Reaction	pK_{sp}
$Ca_4(OH)_2(AsO_4)_2 \cdot 4H_2O$	1	$Ca_4(OH)_2(AsO_4)_2 \cdot 4H_2O + 2\ H^+ = 2\ AsO_4^{-3} + 4\ Ca^{+2} + 6\ H_2O$	0.87
	2		-2.23 - 0.58
	3		-0.06
$Ca_5(AsO_4)_3OH$	1	$Ca_5(AsO_4)_3OH + 1\ H^+ = 3\ AsO_4^{-3} + 5\ Ca^{+2} + 1\ H_2O$	23.88
	2		23.37 - 28.56
	3		23.95
$Ca_3(AsO_4)_2$	4	$Ca_3(AsO_4)_2 \cdot xH_2O = 2\ AsO_4^{-3} + 3\ Ca^{+2} + x\ H_2O$	19.22
$Ca_3(AsO_4)_2 \cdot 2.25H_2O$	2		20.08 - 21.98
$Ca_3(AsO_4)_2 \cdot 3H_2O$	2		20.31 - 22.02
$Ca_3(AsO_4)_2 \cdot 3.66H_2O$	3		20.27
$Ca_3(AsO_4)_2 \cdot 3.67H_2O$	1		21
$Ca_3(AsO_4)_2 \cdot 4\ H_2O$	5		19.18
$Ca_3(AsO_4)_2 \cdot 4.25H_2O$	1		21
$Ca_3(AsO_4)_2 \cdot xH_2O$	6		21

Database Sources: 1: From literature [43]; 2: From literature [42]; 3: From THERMODDEM2011 database [85]; 4: From LLNL database [86]; 5: From MINTEQA2_V4 database [56]; and 6: From ThermoChimie database [87].

A.VIII HFO adsorption of virtual materials

Table A.11 Amount of amorphous and crystalline iron (hydr)oxides, maximum release of Fe from 1313 (available Fe), total iron, and calibrated HFO content in geochemical virtual materials for reference CFAs

Material ID	Measured Values (mol Fe/kg-dry)				Virtual Material (mol Fe/kg-dry)
	Total Fe (XRF)	Am_{FeOOH} [a]	Am_{FeOOH} + Cry_{FeOOH} [a]	Measured Available Fe (EPA 1313)	HFO Content [b]
EFA_U	0.85	0.004	0.066	0.0005	0.008
FFA_U	1.24	0.003	0.048	0.0005	0.031
LAB_U	0.89	0.002	0.018	0.0004	0.012
CDL_AG	3.40	0.019	0.129	0.0207	0.042
KSP_AG	2.38	0.015	0.077	0.0270	0.040
PPB_U	1.14	0.027	0.092	0.0006	0.070

[a] Measured from selective extraction tests - Am_{FeOOH}: amorphous iron (hydr)oxide from ISO Method 12782-1 [63]; Cry_{FeOOH}: crystalline iron (hydr)oxide from ISO Method 12782-2 [64].
[b] HFO content represented by the calibrated available content of Fe used in virtual materials.

Table A.12 AsO_4/HFO, MoO_4/HFO, SeO_4/HFO, SeO_3/HFO, VO_4/HFO, BO_3/HFO, and CrO_4/HFO surface complexation constants reported by Dzombak and Morel [52] and values used in geochemical modeling

		Reported Value [a]	Calibrated Value [b]
AsO_4/HFO			
$\equiv FeOH^0 + AsO_4^{3-} + 3H^+ = \equiv FeH_2AsO_4^0 + H_2O$	log K_1	29.31	29.31
$\equiv FeOH^0 + AsO_4^{3-} + 2H^+ = \equiv FeHAsO_4^- + H_2O$	log K_2	23.51	23.51
$\equiv FeOH^0 + AsO_4^{3-} + H^+ = \equiv FeAsO_4^{2-} + H_2O$	log K_3	/	/
$\equiv FeOH^0 + AsO_4^{3-} = \equiv FeOHAsO_4^{3-}$	log K_4	10.58	10.58
MoO_4/HFO			
$\equiv FeOH^0 + MoO_4^{2-} + H^+ = \equiv FeMoO_4^- + H_2O$	log K_1	9.5	9.5
$\equiv FeOH^0 + MoO_4^{2-} = \equiv FeOHMoO_4^{2-}$	log K_2	2.4	2.4
SeO_4/HFO			
$\equiv FeOH^0 + SeO_4^{2-} + H^+ = \equiv FeSeO_4^- + H_2O$	log K_1	7.73	**5.73** [c]
$\equiv FeOH^0 + SeO_4^{2-} = \equiv FeOHSeO_4^{2-}$	log K_2	0.80	**4.78** [c]
SeO_3/HFO			
$\equiv FeOH^0 + SeO_3^{2-} + H^+ = \equiv FeSeO_3^- + H_2O$	log K_1	12.69	12.69
$\equiv FeOH^0 + SeO_3^{2-} = \equiv FeOHSeO_3^{2-}$	log K_2	5.17	5.17
VO_4/HFO			
$\equiv FeOH^0 + VO_4^{3-} + 2H^+ = \equiv FeHVO_4^- + H_2O$	log K_1	-	**28.00** [d]
$\equiv FeOH^0 + VO_4^{3-} + H^+ = \equiv FeVO_4^{2-} + H_2O$	log K_2	-	**21.70** [d]
$\equiv FeOH^0 + VO_4^{3-} = \equiv FeOHVO_4^{3-}$	log K_3	13.57	13.57
BO_3/HFO			
$\equiv FeOH^0 + H_3BO_3 = \equiv FeH_2BO_3 + H_2O$	log K_1	0.62	0.62
CrO_4/HFO			
$\equiv FeOH^0 + CrO_4^{2-} + H^+ = \equiv FeCrO_4^- + H_2O$	log K_1	10.85	10.85

[a] Reported reaction constants by Dzombak and Morel [52].

[b] The calibrated reaction constants were used to improve predictions for Se and V while values for other constituents were reported values by Dzombak and Morel [52]

[c] The reaction constants (log K_1 and log K_2) involving forming surface species $\equiv FeSeO_4^-$ and $\equiv FeOHSeO_4^{2-}$ were calibrated to improve the predictions for Se leaching.

[d] Two reactions were added with calibrated reaction constants (log K_1 and log K_2) to improve the predictions for V leaching.

A.IX Organic matter complexation of virtual materials

In the ORCHESTRA model, organic matter complexation is represented by an active fraction of the total organic matter (i.e., humic acid or HA) by dividing HA into a solid humic acid (SHA) fraction and a dissolved humic acid (DHA) fraction:

$$HA\ (mg/kg) = [DHA\ (mg/L) + SHA\ (mg/L)] \times L/S(L/kg) \qquad \text{Equation A-2}$$

The HA content for a specific material is a fixed value, while the DHA concentration (mg/L) is a function of pH and available for interaction with elements in the eluate. The model represents DHA concentration as the product of the measured dissolved organic carbon (DOC) in leaching tests eluates and a calibrated parameter representing active proportion (α):

$$DHA = DOC \times \frac{DHA}{DOC} = DOC \times \alpha \qquad \text{Equation A-3}$$

The active fraction (α, DHA/DOC) is a function of pH with the lowest proportion of reactive forms at neutral pH and increasing towards both low and high pH [18,27]. At each test position in the pH-dependent test, a value of α (<1) was calibrated to calculate the DHA concentration according to Equation A-3. The relationship of DHA with pH was then modeled by a polynomial fit through the test positions.

In the model, the total HA was calibrated under the upper limit of measured total organic carbon in the solid (TOC). With the calibrated total HA content and DHA concentration as a function of pH, the concentration of SHA was obtained by Equation A-2 to calculate the fraction of a species adsorbed to the solid fraction of organic matter.

Table A.13 Polynomial coefficients of dissolved humic acid (DHA, mg/L) as a function of pH and amount of total humic acid (dissolved humic acid + solid humic acid) calibrated in geochemical virtual materials for reference CFAs

Material ID	Polynomial Coefficients						Total HA [a] (mg/kg)
	C0	C1	C2	C3	C4	C5	
EFA_U	-8.309E+0	1.493E+0	-4.130E-1	4.140E-2	-1.399E-3	3.518E-6	200
FFA_U	-1.128E+1	4.366E+0	-1.552E+0	2.381E-1	-1.635E-2	4.162E-4	410
LAB_U	-8.275E+0	1.580E+0	-5.290E-1	7.506E-2	-4.734E-3	1.105E-4	100
CDL_AG	-3.814E+0	-2.969E+0	8.201E-1	-1.143E-1	8.021E-3	-2.166E-4	900
KSP_AG	-1.261E+1	6.208E+0	-2.252E+0	3.375E-1	-2.240E-2	5.491E-4	1,000
PPB_U	-1.255E+1	6.576E+0	-2.488E+0	3.837E-1	-2.616E-2	6.619E-4	80

[a] Calibrated values.

A.X Controlling mechanisms for leaching of coal fly ashes in the EPA database

Table A.14 Controlling mechanisms for leaching of As, Se, and V from coal fly ashes in the EPA database [11]

Sample ID	Ca [a] (%)	S [a] (%)	Fe [a] (%)	Natural pH [b]	As [c]		Se [c]		V [c]	
					pH< 8	pH > 8	pH < 8	pH > 8	pH < 10	pH > 10
LAT	0.32	0.22	2.36	4.1	A	A	A	A	A	A
AaFA	0.57	0.27	2.99	4.36	A	A	A	A	A	A
GFA	0.58	0.21	2.96	4.3	A	A	A	A	A	A
AaFB	0.60	0.46	2.98	3.92	A	A	A	A	A	A
EFB	0.65	0.23	4.14	4.2	A	A	A	A	A	A
DaFA	0.68	0.21	3.20	4.32	A	A	A	A	A	A
EFC	0.73	0.26	4.98	4.52	A	A	A	A	A	A
SHT	0.75	0.52	3.28	9.87	A	C	A	A	A	C
WFA	0.97	0.94	4.75	10.18	A	A	A	A	A	A
SHB	1.23	0.43	4.29	11.53	A	C/E	A	A	A	C/E
BPT	1.34	0.64	1.59	9.39	A	A/C	A	C	A	A/C
KFA	1.42	0.30	16.12	9.13	A	C	A	A	A	A/C
AaFC	1.43	0.37	6.29	11.52	A	C	A	C	A	A/C
TFA	1.43	0.75	9.82	8.73	A	A/C	A	A	A	A/C
GAT	1.92	1.18	5.90	7.8	A	C	A	A	A	C
GAB	2.07	0.54	7.43	11.1	A	C	A	A	A	C
DFA	3.11	0.51	11.10	9.86	A	C	A	C/E	A	C
UFA	3.35	0.91	9.90	11.81	A	C	A	C/E	A	C
BFA	3.41	0.71	10.78	8.36	A	C/E	A	C/E	A	C
AFA	3.53	0.36	4.68	9.88	A	C/E	A	C/E	A	C
CFA	3.61	0.39	5.20	10.17	A	C/E	A	C/E	A	C
HFA	4.46	0.63	13.28	8.5	A	C	A	A	A	A/C
BPB	4.69	0.40	3.22	11.71	A	C/E	A	C/E	A	C/E
CaFA	6.29	0.20	3.13	12	A	C/E	A	C	A	C
BaFA	10.60	0.47	3.39	11.7	A	C/E	A	C/E	A	C
JAT	11.42	1.03	5.56	12.2	A	E	A	E	A	E
JAB	12.09	1.23	5.36	12.1	A	E	A	E	A	E
PPT	12.46	1.22	2.93	11.66	A	E	A	E	A	E
XFA	16.30	1.37	3.83	11.5	A	E	A	E	A	E
ZFA	18.49	0.88	3.92	11.98	A	E	A	E	A	E

[a] Total content of Ca, S, and Fe. The samples were ranked in an increasing order based on the total content of Ca. The shading color of row is based on the total content of Ca, S, and Fe, as lower values are in green, medium values are in yellow, and greater values are in red.

[b] Natural pH is defined as the pH response to water extractions for 24 hours at the liquid-to-solid ratio of 10 L/kg-dry.

[c] Mechanisms controlling leaching of constituents. A: adsorption; C: co-precipitation with Ca; E: substitution in ettringite; A/C: adsorption and/or co-precipitation with Ca; and C/E: co-precipitation with Ca and/or substitution in ettringite.

Table A.15 Controlling mechanisms for leaching of B, Cr, and Mo from coal fly ashes in the EPA database [11]

Sample ID	Ca [a] (%)	S [a] (%)	Fe [a] (%)	Natural pH [b]	B [c]		Cr [c]		Mo [c]	
					pH < 8	pH > 8	pH < 8	pH > 8	pH < 8	pH > 8
LAT	0.32	0.22	2.36	4.1	A.L.	A.L.	A	A/C	A	A.L.
AaFA	0.57	0.27	2.99	4.36	A.L.	A.L.	A	A/C	A	A.L.
GFA	0.58	0.21	2.96	4.3	A.L.	A.L.	A	A/C	A	A.L.
AaFB	0.60	0.46	2.98	3.92	A.L.	A.L.	A	A/C	A	A.L.
EFB	0.65	0.23	4.14	4.2	A.L.	A.L.	A	A/C	A	A.L.
DaFA	0.68	0.21	3.20	4.32	A.L.	A.L.	A	A/C	A	A.L.
EFC	0.73	0.26	4.98	4.52	A.L.	A.L.	A	A/C	A	A.L.
SHT	0.75	0.52	3.28	9.87	A.L.	A.L.	A	A/C	A	A.L.
WFA	0.97	0.94	4.75	10.18	A.L.	A.L.	A	A/C	A	A.L.
SHB	1.23	0.43	4.29	11.53	A.L.	C	A	A/C	A	A.L.
BPT	1.34	0.64	1.59	9.39	A.L.	A.L.	A	A/C	A	A.L.
KFA	1.42	0.30	16.12	9.13	A.L.	A.L.	A	A/C	A	A.L.
AaFC	1.43	0.37	6.29	11.52	A.L.	A.L.	A	A/C	A	A.L.
TFA	1.43	0.75	9.82	8.73	A.L.	A.L.	A	A/C	A	A.L.
GAT	1.92	1.18	5.90	7.8	A.L.	C	A	A/C	A	A.L.
GAB	2.07	0.54	7.43	11.1	A.L.	C	A	C	A	A.L.
DFA	3.11	0.51	11.10	9.86	A.L.	C	A	A/C	A	A.L.
UFA	3.35	0.91	9.90	11.81	A.L.	C	A	A/C	A	A.L.
BFA	3.41	0.71	10.78	8.36	A.L.	C	A	A/C	A	A.L.
AFA	3.53	0.36	4.68	9.88	A.L.	C/E	A	A/C	A	C
CFA	3.61	0.39	5.20	10.17	A.L.	C/E	A	C	A	C
HFA	4.46	0.63	13.28	8.5	A.L.	C	A	A/C	A	C
BPB	4.69	0.40	3.22	11.71	A.L.	C/E	A	C	A	A.L.
CaFA	6.29	0.20	3.13	12	A.L.	C	A	A/C	A	A.L.
BaFA	10.60	0.47	3.39	11.7	A.L.	C/E	A	A/C	A	C
JAT	11.42	1.03	5.56	12.2	A	E	A	A/C	A	A.L.
JAB	12.09	1.23	5.36	12.1	A	E	A	E	A	A.L.
PPT	12.46	1.22	2.93	11.66	A	E	A	E	A	E
XFA	16.30	1.37	3.83	11.5	A	E	A	E	A	E
ZFA	18.49	0.88	3.92	11.98	A	E	A	E	A	E

[a] Total content of Ca, S, and Fe. The samples were ranked in an increasing order based on the total content of Ca. The shading color of row is based on the total content of Ca, S, and Fe, as lower values are in green, medium values are in yellow, and greater values are in red.

[b] Natural pH is defined as the pH response to water extractions for 24 hours at the liquid-to-solid ratio of 10 L/kg-dry.

[c] Mechanisms controlling leaching of constituents. A: adsorption; C: co-precipitation with Ca; E: substitution in ettringite; A/C: adsorption and/or co-precipitation with Ca; C/E: co-precipitation with Ca and/or substitution in ettringite; A.L.: available content limited. For the available content-limited (A.L.) leaching behavior, eluate concentrations are a weak function of pH, which are limited by the amount of leachable mass in the solid.

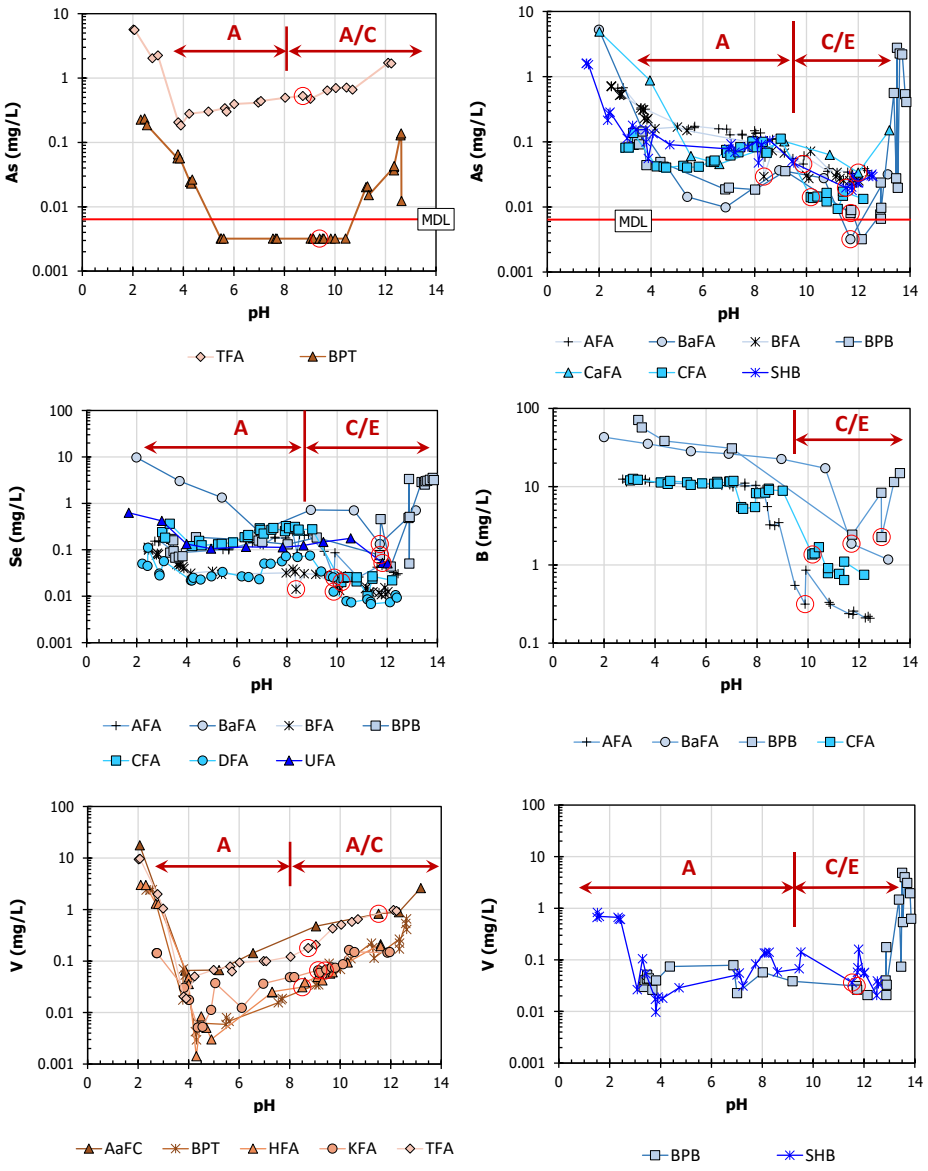

Figure A.2 Leaching behavior of oxyanions for which the controlling mechanisms cannot be confidently identified. A: adsorption; A/C: adsorption and/or co-precipitation with Ca; C/E: co-precipitation with Ca and/or substitution in ettringite.

A.XI Chemical composition, particle size distribution, and summary of crystalline phases of reference CFAs

Table A.16 Source coal type, natural and own pH, and chemical composition of reference coal fly ashes

	Group I			Group II		Group III
	EFA_U	FFA_U	LAB_U	CDL_AG	KSP_AG	PPB_U
Coal Type [a]	Bit.	Bit.	Bit.	Bit.	Blend	Sub-bit.
Natural pH [b]	7.03	4.34	5.39	12.7	11.9	12.1
Own pH [b]	7.15	4.82	6.21	12.7	12.3	11.4
Si (wt%)	26.6	25.6	27.1	18.5	19.7	13.4
Al (wt%)	15.3	12.4	12.2	7.31	8.46	7.31
Fe (wt%)	4.74	6.90	4.95	18.9	13.3	6.38
Ca (wt%)	0.74	1.23	0.83	5.88	8.92	24.7
Mg (wt%)	0.67	0.52	0.57	0.79	0.94	1.81
S (wt%)	0.41	0.30	0.15	0.83	0.73	0.75
K (wt%)	2.14	3.69	4.14	2.41	1.84	0.45
Na (wt%)	0.45	0.45	0.50	1.05	1.10	1.38
TOC (wt%C)	13.5	5.52	10.1	1.99	2.41	2.64
TIC-C (wt%C) [c]	0.05	0.04	0.04	0.09	0.08	0.05
TGA-C (wt%C) [c]	1.17	1.02	1.04	0.60	0.40	0.10

[a] Bit., sub-bit., and blend represent source coal types of bituminous, sub-bituminous, and 50:50 blend of fly ash from bituminous and sub-bituminous coal, respectively.

[b] Natural pH and own pH are defined as the pH responses to water extractions for 24 hours at liquid-to-solid ratios of 10 L/kg-dry and 1 L/kg-dry, respectively.

[c] TIC-C refers to the total inorganic carbon (TIC) measured by the carbon analyzer, while TGA-C is the TIC measured by TGA/MS.

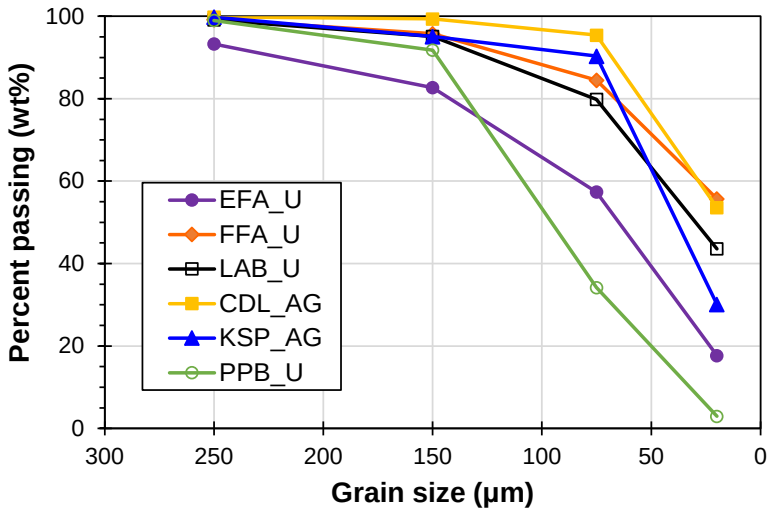

Figure A.3 Particle size distribution of reference coal fly ashes. The particle size distribution analysis was achieved by sieving into six size fractions, < 20 µm, 20-75 µm, 75-150 µm, 150-250 µm, and > 250 µm.

Table A.17 Crystalline phases identified by XRD in reference coal fly ashes

Mineral	Group I			Group II		Group III
	EFA_U	FFA_U	LAB_U	CDL_AG	KSP_AG	PPB_U
Anhydrite [$CaSO_4$]				√	√	√
Calcium aluminum oxide [$Ca_3Al_2O_6$]						√
Calcium aluminum oxide [$Ca_9Al_6O_{18}$]						√
Hematite [Fe_2O_3]				√		√
Lime [CaO]				√	√	√
Mullite [$Al_6Si_2O_{13}$]	√	√	√	√	√	√
Magnetite [Fe_3O_4]				√	√	
Portlandite [$Ca(OH)_2$]				√		
Periclase [MgO]						√
Quartz [SiO_2]	√	√	√	√	√	√

Table A.18 Crystalline phases identified in coal fly ashes from literature. *Common phases identified in more than one study are indicated in red.*

Feed coal	Bituminous					Sub-bituminous			Lignite	
Source	[1]	[2]	[3]	[4]	[5]	[1]	[4]	[6]	[4]	[1]
CaO (wt%)	3-5.3	7.8-8.1	3.9	1.2-8.8	0.6-6.1	7.2	7.9-33.9	22.7-28.5	7.0-20.9	23.7-25.4
Fe_2O_3 (wt%)	14.2-18.5	6.3-8.4	15.4	4.6-24.4	3.3-34.4	3.3	4.5-7.5	4.8-7.4	3.6-9.0	4.7-7.6
Anhydrite [$CaSO_4$]	√	√		√	√		√	√	√	√
Calcite [$CaCO_3$]						√				
Calcium aluminate [$Ca_3Al_2O_6$]							√	√	√	
Ferrite [$(Mg,Fe)_3O_4$]				√			√		√	
Gypsum [$CaSO_4 \cdot 2H_2O$]			√							
Hematite [Fe_2O_3]	√	√		√	√	√	√		√	
Lime [CaO]	√	√		√		√	√	√	√	
Mullite [$Al_6Si_2O_{13}$]	√	√		√	√	√	√		√	
Magnetite-maghemite suite [Fe_3O_4-Fe_2O_3]	√	√			√	√				
Melilite [$Ca_2(Mg,Al)(Al,Si)_2O_7$]							√		√	
Merwinite [$Ca_3MgSi_2O_8$]							√			
Periclase [MgO]				√			√	√	√	√
Portlandite [$Ca(OH)_2$]					√					
Klein's compound [$Ca_4Al_6(SO_4)O_{12}$]								√		
Sodalite-structures [$Na_8Al_8Si_6O_{24}SO_4$]							√			
Sillmanite [Al_2SiO_5]					√					
Quartz [SiO_2]	√	√	√	√	√	√	√	√	√	√

Literature Sources: [1] [74];[2] [75];[3] [76];[4] [77];[5] [78];[6] [79].

A.XII Modeling results

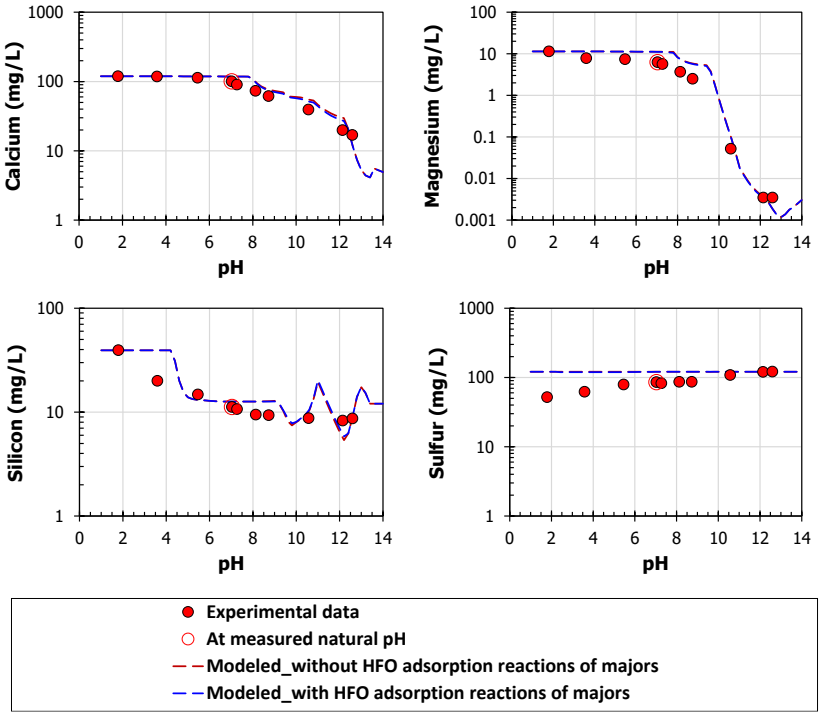

Figure A.4 Comparison of predicted leaching of Ca, Mg, Si, and S from the coal fly ash EFA_U between simulations with and without adding the reported DDL-HFO adsorption reactions of these major elements [52]. Modeling results with/without HFO adsorption reactions of major constituents overlap.

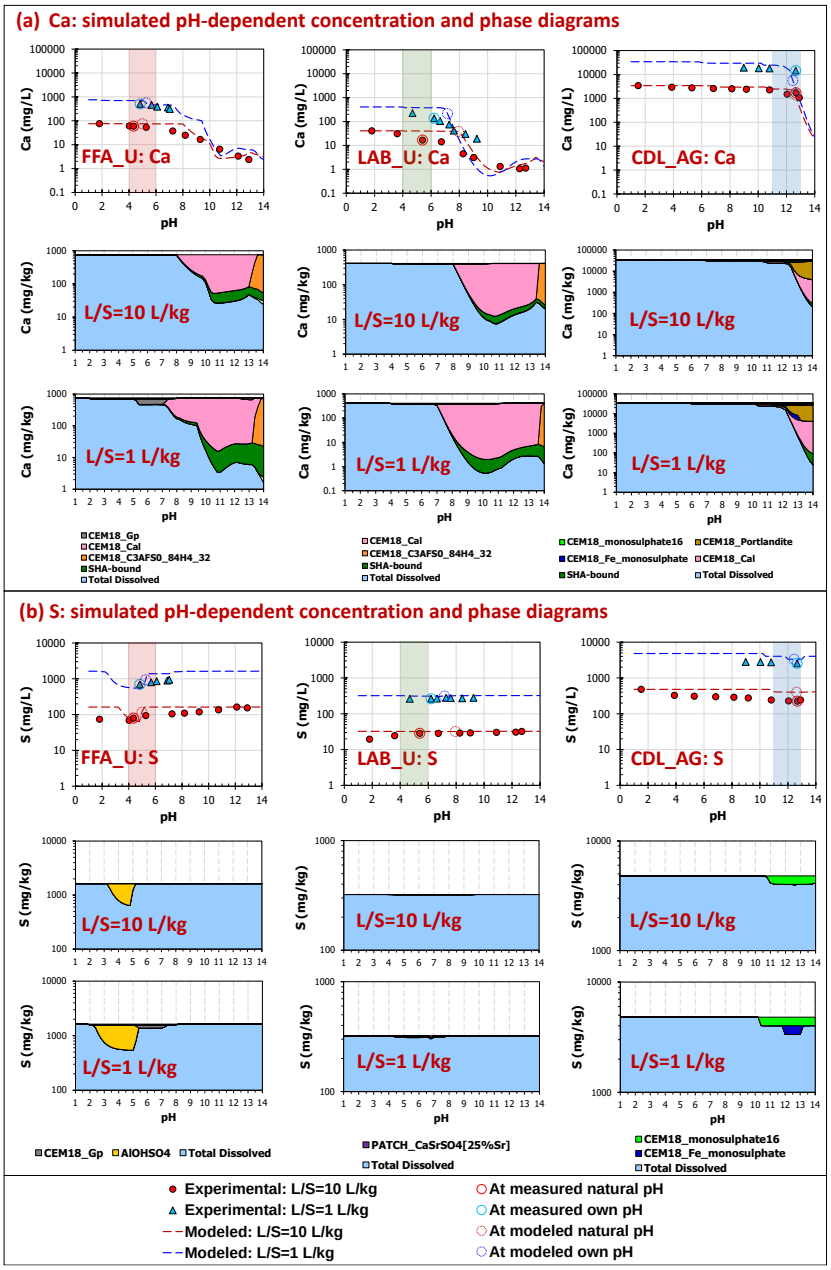

Figure A.5 Geochemical speciation modeling of Ca and S from Group I (FFA_U and LAB_U) and Group II coal fly ash (CDL_AG). CEM18_Gp: $CaSO_4 \cdot 2H_2O$; CEM18_Cal: $CaCO_3$; CEM18_C3AFS0_84H4_32*: $C_3(F,A)S_{0.84}H_{4.32}$; CEM18_monosulfate16*: C_4AsH_{16}; CEM18_Portlandite: $Ca(OH)_2$; CEM18_Fe_monosulphate*: C_4FsH_{10}; AlOHSO4: $AlOHSO_4$ mineral; PATCH_CaSrSO4[25%Sr]: $(Ca_{0.75}Sr_{0.25})SO_4$; SHA-bound: solid humic acid bound; Total dissolved: in dissolved phase, free ions. *Cement chemist notation was used to simplify the formulae of cement phases using C = CaO; S = SiO_2; A = Al_2O_3; F = Fe_2O_3; M = MgO; H = H_2O; c = CO_2; s = SO_3. A specific pH range around the natural and own pH conditions of each material is highlighted in pH-dependent concentration diagram.

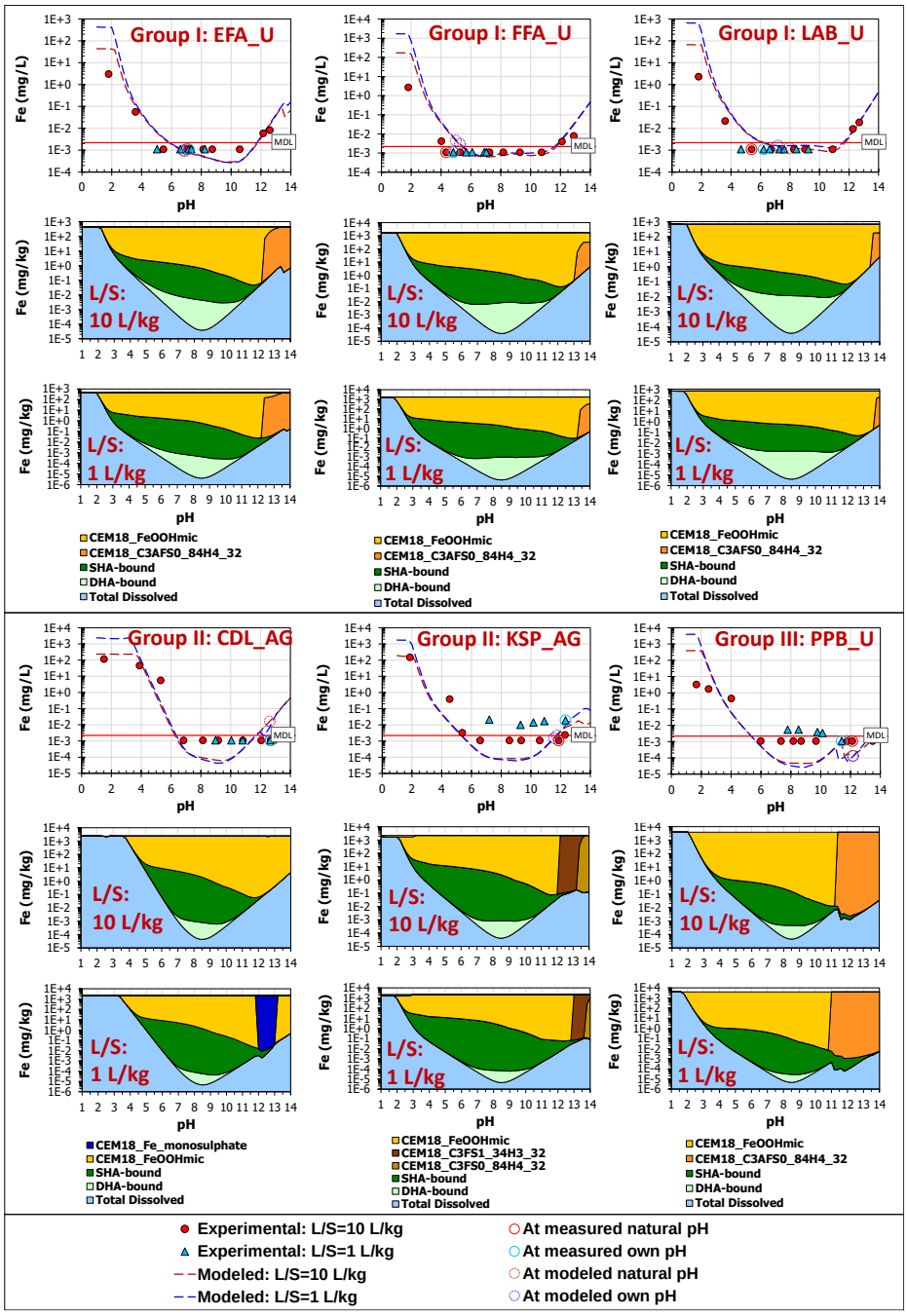

Figure A.6 Geochemical speciation modeling of Fe from Group I (EFA_U, FFA_U, and LAB_U); Group II (CDL_AG and KSP_AG); and Group III (PPB_U) coal fly ashes. MDL: method detection limit. CEM18_FeOOHmic: FeO(OH); CEM18_C3AFS0_84H4_32*: $C_3(F,A)S_{0.84}H_{4.32}$; CEM18_Fe_monosulphate*: C_4FsH_{10}; CEM18_C3FS1_34H3_32*: $C_3FS_{1.34}H_{3.32}$; CEM18_C3FS0_84H4_32*: $C_3FS_{0.84}H_{4.32}$; SHA-bound: solid humic acid bound; DHA-bound: dissolved humic acid bound; Total dissolved: in dissolved phase, free ions. *Cement chemist notation was used to simplify the formulae of cement phases using C = CaO; S = SiO_2; A = Al_2O_3; F = Fe_2O_3; H = H_2O.

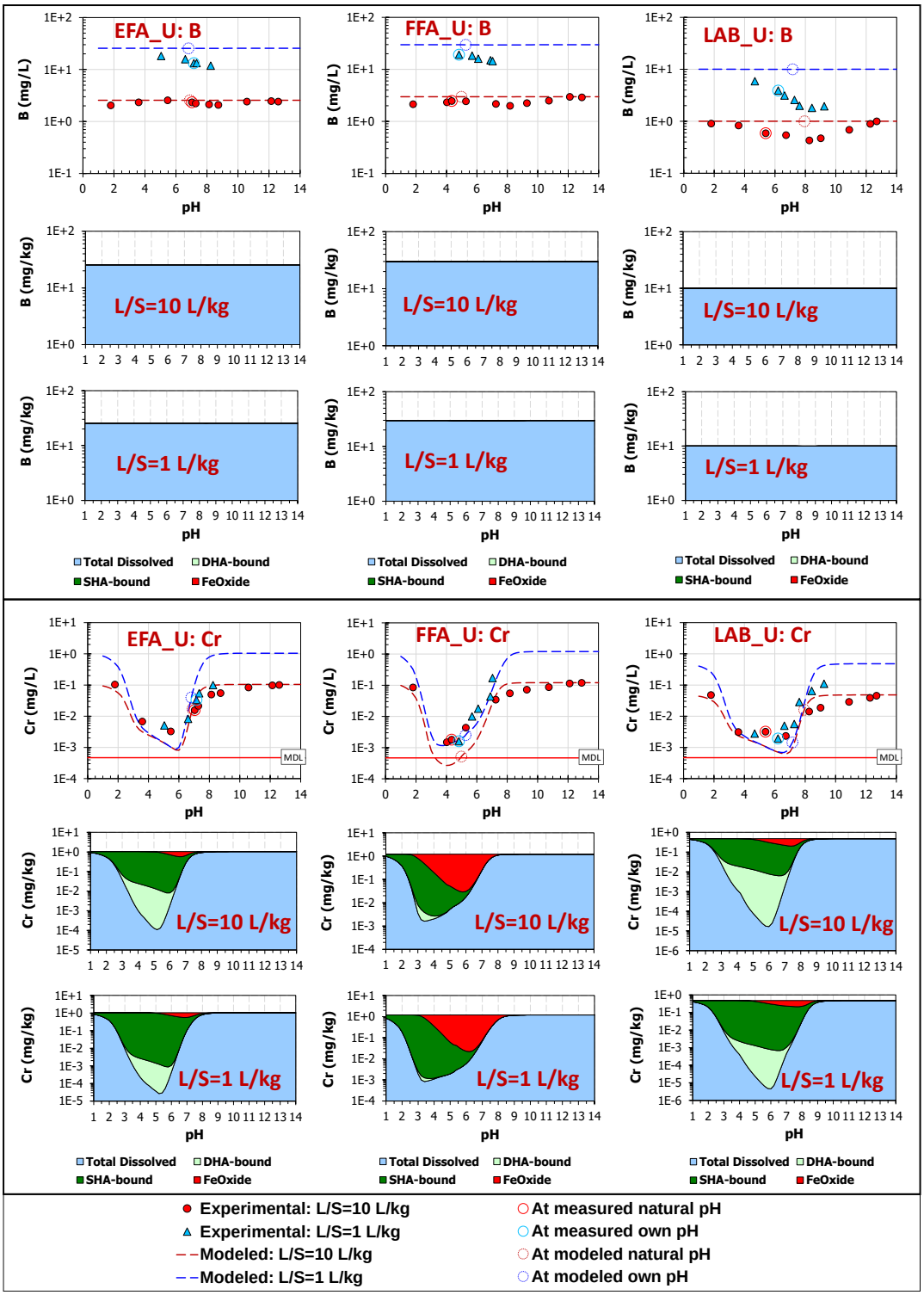

Figure A.7 Geochemical speciation modeling of B and Cr from Group I coal fly ashes (EFA_U, FFA_U, and LAB_U). MDL: method detection limit. SHA-bound: solid humic acid bound; DHA-bound: dissolved humic acid bound; FeOxide: adsorbed onto hydrous ferric oxide (HFO); Total dissolved: in dissolved phase, free ions.

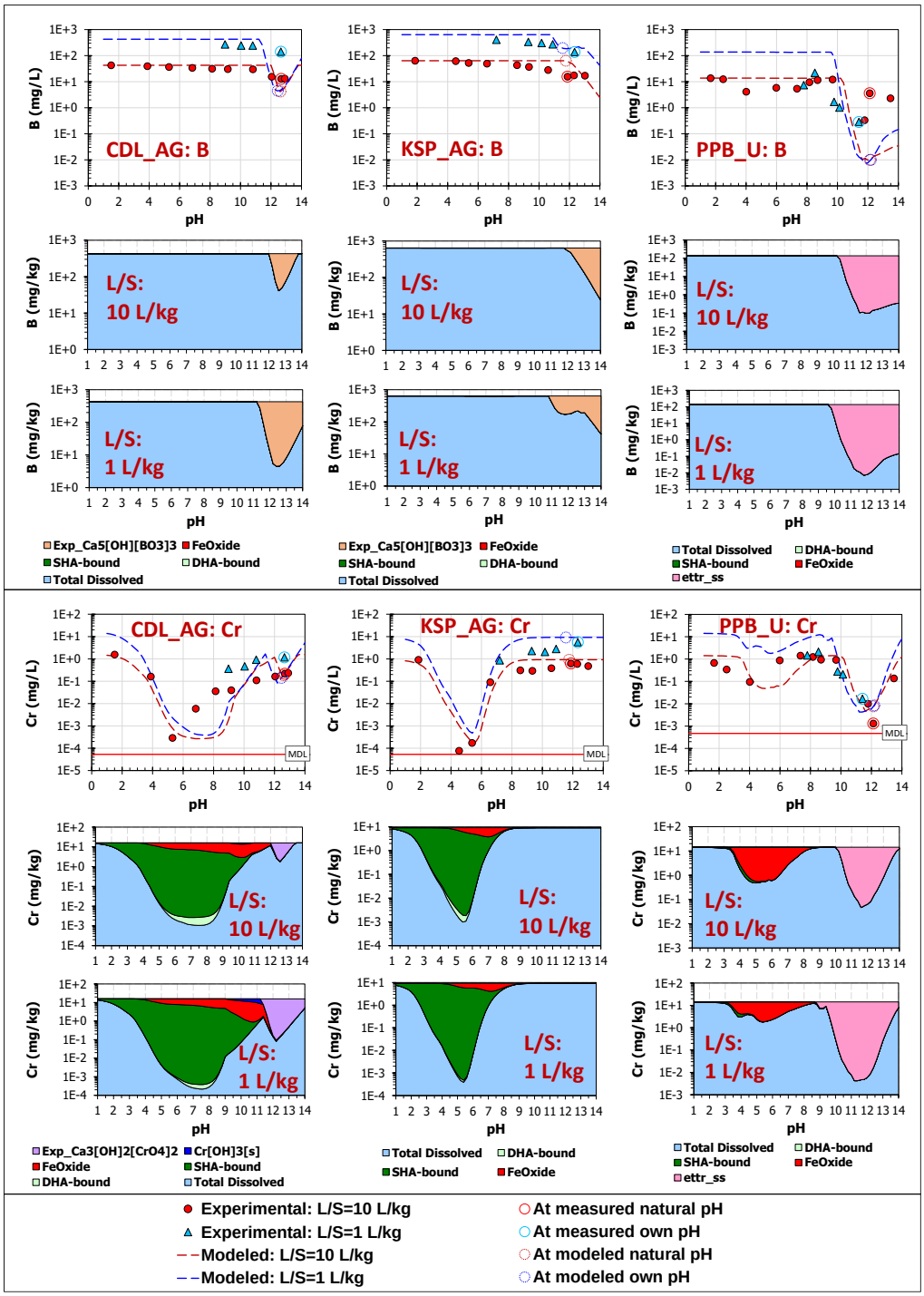

Figure A.8 Geochemical speciation modeling of B and Cr from Group II (CDL_AG and KSP_AG) and Group III coal fly ash (PPB_U). MDL: method detection limit. Exp_Ca5[OH][BO3]3: $Ca_5[OH][BO_3]_3$ (postulated phase); Exp_Ca3[OH]2[CrO4]2: $Ca_3[OH]_2[CrO_4]_2$ (postulated phase); Cr[OH]3[s]: $Cr(OH)_3$ mineral; ettr_ss: ettringite solid solution; SHA-bound: solid humic acid bound; DHA-bound: dissolved humic acid bound; FeOxide: adsorbed onto hydrous ferric oxide (HFO); Total dissolved: in dissolved phase, free ions.

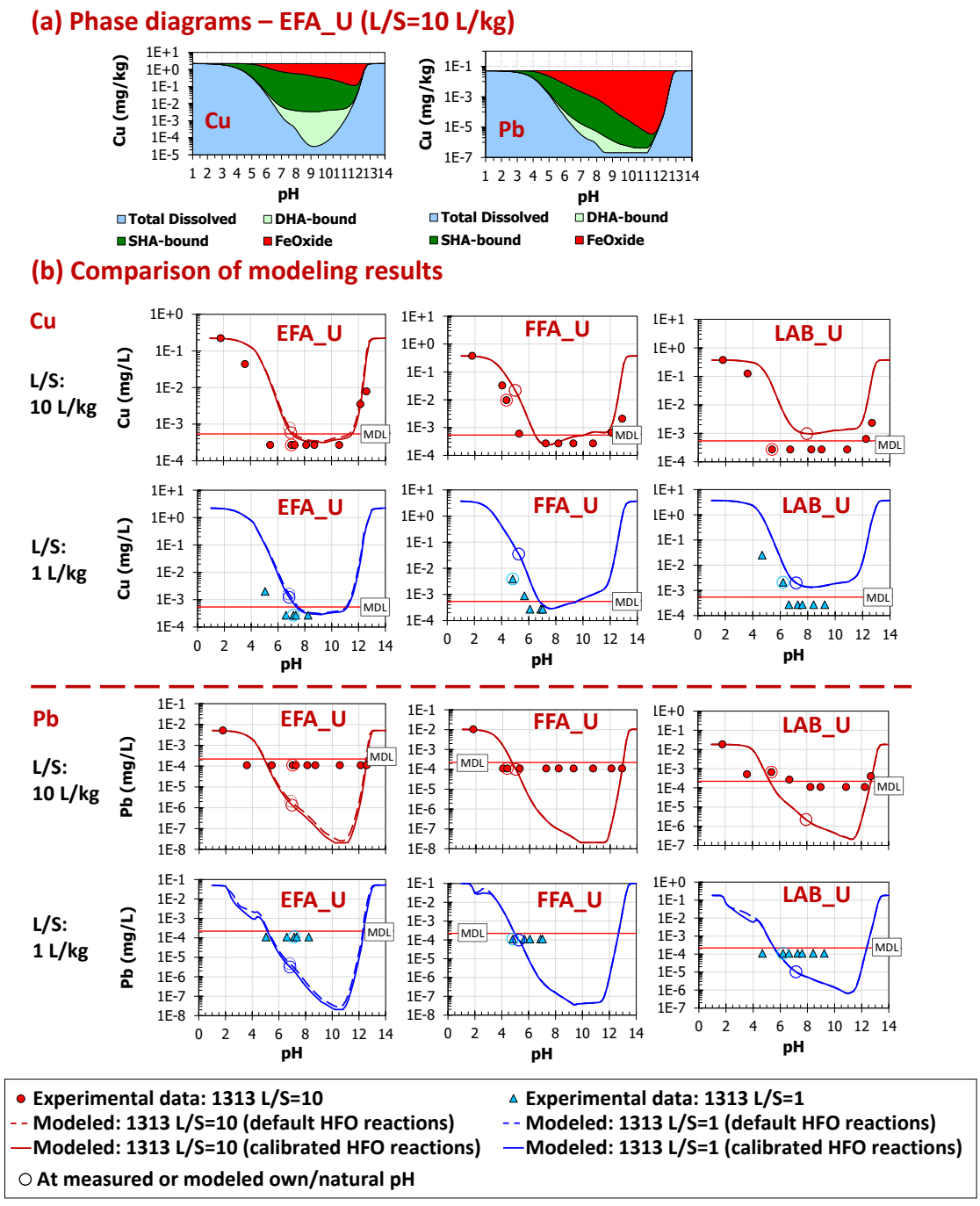

Figure A.9 Comparison of leaching of Cu and Pb from Group I coal fly ashes (EFA_U, FFA_U, and LAB_U) simulated by reported HFO adsorption reactions [52] and calibrated adsorption reaction set. MDL: method detection limit. Phase diagrams in (a) are representative results using reported HFO adsorption reactions at L/S=10 L/kg for EFA_U. SHA-bound: solid humic acid bound; DHA-bound: dissolved humic acid bound; FeOxide: adsorbed onto hydrous ferric oxide (HFO); Total dissolved: in dissolved phase, free ions.

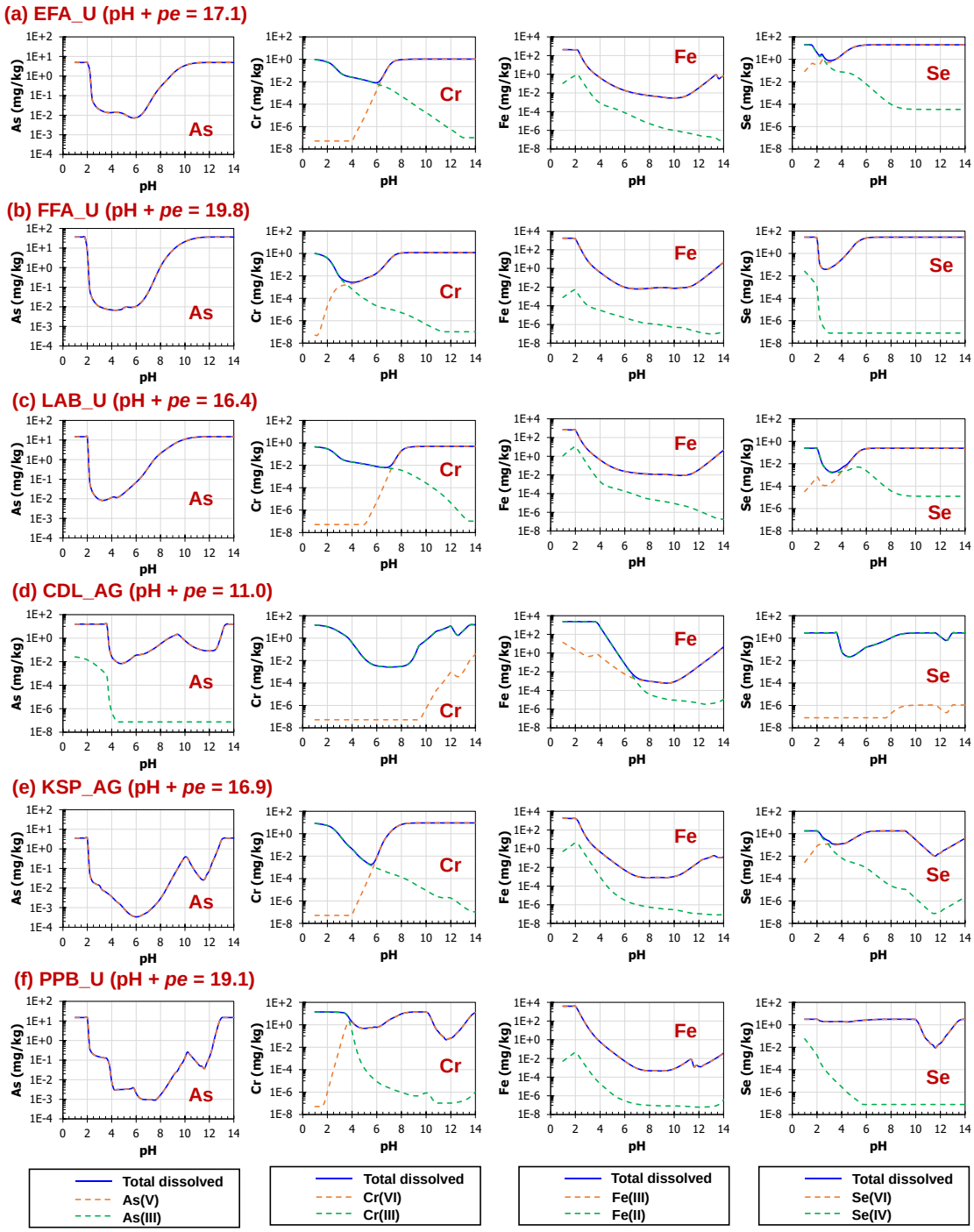

Figure A.10 The speciation of As, Cr, Fe, and Se as a function of pH in simulations of leaching (L/S=10 L/kg) from reference coal fly ashes. Total dissolved concentrations of As overlapped with As(V) concentrations for all ashes. The variation of redox states variation between leaching systems of fly ashes did not impact leaching of As, as As(V) was the major species of As in for all ashes. For Cr, Fe, and Se, the relatively reduced sample CDL_AG showed higher proportions of species in lower valence states than other CFAs, and thus impacting their leaching behavior.

APPENDIX B

SUPPLEMENTARY MATERIAL FOR CHAPTER 3

B.I Porewater, groundwater, and gas sampling

Following the ash sampling, at each borehole location, a 60-cm screen and porewater access well were established within the porewater between ~2.4 and ~3 m below the ash layer surface. Using a bentonite seal above the porewater access well screen, a 0.6-cm diameter stainless-steel tube with a bellhousing at the lower end was set in 30 cm deep porous bed of 1.2 to 1.8 cm river stone to serve as a subsurface gas access point (GAP), with continuation of the bentonite seal above the gas access point. The top of the gas access point tubing had a shutoff valve to isolate the subsurface from the atmosphere. The gas access point was set to sample subsurface gas collected within the unsaturated river stone bed between ~60 and ~90 cm below the ash surface. The porewater access well also was capped between sampling intervals. Elevations of porewater well screen and GAP are provided in Fig. S2.

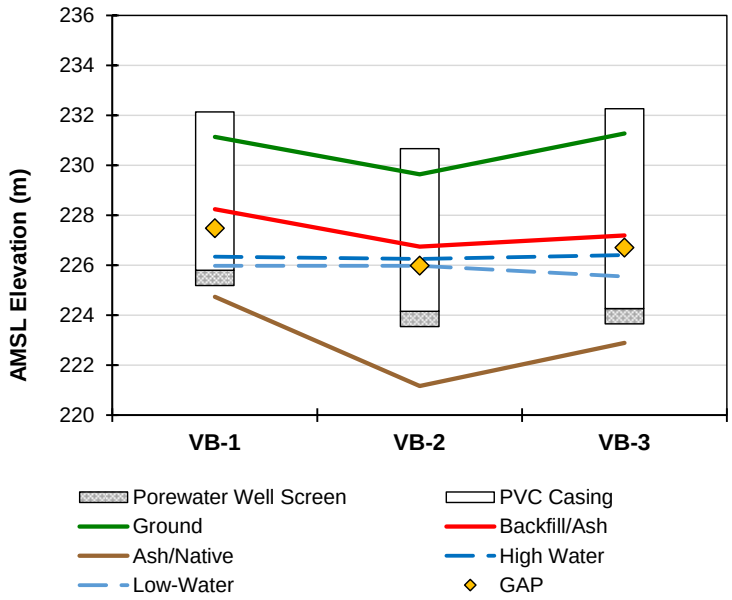

Figure B.1 Schematic presentation of above mean sea level (AMSL) elevations of monitoring wells including the porewater well screen and gas access points (GAPs). Maximum and minimum water table measurements from monthly measurements are also shown.

During porewater and groundwater sampling, field personnel from the fossil plant stabilized the well according to company standard operating procedures and then allowed the research team to collect the porewater. At 5-minute intervals, the sampled water was pumped using low-flow sampling techniques at approximately 100-150 mL/min to minimize drawdown of the water level in each porewater screen well. Two sets of samples were collected in 50-mL Science Digitubes until the turbidity and pH readings were consistent between sampling intervals.

After porewater sampling at VB1, VB2, and VB3, a gas meter was connected to the gas sampling tube for the measurement of subsurface gas composition. To prevent moisture in gas from fouling the vacuum pump of the meter, the subsurface gas was drawn through a 250-mL syringe filled with desiccant.

B.II Procedures to set up field extractions

In the field extraction test, about 150 g of ash was placed into a certified and pre-tared 250-mL high-density polyethylene (HDPE) bottle (Naglene I-Chem #N311-0250). De-oxygenated 18 MΩ reagent water was immediately added to fill the bottle to the top and minimize the headspace. The mass of ash sample and water were recorded. A field blank sample was included for quality assurance (QA) and quality control (QC) by filling the HDPE bottle with reagent water in the field. Extraction bottles and the field blank were transported for laboratory tumbling for 24 hours at room temperature (20±2 ºC). Leachate was separated from the solid by centrifuge at 4,500 rpm for 10 minutes. Liquid to solid ratio (L/S) was calculated by:

$$\mathrm{L/S} = \frac{(m_1 - m_2) + m_2 \times M_F}{m_2 \times (1 - M_F)}$$

where m_1 is the total mass of solid and liquid before centrifuge and m_2 is the mass of remaining wet solid after centrifuge. Moisture content (M_F) of the remaining wet solid was tested on triplicate samples at 105 ºC for 24 hours and checked after 48 hours.

B.III Procedures to set up laboratory extractions

The bulk material from each split spoon was homogenized in the laboratory by being bisected along its longitudinal axis (or along the axis of the vacuum-sealed bag if the sample was too wet and deformed) and separated into two subsamples. One half of the material was immediately re-sealed to preserve the redox state while the remaining half was placed into a plastic bag to minimize air contact and homogenized by hand until the contents were considered well-mixed.

Homogenized material within each split spoon was used for the laboratory extraction test. The L/S in laboratory extractions, different from the field extractions, was pre-determined to be 1 L/kg-dry equivalent solid. To achieve L/S=1 L/kg-dry, mass of wet sample (M_{test}) and volume of reagent water (V_{water}) were calculated by:

$$M_{test} = \frac{M_{dry}}{1 - M_D}$$

$$V_{water} = M_{dry} \times L/S - M_{test} \times M$$

where M_{dry} = mass of dry material (where M_{dry} was specified at 35g in the laboratory extraction test); M_D = moisture content of the homogenized sample measured in triplicates; and *L/S* = 1 L/kg-dry.

The pre-determined amount of homogenized ash (M_{test}) was mixed with reagent water (V_{water}; deoxygenated) and then tumbled for 24 hours.

B.IV Ash composites prepared for pH-dependent leaching test

Borehole composites (VB1, VB2, and VB3) were made from homogenized split spoon materials located from the strata consistent with the porewater well screens based on equal dry mass proportions. Four homogenized split spoon samples from VB1 (two above, one within, and one below the porewater well screen region, Table C.7) were composited to produce sufficient material for all the characterization tests. At VB2 and VB3, three samples around the porewater well screen region (Table C.7) were composited at each borehole, respectively. The selected samples were homogenized by hand through a plastic bag until well mixed. All samples were then vacuum sealed and stored at < 6ºC for subsequent leaching characterization.

Table B.1 Above mean sea level (AMSL) of porewater well screen region and intervals of split spoon samples used in borehole composites

VB1		VB2		VB3	
Porewater screen region (AMSL, m)	Composited sample interval (AMSL, m)	Porewater screen region (AMSL, m)	Composited sample interval (AMSL, m)	Porewater screen region (AMSL, m)	Composited sample interval (AMSL, m)
225.2-225.8	226.4-227.0 225.8-226.4 225.2-225.8 224.7-225.2	223.5-224.1	224.0-224.6 223.4-224.0 222.8-223.4	223.7-224.3	224.3-224.9 223.7-224.3 223.1-223.7

B.V Parameterization of geochemical modeling

Table B.2 Available content of the primary entities used in the geochemical speciation modeling and the measured content of iron (hydr)oxides of field samples, unit (mol/kg)

Element	**VB1**	**VB2/3**
Al [a]	0.0815	0.0898
As [a]	5.71E-04	6.45E-04
CO_3^{2-} [b]	0.0850	0.0300
Ca [a]	0.0378	0.0435
Fe [c]	0.0580	0.0700
Si [a]	0.0489	0.0522
Mo [a]	3.77E-05	5.37E-06
P [a]	0.00349	0.00661
S [a]	0.0239	0.00134
Sb [a]	1.81E-06	1.41E-06
Se [a]	1.73E-05	1.54E-05
V [a]	4.65E-04	4.65E-04
Amorphous iron oxides [d]	0.0163	[*]0.01395
Amorphous + Crystalline iron oxides [e]	0.247	[*]0.158

[a] Available content as the maximum leaching amount which was determined from the EPA 1313 leaching test.

[b] Available content calibrated against the pH dependent leaching behavior of calcium at pH > 8.

[c] Available content calibrated to describe adsorption of As and Se on ferrihydrite.

ISO test results as the lower ([d]) and upper ([e]) limits for the calibration of the available content of Fe.

[*] Average value of the test results of VB2 and VB3.

Table B.3 Thermodynamic reactions for mineral phases used in the geochemical speciation modeling

Name in database	Mineral	Reaction	log K
$AlOHSO_4$ [a]	$AlOHSO_4$	$AlOHSO_4 + 3H_2O = Al(OH)_4^- + 3H^+ + SO_4^{2-}$	-26.44
Calcite [a]	$CaCO_3$	$CaCO_3 = CO_3^{2-} + Ca^{2+}$	-8.46
CEM18_AlOHam [b]	$Al(OH)_3$ (am)	$Al(OH)_3 + H_2O = Al(OH)_4^- + H^+$	-13.76
CEM18_monocarbonate [b]	$Ca_4Al_2CO_9(H_2O)_{11}$	$Ca_4Al_2CO_9(H_2O)_{11} + 4H^+ = 2Al(OH)_4^- + CO_3^{2-} + 4Ca^{2+} + 9H_2O$	25.43
CEM18_straetlingite [b]	$Ca_2Al_2SiO_7(H_2O)_8$	$Ca_2Al_2SiO_7(H_2O)_8 = 2Al(OH)_4^- + 2Ca^{2+} + 5H_2O + H_2SiO_4^{2-}$	-18.59
Fe[VO3]2 [a]	$Fe(VO_3)_2$	$Fe(VO_3)_2 + 2H_2O = Fe(OH)_4^- + 2VO_2^+ + e^-$	-38.28
Ferrihydrite [a]	$Fe(OH)_3$	$Fe(OH)_3 + H_2O = Fe(OH)_4^- + H^+$	-18.18
MINTEQ_Laumontite [c]	$CaAl_2Si_4O_{12} \cdot 4H_2O$	$CaAl_2Si_4O_{12} \cdot 4H_2O + 8H_2O = 2Al(OH)_4^- + Ca^{2+} + 8H^+ + 4H_2SiO_4^{2-}$	-124.84
beta-TCP [d]	$Ca_3(PO_4)_2$	$Ca_3(PO_4)_2 = 3Ca^{2+} + 2PO_4^{3-}$	-29.07
Orpiment [a]	As_2S_3	$As_2S_3 + 20H_2O = 2AsO_4^{3-} + 40H^+ + 3SO_4^{2-} + 28e^-$	-243.66
Pyrite [a]	FeS_2	$FeS_2 + 12H_2O = Fe(OH)_4^- + 20H^+ + 2SO_4^{2-} + 15e^-$	-121.08
Semetal[am] [a]	Se	$Se + 4H_2O = SeO_4^{2-} + 8H^+ + 6e^-$	-88.91
FeSe [a]	FeSe	$FeSe + 8H_2O = SeO_4^{2-} + Fe(OH)_4^- + 12H^+ + 9e^-$	-127.52

[a] MINTEQA2_V4 database [56]

[b] CEMDATA18 database [84]

[c] MINTEQA2 database [103]

[d] From studies by Lindsay, W.L. [154]

Table B.4 AsO_4/HFO, H_3AsO_3/HFO, SeO_4/HFO, and SeO_3/HFO surface complexation constants reported by Dzombak and Morel [52] and values used in geochemical modeling

		Reported Value	Value used in simulation
Arsenate/HFO			
$\equiv FeOH^0 + AsO_4^{3-} + 3H^+ = \equiv FeH_2AsO_4^0 + H_2O$	log K_1	29.31	29.31
$\equiv FeOH^0 + AsO_4^{3-} + 2H^+ = \equiv FeHAsO_4^- + H_2O$	log K_2	23.51	23.51
$\equiv FeOH^0 + AsO_4^{3-} + H^+ = \equiv FeAsO_4^{2-} + H_2O$	log K_3	/	/
$\equiv FeOH^0 + AsO_4^{3-} = \equiv FeOHAsO_4^{3-}$	log K_4	10.58	**11.48***
Arsenite/HFO			
$\equiv FeOH^0 + H_3AsO_3^0 = \equiv FeH_2AsO_3^0 + H_2O$	log K_1	5.41	5.41
Selenate/HFO			
$\equiv FeOH^0 + SeO_4^{2-} + H^+ = \equiv FeSeO_4^- + H_2O$	log K_1	7.73	7.73
$\equiv FeOH^0 + SeO_4^{2-} = \equiv FeOHSeO_4^{2-}$	log K_2	0.80	0.80
Selenite/HFO			
$\equiv FeOH^0 + SeO_3^{2-} + H^+ = \equiv FeSeO_3^- + H_2O$	log K_1	12.69	12.69
$\equiv FeOH^0 + SeO_3^{2-} = \equiv FeOHSeO_3^{2-}$	log K_2	5.17	5.17

* The reaction constant (log K_4) involving forming surface species $\equiv OHAsO_4^{3-}$ was increased from 10.58 to 11.48 within the reported uncertainty range at the 99% confidence level (log K_4 = 9.69 - 11.48) [52] because using the reported mean log K_4 of 10.58 overestimated leaching concentrations within the focused pH range. Model predictions for Se were not affected when using the modified adsorption constant for As.

B.VI Calculation of As:Fe molar release ratio

The As:Fe molar release ratio ($R_{As/Fe}$) was defined as the ratio between the difference of molar release of As and Fe in porewater and in laboratory extracts. The $R_{As/Fe}$ was calculated by:

$$R_{As/Fe} = \frac{(M_{As}^{pore} - M_{As}^{lab})/74.9}{(M_{Fe}^{pore} - M_{Fe}^{lab})/55.8}$$

where M_{As}^{pore} is the released mass of As in porewater (mg/kg-dry),

M_{As}^{lab} is the released mass of As in laboratory extracts at natural pH and L/S = 1 L/kg-dry,

M_{Fe}^{pore} is the released mass of Fe in porewater (mg/kg-dry), and

M_{Fe}^{lab} is the released mass of Fe in laboratory extracts at natural pH and L/S = 1 L/kg-dry.

The release of As and Fe in laboratory extracts (M_{As}^{lab} and M_{Fe}^{lab}) was calculated based on measured concentrations of As (C_{As}^{lab}) and Fe (C_{Fe}^{lab}) in laboratory eluates and the corresponding L/S value (L/S^{lab}, 1 L/kg-dry) at the test condition:

$$M_{As}^{lab} = C_{As}^{lab} \times L/S^{lab}$$

$$M_{Fe}^{lab} = C_{Fe}^{lab} \times L/S^{lab}$$

Similarly, the release of As and Fe in field porewater (M_{As}^{pore} and M_{Fe}^{pore}) was calculated based on measured concentrations of As (C_{As}^{pore}) and Fe (C_{Fe}^{pore}) in porewater and the corresponding L/S value (L/S^{pore}, estimated to be 0.67 L/kg-dry) in the field:

$$M_{As}^{pore} = C_{As}^{pore} \times L/S^{pore}$$

$$M_{Fe}^{pore} = C_{Fe}^{pore} \times L/S^{pore}$$

B.VII Additional figures and tables of results

Table B.5 Total content of trace elements analyzed by acid digestion following EPA Method 3052 in as-generated bituminous fly ashes from the EPA report (EPA_FA) [11] and field ash composites (VB_FA), unit (mg/kg, w/w)

	EPA_FA				VB_FA (VB1, VB2, and VB3)
	N [a]	10th Percentile [a]	Median [a]	90th Percentile [a]	Mean ± S.D.
As	20	20.6	64.5	148.9	104.0 ± 10.4
Ba	12	661.2	1171.0	1938.4	376.7 ± 20.8
Cd	14	0.4	1.0	7.5	1.7 ± 0.6
Co	12	21.3	43.5	62.7	36.3 ± 3.2
Cr	12	122.6	146.5	207.4	143.3 ± 5.8
Mo	12	11.0	16.0	60.8	5.9 ± 2
Pb	20	26.1	55.5	111.9	53.3 ± 7.5
Sb	12	3.3	6.0	13.1	3.8 ± 0.6
Se	19	3.0	13.0	152.0	5.3 ± 0.9
Ni	-	NA [b]	NA	NA	93.0 ± 6.1
Mn	-	NA	NA	NA	210.0 ± 40
Sr	-	NA	NA	NA	120.0 ± 20
V	-	NA	NA	NA	246.7 ± 11.5
Zn	-	NA	NA	NA	116.7 ± 5.8

[a] Statistical parameters including the number of measurements, 10th percentile, median, and 90th percentile were given for fly ashes combusted from bituminous coal in the EPA report (EPA_FA) [11]

[b] Not analyzed.

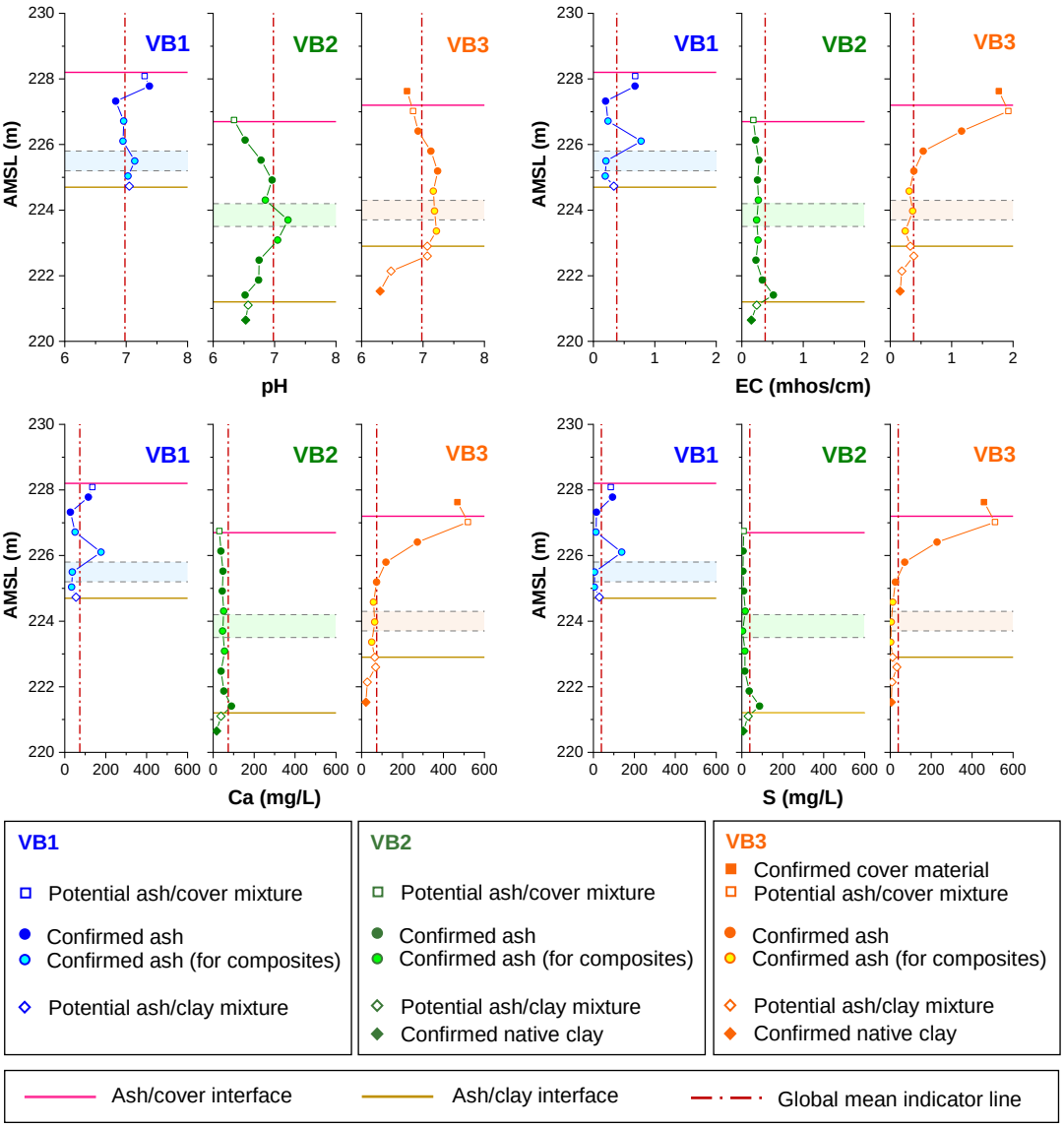

Figure B.2 Depth profiles of pH, EC, Ca, and S concentrations at VB1, VB2, and VB3. The elevations of two interfaces (in pink and brown) were determined from geologist notes. The global mean of each parameter was calculated only based on confirmed ash from three boreholes excluding the confirmed cover soil (■), native clay (♦), potential cover/ash mixtures (□), and ash/clay mixtures (◊). The shaded areas correspond to porewater-screening depth intervals. Bulk ash samples collected from the strata consistent with the porewater well screens were composited for EPA Method 1313 laboratory leaching tests.

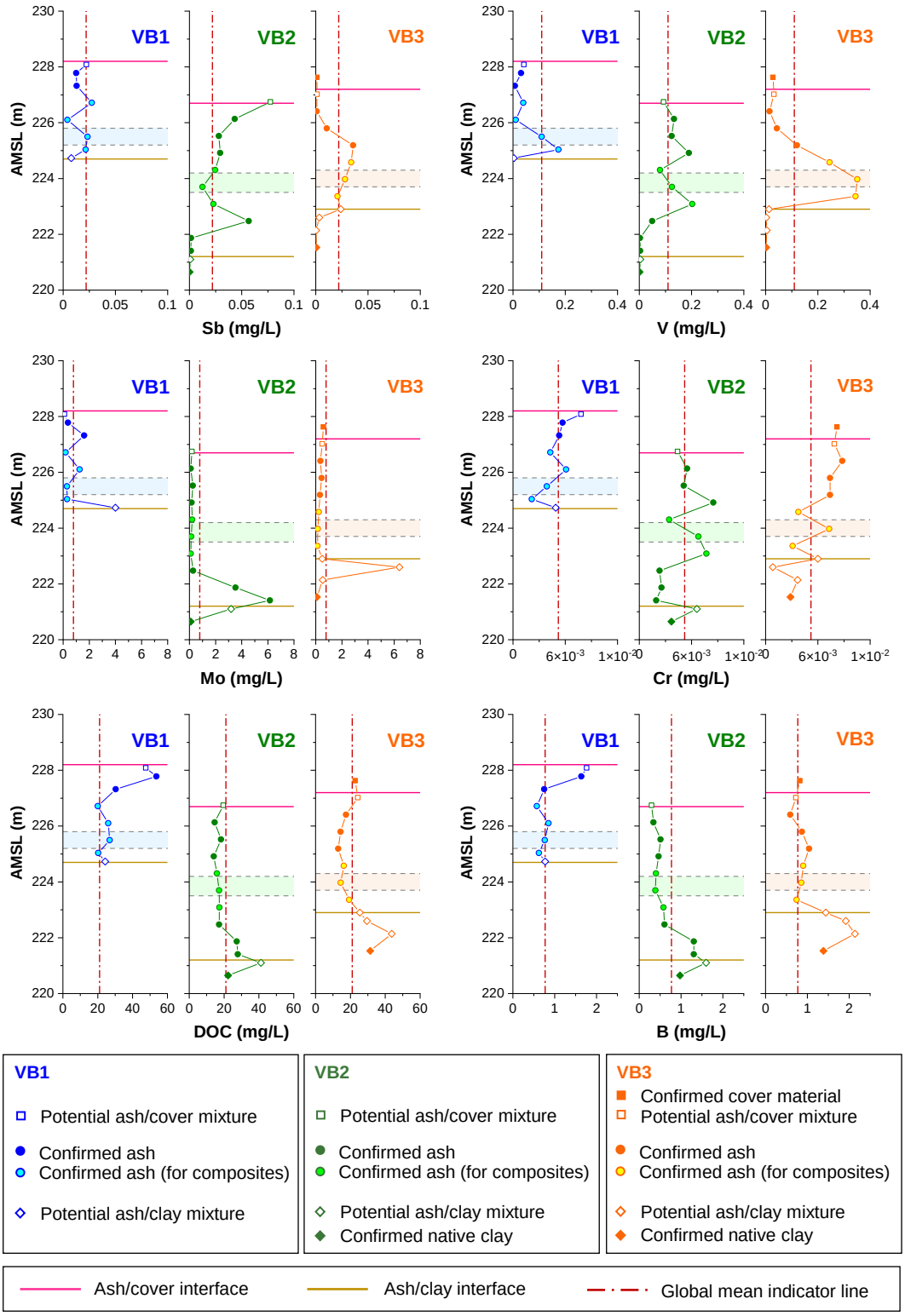

Figure B.3 Depth profiles of Sb, V, Mo, Cr, DOC, and B concentrations at VB1, VB2, and VB3. Further explanations of the interface lines, calculation of global mean, shaded areas indicated in each figure, and selection of samples for EPA Method 1313 tests are provided in Figure B.2.

Table B.6 One-way analysis of variance between laboratory extraction results from the three borehole locations (VB1, VB2, and VB3)

EC

Source	DF[a]	SS[b]	MSE[c]	F Ratio[d]	Prob > F[e]
Location	2	0.16	0.079	1.4	0.27
Error	18	1.0	0.056		
C. Total	20	1.2			

pH

Source	DF	SS	MSE	F Ratio	Prob > F
Location	2	0.42	0.21	5.6	0.013*
Error	18	0.68	0.038		
C. Total	20	1.1			

pe

Source	DF	SS	MSE	F Ratio	Prob > F
Location	2	0.085	0.043	0.37	0.70
Error	18	2.1	0.12		
C. Total	20	2.2			

Ca

Source	DF	SS	MSE	F Ratio	Prob > F
Location	2	11000	5400	1.7	0.21
Error	18	56000	3100		
C. Total	20	67000			

Fe

Source	DF	SS	MSE	F Ratio	Prob > F
Location	2	1.3E-3	6.6E-4	0.32	0.73
Error	18	3.7E-2	2.0E-3		
C. Total	20	3.8E-2			

S

Source	DF	SS	MSE	F Ratio	Prob > F
Location	2	5000	2500	0.75	0.49
Error	18	60000	3300		
C. Total	20	65000			

As

Source	DF	SS	MSE	F Ratio	Prob > F
Location	2	0.43	0.22	2.9	0.078
Error	18	1.3	0.073		
C. Total	20	1.8			

B

Source	DF	SS	MSE	F Ratio	Prob > F
Location	2	0.20	0.099	0.88	0.43
Error	18	2.0	0.11		
C. Total	20	2.2			

Cr

Source	DF	SS	MSE	F Ratio	Prob > F
Location	2	1.1E-5	5.3E-6	1.1	0.35
Error	18	8.5E-5	4.7E-6		
C. Total	20	9.5E-5			

Mo

Source	DF	SS	MSE	F Ratio	Prob > F
Location	2	3.3	1.6	0.76	0.49
Error	18	39	2.2		
C. Total	20	43			

Sb

Source	DF	SS	MSE	F Ratio	Prob > F
Location	2	2.1E-4	1.0E-4	0.47	0.63
Error	18	4.0E-3	2.2E-4		
C. Total	20	4.2E-3			

Se

Source	DF	SS	MSE	F Ratio	Prob > F
Location	2	0.20	0.10	2.1	0.16
Error	18	0.87	0.048		
C. Total	20	1.1			

[a] Degrees of freedom for the sources of variations.

[b] Sum of squares for each source of variation along with the total from all sources.

[c] Mean square, which equals to the sum of squares divided by its associated degrees of freedom.

[d] F ratio is the mean square of the location (MSE-Location) divided by the mean square of the error (MSE-Error).

[e*] Prob > F refers to the p-value. A p-value > 0.05 suggests that there is no significant difference in mean value between the three borehole locations, while a p-value < 0.05 (marked in red) suggests a significant difference in the mean value.

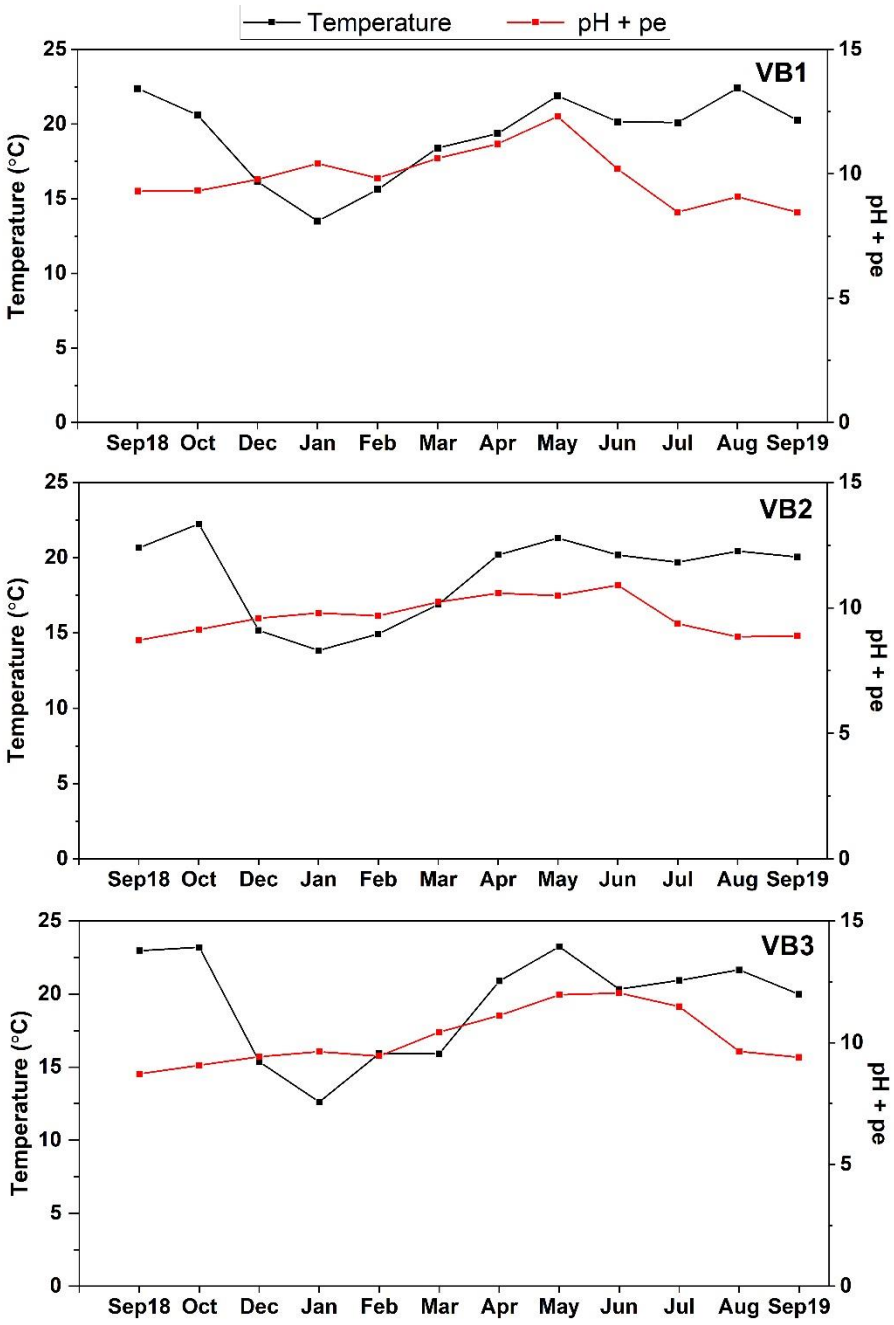

Figure B.4 Temporal variations of porewater temperature and pH + *pe* values at VB1, VB2, and VB3. No readings were taken during November for all wells because of a sampling schedule conflict.

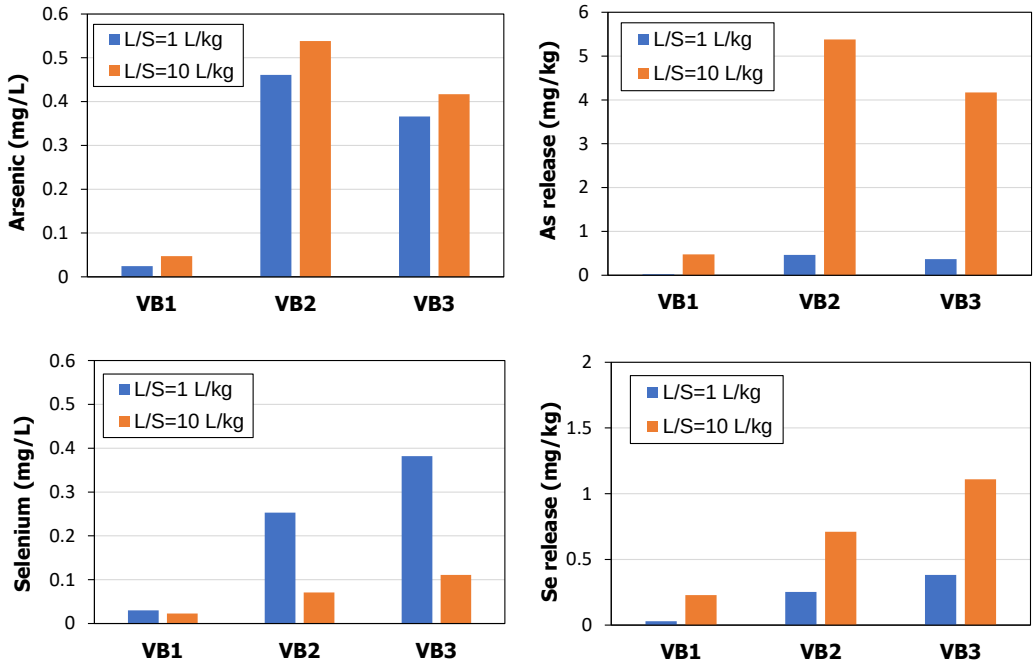

Figure B.5 Comparisons of dissolved concentrations and release of As and Se between L/S = 10 L/kg and L/S = 1 L/kg tests at the natural pH position (NAT). VB1: NAT = 6.91 at L/S 10 L/kg, NAT = 6.84 at L/S 1 L/kg; VB2: NAT = 7.41 at L/S 10 L/kg, NAT = 7.45 at L/S 1 L/kg; VB3: NAT = 7.42 at L/S 10 L/kg, natural pH = 7.59 at L/S 1 L/kg.

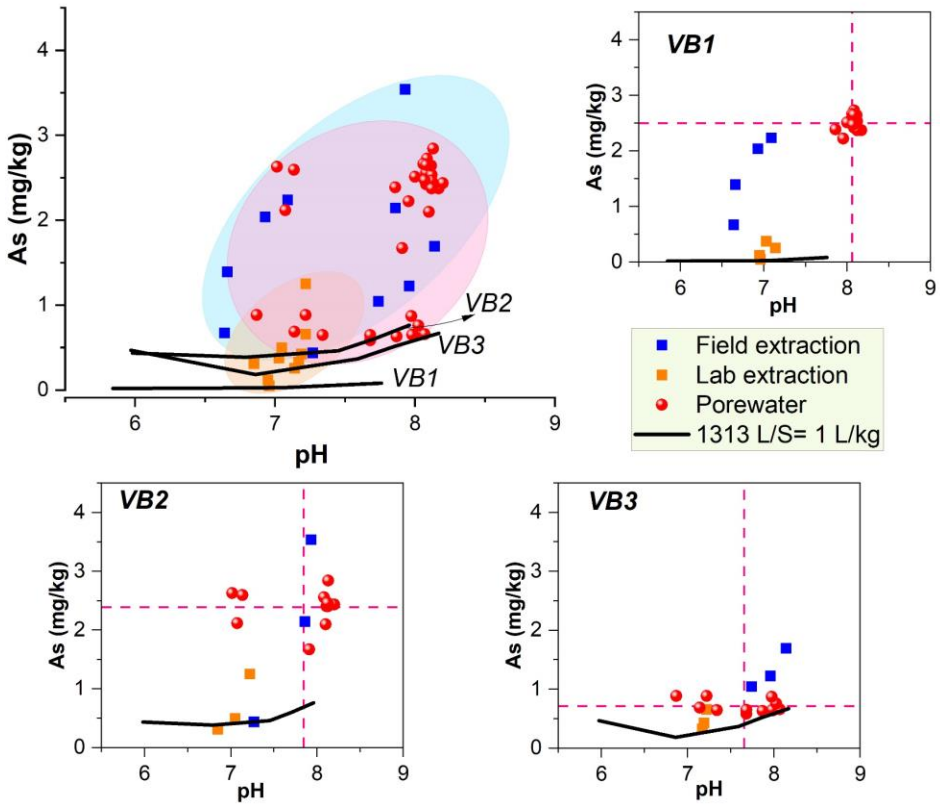

Figure B.6 Arsenic **release** (mg As/kg solid) as a function of pH in the field extractions, laboratory extractions, modified EPA Method 1313 test at L/S = 1 L/kg, and in field porewater at VB1, VB2, and VB3. Porewater was sampled monthly from September 2018 to September 2019. Means of porewater pH and As release are indicated by vertical and horizontal red dash lines, respectively. Release (mg/kg solid) of As in porewater was calculated by multiplying the concentration (mg/L) with an estimated field L/S of 0.67 L/kg (estimated L/S ranges from 0.57 (10th percentile) to 0.86 (90th percentile)).

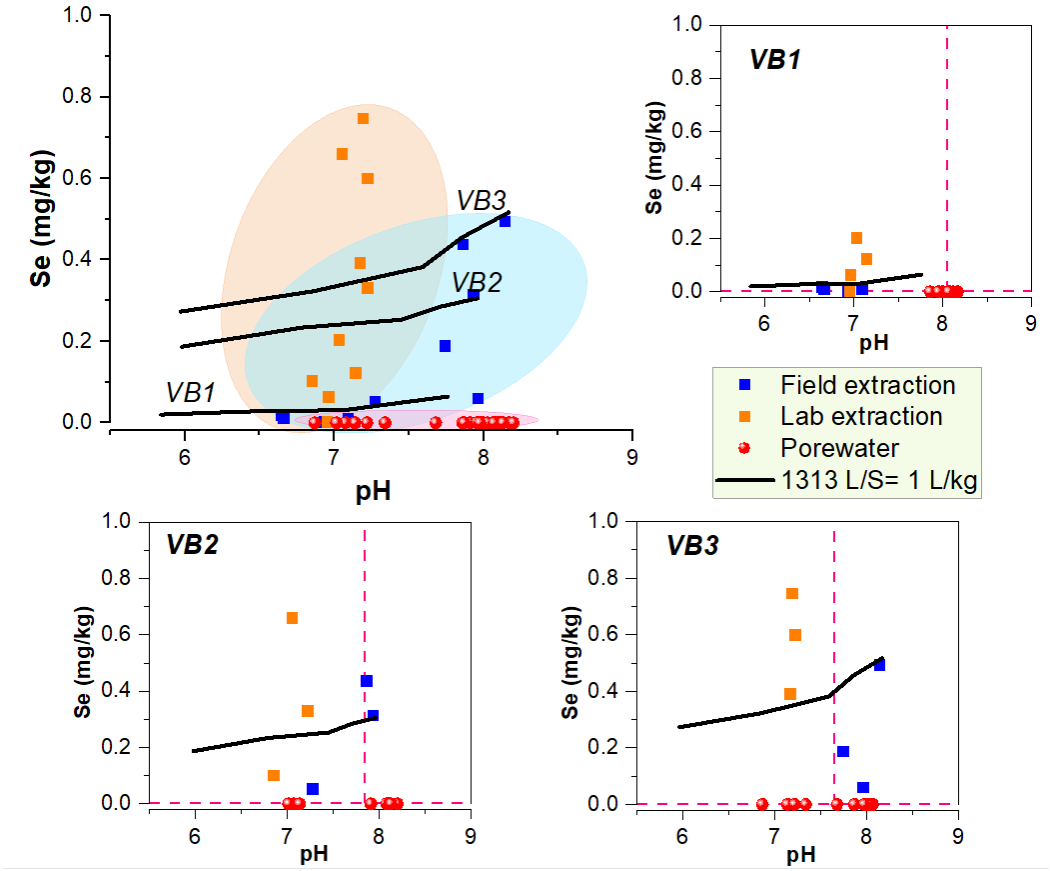

Figure B.7 Selenium **release** (mg Se/kg solid) as a function of pH in the field extractions, laboratory extractions, modified EPA Method 1313 test at L/S = 1 L/kg, and in field porewater at VB1, VB2, and VB3. Legend refers to Figure B.6.

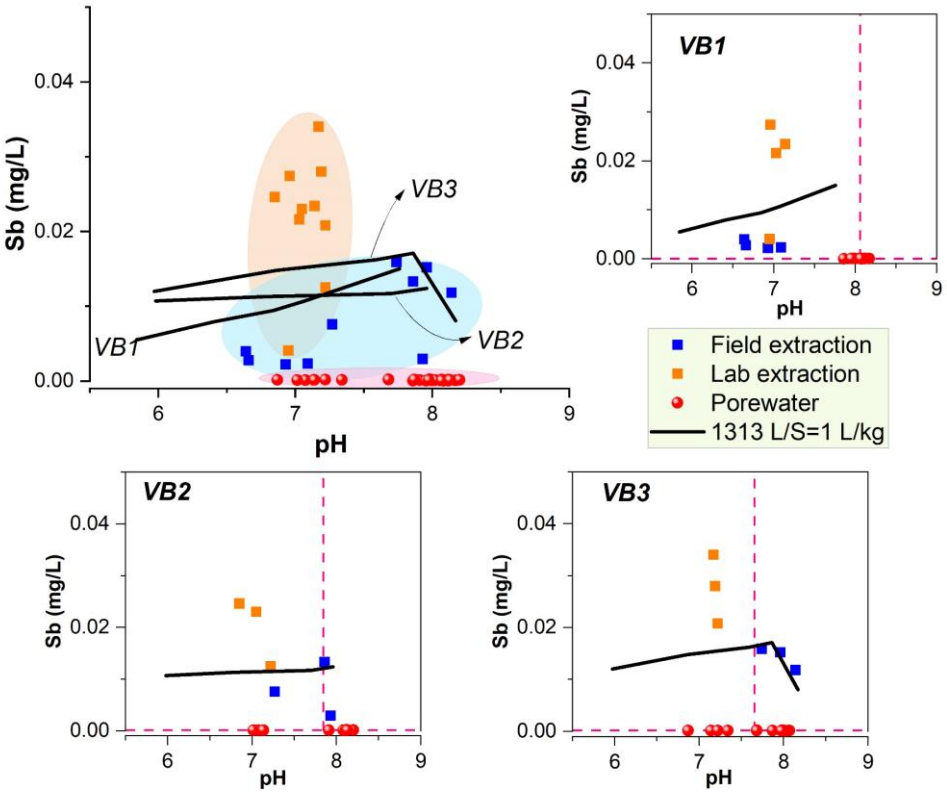

Figure B.8 Antimony concentrations as a function of pH in the field extractions, laboratory extractions, modified EPA Method 1313 test at L/S = 1 L/kg, and in field porewater at VB1, VB2, and VB3. Porewater was sampled monthly from September 2018 to September 2019. Mean of porewater pH and Sb concentrations are indicated by vertical and horizontal red dash lines, respectively.

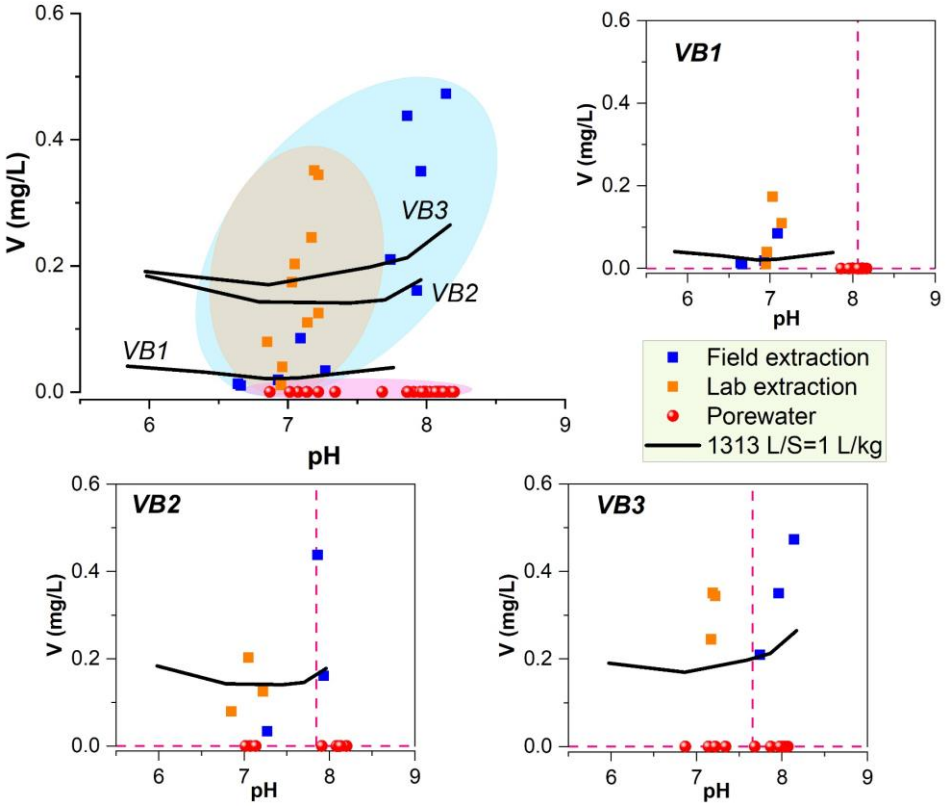

Figure B.9 Vanadium concentrations as a function of pH in the field extractions, laboratory extractions, modified EPA Method 1313 test at L/S = 1 L/kg, and in field porewater at VB1, VB2, and VB3. Legend refers to Figure B.8.

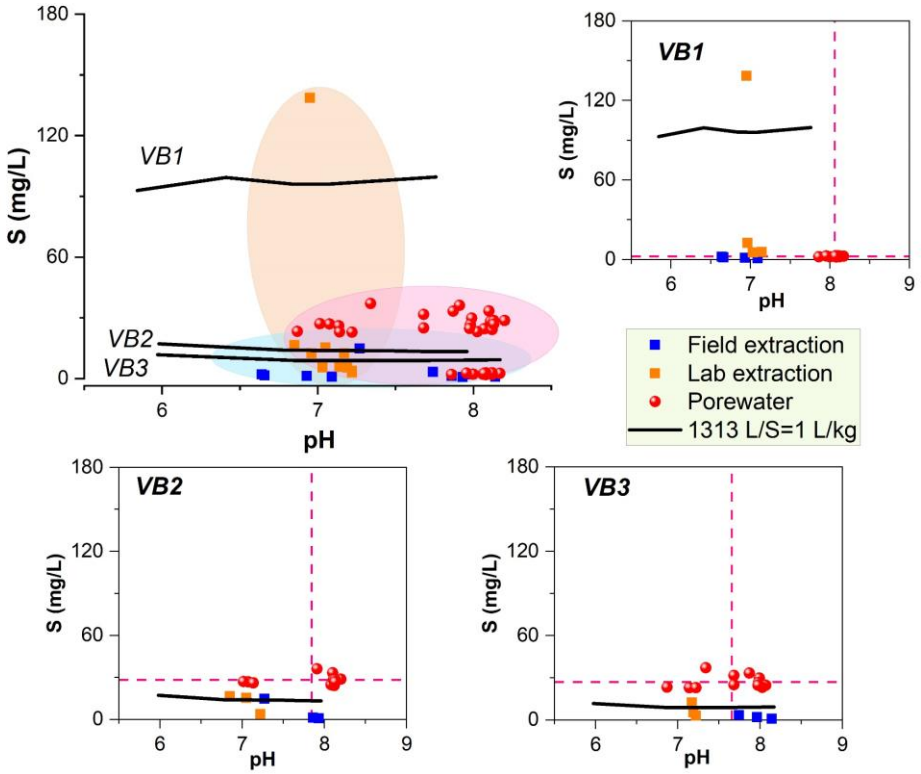

Figure B.10 Sulfur concentrations as a function of pH in the field extractions, laboratory extractions, modified EPA Method 1313 test at L/S = 1 L/kg, and in field porewater at VB1, VB2, and VB3. Legend refers to Figure B.8.

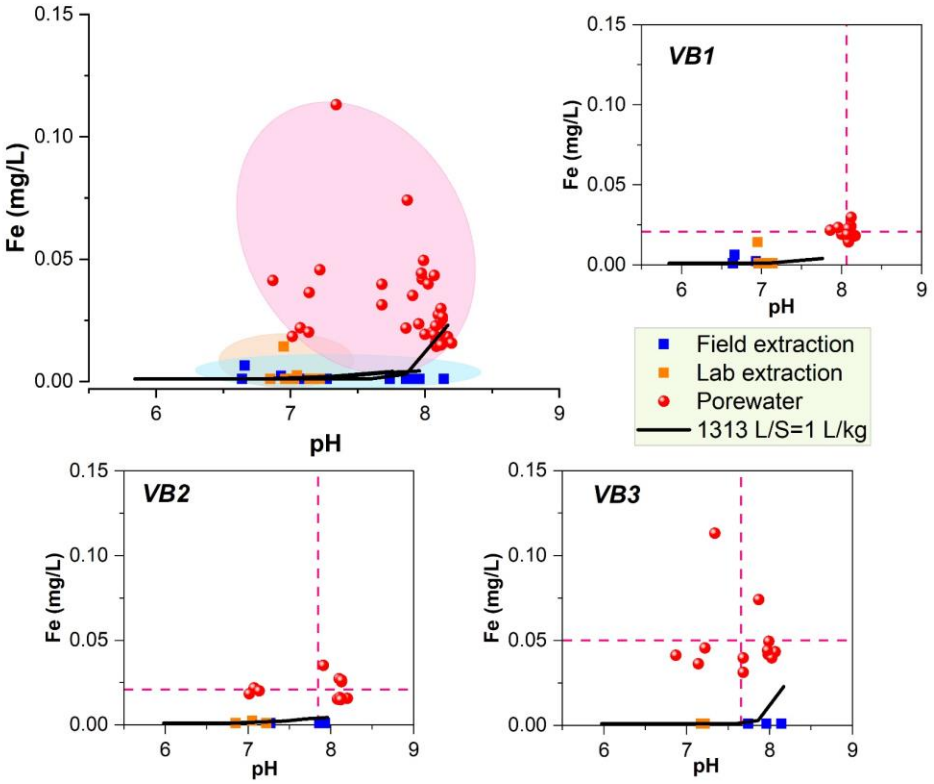

Figure B.11 Iron concentrations as a function of pH in the field extractions, laboratory extractions, modified EPA Method 1313 test at L/S = 1 L/kg, and in field porewater at VB1, VB2, and VB3. Legend refers to Figure B.8.

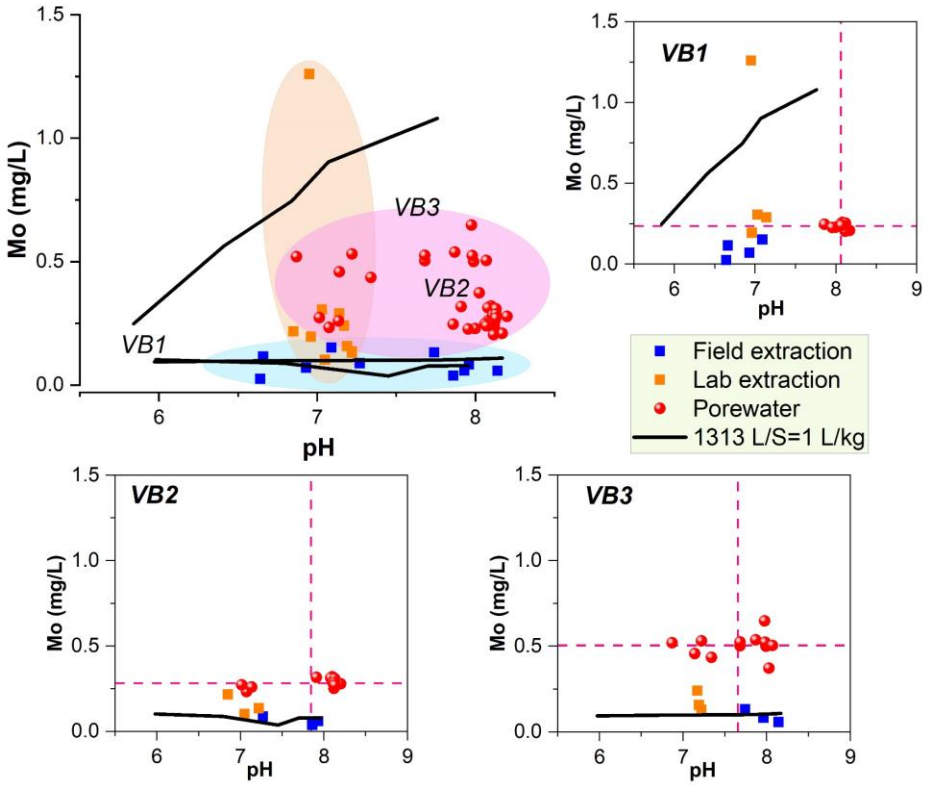

Figure B.12 Molybdenum concentrations as a function of pH in the field extractions, laboratory extractions, modified EPA Method 1313 test at L/S = 1 L/kg, and in field porewater at VB1, VB2, and VB3. Legend refers to Figure B.8.

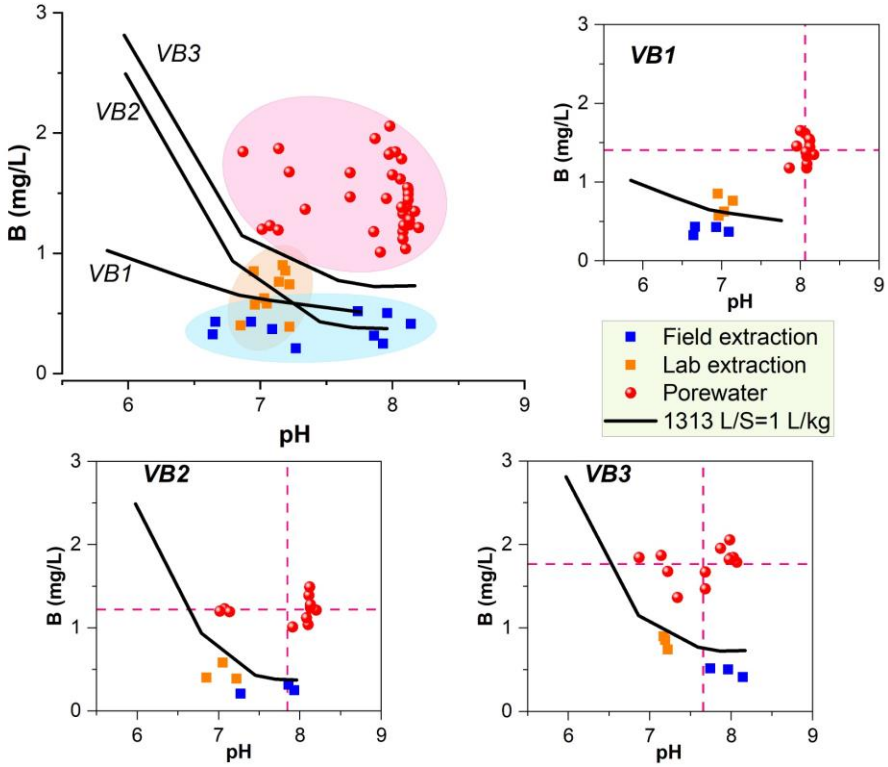

Figure B.13 Boron concentrations as a function of pH in the field extractions, laboratory extractions, modified EPA Method 1313 test at L/S = 1 L/kg, and in field porewater at VB1, VB2, and VB3. Legend refers to Figure B.8.

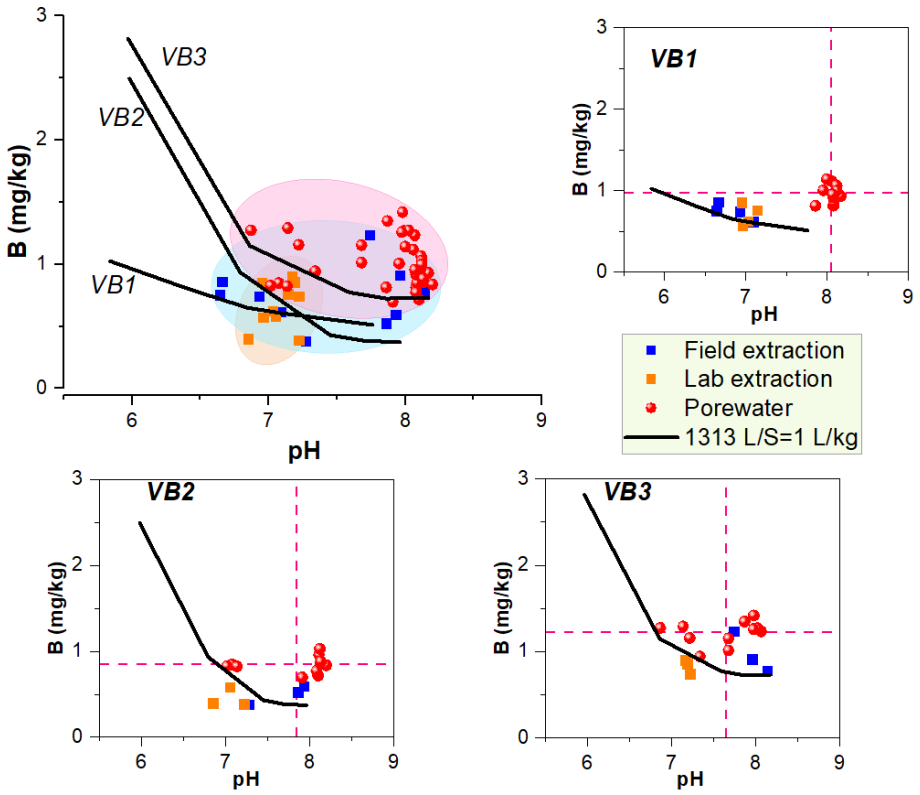

Figure B.14 Boron **release** (mg B/kg solid) as a function of pH in the field extractions, laboratory extractions, modified EPA Method 1313 test at L/S = 1 L/kg, and in field porewater at VB1, VB2, and VB3. Legend refers to Figure B.6.

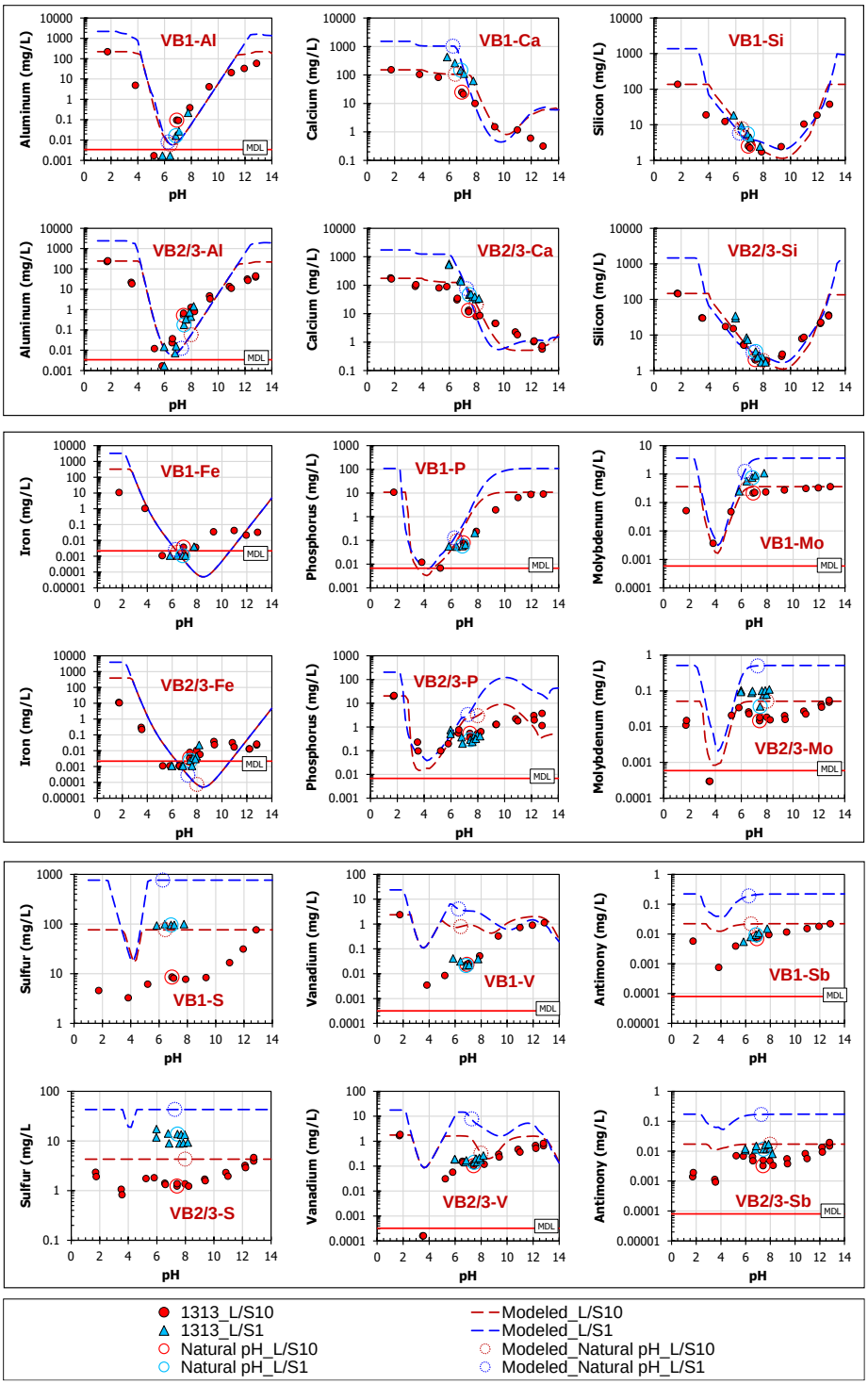

Figure B.15 Simulated leaching concentrations of Al, Ca, Si, Fe, P, Mo, S, V, and Sb as a function of pH according to the EPA Method 1313 at L/S = 10 L/kg and modified Method 1313 at L/S = 1 L/kg for the field ash composites (VB1 and merged results of VB2 and VB3 as VB2/3). VB1: pH + *pe* = 13.9; VB2/3: pH + *pe* = 13.7. Measured concentrations lower than the method detection limit (MDL) were set as half of the MDL.

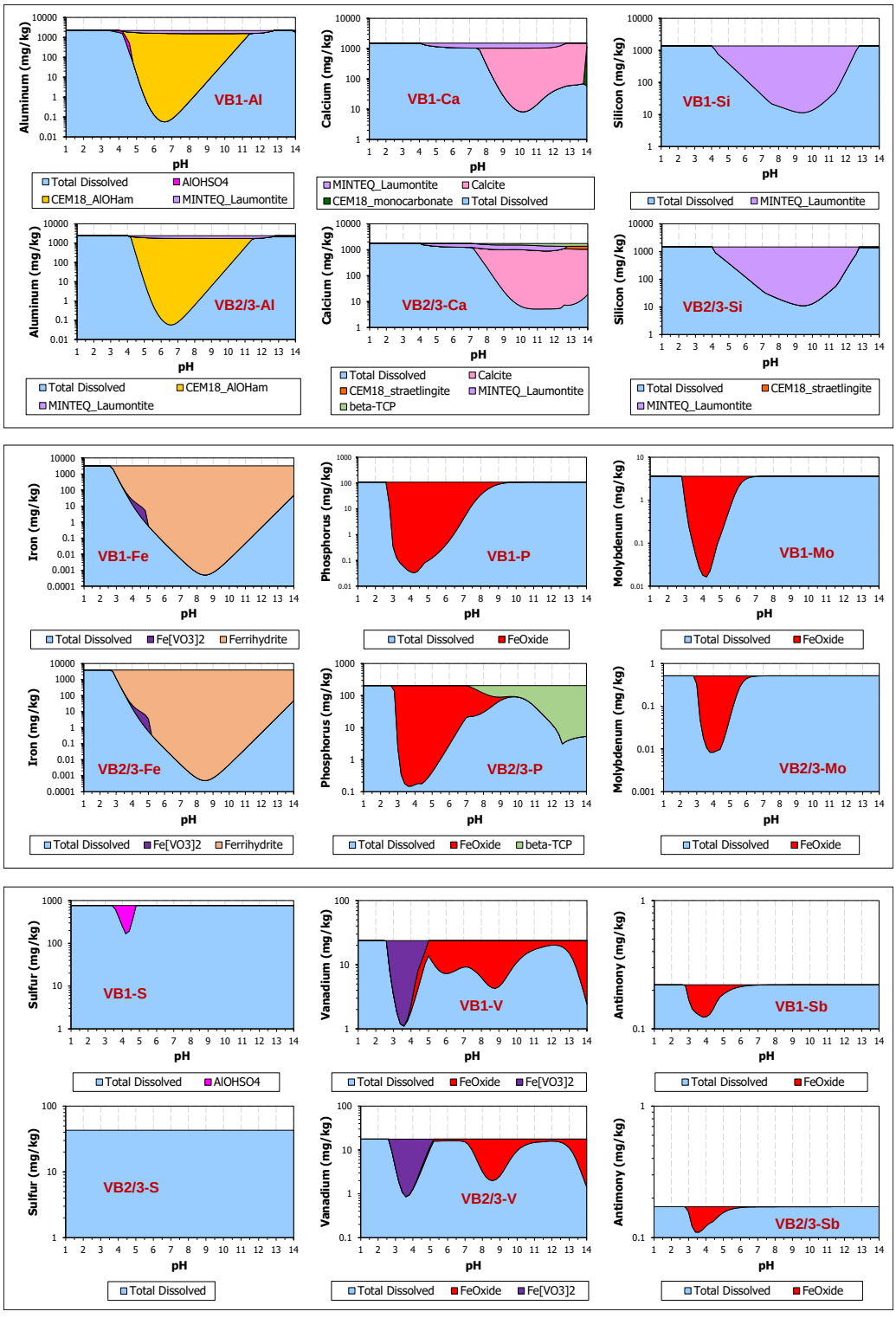

Figure B.16 Phase diagrams of Al, Ca, Si, Fe, P, Mo, S, V, and Sb as a function of pH according to the EPA Method 1313 at L/S = 10 L/kg for the field ash composites (VB1 and merged results of VB2 and VB3 as VB2/3). VB1: pH + *pe* = 13.9; VB2/3: pH + *pe* = 13.7. FeOxide: adsorbed onto hydrous ferric oxide.

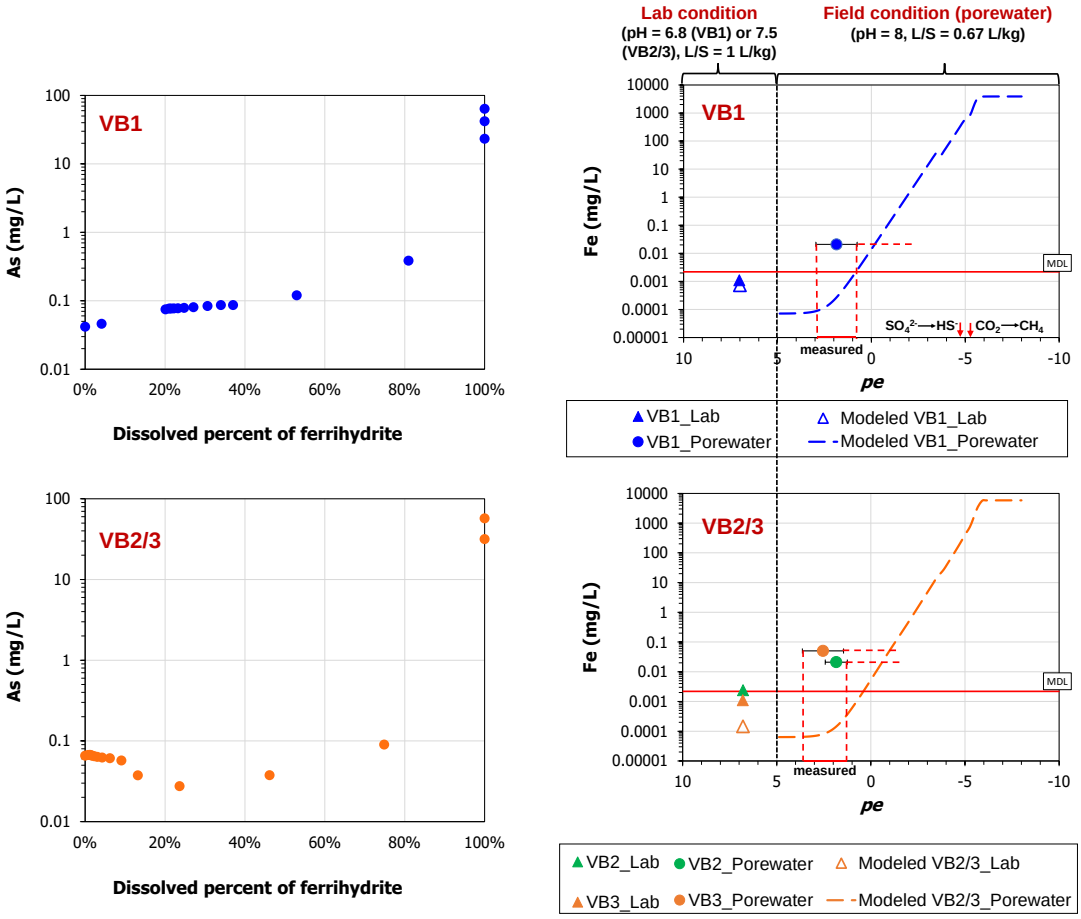

Figure B.17 Correlation of As concentrations with the percent of ferrihydrite dissolved (left) and Fe concentrations as *pe* decreases (right) during simulation of laboratory test conditions and field porewater conditions. The laboratory test condition refers the natural pH condition (pH = 6.8 for VB1, pH = 7.5 for VB2 and VB3) of the modified EPA Method 1313 at L/S = 1 L/kg. The field porewater condition was simulated using pH = 8 for VB1, VB2, and VB3 and L/S = 0.67 L/kg. Measured concentrations of Fe lower than the method detection limit (MDL) were set as half of the MDL.

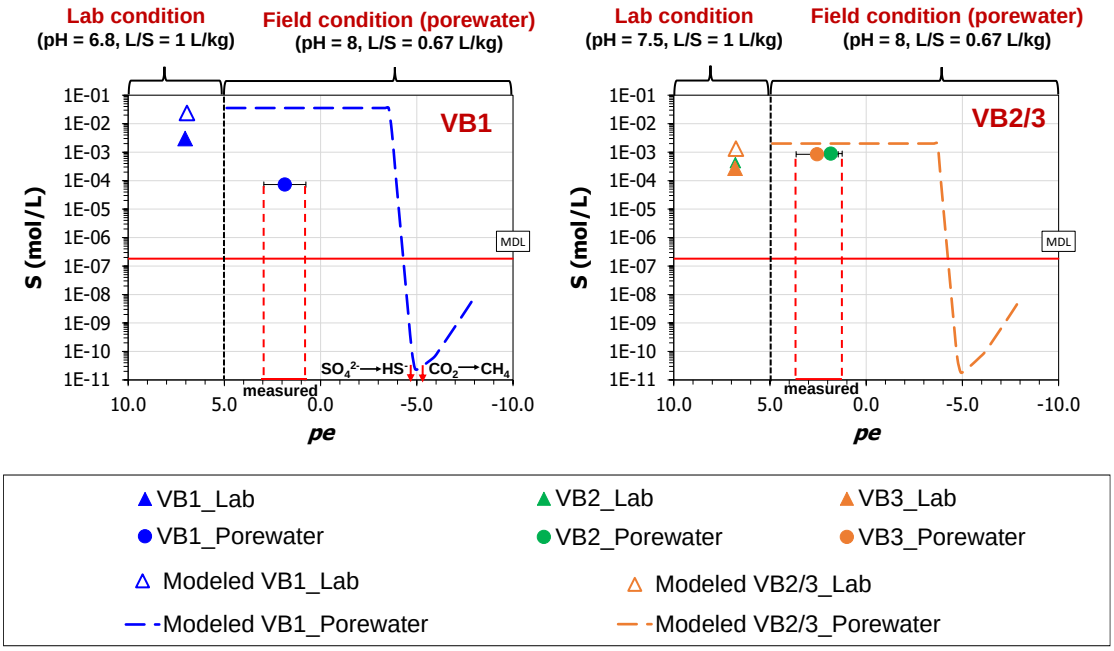

Figure B.18 Simulated leaching concentrations of S as a function of *pe* compared to measurements from laboratory test conditions and field porewater conditions. The laboratory test condition refers the natural pH condition (pH = 6.8 for VB1, pH = 7.5 for VB2 and VB3) of the modified EPA Method 1313 at L/S = 1 L/kg. Field porewater condition was simulated using pH = 8 for VB1, VB2, and VB3 and L/S = 0.67 L/kg. MDL: method detection limit.

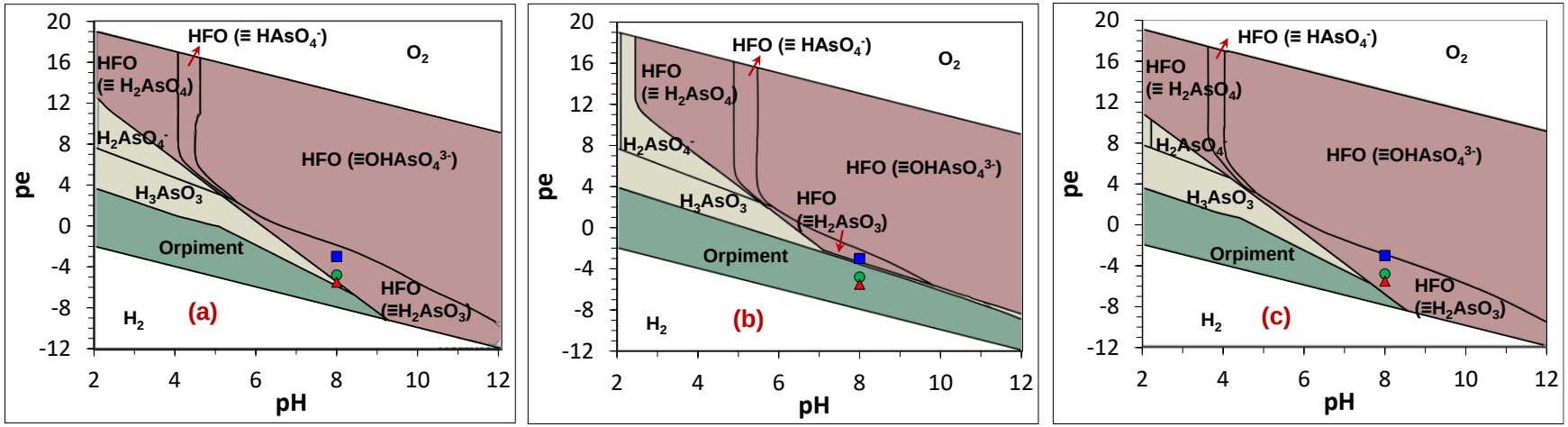

Figure B.19 Effects of changing S/As and Fe/As molar ratios on the *pe*-pH predominance diagrams of As species for VB1 sample. Simulations were conducted with the reported HFO site density (weak site: 0.2 mol/mol Fe; strong site: 0.005 mol/mol Fe) across the full pH and pe ranges. (a) Conditions representing the available content of VB1 from the field case study: S/As = 41.6 mol/mol, Fe/As = 101.6 mol/mol. (b) Increasing S/As molar ratio compared to conditions in (a): S/As = 416 mol/mol, Fe/As = 101.6 mol/mol. (c) Increasing Fe/As molar ratio compared to conditions in (a): S/As = 41.6 mol/mol, Fe/As = 1016 mol/mol.

APPENDIX C

SUPPLEMENTARY MATERIAL FOR CHAPTER 4

C.I Installation of porewater well screen and gas access points

Following the completion of boreholes using a hollow stem auger, a 1.5-m porewater screen section was set into the saturated ash impoundment layer at 21 to 26 m below ground surface (BGS) at each of the four borehole locations using a 5-cm outside diameter (Φ) PVC tube (detailed elevations of porewater wells are provided in Table C.1 and Figure C.1). Clean sand was used to fill the borehole annulus around the well screen from 0.3 m below the bottom of well screen to 0.6 m above the top of well screen. The porewater access well then was sealed with bentonite to within 0.15 m of the gas access point (GAP) target depth. The GAPs were set at different depths into the dry stack layer, including two (1.5 m and 4.5 m BGS) at VC-2 and VC-4 and three (1.5 m, 4.5 m, and 15 m BGS) at VC-1 and VC-3. Each GAP was constructed using 0.6-cm Φ stainless steel tubing with a bellhousing at the lower end and a 2-way shut-off valve at the top. The GAPs were set in a 0.3-m deep porous bed packed with 1.2 to 1.8 cm of washed river stone and sealed from above and below with expanded bentonite clay.

Table C.1 Elevations above mean sea level (AMSL) for borehole locations

	Elevations ASMS (m)			
	VC-1	VC-2	VC-3	VC-4
Top of well casing	135.5	135.7	136.8	136.4
Ground surface	133.9	134.1	135.1	135.1
Gas access point #1	132.4	132.6	133.6	133.5
Gas access point #2	129.4	129.5	130.4	130.5
Gas access point #3	119.2	NA [a]	119.9	NA [a]
Water Table (max) [b]	118.2	118.9	119.1	119.1
Water Table (min) [b]	117.1	117.4	117.5	117.5
Top of porewater well screen	111.4	108.5	109.8	112.6
Bottom of porewater well screen	112.9	110.0	111.3	114.1

[a] Not applicable, meaning no gas access point was placed at ~15 m below ground surface at VC-2 and V-4.

[b] Maximum and minimum water table measurements from monthly porewater sampling.

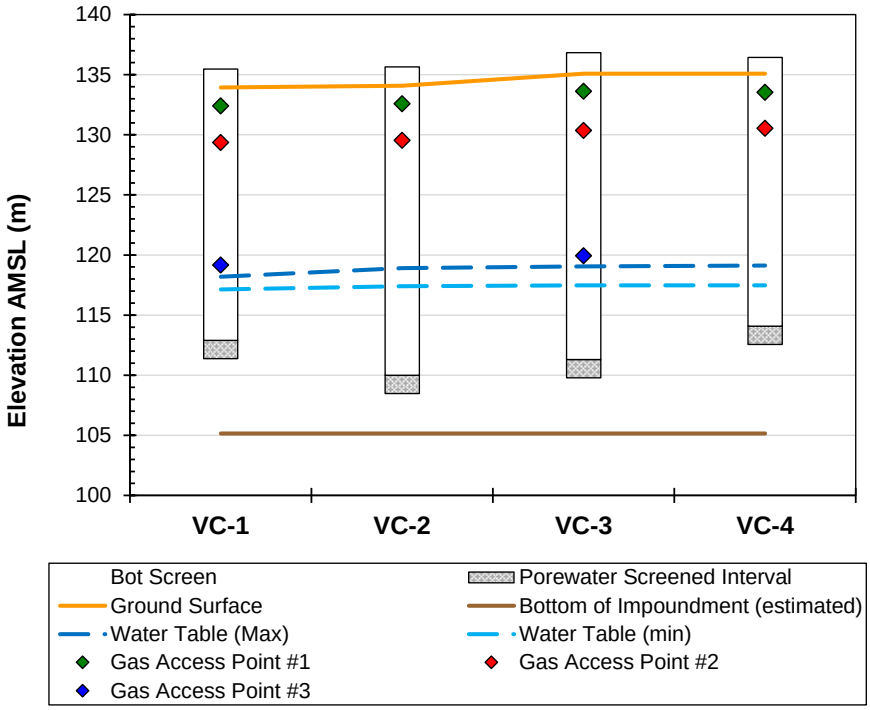

Figure C.1 Schematic presentation of above mean sea level (AMSL) elevations of monitoring wells including the porewater well screen and gas access points. Values of elevations are summarized in Table C.1.

C.II Field extraction apparatus

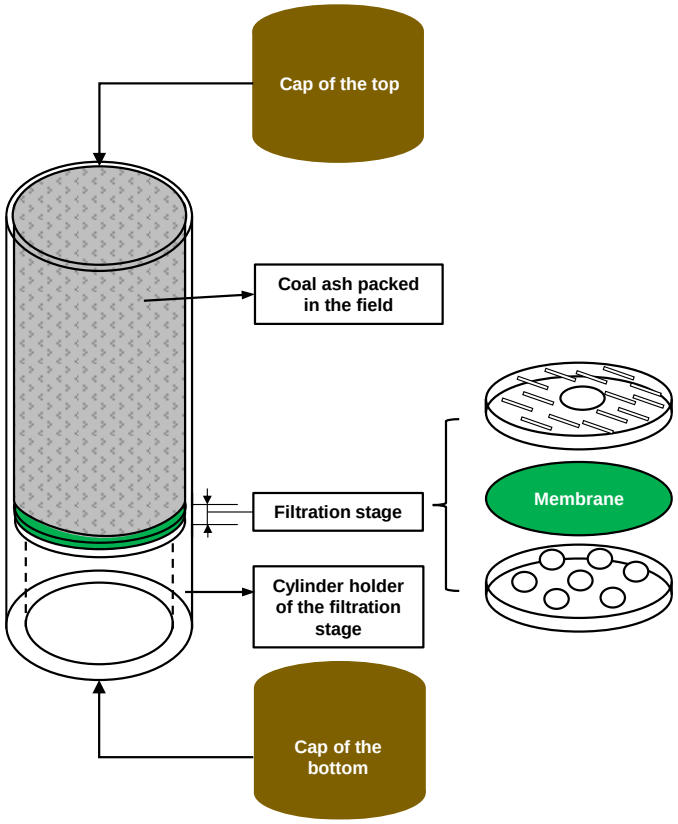

Figure C.2 Conceptual design of the apparatus used in field extractions.

C.III Material homogenization and procedures to create composites

(a) Material homogenization for split spoon samples

Homogenized material from within a split spoon was prepared to create composite samples used in pH-dependent leaching and percolation leaching tests. The split spoon samples stored at < 6ºC in the laboratory were crushed with a rolling pin and homogenized by hand through the plastic bag until the contents were well mixed. All the operations were conducted in a nitrogen purged chamber.

(b) Material preparation for pH-dependent leaching test

Four borehole composites (i.e., VC-1, VC-2, VC-3, and VC-4) were made from homogenized split spoon materials located from the strata and elevations consistent with the porewater well screens based on equal proportions of dry mass equivalent from individual split spoon sample intervals. Elevations of the homogenized split spoon materials used to create each composite sample are provided in Table C.2. In a nitrogen purged chamber, selected samples were homogenized by hand through a plastic bag until well mixed. All samples were then vacuum sealed and stored at < 6ºC for subsequent leaching characterization.

A fifth composite of material of unsaturated ash (hereafter referred to as "Dry") was created by blending homogenized material above the water table from all boreholes in a nitrogen purged chamber. Specifically, three steps were followed to create the Dry composite:

(1) five individual composites (refer to as "1.5-Dry", "4.5-Dry", "7.5-Dry", "10.5-Dry", and "13.5-Dry") representing coal ash from different depth layers in the dry stack, corresponding to 1.5-, 4.5-, 7.5-, 10.5-, and 13.5-m below ground surface, were made by blending homogenized split soon materials (based on equal dry mass proportions) from the same depth layer but from the four different borehole locations together based on equal dry mass proportions;

(2) a global Dry composite was obtained by mixing a portion of materials from each of the five individual composites from step#1 based on equal dry mass proportions. The rest of material of 1.5-Dry, 4.5-Dry, 7.5-Dry, 10.5-Dry, and 13.5-Dry was vacuum sealed and stored at < 6ºC;

(3) the global Dry composite was ground to pass through a 2-mm sieve and then vacuum

sealed and stored at < 6ºC for subsequent leaching characterization.

Table C.2 Intervals below ground surface (BGS) and elevations above mean sea level (AMSL) of homogenized split spoon samples used to create borehole composites (VC-1, VC-2, VC-3, and VC-4) near porewater well screen

		Interval of BGS (m)	**Interval of Elevations AMSL (m)**
VC-1	Porewater well screen	21-22.6	111.4-112.9
	Split spoon samples	20.9-21.3	112.6-113.1
		21.3-22.1	111.8-112.6
		22.1-22.6	111.4-111.8
VC-2	Porewater well screen	24.1-25.6	108.5-110.0
	Split spoon samples	23.9-24.4	109.7-110.2
		24.4-24.8	109.2-109.7
		24.8-25.3	108.8-109.2
VC-3	Porewater well screen	23.8-25.3	109.8-111.3
	Split spoon samples	23.9-24.4	110.7-111.2
		24.4-24.8	110.2-110.7
		24.8-25.3	109.8-110.2
VC-4	Porewater well screen	21.0-22.5	112.6-114.1
	Split spoon samples	20.9-21.3	113.8-114.2
		21.3-21.8	113.3-113.8
		21.8-22.3	112.8-113.3
		22.3-22.7	112.4-112.8

C.IV Eluate analysis

(a) Analysis of pH, EC, and ORP

For eluates from field extractions, pH-dependent leaching, and percolation leaching tests, the pH and EC were measured using an Accumet 20XL multimeter. The ORP was read through an ORPTestr 10 meter and converted to redox potential (Eh) by adding a correction factor (228V) of the standard reference electrode. For field measurements of porewater, however, the probe correction factor was automatically compensated for by the instrument to produce output as Eh values. The *pe*, which is defined in terms of the activity of electrons, was calculated by a conversion equation derived from the Nernst equation:

$$pE = \frac{F}{2.303RT}(Eh/1000)$$

where F is the Faraday constant (23,061 cal/ (V mol)),

R is the gas constant (1.987 cal/ (K mol)),

T is the temperature (K), and

1000 is for unit conversion (1,000 mV = 1 V).

(b) Inductively coupled plasma spectrometry, Ion chromatography, Carbon analysis

The eluate concentrations of cationic constituents were measured by inductively coupled plasma spectrometry; anions were measured by ion chromatography; and dissolved inorganic carbon (DIC) and organic carbon (DOC) were measured by a carbon analyzer. Details of analysis methods, quality assurance (QA), and quality control (QC) can be referred to Appendix A.III.

C.V Methods of solid sample characterization

The major elemental compositions of the field ash composites (i.e., VC-1, VC-2, VC-3, VC-4, and Dry) were measured by X-ray fluorescence (XRF) using an ARL ADVANT'X IntelliPower^{TM} Series 4200 sequential XRF spectrometer (Thermoscientific, Wilmington, DE, USA). The total contents of trace elements were determined by acid digestion following EPA Method 3052 [101] with a subsequent analysis of the digestion solution following EPA Method 6010B [102] by Eurofins TestAmerica (Nashville, TN). The crystalline structures were analyzed by X-ray diffraction (XRD, X'Pert PRO PANalytical B.V., Almelo, the Netherlands).

The carbon analysis was conducted using a Shimadzu model TOC-LCPH with an SSM-5000 unit for solid samples to measure total carbon (TC) and total inorganic carbon (TIC) with total organic carbon (TOC) computed as the difference between TC and TIC. The TIC also was estimated by thermogravimetric analysis combined with mass spectrometry (TGA/MS), using a TA Instruments Q600 SDT analyzer (New Castle, Delaware, USA) and a MS unit. About 50 mg of ground and sieved sample (passing No. 100 sieve, 125um) was loaded for analysis. Each test sample was heated under a continuous flow of nitrogen from 30 °C to 1,000 °C at a rate of 10.0 °C/min. During the heating, the current of m/e species 44 was collected by the MS unit to determine the appropriate temperature range of CO_2 release. The TIC content was calculated based on the mass loss of the sample in the corresponding temperature range (500-900 °C).

The amount of iron (hydr)oxides was determined through analysis of Fe concentrations in eluates from two selective extraction tests. The amorphous iron (hydr)oxides (Am_{FeOOH}) were extracted with ascorbic acid following the ISO Method 12782-1 [63]. The crystalline iron (hydr)oxides (Cry_{FeOOH}) were extracted with dithionite following the ISO Method 12782-2 [64]. Values of Am_{FeOOH} and the total of Am_{FeOOH}+Cry_{FeOOH} were used as the lower limit and upper limit, respectively, to calibrate the amount of hydrous ferric oxides in the geochemical speciation models.

C.VI Approach of geochemical modeling

Table C.3 Model parameters and components of virtual materials for the field ash composites

Conditions of L/S and pH+*pe*			
Parameter	Laboratory simulations (pH-dependent at L/S=10)	Laboratory simulations (pH-dependent at L/S=1)	Porewater simulations
L/S (L/kg-dry) [a]	10	1.0	0.6
pH+*pe* [b]	17.9	17.9	12.9
Organic matter and HFO description			
Total HA content	200 mg/kg	HFO content [c]	0.016 mol Fe/kg
Polynomial coefficients of dissolved HA concentrations			
C0	-5.13E+00		
C1	-9.34E-01		
C2	1.90E-01		
C3	-1.57E-02		
C4	5.55E-04		
C5	-5.09E-06		

Reactant available content			
Reactant	mg/kg	Reactant	mg/kg
Al	4,920	Mn	80.3
As	79.3	Mo	13.7
B	442	NO_3^- [f]	0.056
Ba	6.32	P	417
Ca	17,000	K	669
CO_3^{2-} [d]	9800	Sb	2.49
Cl^-	618	Se	2.58
Cr	9.44	Si	5,050
Cu	3.81	Na	440
Fe [e]	894	Ni	4.94
Pb	8.14	Sr	35.1
Cd	2.54	S	2,830
Co	1.95	V	192
Li	1.81	Zn	10.3
Mg	489		

[a] The L/S (L/kg) used in porewater simulation was estimated by dividing the total release (mg/kg) of K at natural pH condition (laboratory at L/S=10 L/kg-dry) by the porewater concentration of K, given K as a conservative constituent.

[b] The pH+*pe* represents overall redox condition. The pH+*pe* for laboratory leaching simulations was calibrated against leaching of Cr and Fe. The pH+*pe* for porewater simulations was based on measurements.

[c] The HFO content was represented by the calibrated available content of Fe used in the virtual material. Thus, the HFO content is not a fixed value but is based on the precipitated amount of Fe(III) hydroxides controlling the solubility of Fe as a function of simulation conditions.

[d] Available content of CO_3^{-2} was calibrated against the pH-dependent leaching behavior of calcium at pH > 8.

[e] Available content of Fe was calibrated to describe adsorption of As and Mo by iron hydroxide minerals at pH < 8 in models.

[f] Values were below the detection limit and set at one half of the detection limit.

Table C.4 Mineral set identified in geochemical virtual materials for the field ash composites (merged results of VC-1/VC-4)

Phase ID	Formula	log K	Reaction
Mineral phases			
Arsenocrandallite [a]	$CaAl_3(AsO_4)(AsO_3OH)(OH)_6$	-96.51	Arsenocrandallite + 6 H_2O = 3 $Al[OH]_4^-$ + 2 AsO_4^{-3} + 1 Ca^{+2} + 7 H+
Al[PO4][cr] [b]	$Al(PO_4)$	-45.49	Al[PO4][cr] + 4 H_2O = 1 $Al[OH]_4^-$ + 4 H^+ + 1 $PO4^{-3}$
BaSrSO4[50%Ba] [c]	$(Ba_{0.5}Sr_{0.5})SO_4$	-8.22	BaSrSO4[50%Ba] = 0.5 Ba^{+2} + 1 $SO4^{-2}$ + 0.5 Sr^{+2}
Ca2V2O7 [d]	$Ca_2V_2O_7$	17.98	$Ca_2V_2O_7$ + 6 H+ = 2 Ca^{+2} + 3 H_2O + 2 VO_2^+
Ca3[PO4]2[beta] [d]	$Ca_3(PO_4)_2$	-29.08	Ca3[PO4]2[beta] = 3 Ca^{+2} + 2 PO_4^{-3}
Ca5[OH][AsO4]3 [e]	$Ca_5(OH)(AsO_4)_3$	-25.96	Ca5[OH][AsO4]3 + 1 H^+ = 3 AsO_4^{-3} + 5 Ca^{+2} + 1 H_2O
Cd[OH]2[s] [d]	$Cd(OH)_2$	13.93	Cd[OH]2[s] + 2 H^+ = 1 Cd^{+2} + 2 H_2O
CEM18_AlOHam [f]	$Al(OH)_3$	-13.76	CEM18_AlOHam + 1 H_2O = 1 $Al[OH]_4^-$ + 1 H^+
CEM18_C3AFS0_84H4_32 [f]	$(CaO)_3(AlFeO_3)(SiO_2)_{0.84}(H_2O)_{4.32}$	4.17	CEM18_C3AFS0_84H4_32 + 2.32 H^+ = 1 Al[OH]4- + 3 Ca^{+2} + 1 $Fe[OH]_4^-$ + 0.64 H_2O + 0.84 $H_2SiO_4^{-2}$
CEM18_C3FS1_34H3_32 [f]	$(CaO)_3(Fe_2O_3)(SiO_2)_{1.34}(H_2O)_{3.32}$	-13.14	CEM18_C3FS1_34H3_32 + 1.32 H^+ + 1.36 H_2O = 3 Ca^{+2} + 2 $Fe[OH]_4^-$ + 1.34 $H_2SiO_4^{-2}$
CEM18_FeOOHmic [f]	FeO(OH)	-19.25	CEM18_FeOOHmic + 2 H_2O = 1 Fe[OH]4- + 1 H^+
CEM18_Gp [f]	$CaSO_4 \cdot 2H_2O$	-4.58	CEM18_Gp = 1 Ca^{+2} + 2 H_2O + 1 SO_4^{-2}
CEM18_M15SH [f]	$(MgO)_{1.5}(SiO_2)(H_2O)_{2.5}$	-4.28	CEM18_M15SH + 1 H^+ = 2 H_2O + 1 $H_2SiO_4^{-2}$ + 1.5 Mg^{+2}
CEM18_monocarbonate05 [f]	$(CaO)_2(Al_2O_3)0.5(CO_2)_{0.5}(H_2O)_{11}$	12.72	CEM18_monocarbonate05 + 2 H^+ = 1 Al[OH]4- + 0.5 CO_3^{-2} + 2 Ca^{+2} + 4.5 H_2O
CEM18_straetlingite [f]	$(CaO)_2(Al_2O_3)(SiO_2)(H_2O)_8$	-18.59	CEM18_straetlingite = 2 $Al[OH]_4^-$ + 2 Ca^{+2} + 3 H_2O + 1 $H_2SiO_4^{-2}$
Cu[OH]2[s] [d]	$Cu(OH)_2$	8.84	Cu[OH]2[s] + 2 H^+ = 1 Cu^{+2} + 2 H_2O
Eskolaite [a]	Cr_2O_3	-147.52	Eskolaite + 5 H_2O = 2 CrO_4^{-2} + 10 H^+ + 6 e^-
Exp_Ca3[OH]2[CrO4]2 [g]	$Ca_3(OH)_2(CrO_4)_2$	-1.00	Exp_Ca3[OH]2[CrO4]2 + 2 H^+ = 3 Ca^{+2} + 2 CrO_4^{-2} + 2 H_2O
Exp_Ca3[OH]2[SeO4]2 [g]	$Ca_3(OH)_2(SeO_4)_2$	0.52	Exp_Ca3[OH]2[SeO4]2 + 2 H^+ = 3 Ca^{+2} + 2 H_2O + 2 SeO_4^{-2}
Exp_FeVO4:2H2O [g]	$FeVO_4 \cdot 2H_2O$	-23.48	Exp_FeVO4:2H2O_am = 1 $Fe[OH]_4^-$ + 1 VO_2^+
Fe2[SeO3]3:2H2O [d]	$Fe_2(SeO_3)_3 \cdot 2H_2O$	-174.50	Fe2[SeO3]3:2H2O + 9 H_2O = 2 Fe[OH]4- + 14 H^+ + 3 SeO_4^{-2} + 6 e-
Laumontite [b]	$Ca(AlSi_2O_6)_2 \cdot 4H_2O$	-120.78	Laumontite + 8 H_2O = 2 $Al[OH]_4^-$ + 1 Ca^{+2} + 8 H^+ + 4 $H_2SiO_4^{-2}$
Pb[OH]2[s] [d]	$Pb(OH)_2$	8.32	Pb[OH]2[s] + 2 H^+ = 2 H_2O + 1 Pb^{+2}
PbMoO4 [d]	$PbMoO_4$	-15.78	PbMoO4 = 1 MoO_4^{-2} + 1 Pb^{+2}
Semetal[am] [d]	Se	-88.91	Semetal[am] + 4 H_2O = 8 H^+ + 1 SeO_4^{-2} + 6 e^-
Strengite [d]	$FePO_4 \cdot 2H_2O$	-47.96	Strengite + 2 H_2O = 1 $Fe[OH]_4^-$ + 4 H^+ + 1 PO_4^{-3}
Solid solutions			
BaCO3_ss [h]	-	-8.58	BaCO3_ss = 1 Ba^{+2} + 1 CO_3^{-2} + 1 CaCO3_ss
CaCO3_ss [h]	-	-8.45	CaCO3_ss = 1 CO_3^{-2} + 1 Ca^{+2} + 1 CaCO3_ss
CaHBO3_ss [i]	-	4.77	CaHBO3_ss + 1 H^+ = 1 Ca^{+2} + 1 CaCO3_ss + 1 $H_2BO_3^-$

$MgCO3\_ss$ [h]	-	-8.21	$MgCO3\_ss = 1\ CO_3^{-2} + 1\ CaCO3\_ss + 1\ Mg^{+2}$
$SrCO3\_ss$ [h]	-	-9.27	$SrCO3\_ss = 1\ CO_3^{-2} + 1\ CaCO3\_ss + 1\ Sr^{+2}$
$AsO4\_Ettringite\_ss$ [j]	-	-26.79	$AsO4\_Ettringite\_ss + 1\ H^+ + 8\ H_2O = 2\ Al[OH]_4^- + 3\ AsO_4^{-3} + 6\ Ca^{+2} + 1\ ettr\_ss$
$BO3\_Ettringite\_ss$ [j]	-	46.87	$BO3\_Ettringite\_ss + 7\ H^+ + 8\ H_2O = 2\ Al[OH]_4^- + 6\ Ca^{+2} + 3\ H_2BO_3^- + 1\ ettr\_ss$
$CrO4\_Ettringite\_ss$ [j]	-	8.59	$CrO4\_Ettringite\_ss + 4\ H^+ + 8\ H_2O = 2\ Al[OH]_4^- + 6\ Ca^{+2} + 3\ CrO_4^{-2} + 1\ ettr\_ss$
$Ettringite\_ss$ [j]	-	11.99	$Ettringite\_ss + 4\ H^+ + 8\ H_2O = 2\ Al[OH]_4^- + 6\ Ca^{+2} + 3\ SO_4^{-2} + 1\ ettr\_ss$
$MoO4\_Ettringite\_ss$ [j]	-	9.59	$MoO4\_Ettringite\_ss + 4\ H^+ + 8\ H_2O = 2\ Al[OH]_4^- + 6\ Ca^{+2} + 3\ MoO_4^{-2} + 1\ ettr\_ss$
$SeO4\text{-}2\_Ettringite\_ss$ [j]	-	8.59	$SeO4\text{-}2\_Ettringite\_ss + 4\ H^+ + 8\ H_2O = 2\ Al[OH]_4^- + 6\ Ca^{+2} + 3\ SeO_4^{-2} + 1\ ettr\_ss$
$VO3\_Ettringite\_ss$ [j]	-	53.79	$VO3\_Ettringite\_ss + 13\ H^+ + 2\ H_2O = 2\ Al[OH]_4^- + 6\ Ca^{+2} + 3\ VO_2^+ + 1\ ettr\_ss$

Source:
[a] THERMODDEM2011 database [85]
[b] ThermoChimie database [87]
[c] Co-precipitations assuming ideal solid solution.
[d] MINTEQA2_V4 database [56]
[e] From literature [42]
[f] CEMDATA18 database [84]
[g] Experimental minerals proposed with calibrated log K value [115]
[h] Using $BaCO_3$, $SrCO_3$, and $MgCO_3$ end member reactions from MINTEQA2_V4 database in the proposed carbonate solid solution.
[i] End member reaction using HBO_3^{2-} substituted for CO_3^{2-} as one end member reaction in the proposed carbonate solid solution.
[j] Experimental solid solutions derived from modeling of cementitious solid waste [88,115]

C.VII Temporal variations of porewater *pe*, pH+*pe*, and temperature

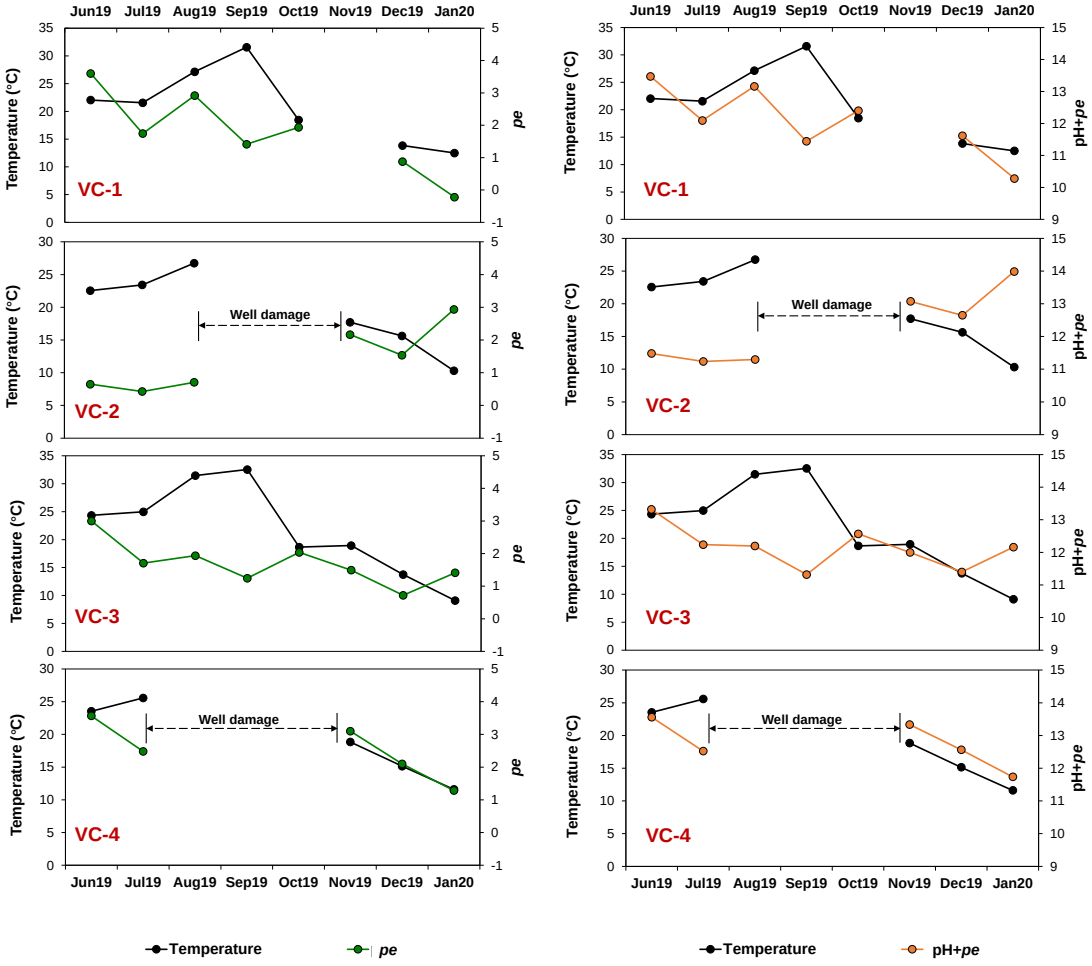

Figure C.3 Temporal variations of porewater *pe*, pH+*pe*, and temperature at VC-1, VC-2, VC-3, and VC-4. Sampling wells at VC-2 and VC-4 were damaged due to operations on the landfill from September 2019 and August 2019, respectively. Porewater sampling was interrupted accordingly and restarted following the restoration of the wells in November 2019.

C.VIII Chemical characterization results of the field ash composites

Table C.5 Total content of trace elements analyzed by acid digestion following EPA Method 3052 in the field ash composites, unit (mg/kg, w/w)

	VC-1 Composite	VC-2 Composite	VC-3 Composite	VC-4 Composite	VC Average (±S.D.) [a]	Dry composite
As	51	63	48	48	53(±7)	54
Ba	370	480	820	820	623(±232)	360
Cd	4.4	3.5	5.1	5.1	4.5(±0.8)	6.0
Co	32	23	20	20	24(±6)	29
Cr	170	140	130	130	143(±19)	160
Cu	81	72	64	64	70(±8)	78
Pb	62	70	67	67	67(±3)	160
Li	68	55	50	50	56(±9)	71
Mn	380	390	430	430	408(±26)	280
Mo	27	26	18	18	22(±5)	62
Ni	130	93	89	89	100(±20)	120
Sb	6.2	4.5	5.0	5.0	5.2(±0.7)	7.4
Se	14	10	9.3	9.3	11(±2)	16
Sr	68	57	67	67	65(±5)	130
V	670	450	480	480	520(±101)	620
Zn	410	430	410	410	415(±10)	460

[a] VC Average is the mean value of the results of VC-1, V-2, VC-3, and VC-4 composites. Standard deviation is indicated in parentheses.

Table C.6 Available content (mg/kg-dry) of constituents in the field ash composites based on the maximum release from EPA Method 1313

	VC-1 Composite	VC-2 Composite	VC-3 Composite	VC-4 Composite	VC Average (±S.D.) [b]	Dry Composite
Al	4,920	4,860	6,230	4,680	5,170 (±713)	5,080
As	32.0	41.6	32.0	79.3	46.2 (±22.5)	28.1
B	442	350	427	391	402 (±41)	459
Ba	4.53	5.50	4.09	6.32	5.11 (±1.00)	2.68
Ca	17,000	16,500	18,600	14,500	16,700 (±1,680)	18,600
CO_3^{-2}	125	143	212	159	159 (±37.5)	66.7
Cl^-	615	458	355	618	512 (±128)	472
Cr	9.44	11.0	10.5	8.03	9.74 (±1.31)	8.26
Cu	3.52	4.22	2.16	3.81	3.43 (±0.892)	7.47
Fe	2,170	2,060	2,240	2,200	2,170 (±76.6)	2,080
Pb	5.45	4.62	2.41	8.14	5.16 (±2.37)	23.8
Cd	2.54	1.54	2.66	2.28	2.25 (±0.502)	3.40
Co	1.08	1.45	1.52	1.95	1.50 (±0.357)	1.87
DOC	185	178	236	167	192 (±30.6)	23.7
Li	1.81	1.04	1.67	1.12	1.41 (±0.388)	3.36
Mg	489	578	757	409	558 (±150)	713
Mn	80.3	75.4	119	57.4	83 (±26)	54.2
Mo	11.1	19.4	9.41	13.7	13.4 (±4.39)	24.9
NO_3^-	0.056 [a]	0.200	0.056 [a]	0.056 [a]	0.092 (±0.072)	0.056 [a]
P	322	509	443	417	423 (±77.6)	296
K	669	819	732	542	691 (±116)	824
Sb	2.49	2.23	4.64	1.98	2.84 (±1.22)	3.79
Se	2.07	0.976	1.27	2.58	1.72 (±0.734)	2.43
Si	5,050	4,880	7,690	4,480	5,530 (±1,460)	5,660
Na	432	330	255	440	364 (±88.5)	302
Ni	4.01	4.03	3.94	4.94	4.23 (±0.475)	4.27
Sr	25.3	20.1	23.6	35.1	26.0 (±6.41)	48.2
S	2,830	2,480	4,120	2,700	3,030 (±741)	5,000
V	192	139	154	187	168 (±25.5)	153
Zn	10.3	8.49	12.9	9.77	10.4 (±1.85)	18.5

[a] Values below the detection limit and set at one half of the detection limit.

[b] VC Average is the mean value of the results of VC-1, V-2, VC-3, and VC-4 composites. Standard deviation is indicated in parentheses.

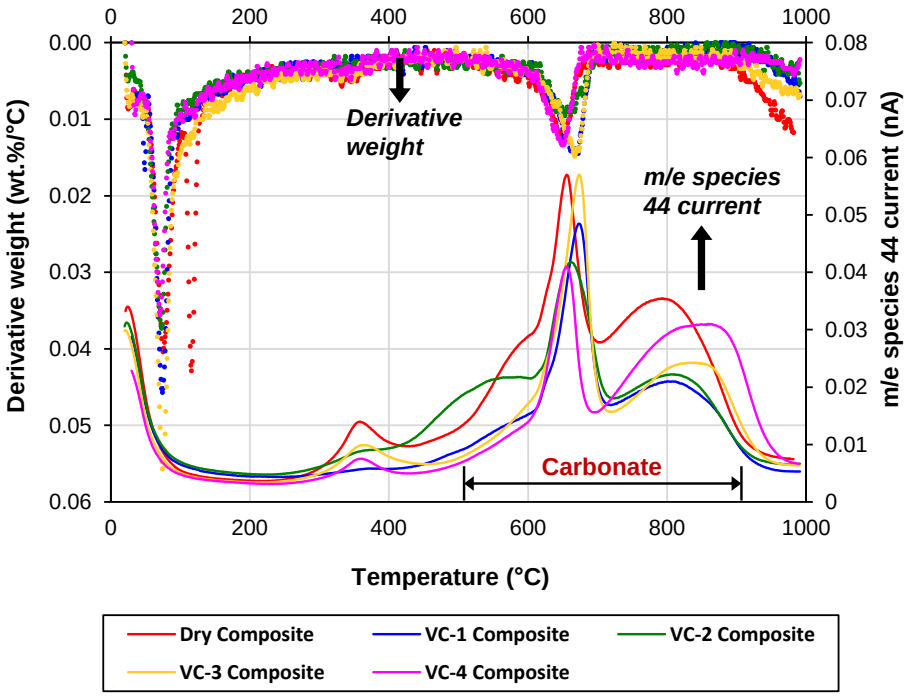

Figure C.4 TGA/MS results showing the derivative of the mass and temperature and current of m/e species 44 versus the temperature.

Table C.7 Crystalline phases identified by XRD in the field ash composites

	VC-1 Composite	VC-2 Composite	VC-3 Composite	VC-4 Composite	Dry Composite
Calcite [$CaCO_3$]	√	√	√	√	√
Ettringite [$Ca_6Al_2(SO_4)_3(OH)_{12}•25H_2O$]	√	√	√	√	√
Gypsum [$CaSO_4•H_2O$]					√
Hematite [Fe_2O_3]	√	√	√	√	√
Mullite [$Al_6Si_2O_{13}$]	√	√	√	√	√
Magnetite [Fe_3O_4]	√	√	√	√	√
Quartz [SiO_2]	√	√	√	√	√

C.IX Comparison of EPA Method 1313 and EPA Method 1314 leaching between the field ash composites

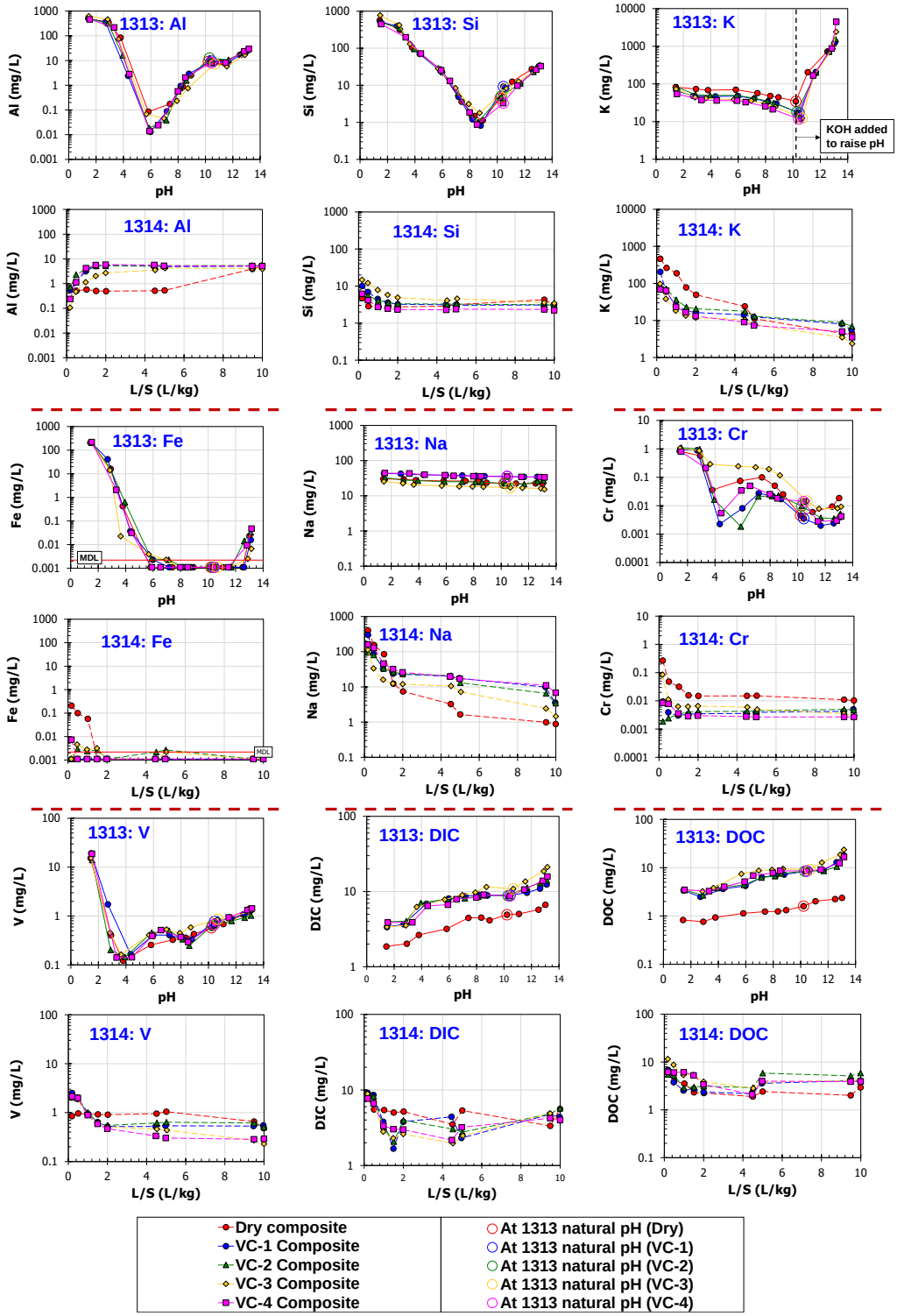

Figure C.5 Comparison of pH-dependent (EPA Method 1313) and L/S-dependent (EPA Method 1314) leaching of Al, Si, K, Fe, Na, Cr, V, DIC, and DOC from the field ash composites.

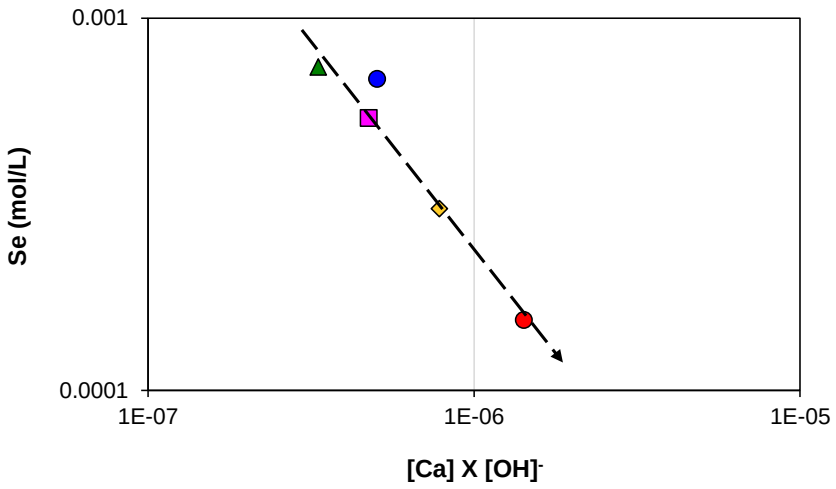

Figure C.6 Relationships of the product of Ca and OH^- concentrations (mol/L) and concentration of Se at the natural pH condition from EPA Method 1313 test.

C.X Comparisons of constituent concentrations in porewater to that in field extractions and in laboratory pH-dependent leaching

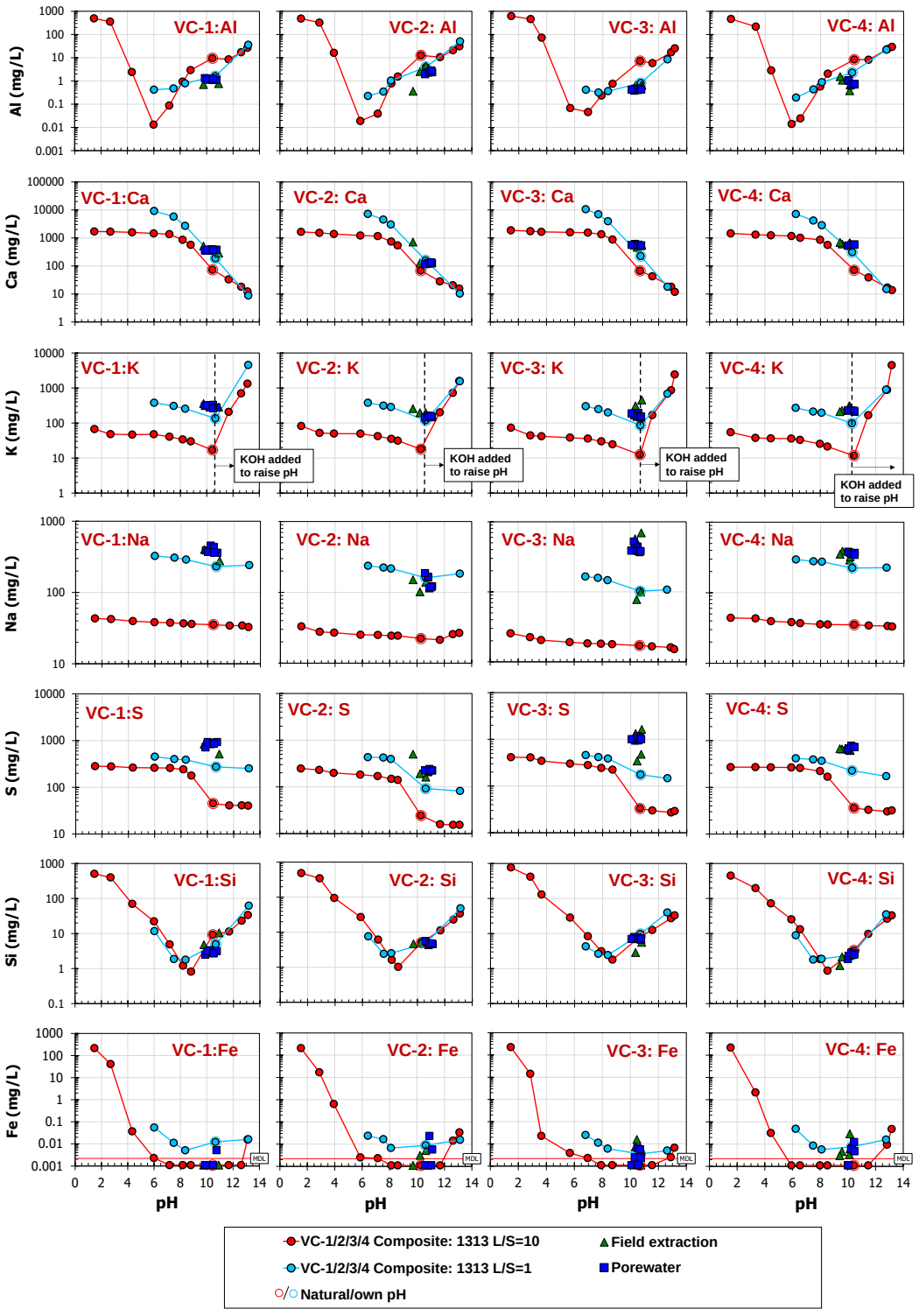

Figure C.7 Concentrations of Al, Ca, K, Na, S, Si, and Fe in porewater and in field extractions compared to laboratory pH-dependent leaching at L/S 1 and 10 L/kg-dry of the field ash composites.

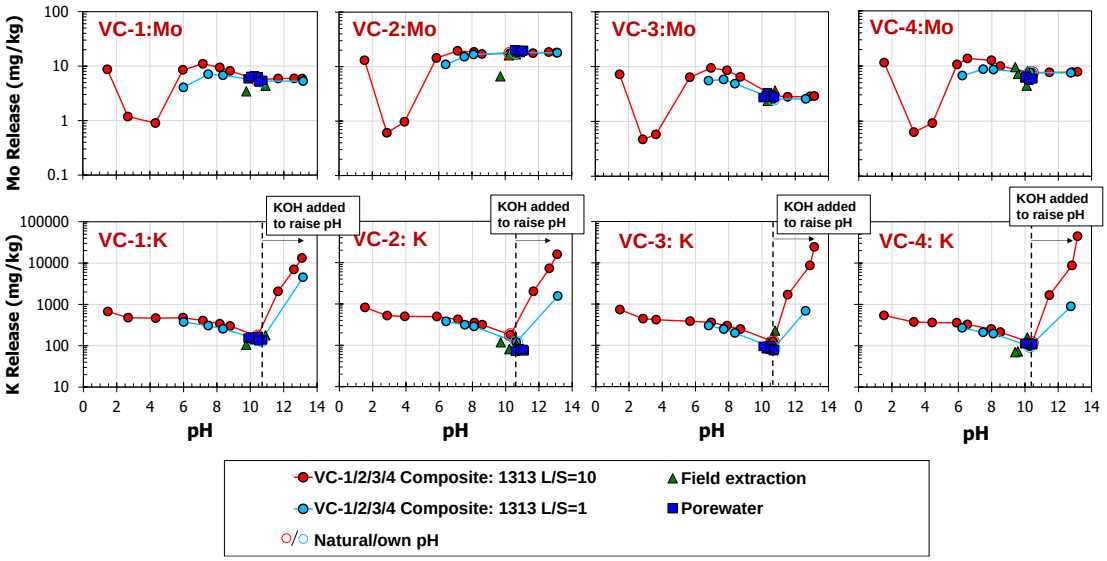

Figure C.8 Release of Mo and K in porewater and in field extractions compared to laboratory pH-dependent leaching at L/S 1 and 10 L/kg-dry of the field ash composites. Release (mg/kg solid) to porewater was calculated by multiplying each concentration (mg/L) with an estimated field L/S at 0.6 L/kg-dry.

C.XI Geochemical modeling results

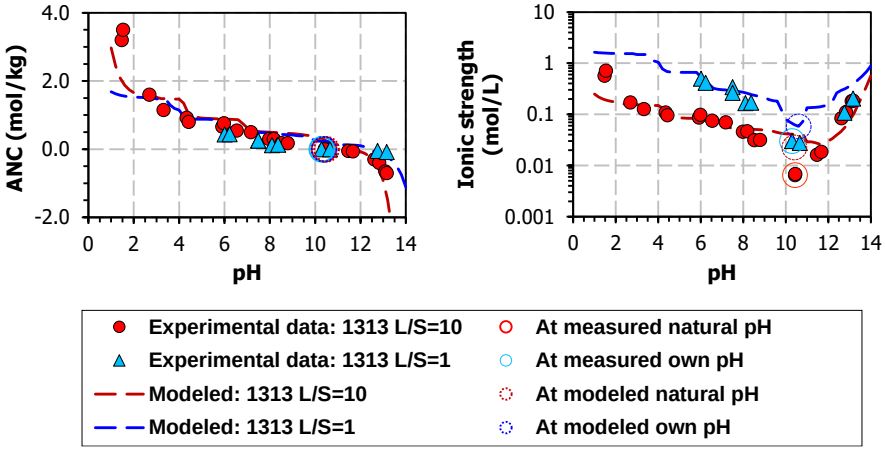

Figure C.9 Simulated acid neutralization capacity (ANC) and ionic strength (*I*) compared to ANC and *I* from laboratory pH-dependent leaching at L/S of 1 and 10 L/kg-dry.

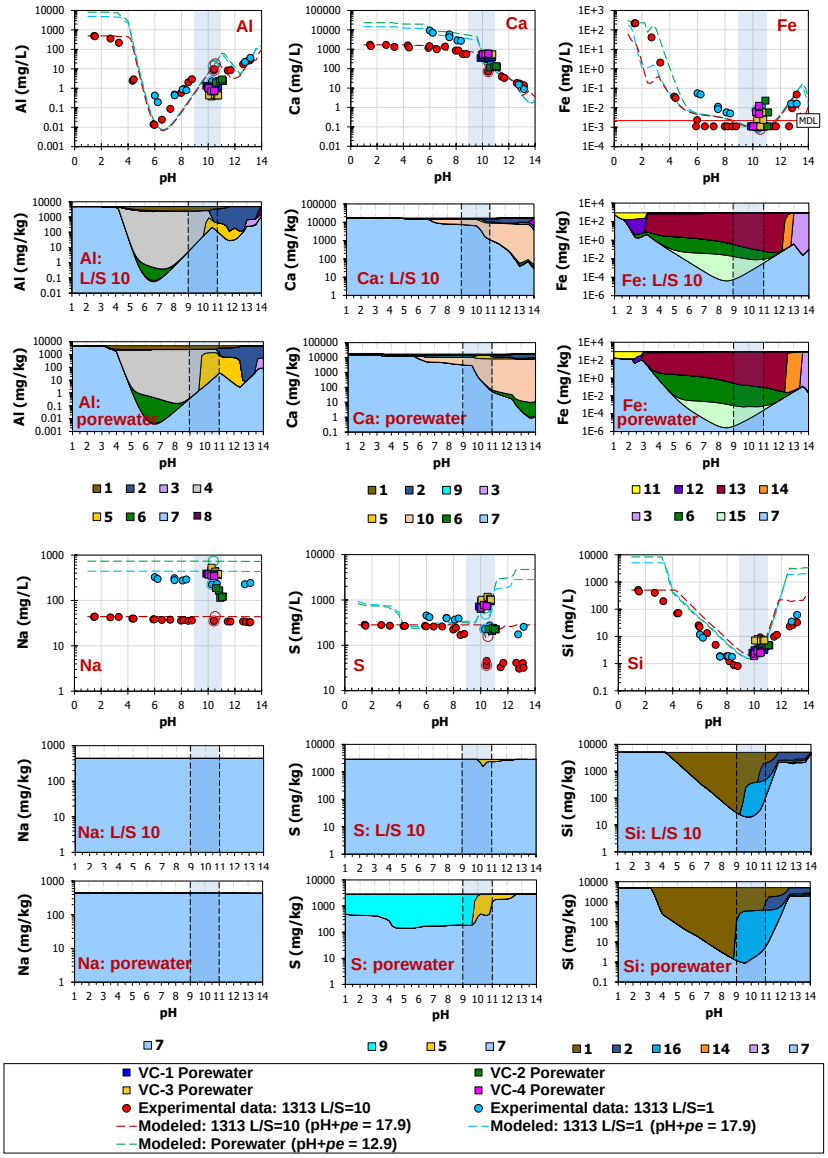

Figure C.10 Geochemical speciation modeling (only primary phases shown) of Al, Ca, Fe, Na, S, and Si under laboratory pH-dependent leaching at L/S of 1 and 10 L/kg-dry and under field porewater conditions at an estimated L/S of 0.6 L/kg-dry. Iron concentrations below the method detection limit (MDL) are indicated as half of the MDL. Phase diagrams are shown for laboratory leaching at L/S=10 L/kg-dry (EPA 1313) and porewater conditions. A specific pH range around the natural pH condition of field ash is highlighted. 1: $Ca(AlSi_2O_6)_2 \cdot 4H_2O$; 2: C_2ASH_8; *3: $C_3(F,A)S0.84H_{4.32}$; 4: $Al(OH)_3$ mineral; 5: ettringite solid solution; 6: solid humic acid bound; 7: total dissolved phase, free ions; *8: $C_2A_{0.5}c_{0.5}H_{11}$; 9: $CaSO_4 \cdot 2H_2O$; 10: carbonate solid solution; 11: $FePO_4 \cdot 2H_2O$; 12: $FeVO_4 \cdot 2H_2O$ (postulated experimental mineral phase); 13: FeO(OH) mineral; *14: $C_3FS_{1.34}H_{3.32}$; 15: dissolved humic acid bound; *16: $M_{1.5}SH_{2.5}$. *Cement chemist notation was used to simplify the formulae of cement phases using C = CaO; S = SiO_2; A = Al_2O_3; F = Fe_2O_3; M = MgO; H = H_2O; c = CO_2; s = SO_3.

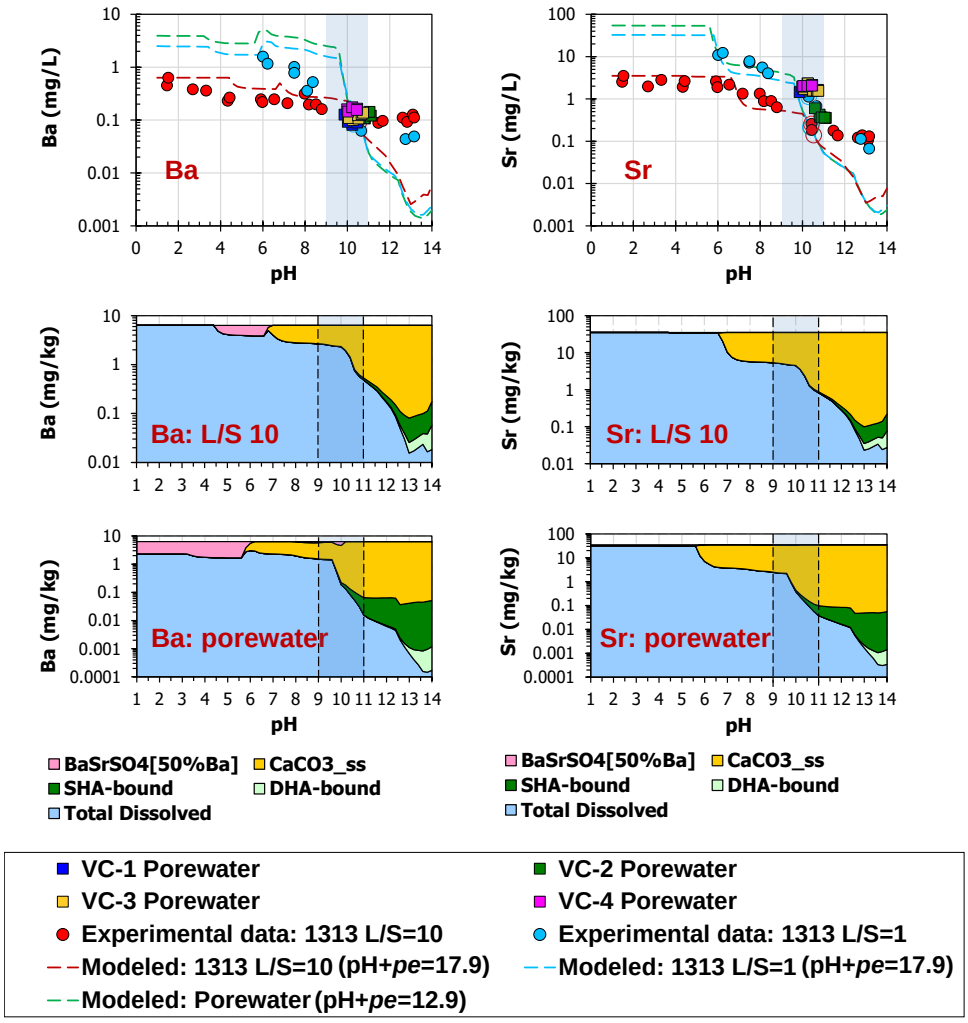

Figure C.11 Geochemical speciation modeling of Ba and Sr under laboratory pH-dependent leaching at L/S of 1 and 10 L/kg-dry and under field porewater conditions at estimated L/S of 0.6 L/kg-dry. Phase diagrams are shown for laboratory leaching at L/S=10 L/kg-dry (EPA 1313) and porewater conditions. BaSrSO4[50%]: $(Ba_{0.5}Sr_{0.5})SO_4$ precipitation; CaCO3_ss: carbonate solid solution; SHA-bound: solid humic acid bound; DHA-bound: dissolved humic acid bound; Total Dissolved: in dissolved phase, free ions. A specific pH range around the natural pH condition of field ash is highlighted.

APPENDIX D

SUPPLEMENTARY MATERIAL FOR CHAPTER 5

D.I Typical types of percolation leaching behavior and the associated leaching-controlling mechanisms

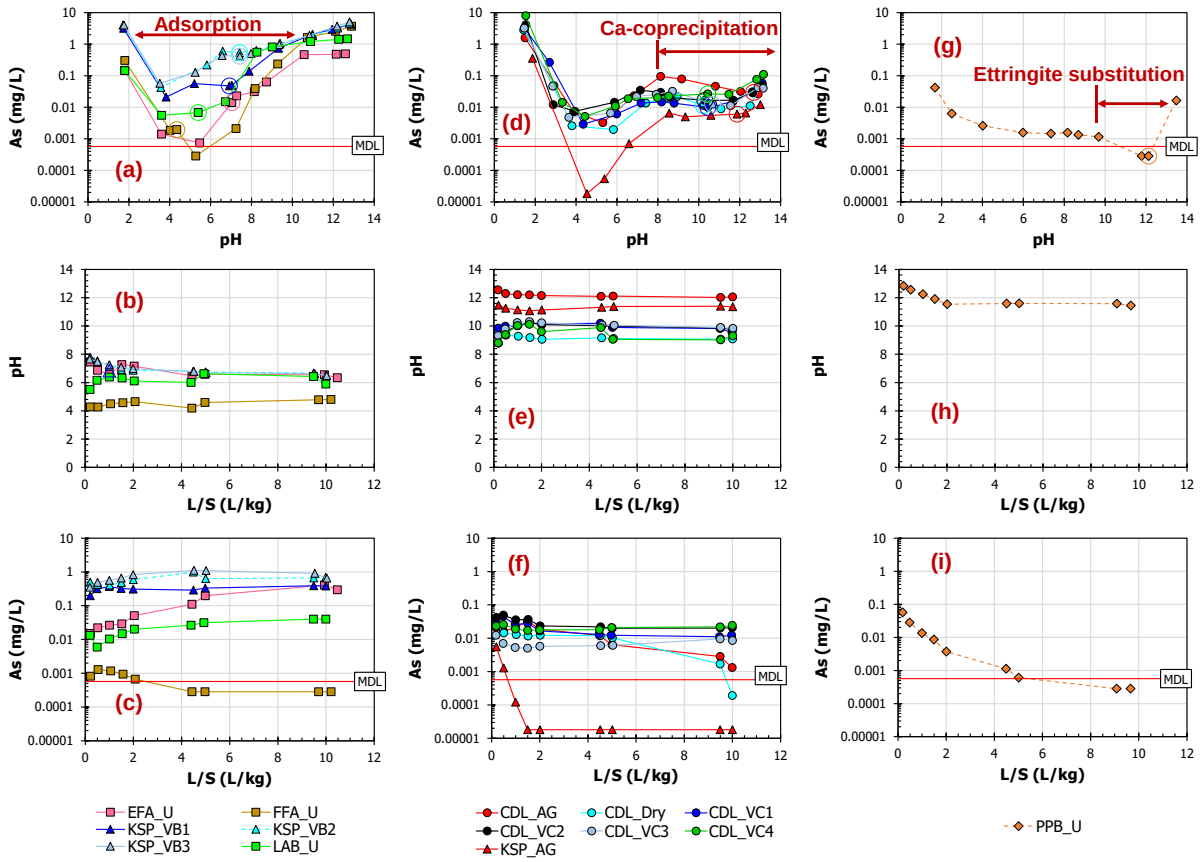

Figure D.1 Summary of the eluate concentration of As from pH-dependent leaching and column tests.

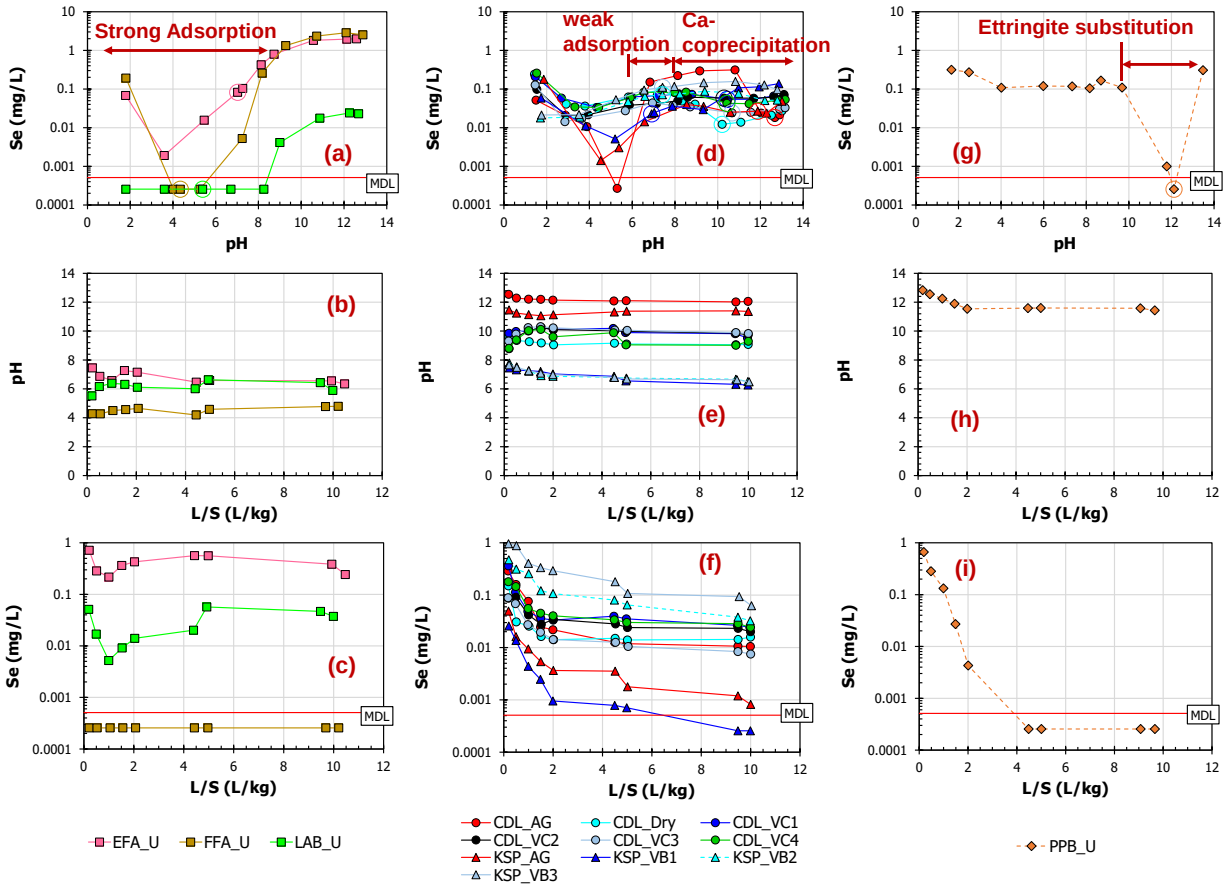

Figure D.2 Summary of the eluate concentration of Se from pH-dependent leaching and column tests.

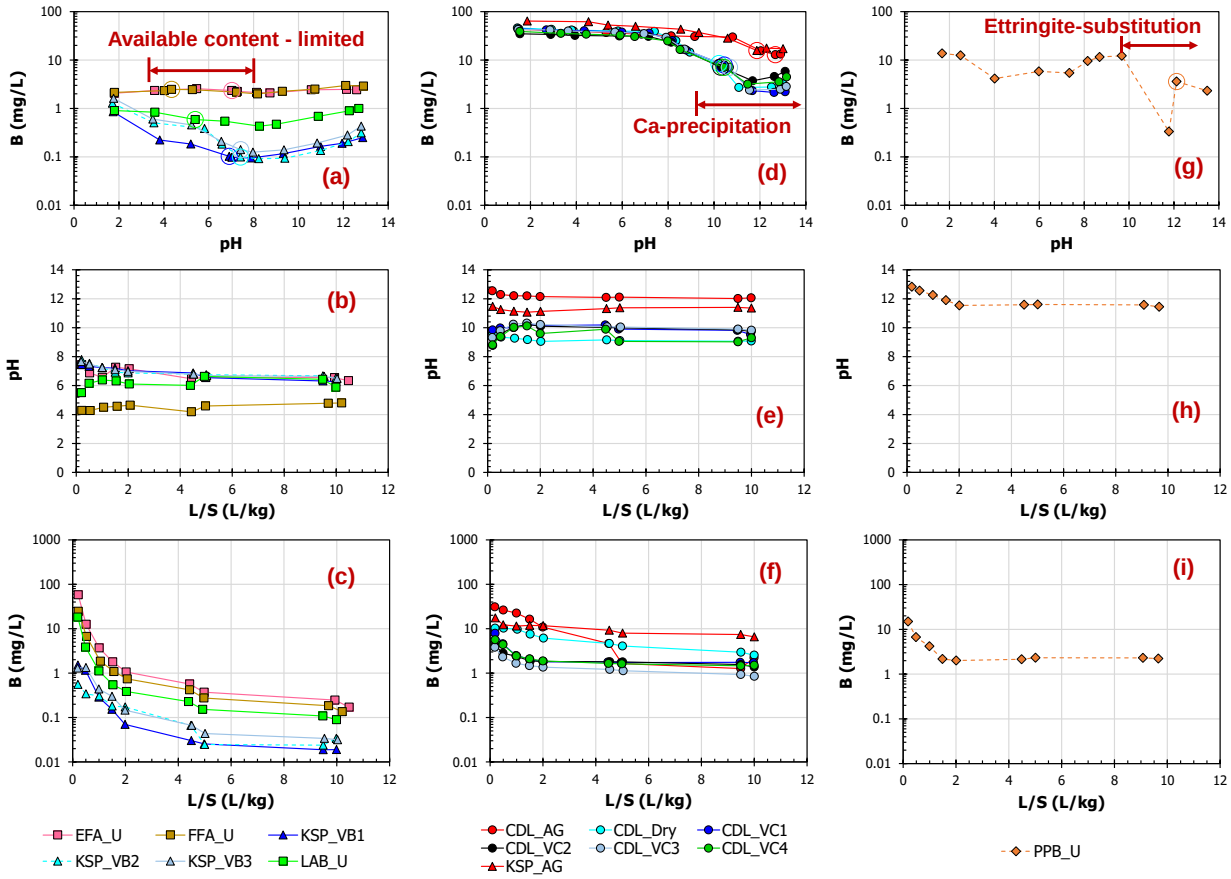

Figure D.3 Summary of the eluate concentration of B from pH-dependent leaching and column tests.

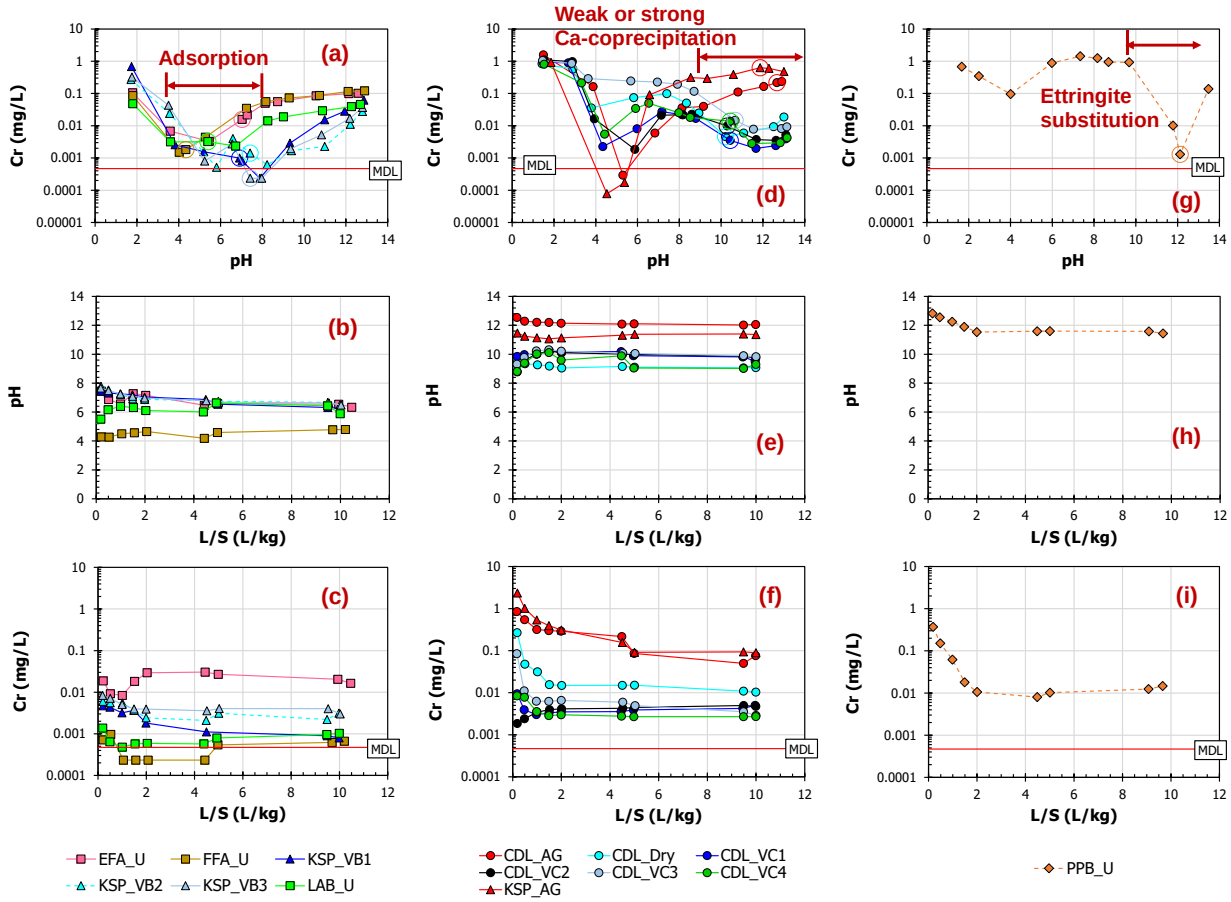

Figure D.4 Summary of the eluate concentration of Cr from pH-dependent leaching and column tests.

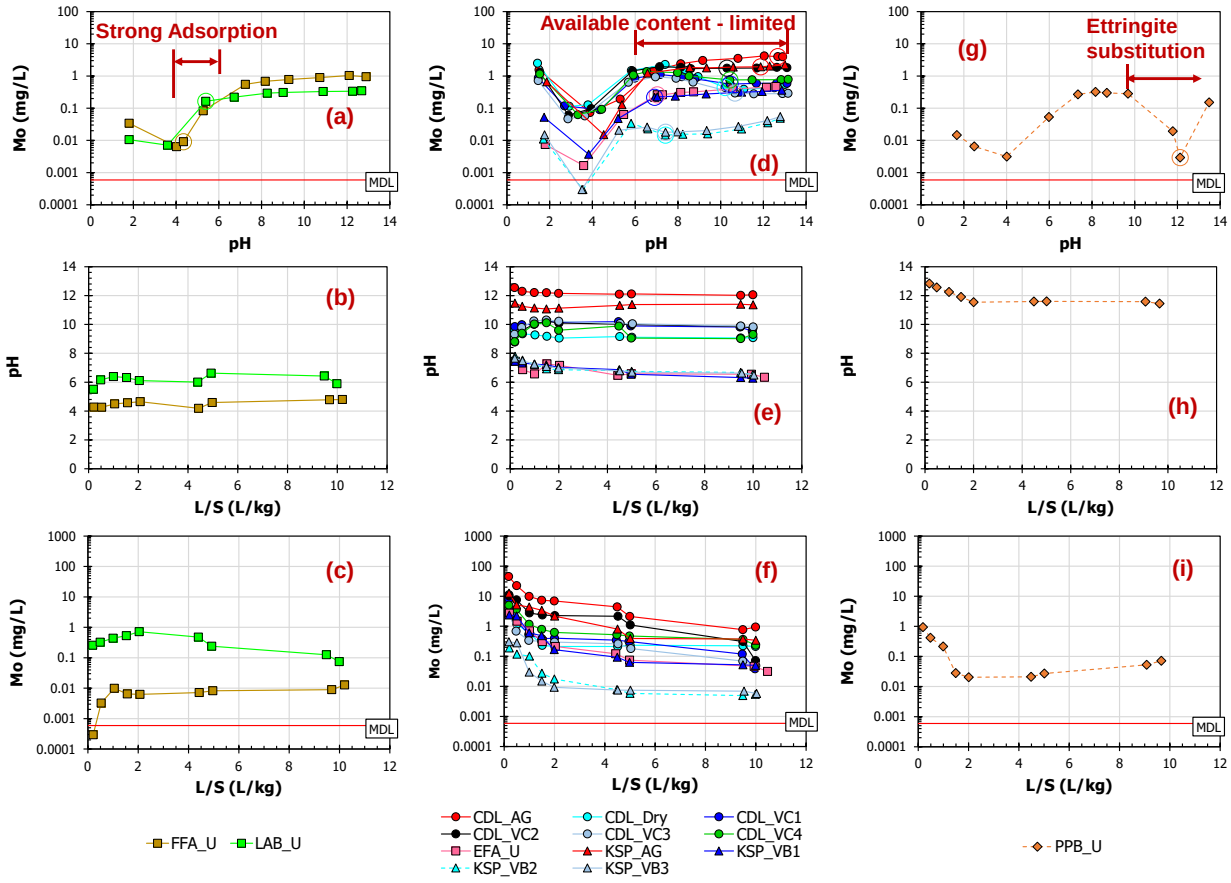

Figure D.5 Summary of the eluate concentration of Mo from pH-dependent leaching and column tests.

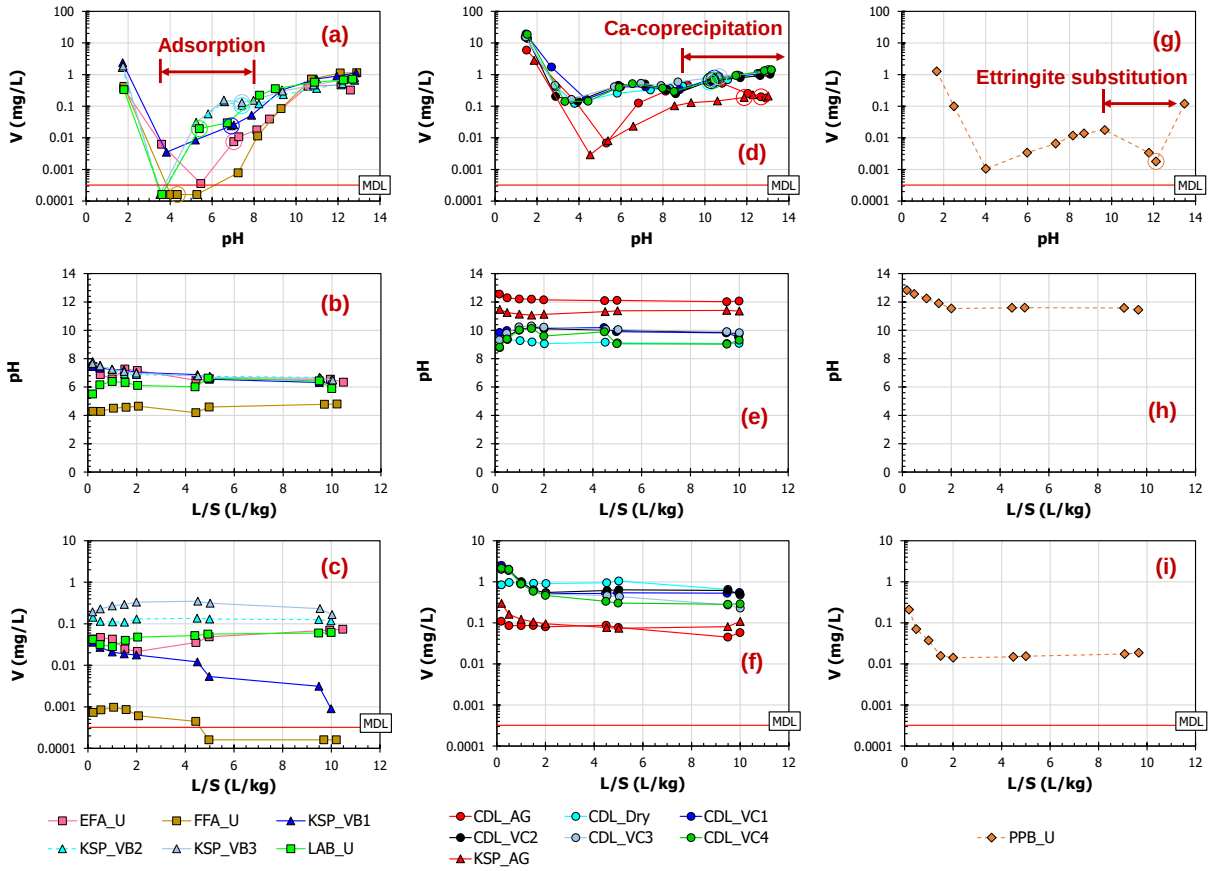

Figure D.6 Summary of the eluate concentration of V from pH-dependent leaching and column tests.

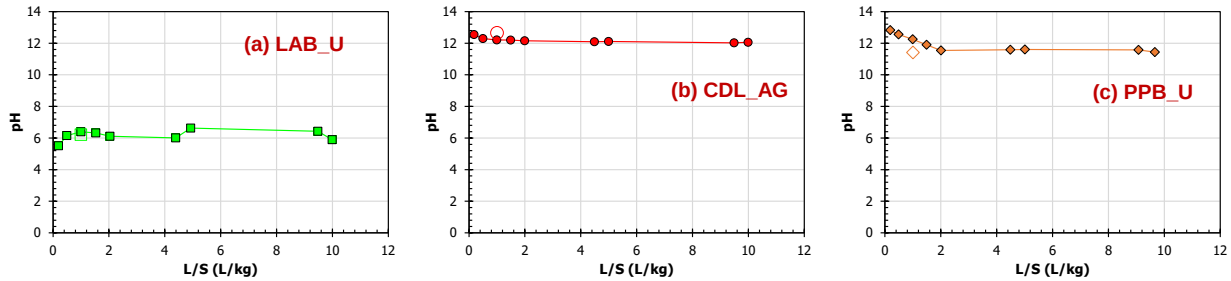

Figure D.7 pH change in the column test for the acidic ash LAB_U and alkaline ashes CDL_AG and PPB_U.

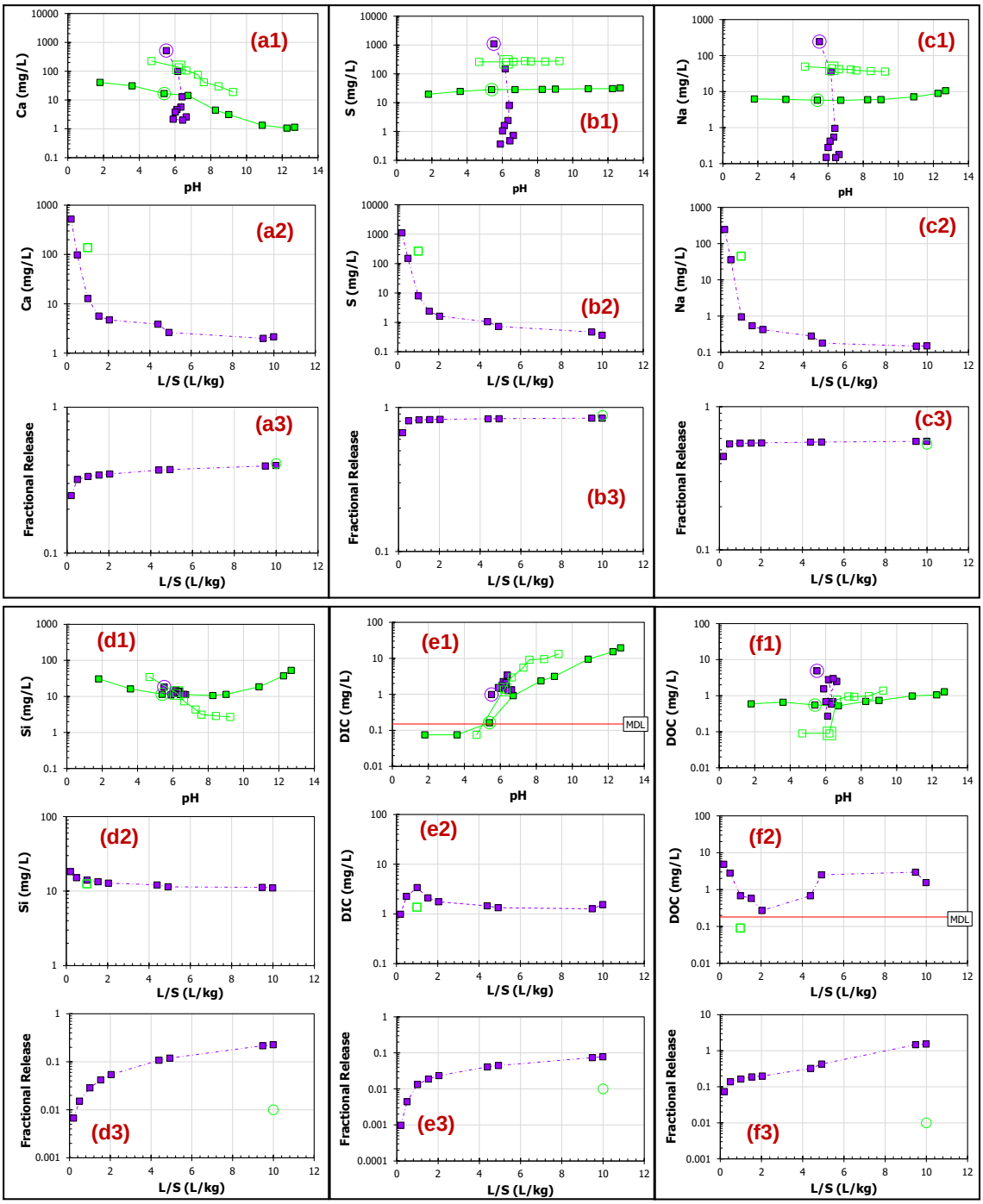

Figure D.8 The pH- and L/S-dependent leaching test results of Ca, S, Na, Si, DIC, and DOC for the acidic as-generated fly ash LAB_U. The fractional release is the fraction of cumulative release relative to the available content (i.e., the maximum release in the pH-dependent leaching test).

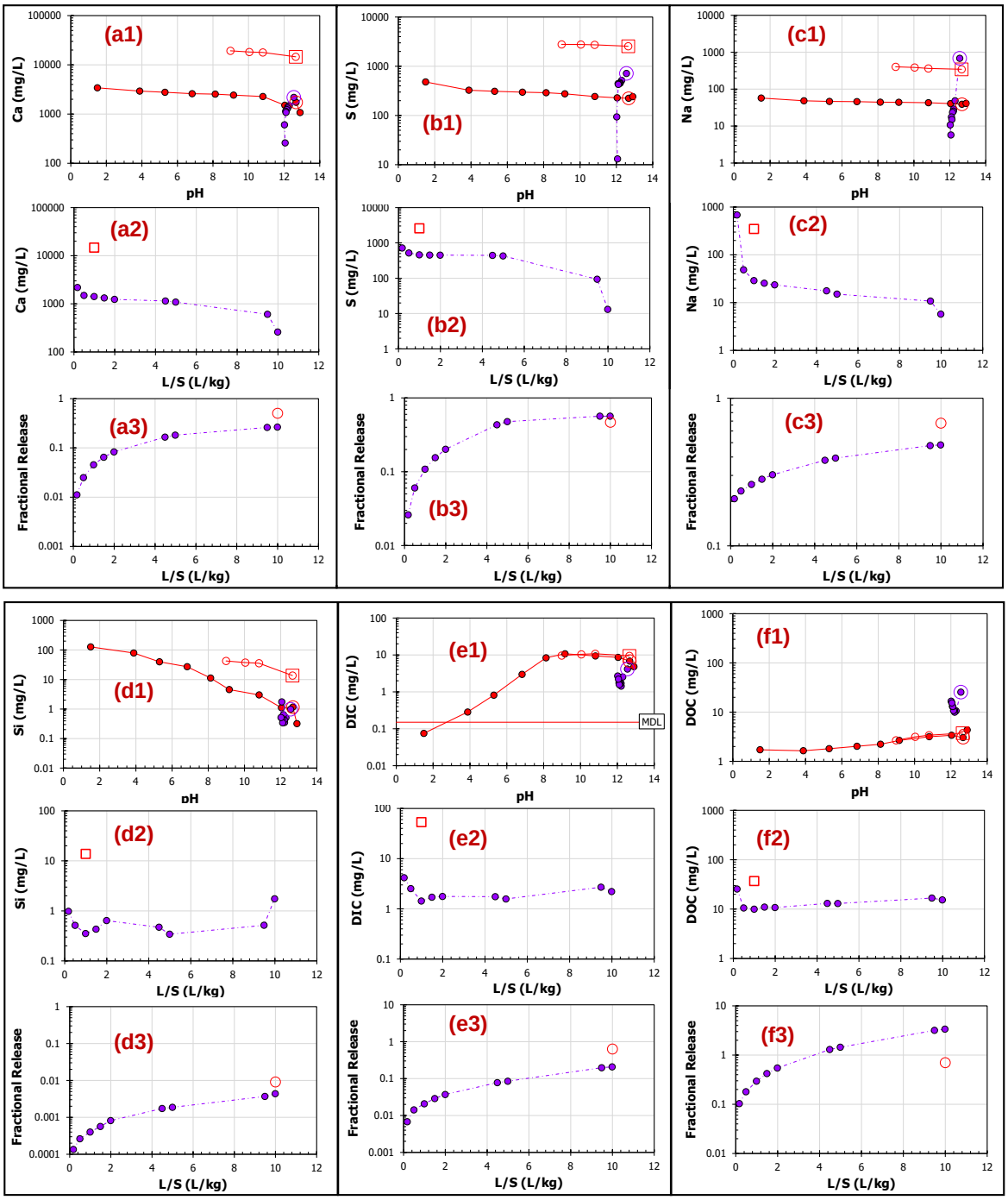

Figure D.9 The pH- and L/S-dependent leaching test results of Ca, S, Na, Si, DIC, and DOC for the alkaline as-generated fly ash CDL_AG. The fractional release is the fraction of cumulative release relative to the available content (i.e., the maximum release in the pH-dependent leaching test).

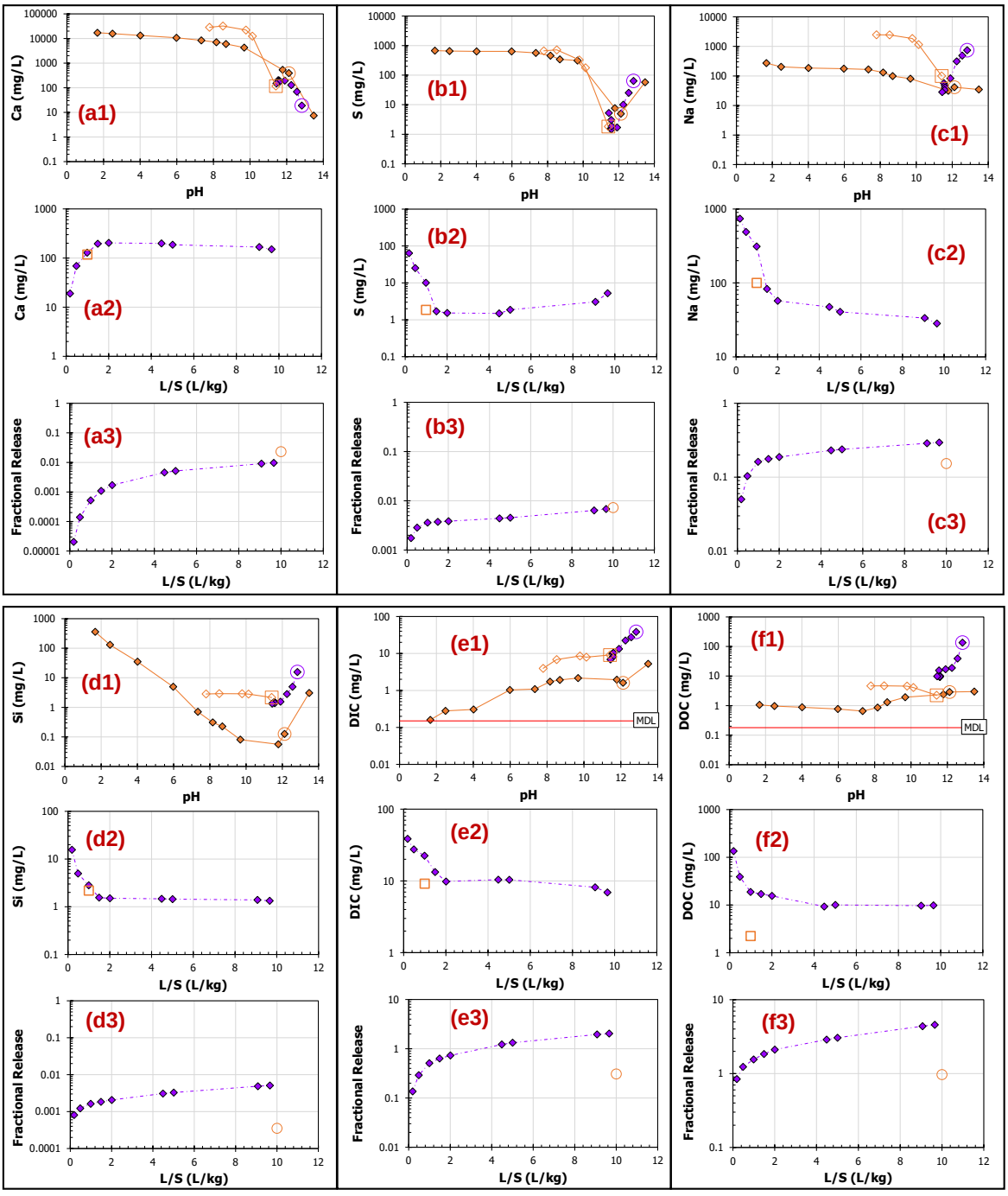

Figure D.10 The pH- and L/S-dependent leaching test results of Ca, S, Na, Si, DIC, and DOC for the alkaline as-generated fly ash PPB_U. The fractional release is the fraction of cumulative release relative to the available content (i.e., the maximum release in the pH-dependent leaching test).

D.II Impacts of field weathering on percolation leaching of coal ashes (Site 2)

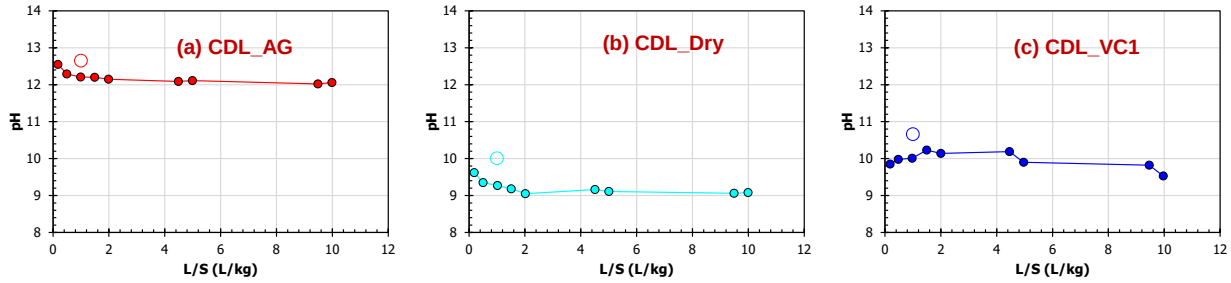

Figure D.11 pH change in the column test for the as-generated ash (CDL_AG) and field ashes (CDL_Dry and CDL_VC1) from the field study on an active coal ash management unit.

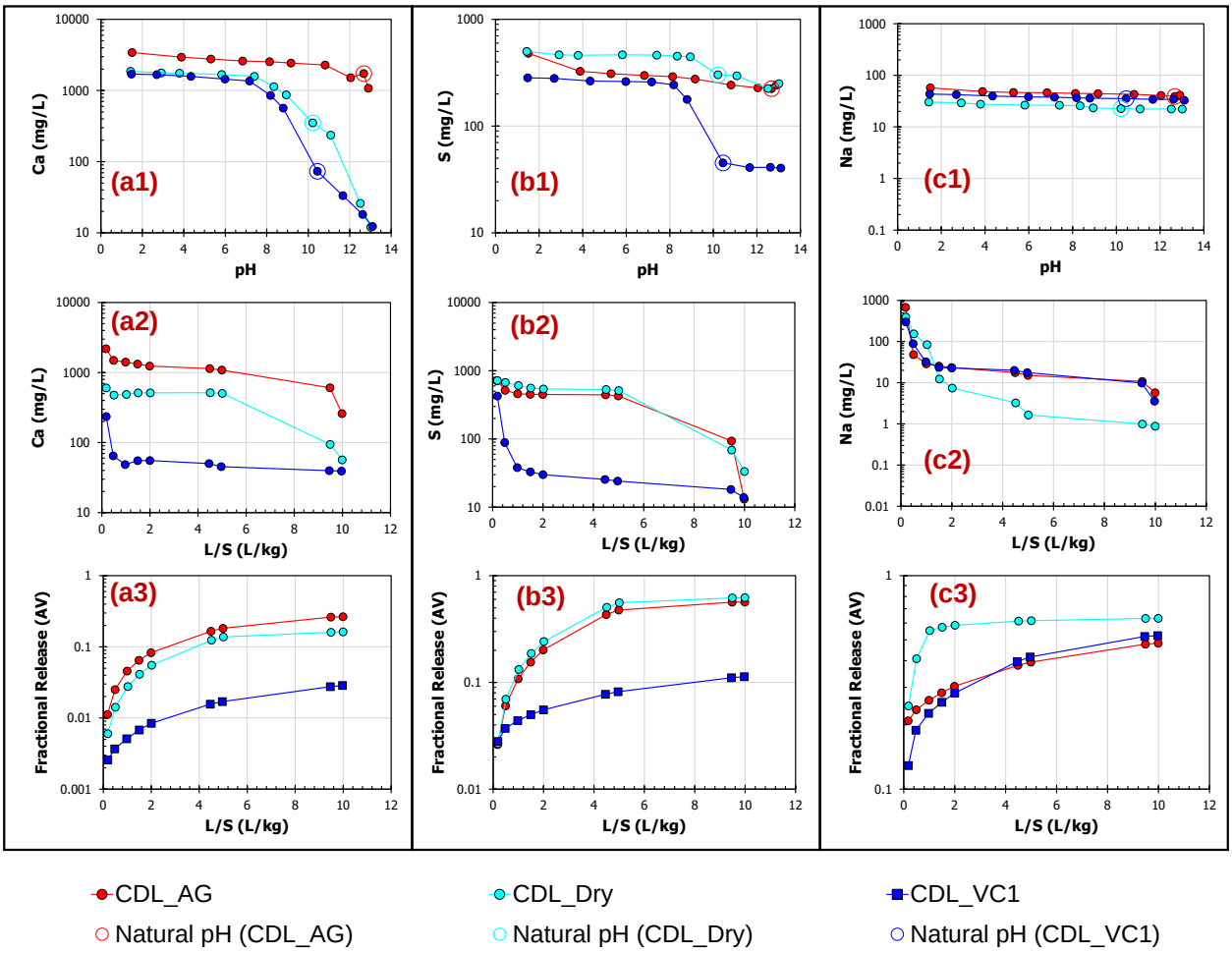

Figure D.12 Comparison of the pH- and L/S-dependent leaching test results of Ca, S, and Na between the as-generated ash (CDL_AG) and field ashes (CDL_Dry and CDL_VC1) from the field study on an active coal ash management unit.

D.III Impacts of redox conditions on percolation leaching of coal ashes (Site 1)

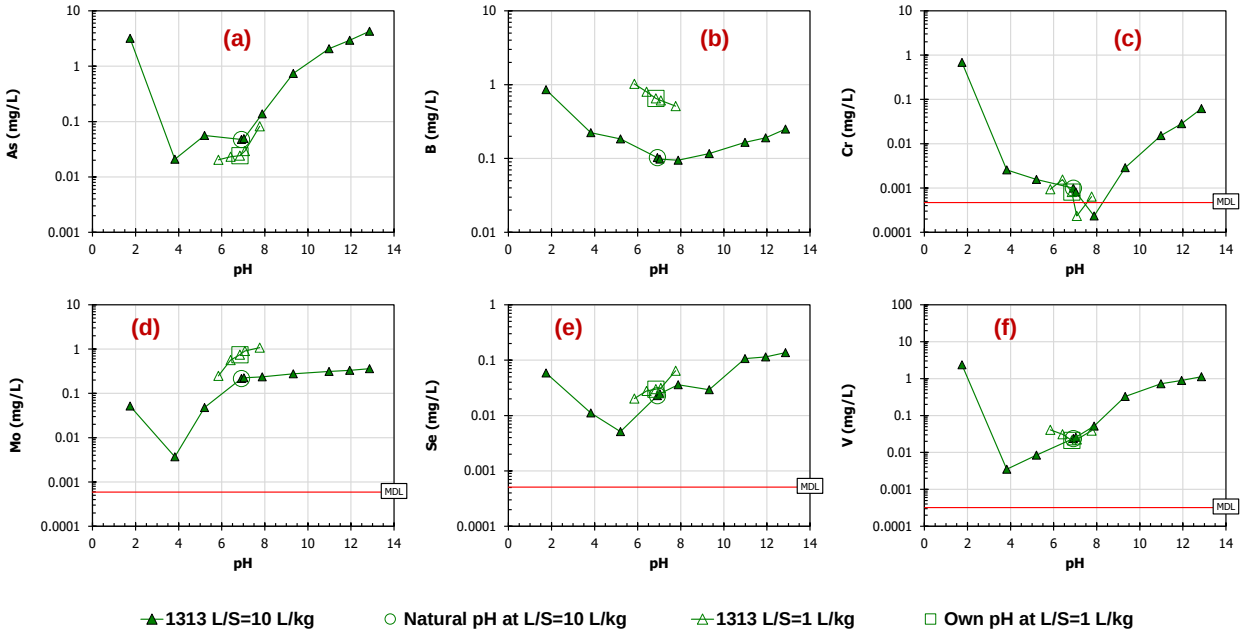

Figure D.13 The pH dependent test results (1313 at L/S=10 L/kg and modified 1313 at L/S=1 L/kg) of the field ash composite KSP_VB1 from the field study on the closed impoundment.